Tectonics and seismic potential along the Caribbean subduction zone in northwestern Colombia based on GeoRED GPS data

(GeoRED GPS データに基づくコロンビア北西部カリブ沈み込み帯のテクトニクスと地震ポテンシャル)

Sindy Carolina LIZARAZO

A dissertation for the degree of Doctor in Science

Department of Earth and Environmental Sciences
Graduate School of Environmental Studies, Nagoya University

2023

ABSTRACT

The Caribbean coast of northwestern Colombia is a region where complex tectonic interactions are taking place between the main oceanic Caribbean plate and several continental blocks known as North Andean, Panamá, Maracaibo, and Bonaire blocks. The existence or lack of subduction of the Caribbean plate beneath the North Andean block margin has been a matter of debate given the absence of a well-defined Wadati-Benioff zone and shallow seismic (and tsunami) activity in instrumental and historical written records. As a result, studies to decipher the Caribbean's seismic/tsunami potential are far from sufficient, which translates into potentially ignored hazards that could have large impacts on the region. Then, it is essential to carry out analyses on this subject.

Existence of an earthquake cycle and seismic potential along a plate subduction zone can be identified through geodetic approaches. Recent dense precise GNSS observations around the world revealed significant strain accumulation during the interseismic period. I made use of the improved spatio-temporal dataset from the GeoRED project (**GEO**desia: **R**ed de **E**studios de **D**eformación in Spanish) of the Geological Survey of Colombia (SGC) to determine interseismic velocities of 87 continuous GPS sites for the period 2008-2017 under the ITRF2014 reference frame. Based on these data, I described motion trends of interacting tectonic plates/blocks in Colombia, which shows general consistency with previous studies. Thanks to the improved spatial resolution of the network, a new tectonic affiliation in the northern part of the country named Macondo block is identified. This interpretation contradicts the previous tectonic framework and has important implications regarding the plate kinematics in northwestern Colombia with a very slow subduction of the Caribbean plate at about 7 mm/yr. In addition, a prevailing compressive pattern of deformation is revealed from horizontal displacement rates, which concentrate mostly along subduction and collision margins, including the Caribbean subduction zone with strain rates of ~65 nanostrain/yr.

The localized contraction at the Caribbean coast of Colombia is intriguing. In order to elucidate if it is due to an ignored seismic potential, an interplate coupling analysis is conducted by inverting 3-dimensional GPS data assuming an elastic half-space medium. The results revealed a locked region on the plate interface offshore Cartagena city, which could cause a M_w8.0 earthquake every ~600 yr based on the size of the locked region and the slow subduction velocity of the Caribbean plate with respect to the Macondo Block. This seismic event could potentially trigger a tsunami

considering the shallowness of the asperity. This interpretation seems to be validated by the consideration of the Caribbean northwestern Colombia as one of the slowest subduction zones characterized by “invisible” megathrust earthquakes and tsunamis occurring over very long recurrence intervals and for which, there is a lack of historical records as well as geological studies. Although the model explains horizontal deformation, a remaining problem is the reproduction of vertical motions, in particular, the large coastal subsidence.

Assuming the Caribbean coast of Colombia is the locus of a future megathrust event that is approaching the final stage of the interseismic period, new modeling is conducted to improve overall data fitting, especially in the vertical component, by taking a regular recurrence of large earthquakes and viscoelastic relaxation of the asthenosphere into account, since it has been proved significant when the recurrence interval is much longer than the relaxation time. Also, the sensitivity of surface deformation to parameters such as the lithospheric thickness, the asthenospheric viscosity, and the earthquake recurrence interval is tested. This modeling attempt confirms the Caribbean subduction zone as a potential locus of a M_w8.1 type earthquake with a recurrence interval still consistent with the absence of historical records and previous estimates. It also reproduces observed velocities to a better degree than the elastic coupling model according to 3-dimensional WRMS values. In this regard, it is demonstrated that early postseismic effects following an earthquake play an important role in increasing interseismic coastal subsidence and then, have important implications regarding the correct interpretation of the geodetic data in terms of seismic and tsunami hazards. Coseismic and postseismic uplift at coastal regions are completely recovered in one earthquake cycle, suggesting that tectonic activity at the subduction interface does not leave a permanent signature in the coastal topography. Regarding the tested parameters, the lithospheric thickness acts as a controlling parameter of the deformation, but the viscosity or recurrence interval assumptions are insensitive and cannot be constrained from the available observation data.

Both the elastic and viscoelastic models conclude the Caribbean subduction zone can potentially generate a M_w8.0 – M_w8.1 earthquake possibly followed by a tsunami in northwestern Colombia for which there is no adequate hazard mitigation and management plans. Besides, if the event takes place in the near future, regional impacts would be devastating. Despite the fact there are no historical records, the absence of these events should not be taken lightly. The slow nature of the

subduction zone produces megathrust over long recurrence times (several hundreds or thousands of years), which cause the earthquakes remain disguised in a seismic quiescence. It remains a challenge for forthcoming studies to integrate paleoseismology and paleotsunami information to corroborate the present dissertation hypothesis and to improve the seismic potential assessment in the Caribbean of Colombia. Additionally, reconciliation of short- and long-term strain inconsistency can be provided by acquiring new geodetic and geological data (older marine terraces) in order to reduce the uncertainties of each observation. Subsequent modeling is needed to solve the time scale discrepancy and to propose a full contemporary/long-term interpretation of the deformation signals.

ACKNOWLEDGMENTS

My deepest gratitude to my advisor, Professor Takeshi Sagiya, for his constant encouragement, patience, and support during the development of this research. Your guidance has been of the utmost value for my personal and academic growth. Also, I would like to thank my thesis committee members, for their valuable suggestions, and everyone at the Earth and Planetary Dynamics Department at Nagoya University, especially Professors Takeo Ito and Angela Meneses Gutierrez, for all their constructive comments through my academic journey. I have learnt probably only a glimpse in relation to Earth Sciences, but you have become an inspiration to keep learning about our magnificent planet.

I am deeply grateful to the GeoRED project of the Geological Survey of Colombia and his creator, Dr. Héctor Mora-Páez, for the trust placed in me at providing the GPS dataset to carry out this research and also, for being a constant mentor and a friend. I feel very lucky to work with data from my country and for my country and I hope my contributions to be useful no matter how small.

I would like to thank the SATREPS Project developed between Colombia and Japan for showing me a wider panorama in relation to seismic, volcanic and tsunami risk management and the importance of collaborative research to generate knowledge that serves to people. Also, I want to thank the Ministry of Education, Culture, Sports, Science and Technology of Japan for sponsoring my studies in Japan. This study was supported by JSPS KAKENHI Grant Numbers 25282111, 2610901 and 26019003.

Infinite thanks to my family for all the support throughout these years I have been far accomplishing this particular goal. It is a blessing to count with you and being able to persist in achieving my dreams, inspired as always by your love that transcends the physical distance. For the ones that are missing from this material world, I only have eternal gratefulness for having believed in me and having teaching me the value of perseverance.

Finally, I would like to thank my friends in Nagoya for being my chosen family here. For having the right words at the right moment and for all the moments we have shared that undoubtedly, have made my time in Japan even more precious.

TABLE OF CONTENTS

ABSTRACT ……i

ACKNOWLEDGMENTS ……iv

GLOSSARY OF ABBREVIATIONS ……viii

1. CHAPTER 1: INTRODUCTION ……..1

2. CHAPTER 2: COLOMBIA'S TECTONIC FRAME ……..9

2.1. General tectonic setting ……9

2.2. Strain distribution ……...11

2.3. Orogeny, Faulting and Volcanism ……....13

2.4. Seismicity ……...15

2.5. Conclusions ……....21

3. CHAPTER 3: GPS OBSERVATIONS ……22

3.1. GeoRED project ……22

3.2. Processing data of the continuous GPS network ……24

3.3. GPS coordinates time series analysis and velocity estimation ……26

4. CHAPTER 4: CRUSTAL MOTIONS ……32

4.1. Interseismic GPS velocities ……32

4.1.1. Horizontal velocity field w.r.t the South American Plate ……33

4.1.2. Horizontal velocity field w.r.t the North Andean Block ……35

4.1.3. Tectonic affiliation of northern Colombia: Macondo Block ……36

4.1.4. Vertical velocity field and its reliability ……43

4.2. Deformation style and its spatial distribution ……49

4.3. Conclusions ……56

5. CHAPTER 5: INTERPLATE COUPLING MODEL ALONG THE CARIBBEAN SUBDUCTION ZONE NORTHWESTERN COLOMBIA PART I – ELASTIC MODEL ……..58

5.1. Methods ……..58

5.1.1. Geodetic inversion method ……58

5.1.2. Caribbean plate configuration ……...62

5.1.3. Model setup ……...63

5.2. Results ……65
5.2.1. Interplate coupling distribution ……65
5.2.2. Model fitting ……..67
5.2.3. Source region width validation ……..67
5.3. Discussion ……..68
5.3.1. Seismogenic strain accumulation – Scenario 1 ……69
5.3.2. Plastic deformation – Scenario 2 ……70
5.3.3. Northwestern Colombia as a case of slow subduction ……..72
5.4. Conclusions ……74
6. CHAPTER 6: INTERPLATE COUPLING MODEL ALONG THE CARIBBEAN SUBDUCTION ZONE NORTHWESTERN COLOMBIA PART II – VISCOELASTIC MODEL ……..76
6.1. GPS velocity data ……...77
6.2. Methods…..……79
6.2.1. Earthquake cycle model formulation ……79
6.2.2. Implementation ……83
6.3. Results ……89
6.3.1. Optimization of location and fault size parameters ……89
6.3.2. Best source fault model ……91
6.3.2.1. Time dependent displacement over an earthquake cycle …….91
6.3.2.2.Comparison of elastic and viscoelastic models ……95
6.3.3. Sensitivity tests of model parameters ……98
6.3.3.1. Sensitivity to the lithospheric thickness – H……....98
6.3.3.2. Sensitivity to the asthenospheric viscosity – η ……...102
6.3.3.3. Sensitivity to the recurrence interval – T ……106
6.4. Discussion ……...…….111
6.4.1. Contemporary vertical motions at the Caribbean slow subduction zone ……..111
6.4.2. Effects of the model configuration ……..111
6.4.3. Seismic and tsunami potential ……114
6.5. Conclusions ……..115

7. CHAPTER 7: DISCUSSION AND IMPLICATIONS ……..117

7.1. Implications of the newly defined Macondo block in the regional kinematics ……117

7.2. Relation between strain distribution and seismicity …….118

7.3. Implications of the elastic and viscoelastic interplate coupling models on the seismogenic/tsunami potential along the Caribbean coast of Colombia ……119

7.4. Long-term vs short-term vertical deformation …….120

8. CHAPTER 8: CONCLUSIONS …….123

BIBLIOGRAPHY …….127

APPENDICES ……...149

APPENDIX A: GPS time series in the Caribbean region northwestern Colombia w.r.t ITRF2014 ……..149

APPENDIX B: Noise parameters for GPS velocity estimations in 3-dimensional components ……..238

GLOSSARY OF ABBREVIATIONS

ABIC	Akaike's Bayesian Information Criterion
BB	Bonaire block
BSMF	Bucaramanga Santa Marta Fault
CESZ	Colombia-Ecuador Subduction Zone
COCONet	Continuously Operating Caribbean GPS Observational Network
CLT	Caldas Lithospheric Tear
CSZ	Caribbean Subduction Zone
DDC	Distance Decay Constant
EFFS	East Frontal Fault System
GNSS	Global Navigation Satellite System
GeoRED	Geodesia: Red de Estudios de Deformación (in Spanish) Geodesy: Deformation Studies Network (in English)
GPS	Global Positioning System
IGS	International GNSS Service
InSAR	Interferometric Synthetic Aperture Radar
ITRF	International Terrestrial Reference Frame
LMV	Lower Magdalena Valley
MB	Maracaibo blokc
NAB	North Andean block
NAS	North Andean Sliver
OF	Oca Fault
PM	Panamá block
RINEX	Receiver Independent Exchange Format
RSL	Relative sea-level

RSNC	Red Sismológica Nacional de Colombia (in Spanish) National Seismological Network of Colombia (in English)
SCDB	South Caribbean Deformed Belt
SGC	Servicio Geológico Colombiano (in Spanish) Geological Survey of Colombia (in English)
SFB	Sinú Fold Belt
SJFB	San Jacinto Fold Belt
SSE	Slow Slip Events
SNSM	Sierra Nevada de Santa Marta
WRMS	Weighted Root Mean Square
w.r.t	with respect to

CHAPTER 1

INTRODUCTION

Colombia is a tectonically active region resulting from the interaction among three main tectonic plates: the Caribbean, the Nazca, and the South American plates, and two major tectonic blocks: the Panamá (PM) and the North Andean (NAB) blocks (Kellogg and Vega, 1995; Bird, 2003). Recent models based on geodetic and geological data have proposed the existence of additional tectonic blocks inside the NAB known as the Maracaibo (MB) and the Bonaire (BB) blocks, that show some degree of kinematic independency (Audemard, 2014). This complexity is responsible for the current orogeny, the intense faulting, seismicity, and volcanism manifestations in the country (Figure 1.1).

The deformation of continental Colombia is mainly controlled by subduction and collisional processes. The ongoing Panamá-arc collision in the northwest at a rate of ~15-18 mm/yr (Mora-Páez et al, 2019) separates two contrasting subduction processes, the Caribbean and the Nazca ones, occurring along the northern and western margins of the country, respectively. In particular, the subduction of the Nazca plate at a rate of ~46 mm/yr (Mora-Páez et al, 2019) has developed a volcanic front along the Central Cordillera and has been responsible for the largest earthquakes/tsunamis (M_w>7.5) along the Colombia-Ecuador subduction zone (CESZ) during the last and present centuries (Mendoza and Dewey, 1984). Remarkable earthquakes have occurred in 1906 (M_w8.8), 1942 (M_w7.9), 1958 (M_w7.8), 1979 (M_w8.2) (Kanamori and McNally, 1982), and the most recent one in 2016 (M_w7.8) (Chlieh et al, 2021). The Caribbean subduction zone (CSZ), on the other hand, is characterized by a very slow velocity of ~11 mm/yr (Mora-Páez et al, 2019), lack of magmatism, low shallow seismicity and no historical records of megathrust earthquakes and/or tsunamis (Vargas and Mann, 2013; Bernal-Olaya et al, 2015; Vargas et al, 2015; Syracuse et al, 2016; Mora et al, 2017; Pérez et al, 2018; Vargas, 2020).

Global Navigation Satellite Systems (GNSS) have been a preferred tool to study active plate boundaries, tectonic motions, and volcano deformation (Burgmann et al, 2000; Wang et al, 2012). Dense GNSS networks in the world have permitted the study of crustal deformation at different stages of the earthquake cycle at subduction zones, which have provided a more comprehensive knowledge of this process in its co-, post-, and interseismic phases. Snapshots of the deformation have revealed a phase of interseismic tectonic strain accumulation at the plate interface, followed

by an instantaneous strain release at the time of the earthquake and a fast transient phase of postseismic deformation where the stress in the rock medium is relaxed.

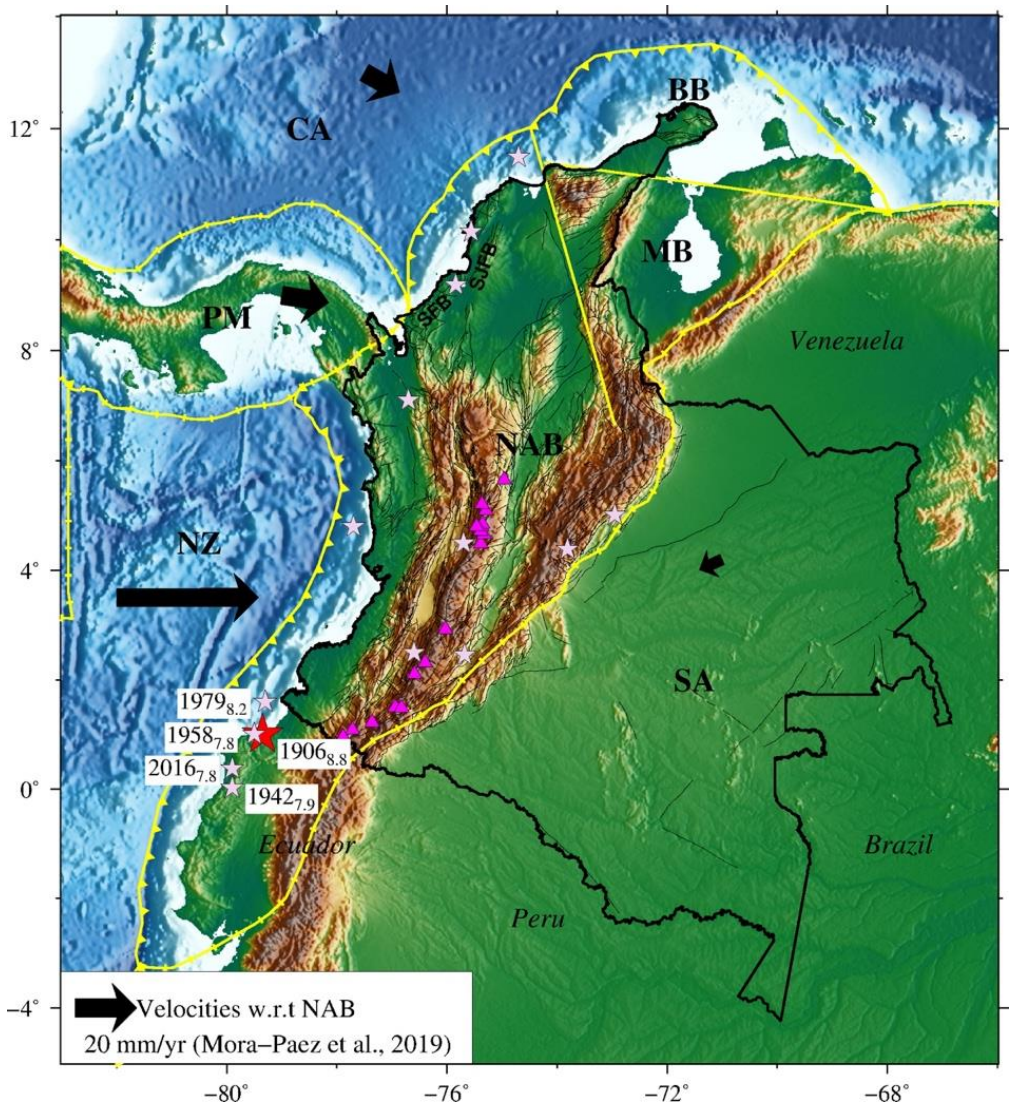

Figure 1.1. *General setting of Colombia. Thin black lines denote geological faults. Magenta triangles represent active volcanoes. Pink stars represent $M_w \geq 5.5$ interplate and intraplate earthquakes. Subduction earthquakes at the CESZ are presented with year and magnitude, being the red star the characteristic 1906 $M_w 8.8$ earthquake. Black arrows represent the velocities w.r.t the NAB according to Mora-Páez et al. (2019). Yellow lines represent plate/block boundaries. Abbreviations as follow SA: South American plate, NZ: Nazca plate, CA: Caribbean plate, PM: Panamá Block, NAB: North Andean Block, MB: Maracaibo Block, BB: Bonaire Block, SJFB: San Jacinto Fold Belt and SFB: Sinú Fold Belt. Relief based on the ETOPO1 Global Relief Model (NOAA - National Oceanic and Atmospheric Administration).*

In general, most of the models to analyze the earthquake cycle applied a kinematic approach that attributes the surface deformation to the elastic response of the slip deficit at the plate interface. The assumption of the elastic model is that interseismic velocity of strain accumulation is constant, which has been proven to be incorrect based on observational data (Wang et al, 2012; Wang, 2017; Meneses-Gutierrez et al, 2022). Contrarily, interseismic deformation is strongly time-dependent, which can reflect the stress relaxation of the upper mantle, variable fault slip or slip deficit on the plate interface, or a combination of them. From these processes, the former one is considered the most important to analyze deformation over earthquake cycles at time scales of decades to centuries (Wang, 2017). The sudden energy release at the earthquake time perturbs the stress state in the upper mantle, which in turn responds in a viscoelastic manner affecting surface motions over long spatial and temporal scales. These effects are especially significant when the recurrence time between earthquakes is much longer than the relaxation time of the asthenosphere (Sagiya, 2015; Noda et al, 2018).

The Geological Survey of Colombia (SGC), through the GeoRED project (**GEO**desia: **R**ed de **E**studios de **D**eformación, in Spanish), has implemented a GPS network (Global Positioning System) since 2007 oriented to the acquisition of data for crustal deformation and geodynamics studies in Colombia and its surroundings (Mora-Páez et al, 2018). As of December 2021, the GeoRED network was composed of 158 continuous GPS stations, and more than 350 campaign-style stations for episodic data acquisition. The enhanced spatial and temporal resolution of the network allows detailed analyses of the distribution of the deformation and its style, which is essential in estimating and mitigating the seismic hazard associated with active boundaries, and the understanding of the seismic cycle.

Based on GPS displacement rates, a predominantly compressive tectonic regime was identified in Colombia along both subduction zones including the intermediate collision region (Arcila et al, 2020; Lizarazo, 2020; Vargas, 2020). This feature has good correspondence with repeated megathrust earthquakes along the CESZ, but not with the low seismicity level at the CSZ. At the CESZ for example, several authors have performed interplate coupling models based on GPS data following the backslip approach by Savage (1983) (e.g, Trenkamp et al, 2002; White et al, 2003; Nocquet et al, 2014; Chlieh et al, 2014; Sagiya and Mora, 2019; Chlieh et al, 2021). They have mapped the distribution of slip deficit at the plate interface, detecting the location and extent of

seismic source regions, and have related them with the sources of past megathrust earthquakes. Based on this information they have reevaluated the slip budget at the subduction zone as well as the recurrence interval between earthquakes.

Figure 1.2 presents the distribution of discrete seismic asperities revealed by steady interseismic velocities from a dense GPS network in Ecuador and Colombia according to Chlieh et al. (2021). The heterogenous interplate coupling pattern exposes a seismic segmentation along the CESZ where high coupling degree regions associated with previous megathrust earthquakes are separated by creeping corridors, some of which are linked to slow slip events (SSE). Based on the analysis of the accumulated co- and postseismic moment released by the 2016 Pedernales earthquake (M_w7.8), they identified the asperity that hosted it was indeed mature enough to free ~70% of the seismic moment buildup since 1942 (M_w7.8). A similar analysis was performed for the earthquakes in 1958 (M_w7.6) and 1979 (M_w8.1) that ruptured two other asperities to the north of the CESZ.

At the CSZ, some authors have proposed that the large shortening is accommodated in the Sinú (SFB) and the San Jacinto (SJFB) Fold Belts along the Caribbean coast (Caro and Spratt, 2003; Figure 1.1), which suggests permanent deformation with no hazardous outcomes for the region. In opposition, other authors have suggested active subduction along the margin (Vargas and Mann, 2013; Bernal-Olaya et al, 2015; Vargas et al, 2015; Syracuse et al, 2016; Mora et al, 2017; Pérez et al, 2018; Vargas, 2020), which entails undoubtedly unknown seismic and tsunami hazards. Therefore, the origin and implications of the large compressive deformation in northwestern Colombia remain controversial. Further, almost no studies to evaluate the slip distribution at the plate interface have been performed due to the low seismicity level, the lack of megathrust/tsunami records, and the slow subduction velocity of the Caribbean plate at the northern margin.

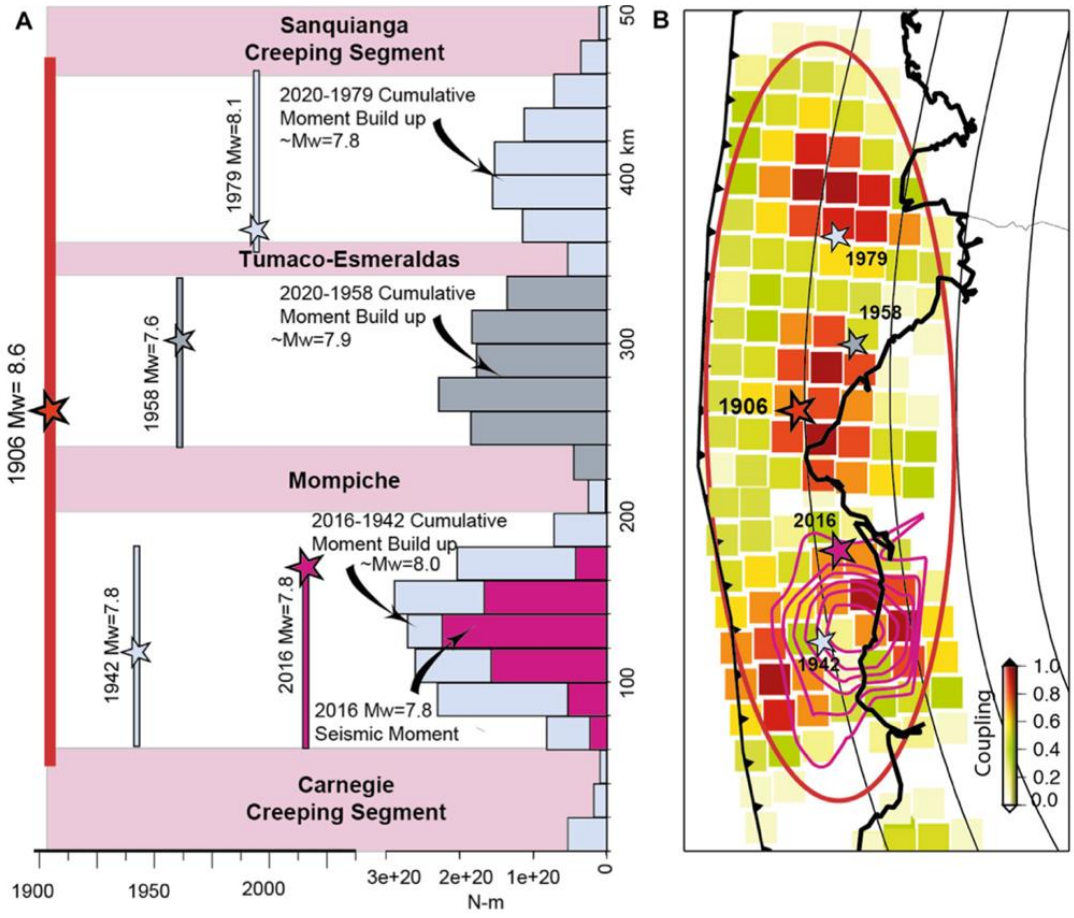

Figure 1.2. *Interplate coupling distribution along the CESZ and cumulative seismic moment buildup comparison since previous earthquakes in 1942, 1958, and 1979 with the 2016 M_w7.8 Pedernales earthquake expressed in N·m (Chlieh et al, 2021). a). Along-trench cumulative moment buildup represented by the horizontal bars, light pink regions denote creeping segments that act as barriers to seismic ruptures, b). Map of the average interseismic coupling and epicenters of previous events denoted by stars. Seismic slip contours of the 2016 M_w7.8 Pedernales event are reported in purple overlapping the 1942 asperity.*

Regarding this last feature, Gutscher and Westbrook (2009) demonstrated that slow subduction margins, where velocities ≤4 cm/yr, can rupture with M_w≥8 earthquakes over long recurrence intervals implying an important seismic and tsunami hazard usually overlooked (Figure 1.3). The regions of southwest Iberia and Sicily, locus of M_w8.7 (1755 Lisbon) and M_w8.0 (1693 Catania) earthquakes/tsunamis, reported subduction velocities <1 cm/yr corresponding to atypically long recurrence intervals of 500 and 1500-2000 yr, respectively. These observations sustain a possibility the CSZ might have ruptured in a megathrust earthquake a long time ago and may

rupture again in the future though the Caribbean coast of Colombia was not considered as such a candidate in Gutscher and Westbrook (2009).

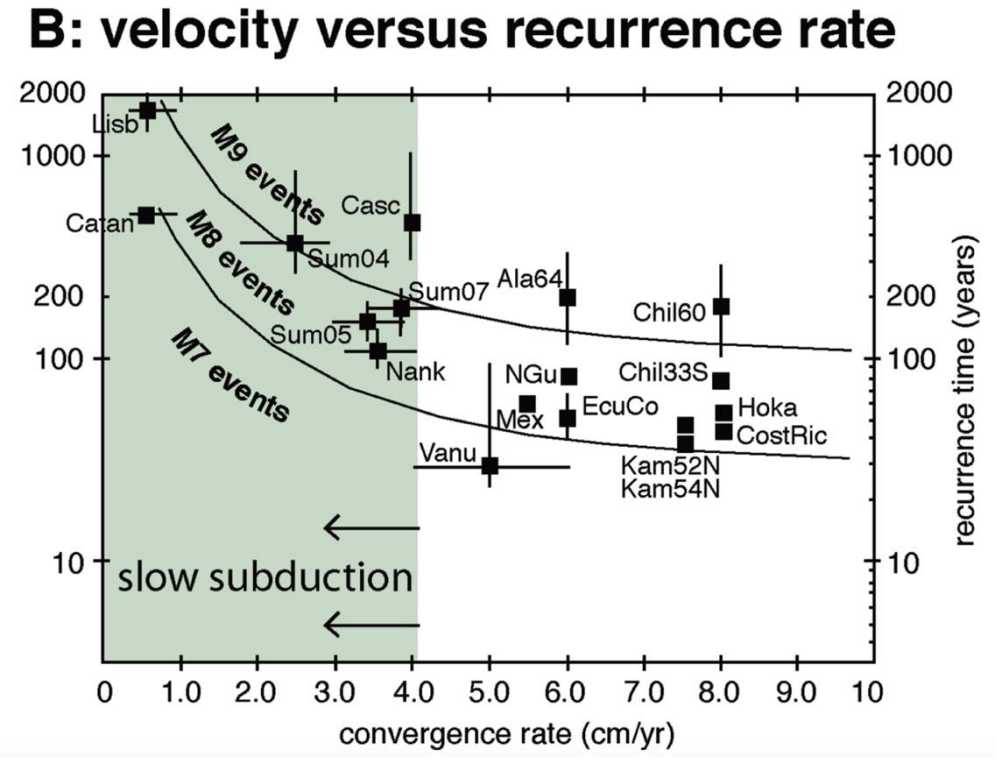

Figure 1.3. *Subduction velocity vs recurrence interval plot as in Gutscher and Westbrook (2009). Green region represents slow subduction zones where velocity is ≤4 cm/yr. Plotted earthquakes with M_w>7.5. Lisb: M_w8.7 (SW Iberia), Catan: M_w8.0 (Sicily), Casc: M_w9.0 (Cascadia), Sum04: M_w9.3 (Sumatra), Sum05: M_w8.7 (Sumatra), Sum07: M_w8.4 (Sumatra), Nank: M_w8.1 (Nankai), Ala64: M_w9.2 (Alaska), NGu: M_w8.0 (New Guinea), Mex: M_w8.1 (Mexico), Chil60: M_w9.5 (Chile), Chile33S: M_w8.5 (Chile), EcuCo: M_w8.8-M_w8.2 (Ecuador-Colombia), Kam52N: M_w8.0 (Kamchatka), Kam54N: M_w8.5 (Kamchatka), Hoka: M_w8.3 (Hokkaido), CostRic: M_w7.8 (Costa Rica). Vanuatu recurrence (Vanu) is taken from Taylor et al. (1990).*

From the few studies to evaluate the seismic potential at the CSZ, the one from Mencin (2018) showed a locked offshore region in northern Colombia based on GPS velocity gradients along profiles and bathymetry data (Figure 1.4).

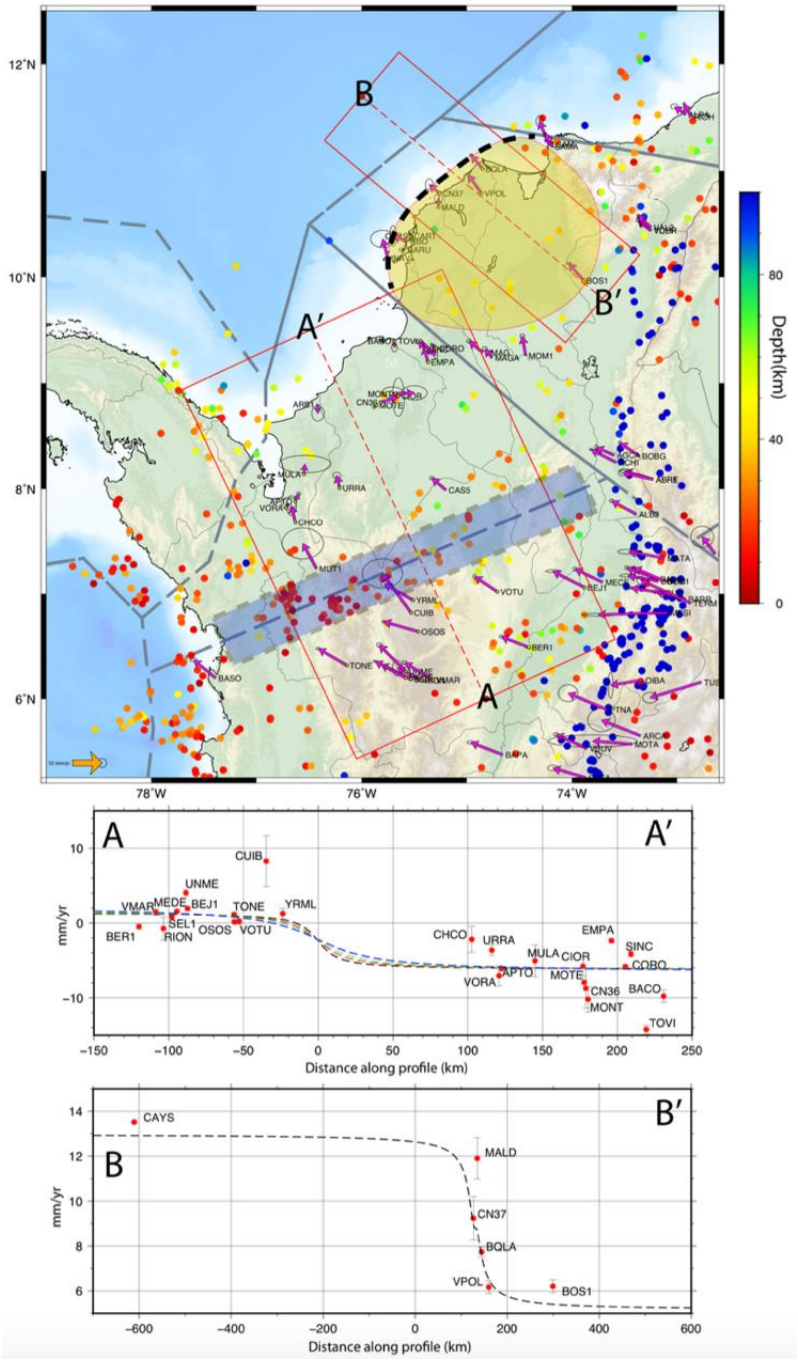

Figure 1.4. *Velocity profiles A-A' and B-B' in northern Colombia expressed in the Caribbean plate reference frame and proposed active subduction region in yellow according to Mencin (2018).*

His interpretation indicated that the source is been loaded at a slow rate of ~8 mm/yr, accumulating enough slip deficit since the last 800CE to rupture in an $8.0 \leq M_w \leq 8.3$ earthquake. Although this study favored the seismogenic scenario in consistency with the categorization of the Caribbean as a slow subduction zone with long recurrence, no written records of such hazards exist.

In addition, neither paleoseismological nor paleotsunami data is available to corroborate this interpretation. Then, more efforts to elucidate the seismic potential of the region are needed.

The present thesis aims to evaluate the seismic potential in the CSZ of northwestern Colombia under elastic and viscoelastic earth models using the interseismic deformation data derived from the GeoRED network during the period 2008-2017. The elastic interplate coupling model gives us the first hint about the location, extent, and potential seismic budget of the study region. The viscoelastic model on the other hand refines previous estimations by including meaningful effects produced over long-term recurrence intervals, which seems to be the case in the Caribbean of northwestern Colombia.

In the following chapters, I will introduce a detailed tectonic setting of Colombia as well as a description of the observational GPS data and methods to compute the interplate coupling along the CSZ. Finally, I will discuss the potential implications for regional kinematics and the seismic budget in the region and a proposal to reconcile short and long-term deformation.

CHAPTER 2

COLOMBIA'S TECTONIC FRAME

2.1. General tectonic setting

Colombia is located in the northwestern corner of South America, a region characterized by a complex tectonic environment where three major lithospheric plates: South American, Nazca, and Caribbean plates, and several crustal blocks: NAB, PM or PM-Choco, MB, and BB blocks, interact with each other under different kinematic conditions (Pennington, 1981; Kellogg and Vega, 1995; Trenkamp et al, 2002; Taboada et al, 2000; Pérez et al, 2001; Bird, 2003; Audemard, 2014; Mora-Páez et al, 2019; Kellogg et al, 2019). The southeastern half of continental Colombia is located on the Amazonian craton, an old rigid undeformed province in the South American plate, while the northwestern half is contained by the NAB and amalgamated blocks north of it. The active structure that separates these two tectonic units is the Eastern Frontal Fault System (EFFS) that constitutes the foothills of the Eastern Cordillera. The remaining boundaries of the NAB are represented by the Nazca subduction zone to the west, which has produced large earthquakes during the 21st century (Mendoza and Dewey, 1984), the collision zone with the PM block to the northwest, and the convergent margin north of the country, where the Caribbean plate sinks below the NAB as recognized by Van Der Hilst and Mann (1994) and Pérez et al. (1997), from the triple junction Caribbean-Panamá-NAB to the islands of Curacao and Aruba (Bird, 2003; Figure 2.1).

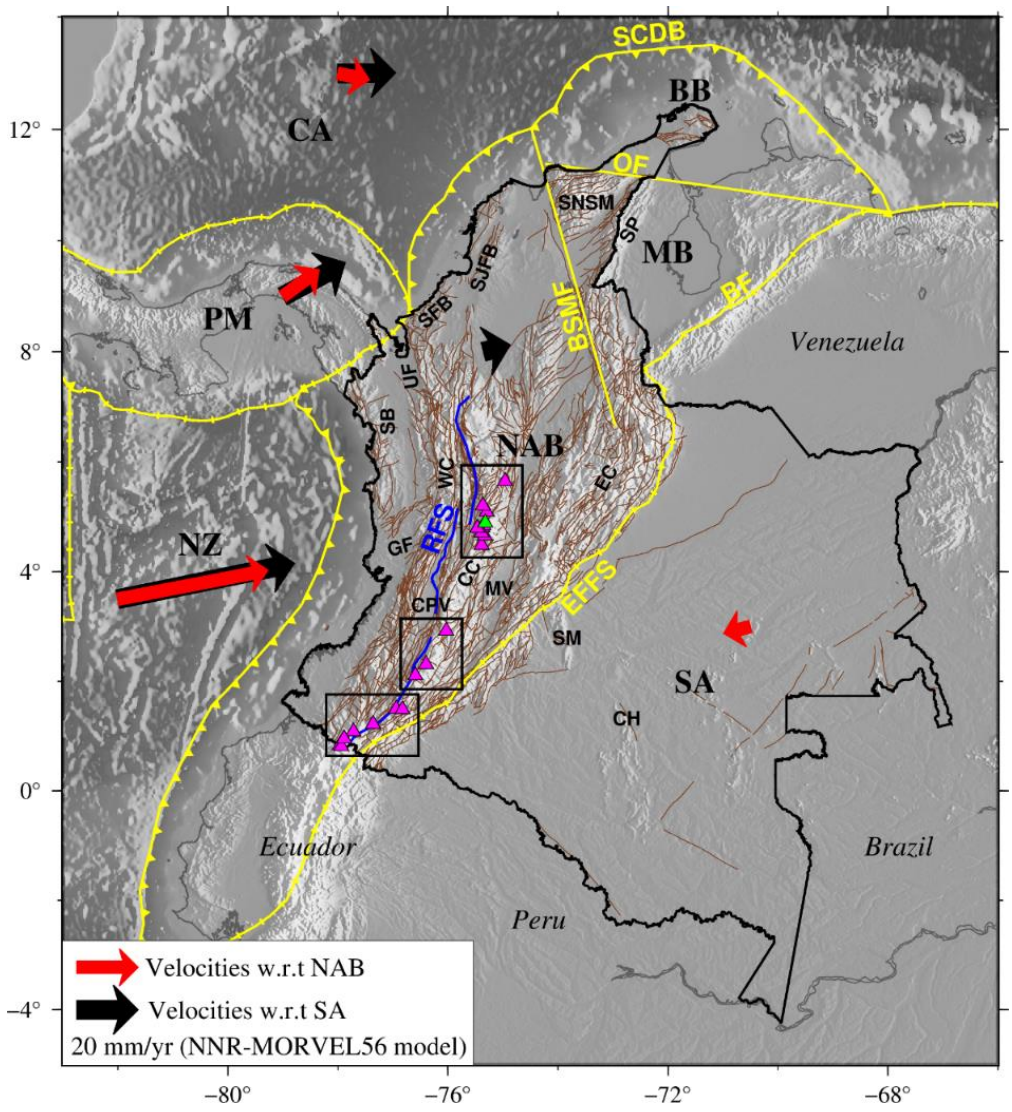

Figure 2.1. *Detailed tectonic setting of Colombia. Thin brown lines denote geological faults and blue line shows the RFZ as in the ATA database (Veloza et al, 2012). Magenta triangles are active volcanoes monitored by volcanological and seismological observatories of the SGC. From north to south these are denoted by the bounding black boxes: SGC-OVSM, SGC-OVSPop and SGC-OVSP. Green triangle shows the location of the Nevado del Ruiz volcano. Red and black arrows show the relative motion in mm/yr w.r.t the NAB and the SA, respectively according to the NNR-MORVEL56 model (Argus et al, 2011). Other symbols and some abbreviations as in Figure 1.1. Additional abbreviations as follow SCDB: South Caribbean Deformed Belt; OF: Oca Fault; BSMF: Bucaramanga-Santa Marta Fault; BF: Boconó Fault; EFFS: Eastern Frontal Fault System, RFZ: Romeral Fault System, SNSM: Sierra Nevada de Santa Marta; SP: Serrania del Perijá; UF: Uramita Fault; SB: Serrania del Baudó; WC: Western Cordillera; GF: Garrapatas Fault; CPV: Cauca Patía Valley; CC: Central Cordillera; MV: Magdalena Valley; EC: Eastern Cordillera; SM: Serrania de la Macarena and CH: Chiribiquete.*

According to the Global Plate Motion Model NNR-MORVEL56 (Argus et al, 2011), the Nazca plate subducts eastward offshore the Pacific coast of Colombia at ~50 mm/yr in a normal subduction margin, while the Caribbean plate, a slow and flat non-volcanic subduction zone (Mantilla-Pimiento et al, 2007; Lara et al, 2013; Vargas and Mann, 2013; Bernal-Olaya et al, 2015; Mora et al, 2018; Kellogg et al, 2019; Vargas, 2020), presents a relative southeastward motion of ~11 mm/yr, both with respect to the NAB. These motions are slightly faster when represented relative to the South American plate with velocities of ~59 mm/yr and ~19 mm/yr, respectively. The collision of the PM/PM-Choco block in northwestern Colombia initiated underwater about 24 Ma (O'Dea et al, 2016) with closure between 15 Ma and 3 Ma (Coates et al, 2004 and Coates and Stallard, 2013; O'Dea et al, 2016), continues until now at rates of ~15 mm/yr with respect to the NAB and ~23 mm/yr relative to the South American plate (Figure 2.1). The formation of the Panamá isthmus was an important event in a biological, ecological, climatic, and evolutionary sense, but also in a tectonic one since it separates distinctive subduction processes taking place in western and northern Colombia adding to the complexity of the region (Vargas and Mann, 2013). The remaining MB and BB blocks have been defined geologically in local and regional tectonic models (Audemard, 2003; Audemard., 2014). However, they seem to amalgamate into the northern part of the NAB where data is far from sufficient to describe their kinematic independence (Freymueller et al, 1993; Trenkamp et al, 2002; Lizarazo et al, 2021). To this respect, Lizarazo et al. (2021) identified the rigid motion of the northern NAB based on recent GPS data, which encompasses the previously mentioned BB and MB blocks into a unique block named Macondo that amounts to ~13 mm/yr relative to the NAB in E-SE direction. More details about the definition of the Macondo Block will be given in Chapter 4.

2.2. Strain distribution

Regarding the strain regime in Colombia, Arcila et al. (2020) provided a description of stress and strain concentration zones and their orientation through an integrated analysis of CMT (Centroid Moment Tensor) and GPS data (Figure 2.2). In particular, they found a compressive stress field at the southwestern and northwestern corners of the country at depth, related to subduction and collision environments, and also, along the Eastern Cordillera. These regions are in fair agreement with the strain rate distribution at the surface derived from geodetic data. However, discrepancies in the maximum compression axes orientations derived from both datasets

can be found mainly in the northern part of the country, which can be attributed to an uneven spatial distribution of the data and different depths at which data was acquired.

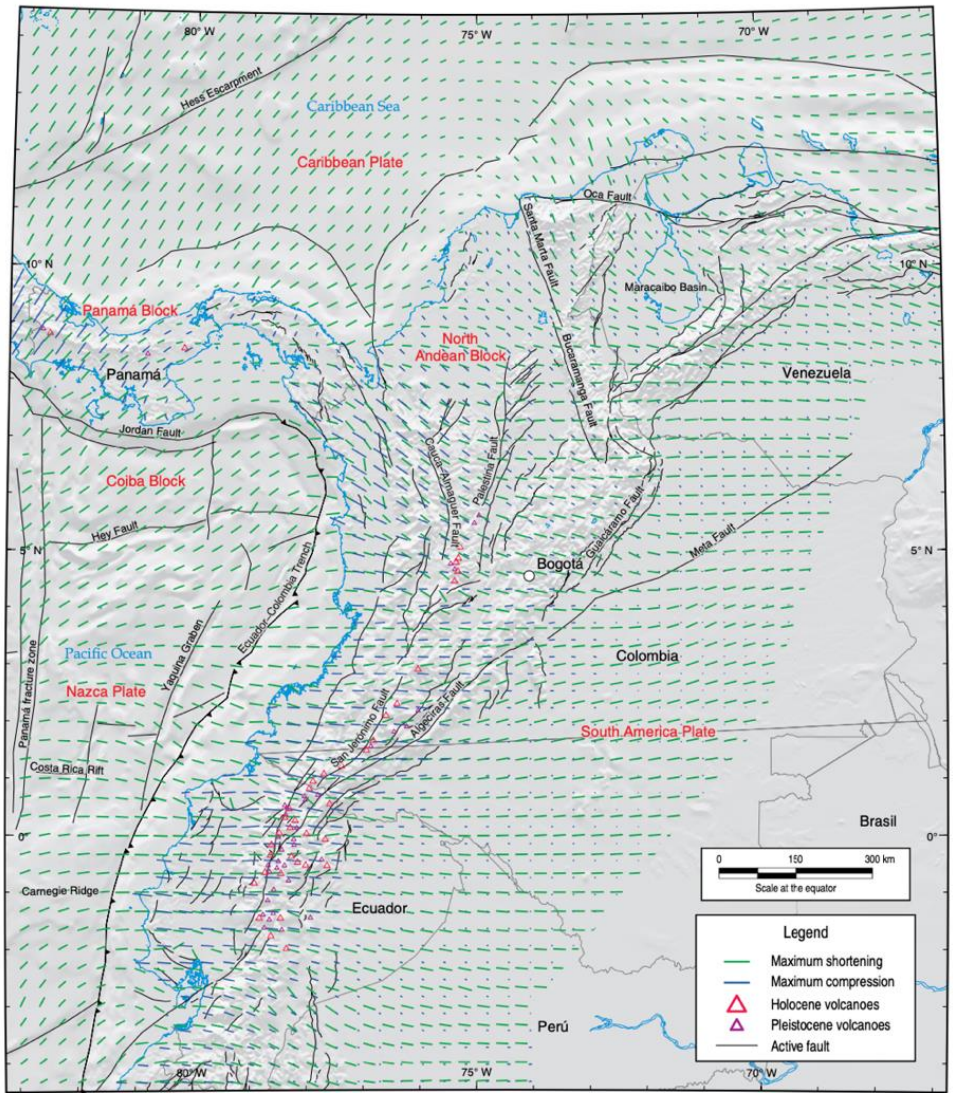

Figure 2.2. *Orientation of maximum shortening based on CMT data (green) and GPS data (blue) by Arcila et al. (2020). Regions with larger strain rates are denoted by areas where CMT and GNSS shortening orientations are consistent with each other.*

Vargas (2020) conciliated deep and shallow seismotectonic observations to propose a model for the subduction geometries in northwestern South America. He found significant deformation from GPS data along the CESZ and the CSZ with compression rates between ~5.0 and ~3.5 nanostrain/yr, respectively. Likewise, he identified gradual effects of the PM block or PM indenter in SE direction and its southern boundary coincident with the location of the Caldas Lithospheric

Tear (CLT), a weak east-west trending feature that shifts intermediate seismicity and represents the termination of subduction-related volcanism. The CLT has been proposed as the limit between subduction zones north and south of Colombia (Figure 2.3).

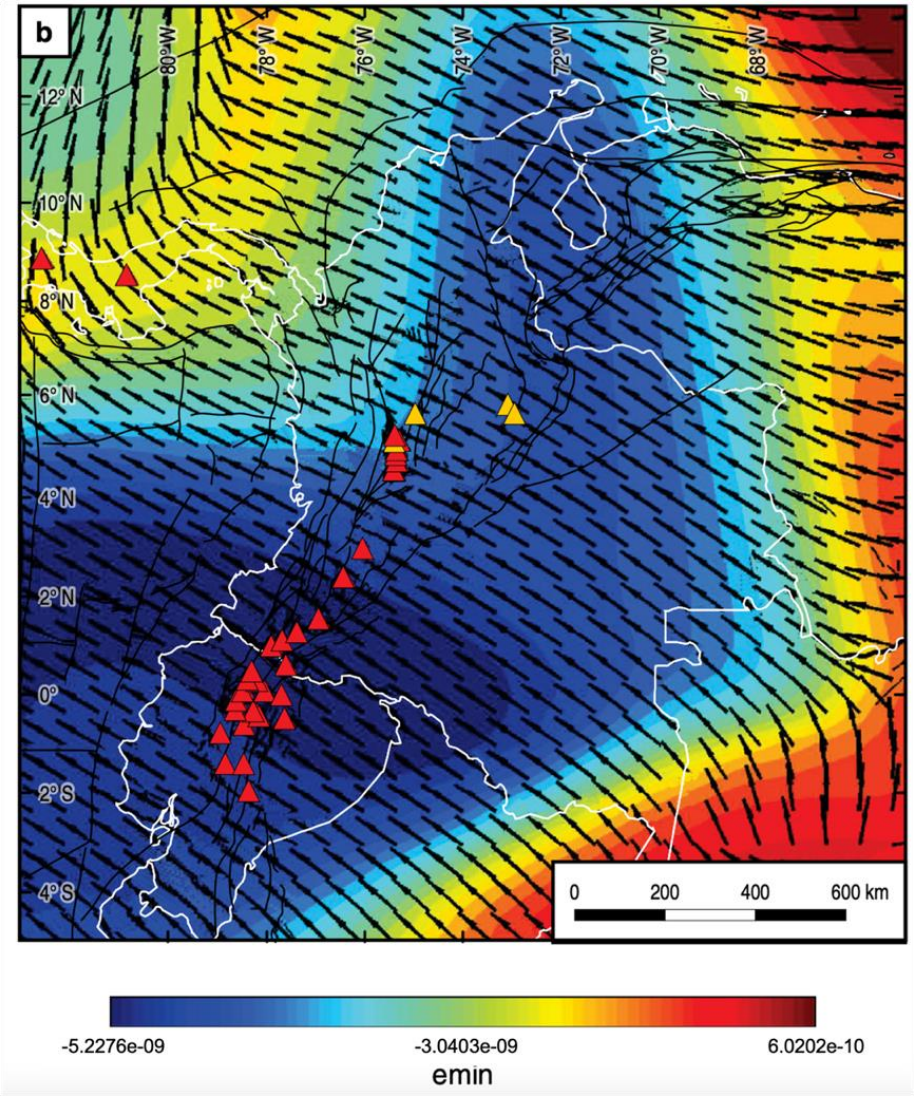

Figure 2.3. *Strain field map based on GPS observations representing horizontal contraction by Vargas (2020). Strain rate as in the color scale and orientations given by the arrows.*

2.3. Orogeny, Faulting and Volcanism

Orogeny, faulting, volcanism and seismicity are among the most important manifestations of the deformation driven by the tectonics in Colombia. In the following, I will describe them in further detail with exception of the seismicity, which will be treated in an independent section.

The more distinctive and spectacular orogenic feature of South America is the Andes, a more than 7000 km long mountain range formed during mid- and late-Cenozoic times as a result of the sinking of the oceanic Nazca plate beneath western South America (Schellart, 2008).

The Andes goes across the continent from Chile to Ecuador in a single range and continues in Colombia divided into three different south-north oriented ones: Western, Central and Eastern cordilleras, which form part of the Northern Andes (Taboada et al, 2000; Figure 2.1). Among these ones, the Western and Central cordilleras are aligned parallel to the Pacific coast and separated by the Romeral Fault System (RFS) and the intermediate Cauca-Patía Valley (Taboada et al, 2000). The Western cordillera which is formed by oceanic crust (Taboada et al, 2000; Hermelin, 2015), is the lowest of the three, reaching heights up to ~4200 m. On the intermediate height Central cordillera, the subduction of the Nazca plate has produced a volcanic arc where at least 23 active volcanoes have been identified up to a latitude of ~5.5ºN where volcanic activity has completely ceased (Paris and Romero, 1993; Taboada et al, 1998; Robertson et al, 2002; Kellogg et al, 2019; Gómez-Martínez et al, 2021; Figure 2.1). Three observatories were established at the northern (Manizales city), central (Popayán city) and southern (Pasto city) segments of the cordillera as a response to the Nevado del Ruiz eruption in 1985 that is, until now, the deadliest natural disaster in Colombian history with more than 25000 casualties (Gómez-Martínez et al, 2021). They are in charge of monitoring the volcanic activity, issuing early warnings, and managing volcanic crisis as part of the SGC mission. On the other hand, the Eastern Cordillera extends in the N-NE direction to the northwestern part of Venezuela in what is known as the Merida Andes (Audemard, 2003) reaching maximum heights of ~5400 m in the widest part of the chain. It is separated from the Central Cordillera by the Magdalena Valley and from the South American plate by the EFFS.

Other important and independent mountain bodies that configure the relief of the country are the Sierra Nevada de Santa Marta (SNSM), a ~5800 m height tetrahedral-shaped range located in the Caribbean (Taboada et al, 2000) that is considered to have uplifted as a result of the changes in the CSZ from flat to step at the weakened zone of the Bucaramanga Santa Marta Fault (BSMF) according to Vargas (2020). In addition, the Serranía del Perijá at the Colombia-Venezuela border, the SFB and SJFB, both located in the northwestern Caribbean (Taboada et al, 1998; Mora et al, 2017), the Serrania del Baudó as an extension of the Panamá isthmus accreted to Colombia (Taboada et al, 1998; Taboada et al, 2000) and the Serranía de la Macarena and Chiribiquete

located in the South American plate as part of the Guiana shield also known as the exhumed part of the Amazonian craton, configure the topography of Colombia (Figure 2.1).

Given the complex relief system across a large part of Colombia and as an accommodation mechanism of the relative motion of the Nazca plate at the CESZ, intense faulting is produced following a predominant NS and NNE orientation, although other orientations can also be found (Taboada et al, 2000; Figure 2.1). Important fault systems such as the EFFS and RFS define the foothills of the cordilleras as previously mentioned, and in the case of the latter, separate terrains of oceanic affinity from terrains of continental origin (Pulido, 2003). Generally, these fault systems are segmented into many traces and present combined strike-slip and reverse mechanisms with variable levels of motion that have triggered some of the largest inland earthquakes in Colombia. Other important fault systems are the left-lateral NW-SE trending BSMF in the Eastern cordillera septentrional area (Paris and Romero, 1993) that extends to the Caribbean and defines the western limit of the MB and the SNSM. In the north, the right-lateral E-SE trending Oca Fault (OF), defines the northern limit of the MB and the southern limit of the BB blocks (Audemard, 2014). In the Pacific region, NW-SE Uramita Fault defines the east boundary of the PM-Choco block, while the E-NE right-lateral Garrapatas Fault acts as the suture of the accreted PM-Choco block in the south (Duque-Caro, 1990; Taboada et al, 2000; Vargas and Duran, 2005).

2.4. Seismicity

Tectono-dynamic configuration of Colombia generates interplate and intraplate earthquakes. Figure 2.4 shows instrumental seismicity plotted by depth and magnitude. Shallow seismicity at the western margin as a result of the subduction of the Nazca plate and their gradual transition to intermediate and depth seismicity to the east in alignment with the cordilleras and north-south trending fault systems is observed.

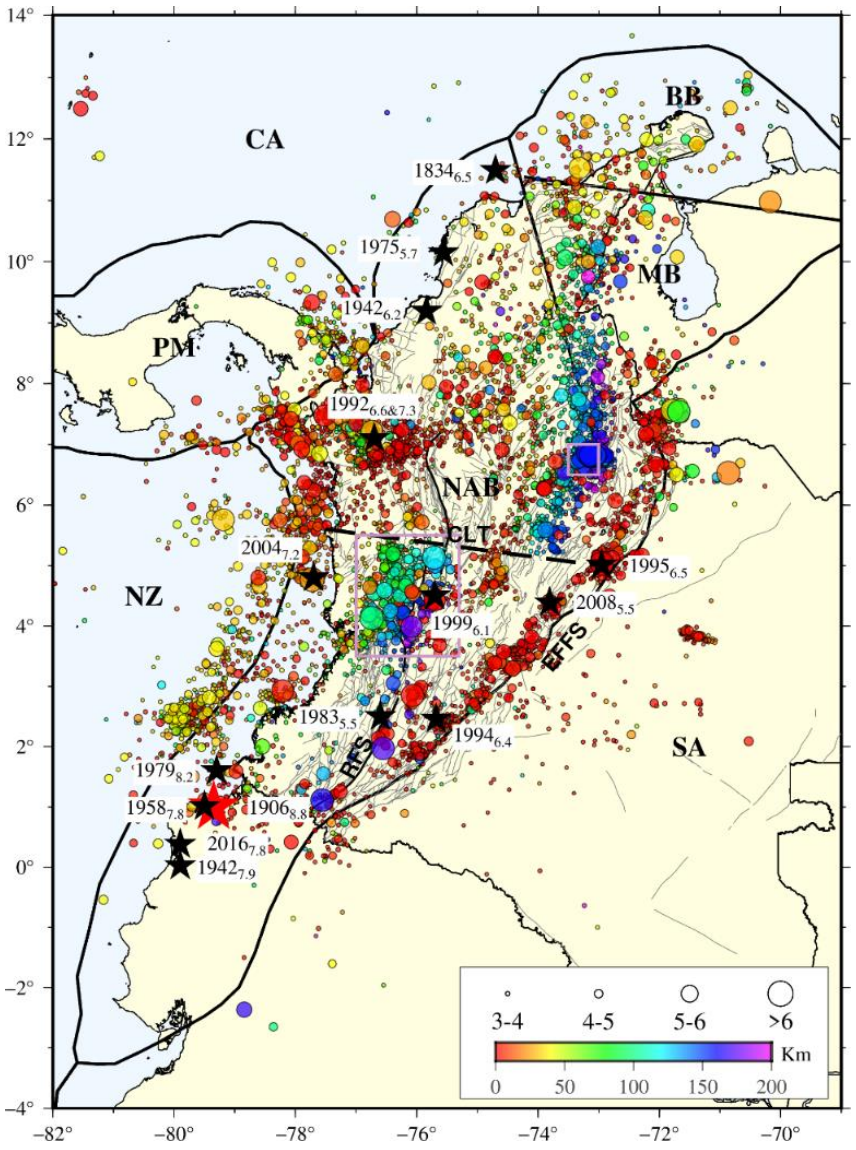

Figure 2.4. *Instrumental seismicity 1993-2022 ($M_w \geq 3.0$) plotted by depth and magnitude. Large subduction and inland earthquakes are presented as black stars labeled by year and magnitude. Characteristic 1906 earthquake (M_w8.8) denoted by the red star. Thin gray lines represent geological faults. Thick black lines denote plate/block boundaries with abbreviations as in Figure 1.1. The dashed line indicates the location of the CLT. Purple boxes show the location of seismic nests: Bucaramanga nest (BN) in the northeast (Sepúlveda-Jaimes and Cabrera-Zambrano, 2018) and Cauca nest (CN) in the southwest (Chang et al, 2017). Source: RSNC.*

An offset of the seismicity is presented at a latitude of ~5.5ºN, which as mentioned before, corresponds to the CLT, a structure that separates two distinctive subducting slabs, a non-volcanic one in the Panamá-Caribbean Sea area, and a volcanic one to the south related to Nazca plate

subduction between 3ºN and 5.6ºN. Both slabs interact at depth according to Gómez-García (2020) (Figure 2.5). This idea is also supported by the studies of Syracuse et al. (2016), Bernal-Olaya et al. (2015), Mora et al. (2017), and others.

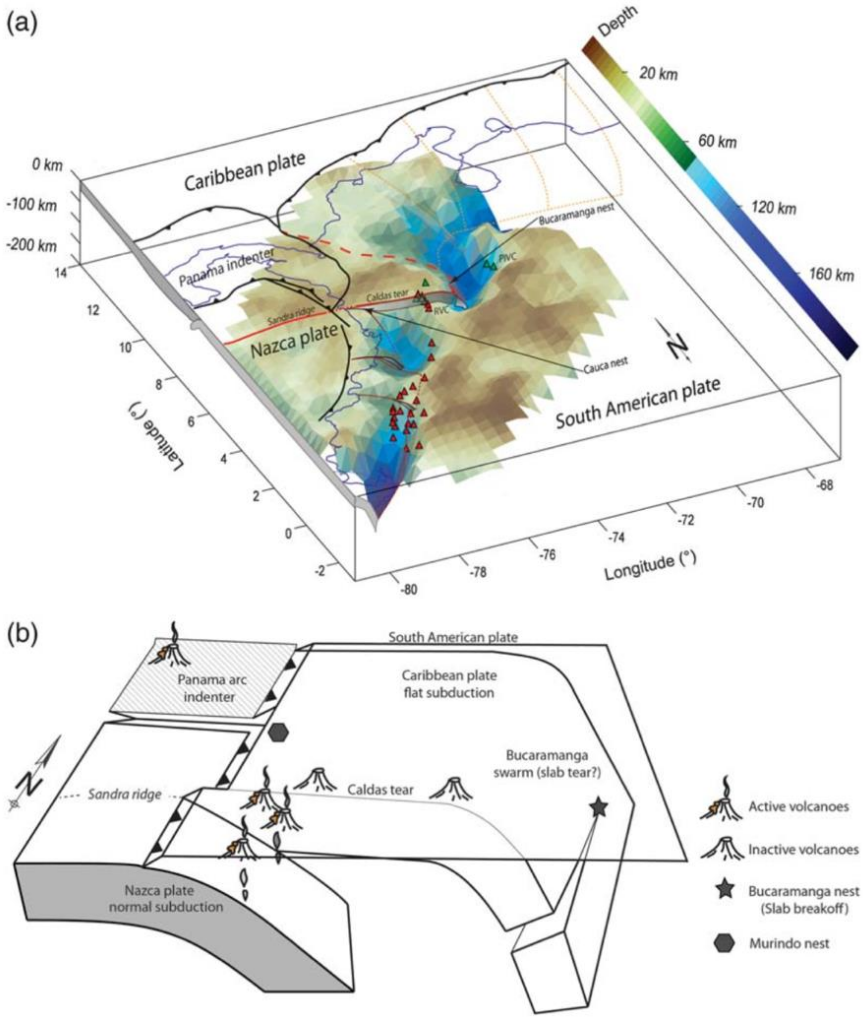

***Figure 2.5**. Proposed geometry of Nazca and Caribbean subduction zones in Colombia and their bounding limit represented by the Caldas Lithospheric Tear (CLT) by Vargas and Mann (2013).*

On one hand, the Nazca subduction zone is considered one of the largest ones in the world with ~7500 km length (Klotz et al, 2001) and it is characterized as a relatively young and warm subduction according to Muller et al. (2008) with an oceanic lithosphere age of ~11-17 Ma at the trench (Syracuse and Abers, 2003). At the CESZ it has a well-defined Wadati-Benioff zone (Pennington, 1981; Vargas and Mann, 2013; Syracuse et al, 2016; Kellogg et al, 2019) dipping to the east with angles between 30º and 40º (Vargas and Mann, 2013). Large megathrust earthquakes

have occurred along the CESZ as a result of elastic strain accumulation and subsequent release in 1906 (M_w8.8), 1942 (M_w7.9), 1958 (M_w7.8), 1979 (M_w7.7), 2004 (M_w7.2), and the most recent one in 2016 (M_w7.8) (Kanamori and McNally, 1982; Freymueller et al, 1993; Trenkamp et al, 2002; Salcedo-Hurtado and Alvarado-Flórez, 2007; Mothes et al, 2013; Chlieh et al, 2014; Ye et al, 2016; Yoshimoto et al, 2019; Yamanaka et al, 2017; Mora-Páez et al, 2019; Sagiya and Mora-Páez, 2020; Chlieh et al., 2021; Mariniere et al, 2021; Figure 2.6). Some of these events were followed by tsunamis and had a large impact on the infrastructure and people's lives. Several authors have demonstrated the existence of slow slip events (SSEs) in the CESZ (Vallée et al, 2013; Rolandone et al, 2018; Vaca et al, 2018; Chlieh et al, 2021) and recently, Bermúdez and Kumagai (2020) found repeating earthquakes near the trench by means of a waveform similarity analysis.

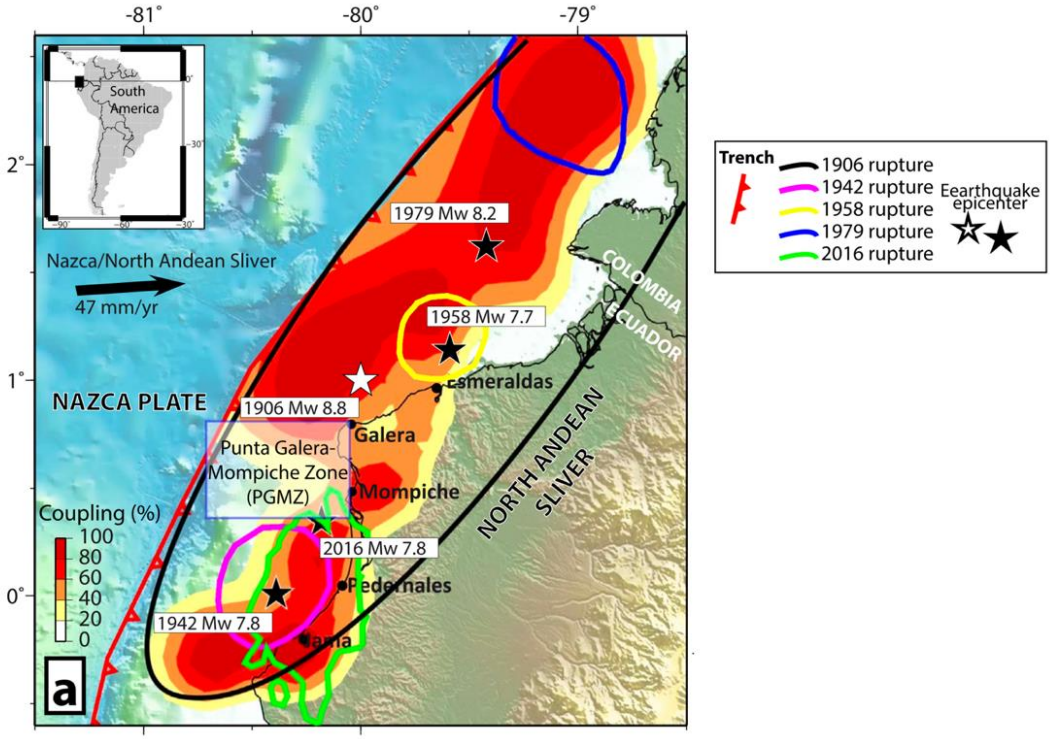

Figure 2.6. *Megathrust earthquakes along the Nazca subduction zone at the Colombia-Ecuador border. Color lines and stars indicate the rupture area of historical earthquakes and epicenters as in the legend. Coupling distribution as in the color bar. PGMZ region represents the transition between two highly coupled areas. Taken and modified from Vaca et al. (2018)*

On the other hand, the Caribbean plate is formed by a very old oceanic thickened crust of about 73-120 Ma (García-Reyes and Dyment, 2021). The Wadati-Benioff zone at the CSZ is poorly defined and discontinuous, which can be due to the lack of good coverage of the seismic network, and slow relative motion, among others. The above reasons plus the absence of subduction-related magmatism, have contributed to the controversy about whether a subduction process is taking place or not along this margin (Rossello and Cossey, 2012). Nevertheless, recent studies support the existence of an ongoing flat and slow subduction (Vargas and Mann, 2013; Lara et al, 2013; Vargas et al, 2015; Bernal-Olaya et al, 2015; Syracuse et al, 2016; Mora et al, 2017, Pérez et al, 2018; Kellogg et al, 2019; Vargas, 2020). The slab dips to the southeast with a dip angle of ~8º up to an inland distance between 250-300 km below the SJFB and the Lower Magdalena Valley (LMV) (Mora et al, 2017). The most likely cause of the flat geometry is the buoyant and thickened oceanic crust that composes the slab that hampers its bending below northwestern Colombia (Syracuse et al, 2016; Mora et al, 2018). The CSZ has not been the locus of megathrust earthquakes according to available historical records. Nevertheless, a recent study from Lizarazo et al. (2021), indicated that there is a possibility of a M_w8.0 earthquake offshore Cartagena city which could lead to a tsunami every ~600 years. Detailed results derived from Lizarazo et al. (2021) will be presented in Chapter 5. Important historical earthquakes in the Caribbean region are the 1834 (M_w6.5) Santa Marta earthquake (Cifuentes and Sarabia, 2006), the 1942 (M_w6.2) Lorica earthquake (Cifuentes and Sarabia, 2009), and the 1975 (M_w5.7) Cartagena earthquake (Cifuentes and Sarabia, 2010), although, their magnitudes are smaller than expected for a subduction megathrust event.

Similar settings such as the Calabrian arc and the Gibraltar subduction zone have experienced $M_w \geq 8.0$ despite the slow relative motion (<1 cm/yr), long recurrence intervals and flat geometry (Gutscher, 2002; Gutscher, 2006; Gutscher et al, 2006; Gutscher and Westbrook, 2009; Gutscher et al, 2012; Figure 2.7). These common features also illustrate the possibility of a large seismic potential in the Caribbean of Colombia; although further study is required, especially in terms of searching for past earthquakes/tsunami evidence.

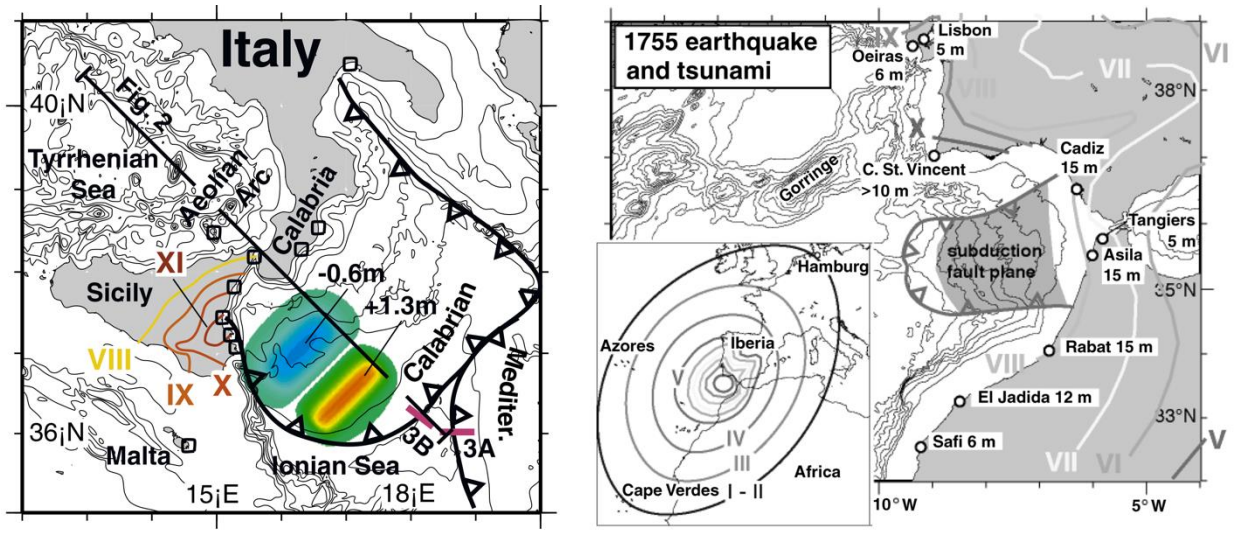

(a) (b)

Figure 2.7*. Slow subduction zones in a). Calabrian Arc southeastern Italy and the source region (colored) of the M_w8.0 Catania earthquake in 1693. Colors indicate zones of vertical uplift (red) and subsidence (blue) with respective values in meters. Isoseismal curves are presented and b). Gibraltar in southern Spain and source region (shaded) of M_w8.7 Lisbon earthquake in 1755. Isoseismals and tsunami heights are also presented (Taken from Gutscher et al, 2006 and Gutscher, 2006; respectively).*

Inland seismicity is distributed along main inland fault systems, named EFFS and RFS (Paris et al, 2000). Representative crustal earthquakes with $M_w \geq 5.5$ such as the Popayán earthquake (M_w5.6) in 1983 and the Quindío/Coffee region earthquake (M_w6.1) in 1999 can be attributed to the RFS, while the Tauramena earthquake (M_w6.5) in 1995 and the Quetame earthquake (M_w5.6) in 2008 had a source at the EFFS. Other important inland earthquakes are the Murindó sequence (M_w6.6 and M_w7.3) in 1992 and the Páez earthquake (M_w6.8) in 1994 caused by minor fault systems. All epicenters are presented in Figure 2.4.

Two important seismic clusters, known as the Cauca (CN) and Bucaramanga (BN) nests, have been recognized in Colombia as stated by Vargas and Mann (2013) at depths ~150 km (Figure 2.4). The former is located south of the offset of intermediate seismicity caused by the CLT (Chang et al, 2017), and the latter is in the northeast of Colombia on the western edge of the Eastern Cordillera at the termination of the BSMF to the south. From these two, the BN stands out given its high rate of moderate seismic activity in a much smaller volume (Zarifi et al, 2007; Vargas and Mann, 2013; Bernal-Olaya et al, 2015; Sepúlveda-Jaimes and Cabrera-Zambrano, 2018). Its origin

has been debated by several authors that propose a two-slab collision origin (Van Der Hilst and Mann, 1994; Zarifi et al, 2007), a two-slabs overlapping (Taboada et al, 2000), and dip angle steepness or a single slab extreme bending (Cortés and Angelier, 2005).

2.5. Conclusions

Orogeny, intense faulting, volcanism, and interplate/intraplate seismicity are manifestations of the complex tectonics that drives deformation at active boundaries in Colombia. Among these processes, the occurrence of earthquakes and volcanic eruptions are the most concerning ones given their unpredictability and the large negative effects these have on society, situations that have occurred in the recent past affecting thousands of people. Fortunately, there is more awareness regarding the importance of investigating these phenomena focusing on preparedness and early warning. The above has led to a gradual and ongoing improvement of monitoring observational networks as tools that provide important data to study seismic and volcanic potential as well as to highlight understudied areas able to trigger geological hazards. In this way, researchers are able to elucidate the current knowledge of crustal processes and promote better decision-making in terms of geohazards.

CHAPTER 3

GPS OBSERVATIONS

This chapter presents a general description of the input data from the continuous GNSS stations provided by the GeoRED project, as well as basic processing strategies for daily solutions and subsequent velocity estimation.

3.1. GeoRED project

GeoRED – **Geo**desia: **R**ed de **E**studios de **D**eformación (acronym in Spanish), corresponds to the project devoted to the implementation of the national continuous and campaign GNSS network in Colombia to study the geodynamics of the northwestern corner of South America. It has been developed under the Geohazards Directorate of the SGC since 2007 (Mora-Páez, 2006) and serves to improve the technical and scientific capacity in terms of disaster risk reduction related to seismic and volcanic activity as well as other geological hazards. As of December 2021, GeoRED GNSS network counted with 158 continuous stations (Figure 3.1), and more than 350 field sites of episodic data acquisition distributed across the country.

Densification of geodetic stations responds mainly to geological and geodetic criteria including the location of pre-defined geological blocks far from active faults on bedrock or consolidated soil, as well as good satellite visibility and minimization of multipath effects that could affect the GNSS signals. Other important aspects such as security, access, and potential telecommunications of selected sites are considered (Mora-Páez, 2020). The primary goal is to guarantee the permanence of the infrastructure to obtain data to determine reliable crustal motions.

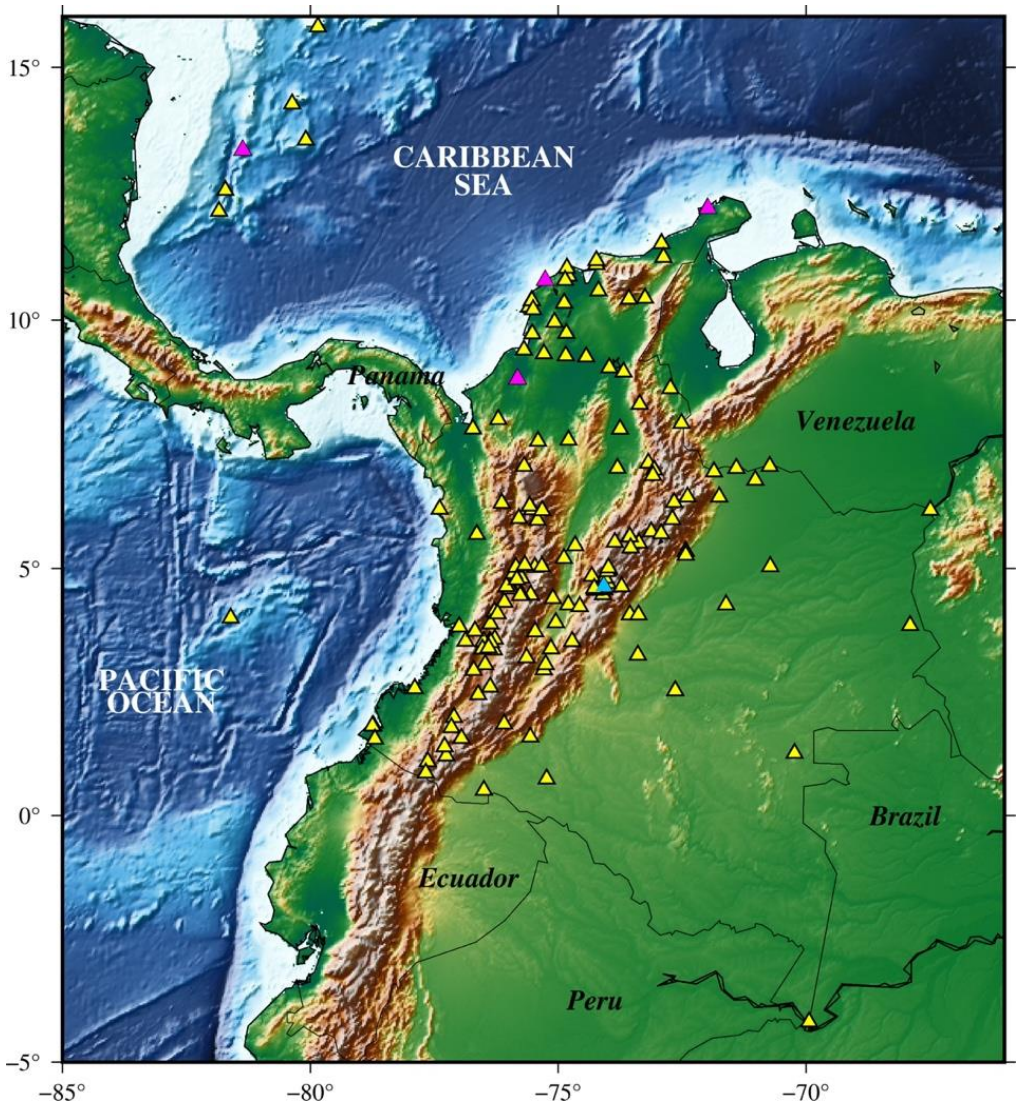

Figure 3.1. *GeoRED continuous GPS geodetic network as in December 2021. Yellow and magenta triangles correspond to stations of the GeoRED and the COCONet projects, respectively. Blue triangle is the BOGT site part of the International GNSS Service – IGS.*

Typical GeoRED continuous GPS stations are composed of ground-based monuments with a central stainless rod of 1" buried up to 20 m (in some cases), in which the top part, a geodetic dual-frequency antenna is installed to receive satellite signals. A geodetic receiver, power supply, and transmission instruments are installed at a distance from the antenna inside airtight cabinets (Figure 3.2). Some of the stations also have meteorological sensors.

(a)

(b)

Figure 3.2. *Typical GeoRED continuous GPS station (Hydroelectric power station of Urrá – URR0). a). A geodetic antenna on top of a shallow-drilled braced monument, b). The airtight cabinet where GNSS receiver, batteries, and transmission systems are stored and solar panel for additional power supply.*

Data is sampled with frequencies of 1 Hz and 15 Hz (in case no connection for remote data download) and transmitted to a processing center in Bogotá SGC headquarters for daily processing with the software GIPSY-OASIS (currently GipsyX) developed by the Jet Propulsion Laboratory (JPL) of NASA. Precise coordinates are obtained in the International Terrestrial Reference Frame (ITRF) 2008 (Altamimi et al, 2011; Altamimi et al, 2012) and these are shared with the general public (under request) and governmental institutions.

3.2. Processing data of the continuous GPS network

For this study, I performed the processing of RINEX (Receiver Independent Exchange Format) data of 87 continuous GPS stations in and around Colombia (Figure 3.3) during the period 2008-2017 using GAMIT/GLOBK v10.7 software (Herring et al, 2018). Among these stations, 68 sites correspond to the GeoRED project (Mora-Páez et al, 2018a), 15 sites are part of the Continuously Operating Caribbean GPS Observational Network (COCONet) (Feaux et al, 2012), and 4 sites in

the South American, Nazca and Cocos plates are a part of the International GNSS Service (IGS). The last ones are used to constrain the regional reference frame.

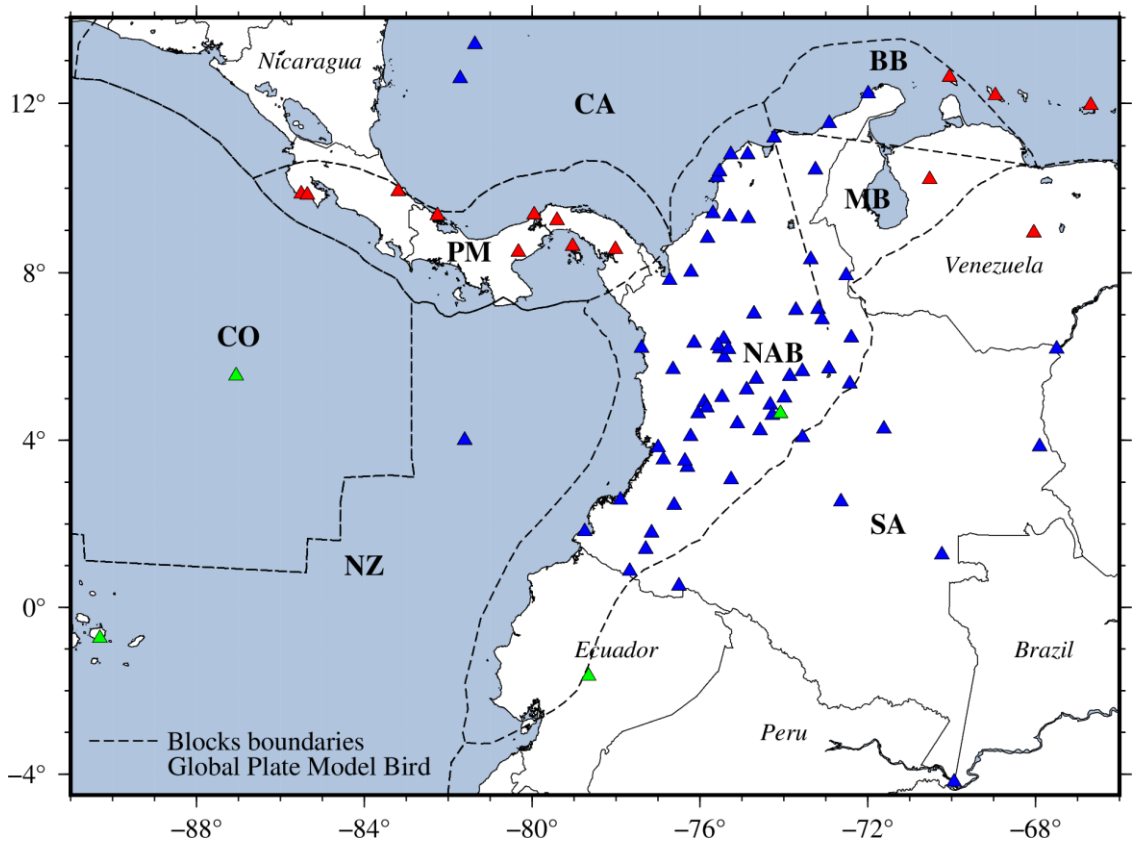

Figure 3.3*. GPS stations used in this study. Blue triangles denote GeoRED project sites including COCONet sites in the Caribbean of Colombia, red triangles are part of the COCONet network in Costa Rica, Panamá, and Venezuela, and green triangles are part of the IGS network.*

GAMIT/GLOBK software follows a relative positioning strategy in order to obtain daily coordinate solutions and their variance-covariance at mm level accuracy with respect to an indicated ITRF. In my case, I expressed coordinates in the ITRF2014 referred to the epoch 2010.0 (Altamimi et al, 2016; Altamimi et al, 2017). I used the automated routines available in GAMIT/GLOBK shell scripts *sh_gamit* and *sh_glred* that contains the sequence of steps from the phase and pseudo-range data in RINEX files to the obtention of time series of position estimates in a defined reference frame according to several parameters set in few control files. During the processing, IGS products such as precise satellite orbits (SP3), Earth Orientation Parameters (EOP), and satellite clock data, as well as mapping functions for the tropospheric delay, and atmospheric/ocean pressure grid files for loading corrections were used to model observations

iteratively and solve for parameter estimation, time series generation and combination of solutions for velocities estimation under a specified reference frame.

Most of the stations count with more than 2.0 years of stable data. VORI site's shorter time series are due to coseismic and postseismic effects from the Muisne/Pedernales M_w7.8 earthquake on April 16th, 2016 (Yoshimoto et al, 2017), while CN42 station, located in the Caribbean of Venezuela, has corrupted data files during the latest period of 2016 and throughout 2017. In both cases, the estimation of velocities presents a large uncertainty, and they are excluded from further analysis.

3.3. GPS coordinates time series analysis and velocity estimation

After obtaining daily solutions for all GPS sites, a time series analysis was performed using the Hector software version 1.6 (Bos et al, 2013) to estimate three-dimensional velocities and their uncertainties following Eq. (3.1).

$$x = \sum_{i=0}^{n_P} p_i (t - t_R)^i + \sum_{j=1}^{n_J} b_j H(t - t_j) + \sum_{i=1}^{n_F} [s_i \sin(\omega_i t) + c_i \cos(\omega_i t)] + e \qquad (3.1)$$

Daily coordinates x in a local cartesian coordinate system ENU (East-North-Up) are fitted by a one-degree polynomial $n_P = 1$ (linear trend) at the ITRF2014 reference epoch t_R =2010.0. Instrumental changes offsets of amplitude b_j are included by using a Heaviside step function $H(t)$, as well as seasonal components (annual and semiannual) modeled by a four-term periodic function (n_F =2). I applied a seasonal correction to all the GPS time series under analysis considering the marked effects of bi-modal climatic patterns in Colombia (rainy and dry seasons), along with some localized effects such as groundwater pumping (case BOGT site, Mora-Páez et al, 2019), which are most noticeable in the vertical component. A popular choice of a temporally correlated noise model e for GPS time series is a combination of white and power-law noise components that was used to characterize the accuracy of the estimated GPS velocities (Mao et al, 1999; Zhang et al, 1997; Bos et al, 2013). We confirmed the selection of the noise model according to the power spectral density of the residuals of each GPS site.

Table 3.1 presents the estimated velocities with their respective uncertainties in the three components at each GPS site expressed in mm/yr with respect to the ITRF2014.

No.	ID station	Longitude	Latitude	East vel	North vel	Up vel	Sigma east	Sigma north	Sigma up
1	ACP1	280.050	9.371	16.977	11.487	2.233	0.239	0.236	0.697
2	ACP6	280.592	9.238	16.986	12.246	0.002	0.201	0.170	0.409
3	AJCM	285.115	5.210	3.673	15.640	-0.141	0.356	0.204	0.940
4	ALPA	287.082	11.528	9.065	14.283	-4.682	0.356	0.331	1.114
5	ANCH	283.130	3.535	4.027	14.552	1.123	0.377	0.364	1.000
6	BAAP	286.446	4.072	-4.782	10.681	-0.421	0.226	0.149	0.676
7	BAME	285.435	4.236	0.895	14.454	-0.621	0.327	0.215	0.562
8	BAPA	285.342	5.466	2.698	15.033	0.426	0.193	0.142	0.737
9	BARU	284.410	10.258	11.928	10.337	-5.575	0.300	0.190	1.046
10	BASO	282.607	6.203	5.666	15.203	2.609	0.244	0.178	0.617
11	BOBG	286.642	8.312	6.937	15.328	2.336	0.327	0.216	0.977
12	BOGT	285.919	4.640	-0.850	15.135	-31.653	0.154	0.138	0.979
13	BUGT	283.004	3.826	5.257	15.113	1.035	0.166	0.171	0.667
14	CAPI	287.572	5.351	-3.377	11.908	1.317	0.212	0.216	0.767
15	CAYS	280.154	15.795	9.906	6.926	-3.240	0.266	0.240	0.992
16	CCAN	283.700	3.360	2.225	14.120	-0.949	0.311	0.242	1.316
17	CIA1	283.643	3.505	1.962	13.886	-5.691	0.312	0.219	0.966
18	CIOH	284.466	10.391	11.830	11.126	-3.087	0.284	0.302	1.002

Table 3.1. *Geographic coordinates of GPS analyzed in the present dissertation and estimated 3-dimensional velocities with their uncertainties expressed in mm/yr w.r.t the ITRF2014.*

(continued on next page)

No.	ID station	Longitude	Latitude	East vel	North vel	Up vel	Sigma east	Sigma north	Sigma up
19	CN19	289.951	12.612	12.387	13.174	0.010	0.415	0.354	0.958
20	CN20	277.744	9.352	15.610	10.527	2.810	0.369	0.359	1.292
21	CN28	280.966	8.625	19.146	14.372	-2.564	0.484	0.353	1.245
22	CN33	279.673	8.487	19.716	7.826	-3.803	1.153	1.658	3.843
23	CN34	281.985	8.549	24.524	19.533	-20.849	2.773	1.978	8.025
24	CN35	278.637	13.375	11.063	6.652	0.366	0.432	0.306	0.955
25	CN36	284.179	8.820	18.825	10.290	-7.767	0.574	0.640	1.467
26	CN38	288.012	12.222	10.947	13.920	3.159	0.390	0.261	0.846
27	CN39	289.476	10.206	5.818	12.859	-3.587	0.547	0.505	1.147
28	CN40	291.042	12.180	11.836	13.399	0.395	0.348	0.308	1.312
29	CN41	291.959	8.943	-5.015	12.394	-1.685	0.325	0.301	1.346
30	CN42	293.318	11.953	7.885	15.854	10.023	1.514	1.274	3.697
31	CORO	284.712	9.328	11.583	12.028	-0.834	0.226	0.173	0.955
32	COVE	284.308	9.402	12.909	8.732	-4.185	0.339	0.461	1.138
33	CUC1	287.487	7.932	5.896	13.491	-0.833	0.344	0.221	0.603
34	DIMA	285.768	11.188	8.624	15.725	-3.523	0.344	0.312	0.814
35	GALE	284.737	10.793	6.923	13.855	-2.256	0.577	0.734	1.969
36	GLPS	269.696	-0.743	50.386	11.013	-0.380	0.223	0.177	0.635
37	GUAP	282.105	2.574	8.408	13.155	1.622	0.306	0.155	1.049

Table 3.1. *(continued)*

(continued on next page)

No.	ID station	Longitude	Latitude	East vel	North vel	Up vel	Sigma east	Sigma north	Sigma up
38	IND1	274.498	9.865	17.275	31.976	-11.204	0.668	0.592	1.504
39	INRI	284.103	4.909	3.264	14.690	-3.323	0.471	0.405	1.219
40	INTO	283.957	4.642	2.756	14.679	-0.660	0.328	0.146	0.425
41	ISCO	272.944	5.544	49.226	73.951	-3.015	0.310	0.393	0.584
42	MALO	278.394	4.003	48.081	14.050	-1.144	0.228	0.162	0.772
43	MECE	286.288	7.107	5.234	14.946	0.620	0.186	0.163	0.672
44	MITU	289.768	1.261	-4.438	11.467	0.013	0.199	0.088	0.684
45	MZAL	284.529	5.030	1.412	18.344	2.165	0.201	0.225	0.732
46	OAMU	286.442	5.647	-3.849	7.658	1.516	0.725	0.475	1.239
47	OCEL	288.384	4.271	-4.676	11.632	-0.975	0.231	0.137	0.450
48	PAL2	286.816	7.131	3.466	15.784	-2.289	0.297	0.329	0.900
49	PASI	283.501	0.513	-2.127	10.068	-1.056	0.185	0.091	0.500
50	POVA	283.385	2.449	4.460	13.641	-2.396	0.161	0.156	0.644
51	PUIN	292.097	3.851	-4.902	11.678	0.248	0.239	0.250	1.257
52	QSEC	274.643	9.840	16.006	27.782	-5.413	0.516	0.407	0.663
53	QUIL	282.709	1.394	4.451	14.101	-0.405	0.234	0.198	0.684
54	RIOP	281.349	-1.651	1.628	7.571	0.969	0.262	0.185	0.692
55	SAN0	278.284	12.580	12.557	6.961	-0.733	0.241	0.178	0.522
56	SEL1	284.471	6.191	3.786	15.166	1.888	0.248	0.165	0.836

Table 3.1. *(continued)*

(continued on next page)

No.	ID station	Longitude	Latitude	East vel	North vel	Up vel	Sigma east	Sigma north	Sigma up
57	SUAM	287.075	5.710	-0.368	12.761	-1.255	0.563	0.512	0.768
58	TASA	284.565	6.424	5.107	14.034	-1.683	0.548	0.366	1.327
59	TGPM	277.742	9.351	16.802	11.074	-1.693	0.747	0.452	2.125
60	TICU	290.061	-4.187	-3.675	11.171	0.942	0.219	0.130	1.125
61	TONE	283.861	6.324	4.217	15.895	1.191	0.174	0.111	0.434
62	TUCO	281.252	1.815	14.214	12.914	4.569	0.277	0.149	0.734
63	UNME	284.423	6.264	5.903	18.549	-0.614	0.400	0.339	1.196
64	URR0	283.790	8.012	12.600	12.384	-3.504	0.166	0.320	1.193
65	UWAS	287.609	6.451	0.180	13.386	1.470	0.147	0.128	0.595
66	VBUV	286.141	5.533	3.242	15.648	0.321	0.245	0.217	0.662
67	VCAR	292.505	6.183	-5.127	11.964	0.037	0.532	0.437	1.832
68	VCRG	284.581	5.981	2.829	15.310	-1.328	0.391	0.282	1.404
69	VDPR	286.752	10.436	8.454	15.689	2.204	0.132	0.179	0.791
70	VMAG	285.153	9.287	7.922	14.240	2.180	0.185	0.157	0.624
71	VMAR	284.676	6.176	4.882	15.250	0.320	0.321	0.157	0.618
72	VMER	282.847	1.785	3.837	14.306	3.933	0.253	0.174	0.701
73	VMES	286.908	6.883	2.624	14.482	-0.408	0.240	0.147	0.996
74	VNEI	284.745	3.062	-0.750	14.291	1.155	0.217	0.163	0.513
75	VORA	283.278	7.818	14.502	12.595	-7.754	1.023	1.099	3.445

Table 3.1. *(continued)*

(continued on next page)

No.	ID station	Longitude	Latitude	East vel	North vel	Up vel	Sigma east	Sigma north	Sigma up
76	VORI	282.328	0.863	-3.320	2.458	3.471	5.170	3.964	23.614
77	VOTU	285.290	7.019	6.160	15.667	1.798	0.209	0.192	0.663
78	VPIJ	284.893	4.397	1.454	14.928	0.772	0.218	0.113	0.718
79	VPOL	285.139	10.794	7.834	16.119	3.900	0.308	0.191	0.976
80	VQUI	283.358	5.692	2.966	15.597	-2.424	0.276	0.152	0.480
81	VRAI	276.809	9.925	16.700	11.784	-8.217	0.435	0.342	1.664
82	VROS	285.677	4.847	0.897	14.333	0.501	0.293	0.203	0.804
83	VSJG	287.361	2.533	-5.802	11.500	-0.016	0.332	0.211	1.091
84	VSJP	284.164	4.781	1.452	15.386	0.526	0.198	0.166	0.713
85	VSOA	285.727	4.603	0.265	14.489	-1.072	0.286	0.258	0.665
86	VTUL	283.776	4.092	8.214	16.481	3.856	0.809	0.545	0.958
87	VZPQ	286.013	5.019	1.937	15.223	-3.610	0.505	0.536	0.849

Table 3.1. *(continued)*

Appendix A includes time series plots of each GPS site and Appendix B contains the tables of noise parameters per GPS site and component.

In Chapter 4, I use the velocities to describe regional kinematics with respect to different fixed tectonic plates (or blocks) to determine patterns of horizontal and vertical crustal motions. It also presents a description of the deformation style and its distribution in the country.

CHAPTER 4
CRUSTAL MOTIONS

In this chapter, I present an interpretation of the observed crustal motions in Colombia based on horizontal and vertical GPS velocities along with the identification of regions affected by significant deformation and its potential underlying causes and effects. Current motions are expected to coincide with previous global and regional tectonic models. However, GPS data increasing spatial and temporal density helped me to refine the kinematics in the northern part of the country, somehow contradictory with the traditional tectonic framework. Based on this finding, I propose a new tectonic affiliation whose implications are relevant to analyze seismic and tsunami potential along plate boundaries.

4.1. Interseismic GPS velocities

Stable interseismic velocities are expressed originally in the ITRF2014 (Figure 4.1), an Earth-Centered-Earth-Fixed (ECEF) or geocentric reference frame, relative to which crustal motions for the most central part of Colombia are oriented in the E-NE direction across the whole NAB (or NAS: North Andean Sliver according to Nocquet et al, 2014) with an average magnitude of ~15.8±2.5 mm/yr (VORI site not included as explained in section 3.2). The same E-NE pattern is presented by the stations located on the Caribbean and Nazca plates as well as on the PM block, with slight azimuthal variations. In this respect, the stations on the Nazca plate show the largest motion of all with ~50.8±1.0 mm/yr, while the Caribbean and Panamá sites show motions on the order of 15.0±2.7 mm/yr and 20.9±1.6 mm/yr, respectively. For the PM block average velocity, I excluded the stations of IND1, QSEC for presenting larger magnitudes as an effect of the rapid subduction of the Cocos plate beneath Costa Rica as well as CN34 in Panamá, due to the large discrepancy with surrounding stations in the same block. Meanwhile, GPS on the South American Plate have a clear northwest trend of ~11.8±1.7 mm/yr that is gradually rotating clockwise to the north at the tectonic boundary with the NAB.

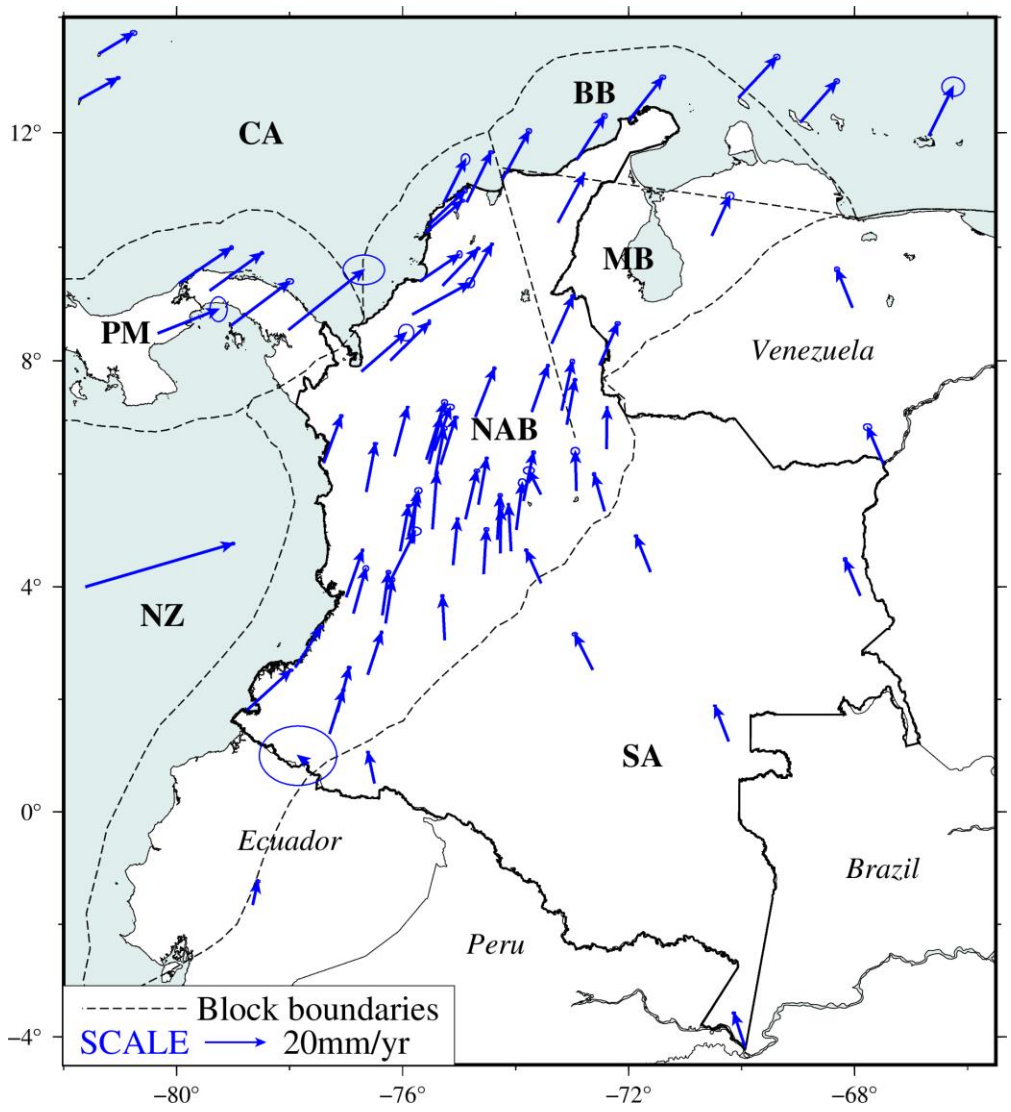

Figure 4.1. *Horizontal GPS velocity field presented in mm/yr with respect to the ITRF2004 (includes 95% error ellipses). Broken black lines denote the tectonic block boundaries, SA: South American plate, NZ: Nazca plate, CA: Caribbean plate, PM: Panamá Block, NAB: North Andean Block, MB: Maracaibo Block, and BB: Bonaire Block.*

For interpretation purposes, ITRF2014 horizontal velocities were transformed into a variety of plate-fixed reference frames.

4.1.1. Horizontal velocity field w.r.t the South American Plate

Figure 4.2 represents horizontal velocities with respect to the South American plate (Altamimi et al, 2017). The northeastward differential motions of GPS sites are observed for stations located on the Nazca plate, the NAB, and the PM block with average rates of 53.9±0.3 mm/yr, 25.4±0.6

mm/yr, and 11.3±0.4 mm/yr, respectively, and southeastward for sites on the Caribbean plate with an average velocity of 16.8±0.3 mm/yr (Lizarazo et al, 2021). These motions are in general consistent with previous studies (Nocquet et al, 2014; Mora-Páez et al, 2019).

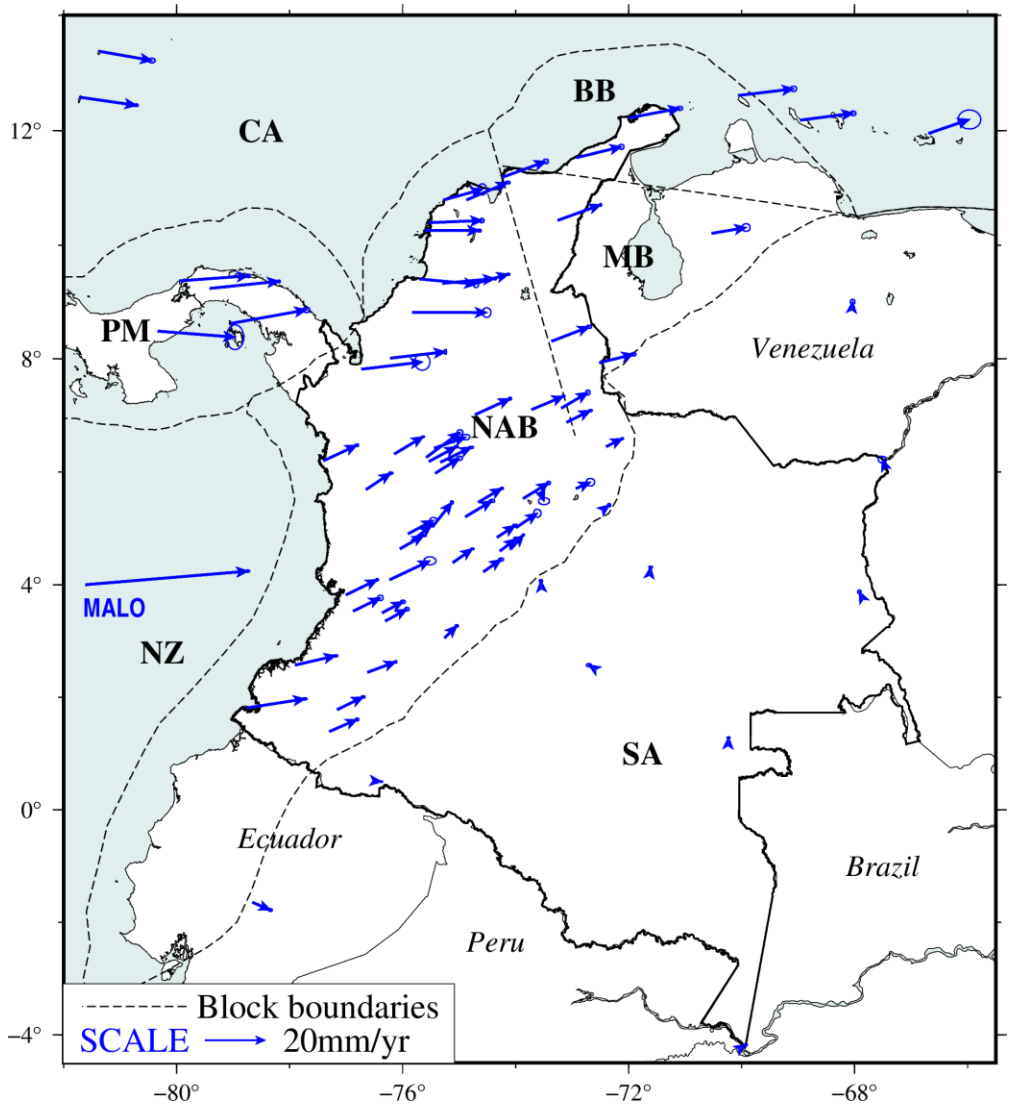

Figure 4.2. *Horizontal GPS velocity field presented in mm/yr with respect to South American Plate (includes 95% error ellipses). The same description of symbols and abbreviations as in Figure 4.1.*

Subduction of the Nazca plate is observed by the decreasing magnitude of velocity vectors from the Malpelo site (MALO, Figure 4.2) to stations located along the Pacific coast of Colombia, where a process of shortening is evident as it represents the elastic strain accumulation along the boundary. In the northwestern part of the NAB, velocities present a deviation from the general NE trend, with

a more pronounced eastern motion probably due to the combined interaction with the Caribbean plate along the South Caribbean Deformed Belt (SCDB) and the colliding PM block (Figure 2.1).

4.1.2. Horizontal velocity field w.r.t the North Andean Block

A representation of horizontal velocities with respect to the NAB defined by Nocquet et al. (2014) indicates the current definition of the whole block should be reconsidered (Figure 4.3).

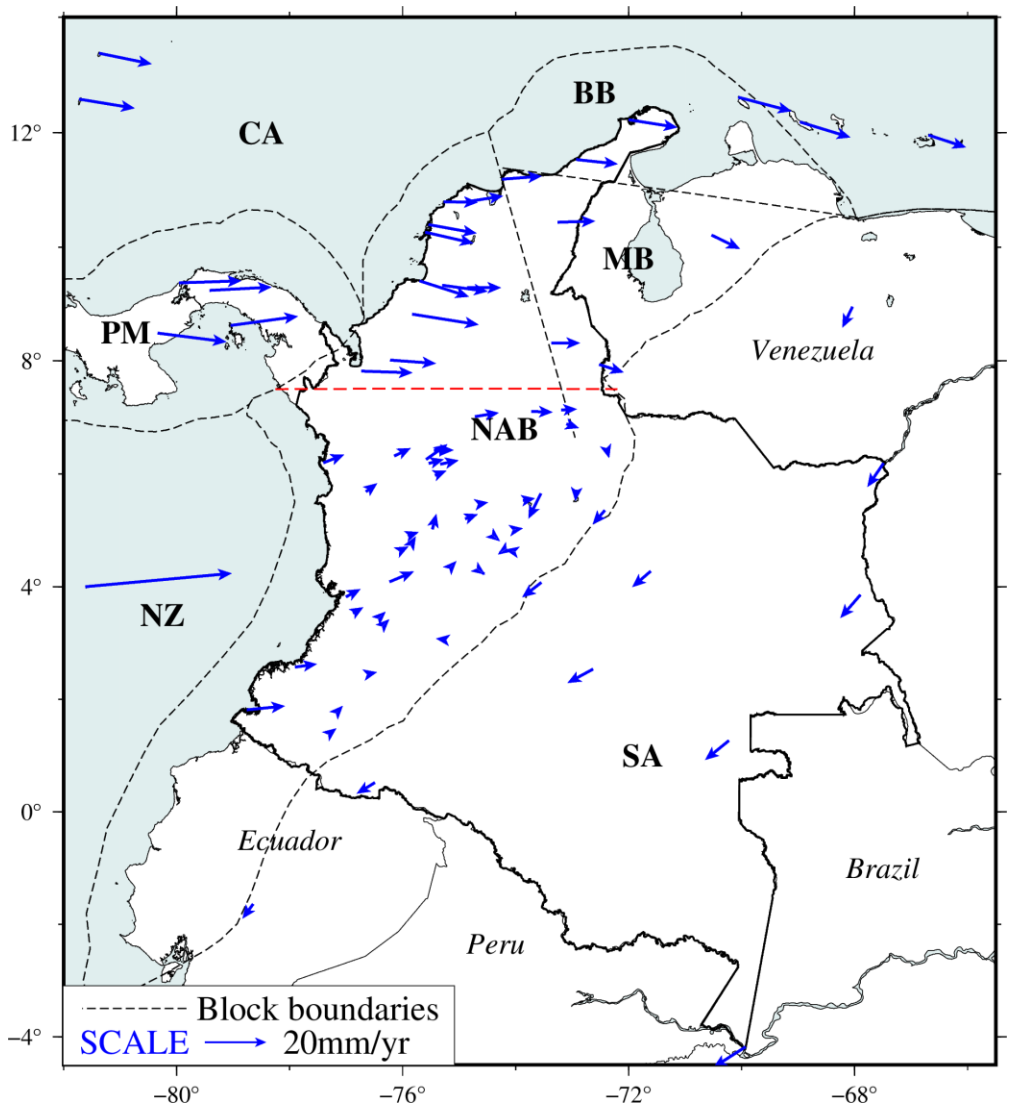

Figure 4.3. *Horizontal GPS velocity field presented in mm/yr with respect to the North Andean Block – NAB definition by Nocquet et al. (2014). Sites north of the broken red line at 7.5°N show a systematic deviation with respect to the main part of the NAB. The same description of symbols and abbreviations as in Figure 4.1.*

According to the systematic behavior of velocity vectors, the northern part of the NAB (north of 7.5º of latitude) behaves as an independent rigid block suggesting a significant interaction with the Caribbean Plate (Lizarazo et al, 2021).

4.1.3. Tectonic affiliation of northern Colombia: Macondo Block

The horizontal velocity field referred to the NAB strongly suggest the need for a new definition of northern Colombia's tectonic framework.

The estimation is done using the ECP software by Goudarzi et al. (2014). Initially, we select 11 GPS sites (ALPA, BOBG, CN19, CN38, CN39, CUC1, DIMA, GALE, VDPR, VMAG, and VPOL) to estimate a rigid motion of the northern NAB. These sites are located to the north of 7.5ºN in the NAB defined by Bird (2003), and away from the collision boundaries with the PM block and the CSZ in order to guarantee that the rigid motion is free from the elastic effects induced by the interaction of different blocks (Figure 4.4).

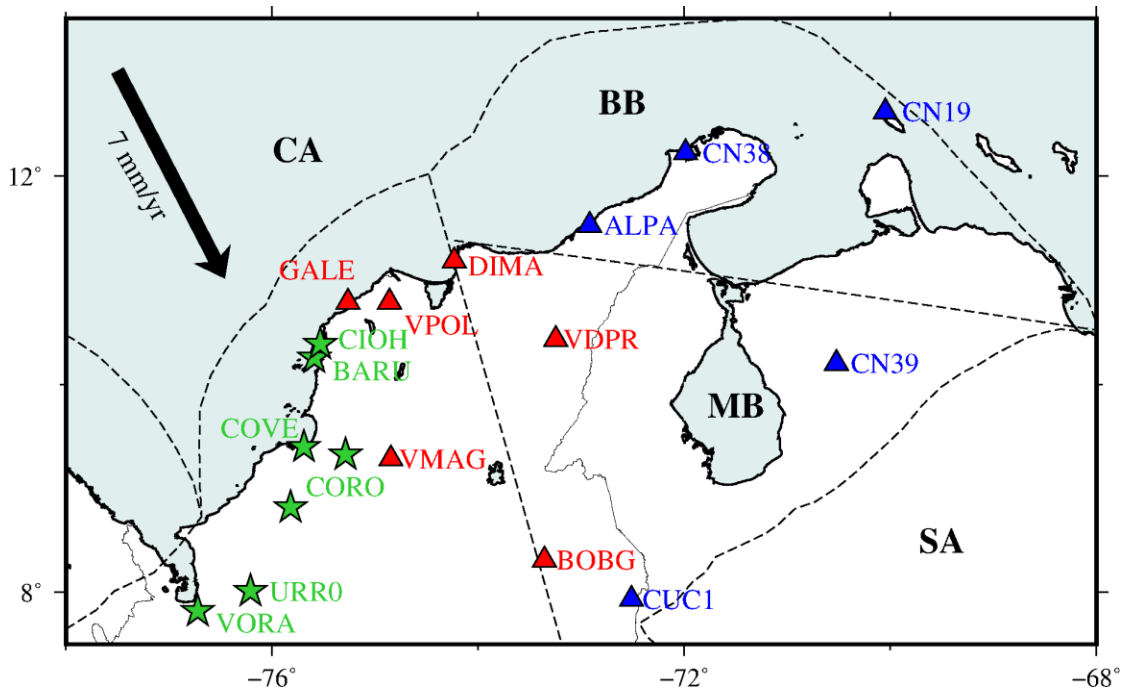

Figure 4.4. *GPS sites used in the determination of the rigid motion of the Macondo Block for the initial model (blue plus red triangles) and the final model (only red triangles). Stations affected by the Caribbean plate subduction are presented as green stars. The black arrow denotes the relative motion of the Caribbean plate w.r.t Macondo Block. Other symbols and abbreviations as in Figure 4.1.*

The selected sites present an average velocity with respect to ITRF2014 of 8.3±2.0 mm/yr and 14.4±1.1 mm/yr in the east and the north components, respectively. We evaluate the residual velocities against the estimated Euler pole to confirm the rigid behavior of the block. Then, three GPS sites (CN19, CN39, and CUC1) with large residuals (~2.2 mm/yr) are removed. ALPA and CN38 are also removed due to possible effects of the Caribbean plate convergence. Finally, the Euler pole is estimated with 6 sites (BOBG, DIMA, GALE, VDPR, VMAG, and VPOL) with a root mean square error (RMSE) less than 1 mm/yr for both components (Table 4.1). In addition, we analyzed the reduced χ^2 per degree of freedom defined by Nishimura et al. (2005) as:

$$\chi^2 = \frac{1}{(2n-3)} \sum_{i=1}^{n} \left(\frac{r_i}{\sigma_i}\right)^2 \tag{4.1}$$

where n indicates the number of GPS stations, r_i the residual (observation minus calculated data) and σ_i the data uncertainty. A good model solved for the three Euler pole parameters should have a reduced $\chi^2 \sim 1$. We found a reduced χ^2 of 1.5 for our initial model (11 GPS sites) and a reduced χ^2 of 1.0 for our best fitting model (6 GPS sites).

MODEL	φ_{EP} (◦)	λ_{EP} (◦)	ω_{EP} (◦/Myr)	RMSE East (mm/yr)	RMSE North (mm/yr)	GPS sites
Model 1 Whole NAB 45 GPS sites	0.09	128.5	0.338	1.73	1.28	AJCM, ALPA, ANCH, BAME, BAPA, BOBG, BOGT, CCAN, CIA1, CN19, CN38, CN39, CUC1, DIMA, GALE, INRI, INTO, MECE, MZAL, PAL2, POVA, QUIL, SEL1, SUAM, TASA, TONE, UNME, UWAS, VBUV, VCGR, VDPR, VMAG, VMAR, VMER, VMES, VNEI, VOTU, VPIJ, VPOL, VQUI, VROS, VSJP, VSOA, VTUL and VZPQ.
Model 2 Southern NAB 34 GPS sites	6.08	165.9	0.154	4.55	0.96	Same as model 1 except BOBG, DIMA, GALE, VDPR, VMAG and VPOL sites.

Table 4.1. *Comparative RMSE values for east and north components of velocity for GPS sites: BOBG, DIMA, GALE, VDPR, VMAG, and VPOL under different assumptions of the NAB extension. Euler pole parameters in ITRF2014 are shown for each model in columns 2, 3, and 4. The set of GPS sites used in the estimation of each Euler pole is also included.*

(continued on next page)

MODEL	φ_{EP} (◦)	λ_{EP} (◦)	ω_{EP} (◦/Myr)	RMSE East (mm/yr)	RMSE North (mm/yr)	GPS sites
Model 3 Northern NAB 11 GPS sites	3.39	129.8	0.337	1.35	1.14	ALPA, BOBG, CN19, CN38, CN39, CUC1, DIMA, GALE, VDPR, VMAG and VPOL.
Model 4 Northern NAB 6 GPS sites	27.3	-170.9	0.155	0.72	0.84	BOBG, DIMA, GALE, VDPR, VMAG and VPOL.

Table 4.1. *(continued)*

The Euler pole that characterizes the northern NAB rigid motion is located at 27.3˚±5.5˚N, -170.9˚±58.4˚E with an angular velocity of 0.1552˚±0.004˚/Myr with respect to the ITRF2014. Although the estimation error of the Euler pole parameters is large, these values do not represent a lack of precision on the evaluation of the velocities but reflect that the area covered by the selected GPS sites is too small to constrain the Euler pole uniquely.

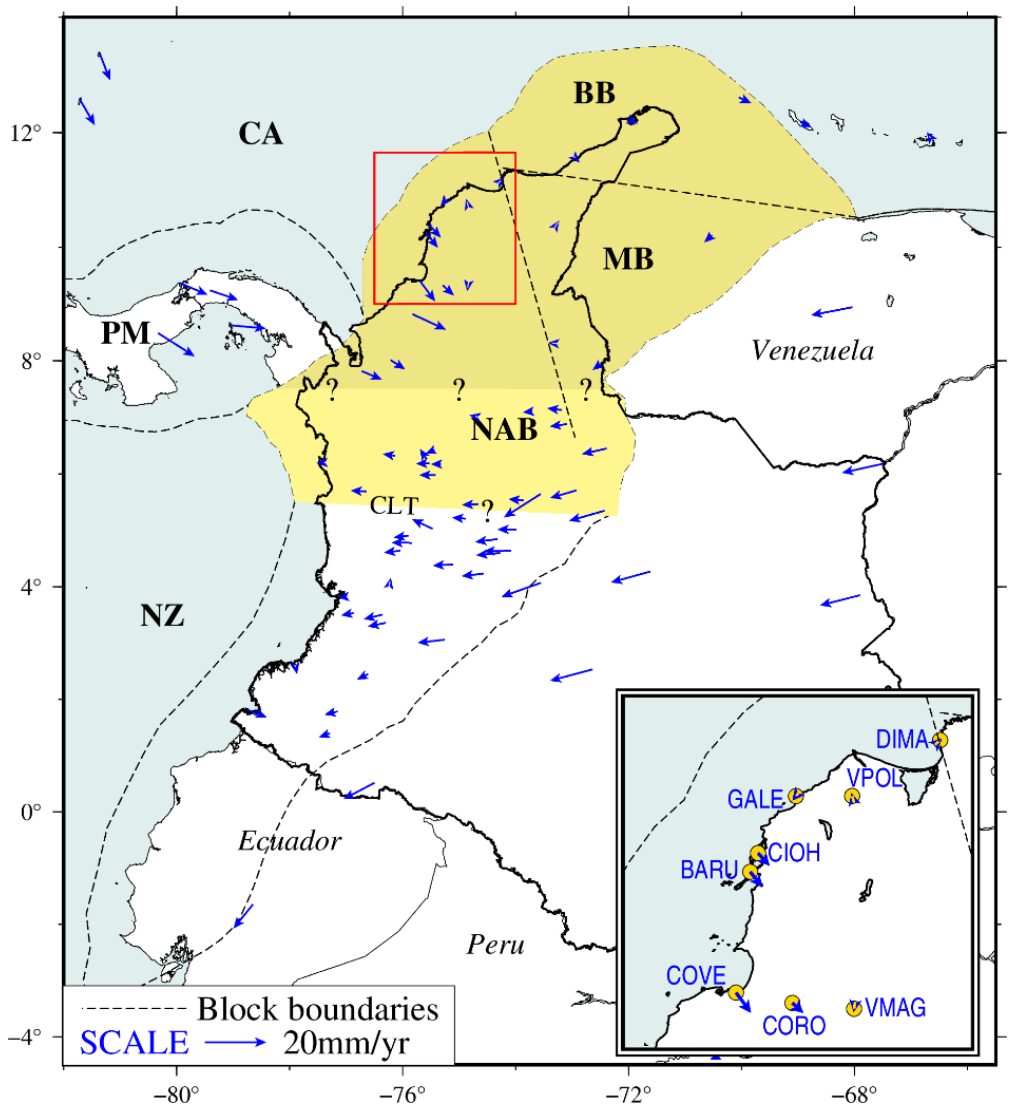

Figure 4.5. *Horizontal GPS velocity field presented in mm/yr with respect to the Macondo Block defined in this study. A detailed view of velocities in northwestern Colombia (red rectangle) is presented in the inset map. GPS station IDs are included for reference. The extension of the Macondo Block is presented as a dark-colored region. Its southern boundary with the main part of the North Andean Block is uncertain (?) and could be located somewhere inside the light-yellow region delimited by the CLT: Caldas Lithospheric Tear. The same description of symbols and abbreviations as in Figure 4.1.*

Figure 4.5 represents the velocities relative to the new block that seems to fit observed GPS velocities north of 7.5ºN of latitude except for the northwesternmost GPS sites, which show a general southwestward motion of few mm/yr that is attributed to the effect of the Caribbean plate subduction.

In the velocity diagram centered on our study region (Figure 4.6), the 6 sites for the Euler pole calculation fall inside an uncertainty of 2 mm/yr, which validates the existence of a well-constrained rigid block. We name this tectonic block the "Macondo" block, after a fictional town from the novel "One hundred Years of Solitude (Cien años de soledad)" by Colombian Nobel prize writer Gabriel García Márquez.

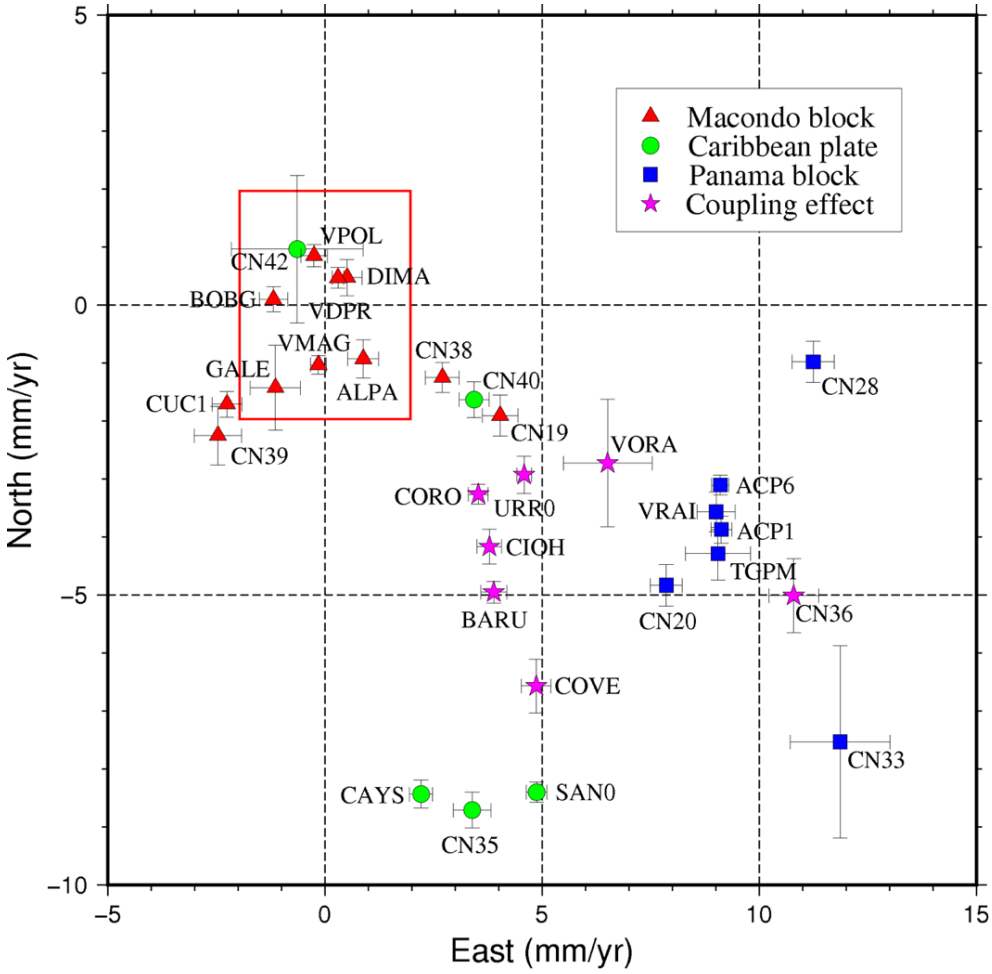

***Figure 4.6**. Detailed E-N velocity diagram w.r.t Macondo block estimated in this study. Symbols denote GPS velocities with error bars of sites located in the Macondo block (red triangles), the Caribbean plate (green circles), and the Panamá block (blue squares). Magenta stars denote the sites potentially affected by the coupling effect due to the subduction of the Caribbean plate in northwestern Colombia. The red rectangle denotes a 2 mm/yr uncertainty region for the rigid motion of the Macondo block. Broken grid lines are depicted every 5 mm/yr for reference.*

In Figure 4.6, groups of similar GPS velocities corresponding to each interacting block in northwestern Colombia, highlight the combined contribution of the Caribbean plate subduction and the PM block collision on the Macondo block dynamics.

The Macondo block represents the contemporary motion of northern Colombia and can be clearly differentiated from the rest of the NAB though its extent is not fully resolved by the current GPS network. Indeed, the Macondo block is not compatible with the traditional tectonic frame consisting of two geologically defined blocks named MB and BB blocks (Audemard., 2014). The MB block is bounded to the west by the left lateral BSMF whose slip rates are estimated less than 0.2 mm/yr and 3 mm/yr along the northern and southern segments, respectively (Paris et al, 2000; Diederix et al, 2009; Jimenez et al, 2015). The BB block is separated from the MB block by the dextral OF with a slip rate between 0.2 mm/yr to 2 mm/yr (Paris et al, 2000; Audemard et al, 2006).

In our definition of the Macondo block, we use the velocities of VDPR and BOBG sites located in the aforementioned MB block (See Figure 4.4). A preliminary estimation of the relative motion along the BSMF and the OF using the GPS data leads us to the conclusion that these motions cannot be detected with our dataset since the expected relative motions across these faults are within the uncertainty level of the GPS slip rates (<0.3 mm/yr). On the other hand, the Macondo block does not have a clear expression of its southern boundary in geology and seismotectonics (Figure 4.7). There is no geological E-W-oriented alignment separating the main part of the NAB and the Macondo Block. It is possible that the southern boundary is somewhere between 5.5ºN, which is the location of the east-west trending CLT (Vargas and Mann, 2013; Vargas, 2020), and 7.5ºN where shallow seismicity is concentrated. However, the current resolution of the GPS network does not allow to identify a clear boundary. Therefore, the Macondo block derived from GPS velocities would be currently delimited by the SCDB to the north, the SCDB and PM block to the west, and the Boconó fault to the east (See Figure 2.1 for location), while the southern limit remains uncertain. Nonetheless, the geological implications of the Macondo block and its relationship with the existing blocks are to be discussed in future studies.

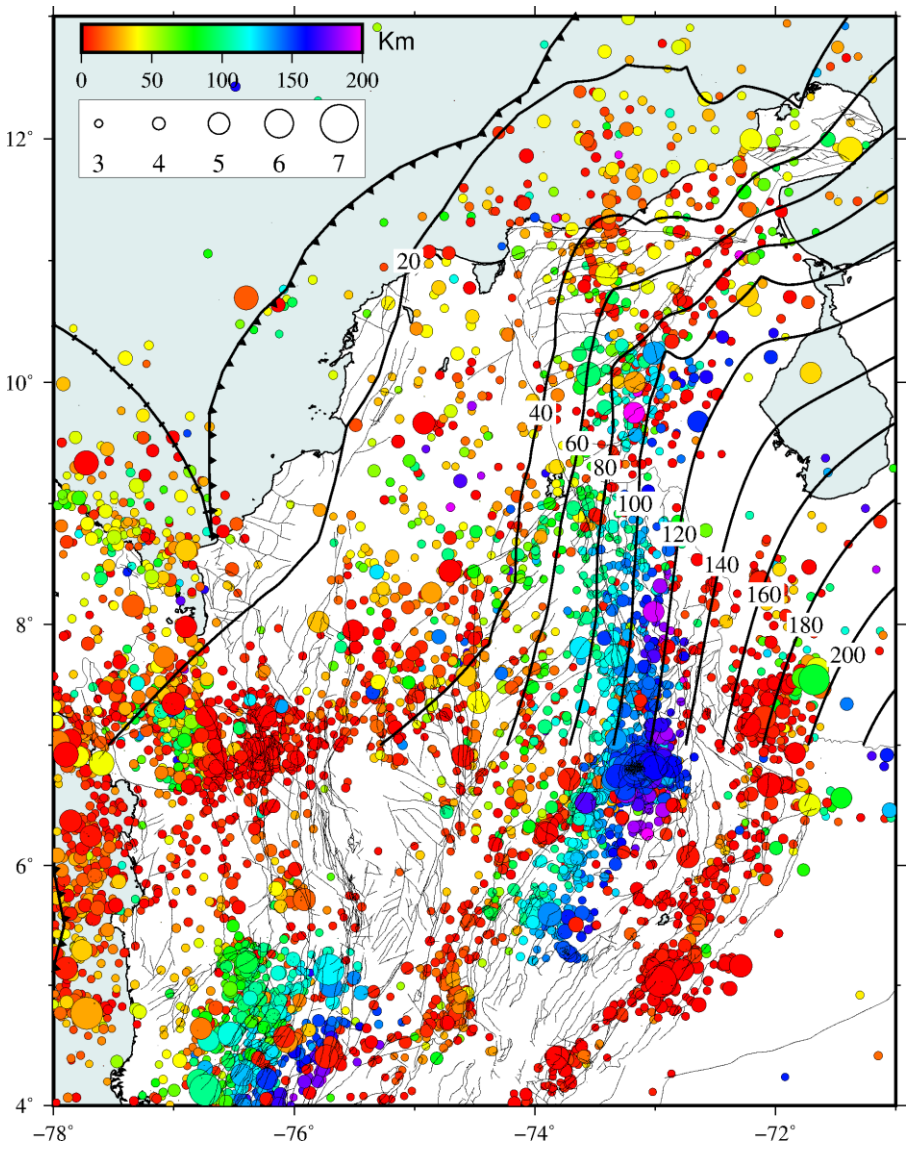

Figure 4.7. *Instrumental seismicity of northern Colombia for the period 1993-2022 (M_w≥3) plotted by depth and magnitude and geological faults (thin black lines). Thick black lines represent the iso-depth contours (in km) of the upper boundary of the Caribbean plate. Sources: RSNC and Research Group Geology map of Colombia, SGC.*

4.1.4. Vertical velocity field and its reliability

Unlike horizontal motions, vertical ones present larger errors and show a variable pattern that does not respond uniquely to the tectonic plate or block kinematics but can be affected simultaneously by localized effects (Figure 4.8).

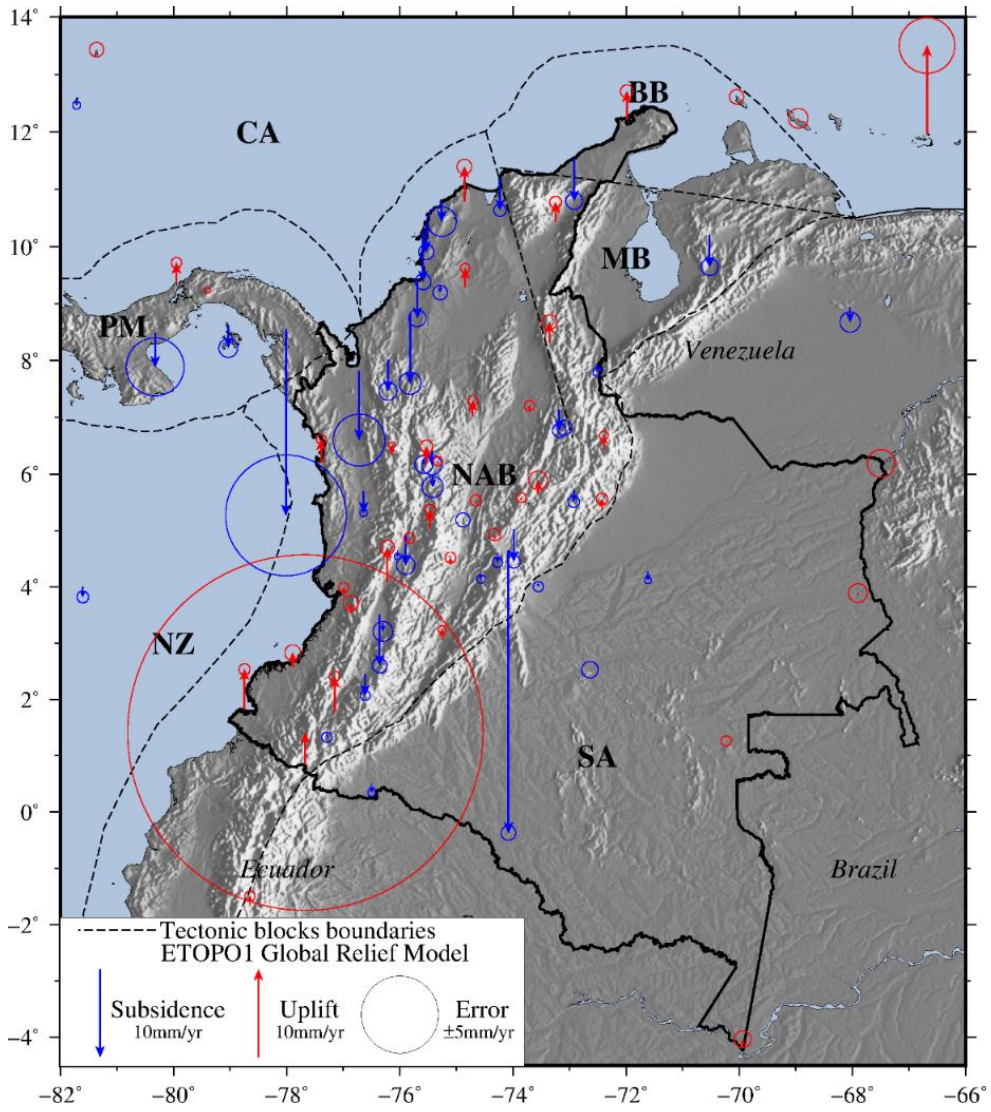

Figure 4.8*. Vertical GPS velocity field. Blue arrows represent the subsidence of the GPS site and red ones indicate uplift, both in mm/yr with respective error ellipses. Relief based on the ETOPO1 Global Relief Model (NOAA - National Oceanic and Atmospheric Administration). The same description of symbols and abbreviations as in Figure 4.1.*

Uplift is observed at coastal sites located along the CESZ with motions smaller than 5 mm/yr. In opposition, subsidence is recognized along the Caribbean coast in northwestern Colombia with rates between 0.8 mm/yr to 5.8 mm/yr. Stations located on the stable South American plate and lowlands between mountain ranges show small vertical motions in both, upward and downward directions (≤2 mm/yr). Atypical large subsidence signal at the BOGT site is usually related to groundwater withdrawal (Lobo-Guerrero, 2003; Mora-Páez et al, 2019). Large error ellipses at

VORI and CN42 sites are associated with shortened time series for velocity estimation as mentioned in section 3.2. For the CN34 site located in PM block, noisier time series caused significant uncertainty values.

I will focus on explaining the subsidence in northwestern Colombia, as they constitute an overall persistent signal on the GPS sites reflecting the subduction of the Caribbean plate along the boundary with the newly defined Macondo Block.

It is well known that vertical GPS motions are affected by different factors, some of which can be corrected during the velocity and its uncertainty estimation (e.g, seasonal effects, instrumental changes, and earthquake offsets). Nevertheless, there are some other phenomena that can be responsible for the observed uplift or subsidence. Among these processes we can find mud volcanism, natural resources extraction (water, oil, gas, etc.), sedimentation, and monument instability, among others (Gurevich and Gilingarian, 1993; Amelung et al, 1999; Baloglanov et al, 2018, Itoh et al, 2019). Therefore, it becomes important to assess if the observed motions are affected by any of the abovementioned processes.

In the Caribbean region, there are extensive manifestations of mud volcanism (Figure 4.9) where localized deformation from campaign GPS data has been observed on top of a few volcanic edifices (Carvajal, 2016; Carvajal and Mendivelso, 2017). Although subsidence signals are large, on the order of ~17 to 35 mm/yr at Pueblo Nuevo and El Totumo volcanoes north of Cartagena (Figure 4.10), they cannot be considered a regional feature given the sparse distribution of geodetic stations and the large uncertainties associated with episodic data velocity estimation. Additionally, velocity values differ largely from the closest permanent GPS station called CN37 (renamed GALE in our study) which only reported values of ~2 mm/yr according to the same studies.

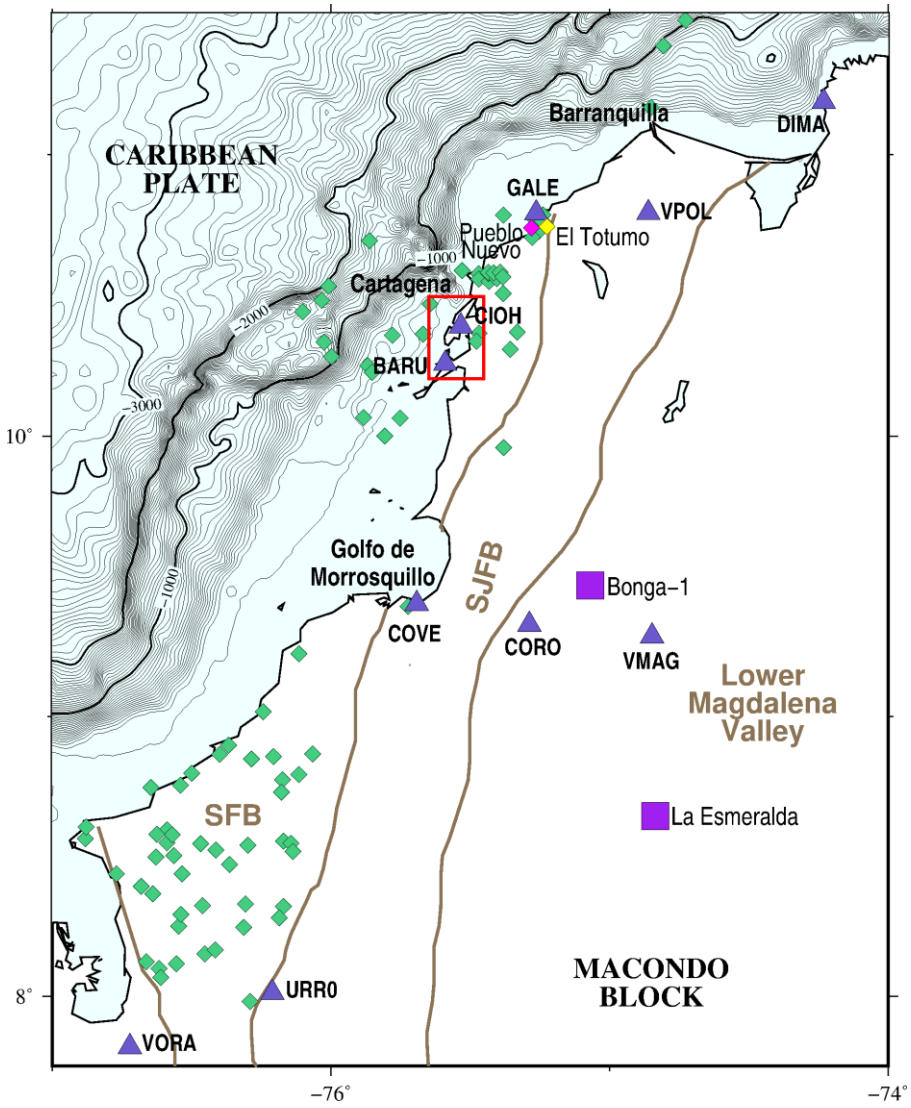

Figure 4.9*. Caribbean region and distribution of mud volcanoes (green diamonds) as in Carvajal and Mendivelso (2017), wells (purple rectangles) as in Mora et al. (2018) and permanent GPS sites (blue triangles). Magenta and yellow diamonds denote the location of the Pueblo Nuevo and El Totumo volcanoes. Red square denotes the area analyzed with Sentinel-1 and TerraSAR-X imagery by Restrepo-Angel et al. (2021). Bathymetry based on the ETOPO1 Global Relief Model (NOAA - National Oceanic and Atmospheric Administration).*

Figure 4.10*. El Totumo mud volcano located northern Cartagena (Figure 4.9). Upper picture represents the view of the volcano from the western side. Lower picture taken at the top of the volcano.*

The subsidence history in the LMV, northwestern Colombia, as a result of sedimentation was analyzed by Mora et al. (2018). Their study suggests that recent geological subsidence (last 13 Ma) can be related to high sedimentation rates of ~0.3 mm/yr observed at La Esmeralda-1 and

Bonga-1 wells (Figure 4.9). However, these estimates are not representative of the faster GPS subsidence observed at coastal locations, which are less reliable due to the poor preservation of geological deposits. Sediment-load subsidence rates are, therefore, not significant at the uncertainty level of current GPS data in addition to the localized survey points, suggesting that this process does not represent the main origin of subsidence in the northwestern Caribbean.

Anthropogenic-related subsidence due to groundwater, oil, and gas withdrawal has been recognized in different parts of the world (Gambolati et al, 2005; USGS, 2022). The over-extraction of subsoil resources reduces the compaction of rocks that fail on themselves producing gradual sinking of the ground. In the area of Cartagena, groundwater pumping for consumption or agricultural activities has not been reported according to Restrepo-Ángel et al. (2021). Although there are several natural gas production fields under operation (Hocol S.A, 2022), as well as offshore bathymetric active fluids and natural gas release features on Cartagena Bay (Mora-Páez et al, 2018b), no quantification of natural gas extraction induced subsidence has been performed by private or governmental parties as far as we know. In addition, no estimation of the volume of gas and/or fluids released by the vents in the mapped ocean bottom has been estimated. However, effects of these activities, if any, do not represent a regional pattern but a localized one and therefore, are not representative of the current vertical motions.

Analysis of Interferometric Synthetic Aperture Radar data (InSAR) by Restrepo-Ángel et al. (2021) showed negative vertical trends in the region of Cartagena and surroundings with average rates of 3.4 ± 0.4 mm/yr (Sentinel-1) and 4.7 ± 1.9 mm/yr (TerraSAR-X) (Figure 4.9). At the location of the CIOH GPS site in Cartagena, Sentinel-1 and TerraSAR-X data showed subsidence of 1.94 ± 0.41 mm/yr and 2.49 ± 1.65 mm/yr, respectively, in agreement with their GPS subsidence rate of 2.85 ± 0.84 mm/yr. Our estimated subsidence at the CIOH site of 3.08 ± 1.0 mm/yr shows consistency within the uncertainty level of both geodetic datasets. These results demonstrate that observed subsidence represents a regional feature in the study region.

Having ruled out possible non-tectonic origins for the observed subsidence in northwestern Colombia (mud volcanism, sedimentation, and fluids/gas exploitation) we can interpret the contemporary vertical deformation as a product of the tectonic activity, that is, the interplate coupling due to slow subduction of the Caribbean plate under the Macondo block and the seismic cycle.

4.2. Deformation style and its spatial distribution

Computing the strain rate distribution from GPS relative velocities allows the identification of localized strain concentrations that are likely associated with regions of significant seismic potential. It can be obtained by spatial interpolation of discrete geodetic measurements as continuous functions in the study area independently of the reference frame in which the displacement rates are expressed.

I evaluate the strain rate distribution by following the method of Shen et al. (1996) from horizontal velocities for a subset of 78 GPS stations and a grid for calculation of 0.05°. Stations located far offshore at distances larger than 50 km such as CAYS, CN35, GLPS, ISCO, MALO, and SAN0, and those located in Costa Rica IND1 and QSEC, were excluded. Also, the site CN34 and VORI for presenting a noisy trend and large horizontal uncertainties.

We estimate rigid motion (U_x, U_y), strain rate components ($\dot{\varepsilon}_{xx}, \dot{\varepsilon}_{xy}, \dot{\varepsilon}_{yy}$) and rigid rotation (ω) applying the following equation (Eq. 4.2):

$$\begin{pmatrix} V_x^I \\ V_y^I \end{pmatrix} = \begin{pmatrix} 1 & 0 & \Delta x_I & \Delta y_I & 0 & \Delta y_I \\ 0 & 1 & 0 & \Delta x_I & \Delta y_I & -\Delta x_I \end{pmatrix} \begin{pmatrix} U_x \\ U_y \\ \varepsilon_{xx} \\ \varepsilon_{xy} \\ \varepsilon_{yy} \\ \omega \end{pmatrix} + \begin{pmatrix} \epsilon_x^I \\ \epsilon_y^I \end{pmatrix} \tag{4.2}$$

here, V_x^I and V_y^I represent the east and north components of the velocity at the station I, Δx_I and Δy_I are the components of the displacement rate (ΔR_i) between the station I and the point where we compute strain rate and ϵ_x^I and ϵ_y^I, are the observational errors which are weighted by the following equation (Eq. 4.3):

$$\epsilon_{x,y}^i = \sigma_{x,y}^i \exp\left(\frac{\Delta R_i^2}{2D^2}\right) \tag{4.3}$$

where $\sigma_{x,y}^i$ is the original observation error for each component of the velocity and D represents distance decay constant (DDC), a value in km that smooths the distribution of strain rate over an area and whose definition should be a function of the tectonic deformation features and the spacing of the observation points. To determine the appropriate value of the DDC, we estimate the average

distance between the GPS stations located inside the NAB defined by Bird (2003), and we obtained a value of 45±27 km. Nonetheless, we tested several values for the DDC parameter from 45 km to 100 km (2 times the standard deviation). In the estimation, sites located over distances larger than three times the defined DDC value were excluded from the strain rate calculation.

Once the six parameters in eq. (4.2) are estimated, we can compute the dilatation (Δ) in Eq. 4.4 and shear strain (Σ) rates in Eq 4.5 at each point as follows (Sagiya et al, 2000):

$$\Delta = \dot{\varepsilon}_{xx} + \dot{\varepsilon}_{yy} \tag{4.4}$$

$$\Sigma = \sqrt{\dot{\varepsilon}_{xy}^2 + (\dot{\varepsilon}_{xx} - \dot{\varepsilon}_{yy})^2/4} \tag{4.5}$$

We analyze the strain distribution using three different values for the DDC: 45 km, 75 km (one standard deviation) and 100 km (two standard deviations). Despite the fact that main features are preserved in the three estimations (mainly contraction), the level of spatial smoothing of the strain distribution changes. For the smaller DDC value (45 km), the pattern is very rough (Figures 4.11a), while in the case of the largest one (100 km), the pattern looks smoother, presenting smaller variation of the strain pattern over large distances (Figures 4.11b). In the latter case, the error weighting is too strong, which causes that important information is being discarded as noise.

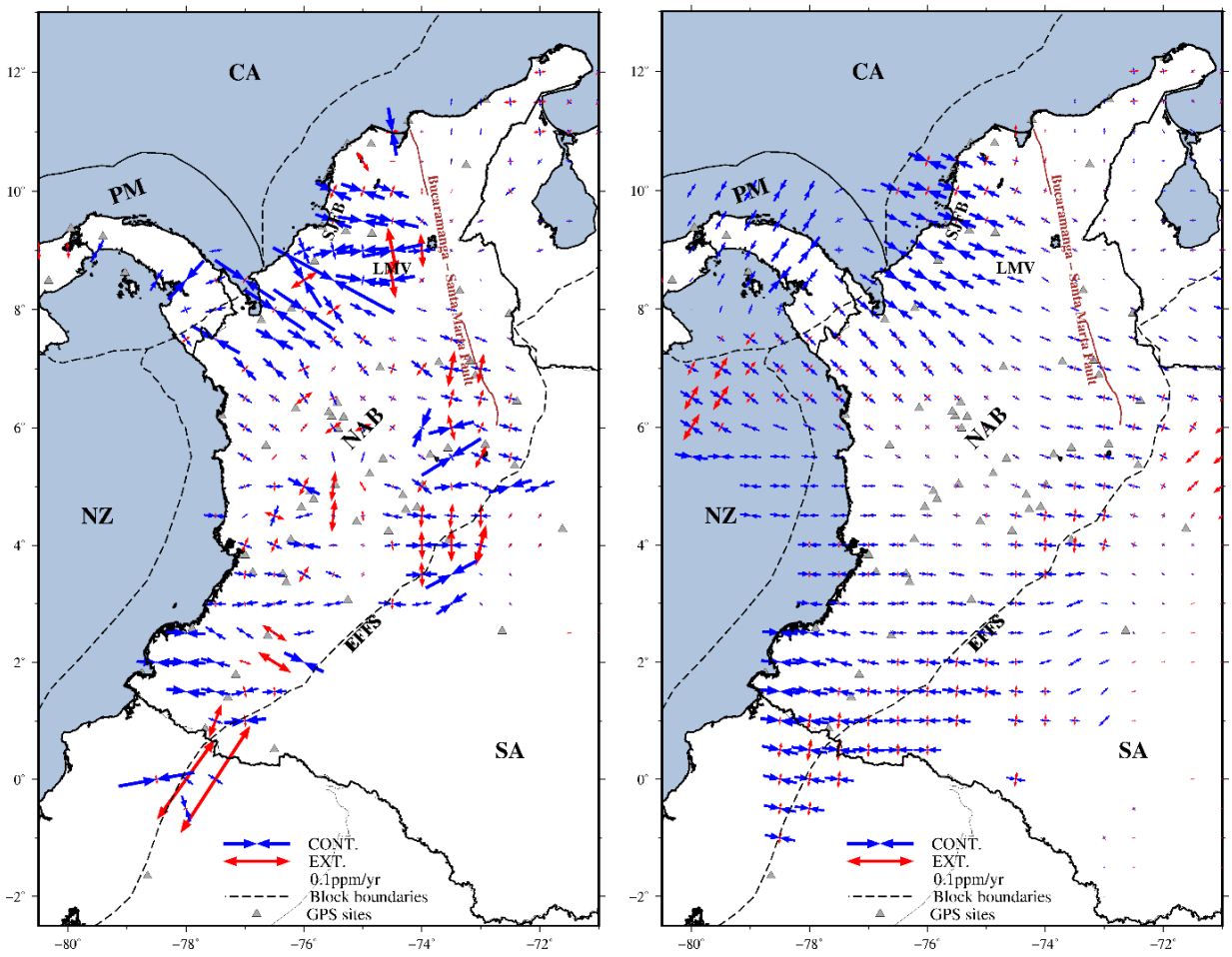

Figure 4.11. *Principal strain axes with a). DDC=40 km and b). DDC=100 km. The blue arrows represent contraction while red ones, represent extension. The scale of the deformation is 1 ppm/yr. Grey triangles show the location of the GPS stations in the area. Broken black lines represent the boundaries of the Global Plate Model by Bird. (2003) SA: South American plate, NZ: Nazca plate, CA: Caribbean plate, PM: Panamá Block and NAB: North Andean Block. Abbreviations as follow SJFB: San Jacinto Fold Belt, LMV: Lower Magdalena Valley, EFFS: Eastern Frontal Fault System.*

A DDC value of 75 km seems to be more adequate to highlight strain concentration zone, representing the tectonic deformation features allowed by the resolution of the GPS network (Figures 4.12). Discussion of the strain distribution is going to be based on this DDC value.

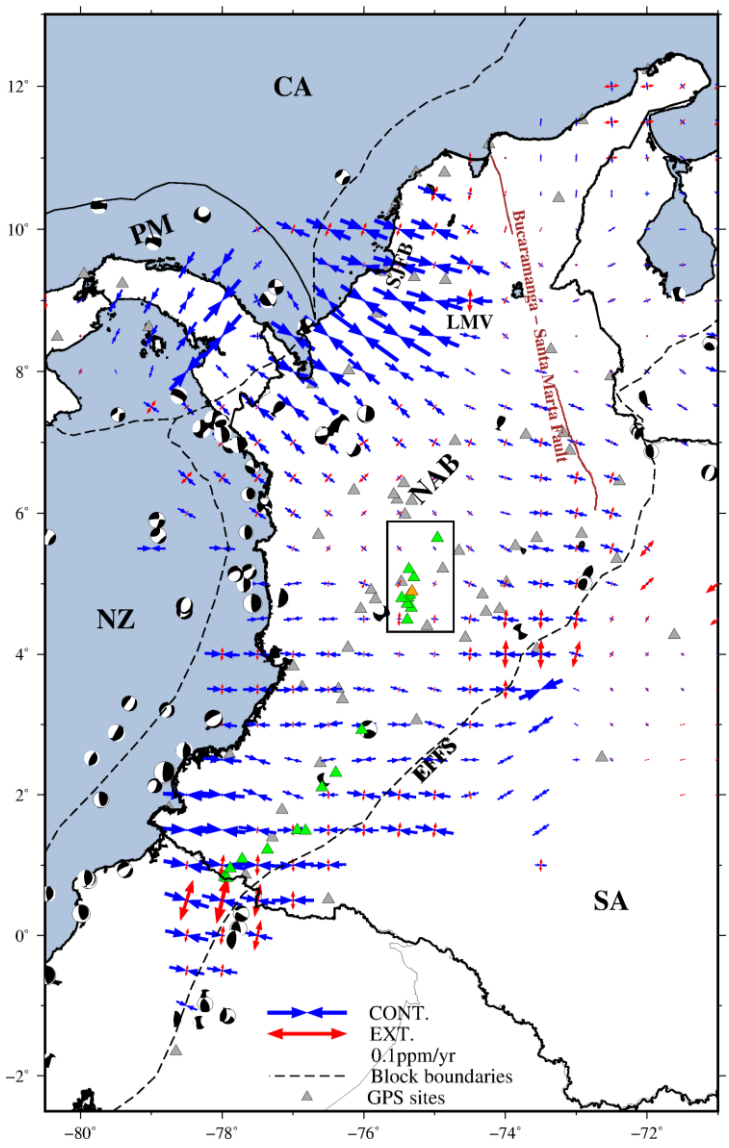

Figure 4.12. *Principal strain axes with best DDC value of 75 km. Green triangles represent quaternary volcanoes along the Central Cordillera. Orange triangle shows the location of the Nevado del Ruiz volcano. Same description of abbreviations as in Figure 4.11.*

The compressive strain was identified as the prevailing tectonic feature (Figure 4.12) with significant signals along the southwestern and northwestern corners of Colombia, which correspond to the CESZ and the Caribbean-Macondo boundary, respectively. Unlike the CESZ, where the Nazca plate is subducting steadily and has generated large megathrust earthquakes in the past (Mothes et al, 2013; Nocquet et al, 2014; Chlieh et al, 2014; Ye et al, 2016; Yoshimoto et al, 2017; Yamanaka et al, 2017; Mora-Páez et al, 2019; Sagiya and Mora-Páez, 2020), the Caribbean-Macondo boundary is not as seismically active as the former. The above result might

indicate the region is potentially hazardous although the area has been silent over the last 530 years. On the other hand, some areas in the northeast of Colombia and between 4˚N and 6.5˚N of latitude and 74˚W and 77˚W of longitude, where Quaternary volcanoes are located, present almost no deformation (Figure 4.12). This implies that volcanic activity is low and stable in the northern part of the Central cordillera throughout the monitoring period (2008-2017) with no detectable signals on the surface. On this respect, the Volcanological and Seismological Observatory of Manizales city (SGC-OVSM) (Sanabria et al, 2021) showed that from 2010 to 2020 the volcanoes on the northern volcanic segment present levels of activity between III (changing in the behavior of volcanic activity) and IV (active volcano and stable behavior) (Figure 4.13).

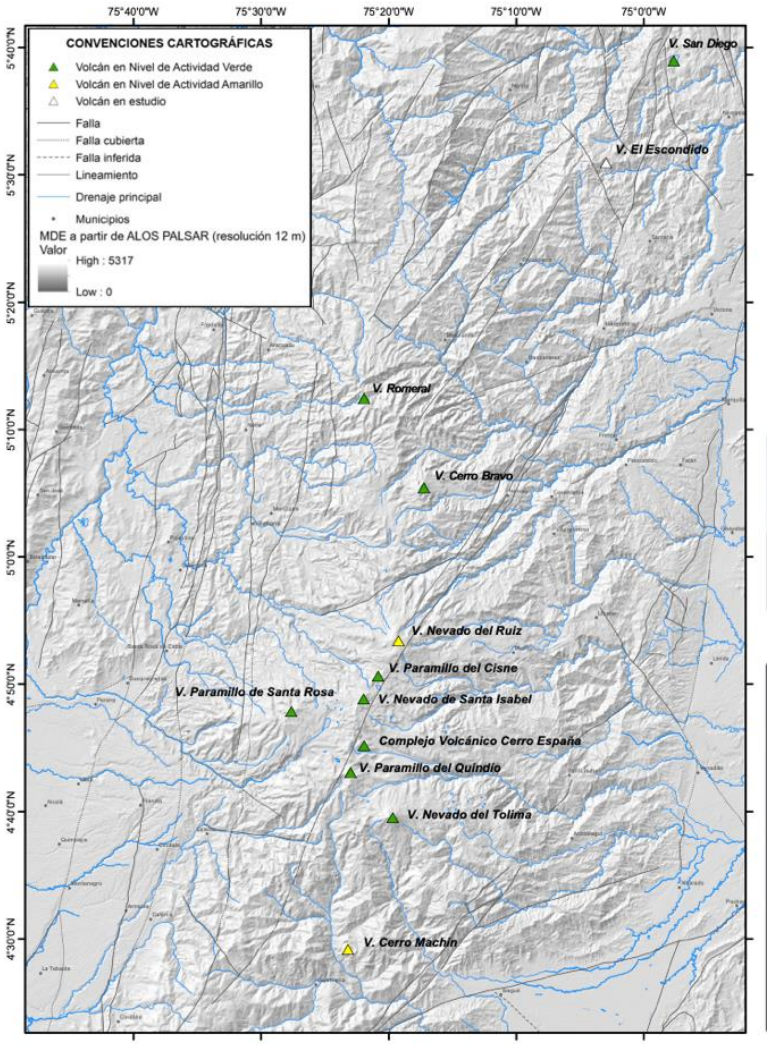

Figure 4.13. *Level of activity at volcanoes that comprise the northern volcanic segment. Yellow and green triangles reported level III and IV of activity, respectively. Taken from Sanabria et al. (2021).*

In addition, they reported that GNSS positions and baselines, as well as tiltmeters, did not present significant deformation (Figure 4.14).

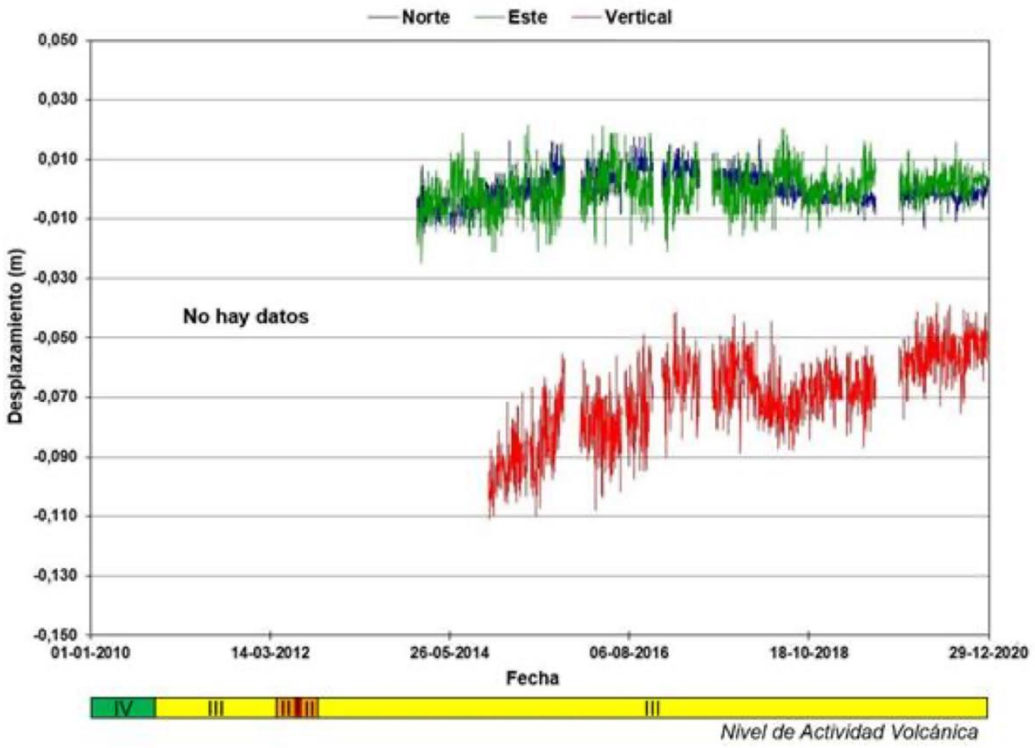

Figure 4.14. *Deformation signals in m observed from 2014 to 2020 at the GNSS site located at the Olleta crater on the Nevado del Ruiz volcano (Location in Figures 2.1 and 4.11). Blue, green and red lines represent north, east and vertical components, respectively. Lower color bar indicates the level of activity during GNSS site operation. Taken from Sanabria et al. (2021).*

Along the CSZ, the magnitude of the NW-SE strain rate is ~65 nanostrain/yr occurring mainly in lowlands corresponding to the LMV basin, limited to the east by the BSMF. South in the collision region inland Colombia, the contraction keeps the same orientation but with a smaller rate of ~40 nanostrain/yr.

NE-SW contraction is also observed in the PM block with rates of ~50 nanostrain/yr. This could be attributed to the Caribbean plate interaction along the SCDB north of Panamá or due to the internal deformation of the entire block.

Compressive strain at the CESZ zone in the EW direction is consistent with the motion of the Nazca plate subduction. Maximum strain rates of ~60 nanostrain/yr decrease to the north along

the Pacific coast of Colombia, which can be interpreted as an effect of weak coupling (<0.5) between the Nazca plate and continental Colombia related to the M_w8.1 earthquake in 1979 and/or with the limited spatial resolution of the GPS network (Sagiya and Mora, 2020).

The Eastern Cordillera foothills present contraction in the EW direction with magnitudes of ~30 nanostrain/yr, which could be related to the shortening of the mountain range between 3ºN and 4.5ºN of latitude in comparison with the northern part of it.

From the CMT solutions of earthquakes shown in Figure 4.12, I can point out, at least qualitatively, that the orientation of the strain axes corresponds well to the rupture mechanisms of seismic events especially along the subduction and collision zones, where the rupture mode is mainly due to reverse faults and along the foothills of the Eastern Cordillera, where the events present mixed strike-slip and reverse mechanisms.

By analyzing the maximum shear strain results (Figure 4.15), a 1000 km long shear stripe along the Eastern Cordillera foothills defined by the EFFS is recognized. This structure is considered the limit between the NAB and the South American plate in the Global Plate Model by Bird (2003). The shear strain rate along this boundary is about 55 nanostrain/yr and relative motion from GPS data variates along the EEFS strike with average values of ~7.7 mm/yr (BAME, BOGT, POVA, QUIL, VMER, VNEI, VSOA and VZPQ). The latter is slightly larger than the most updated slip estimation for the EFFS based on paleoseismological data at the Potrerillos and Miraflores trenches along the EFFS, which indicate right lateral motions on the order of 4 mm/yr and 1 mm/yr, respectively (Gómez-Hurtado et al, 2022).

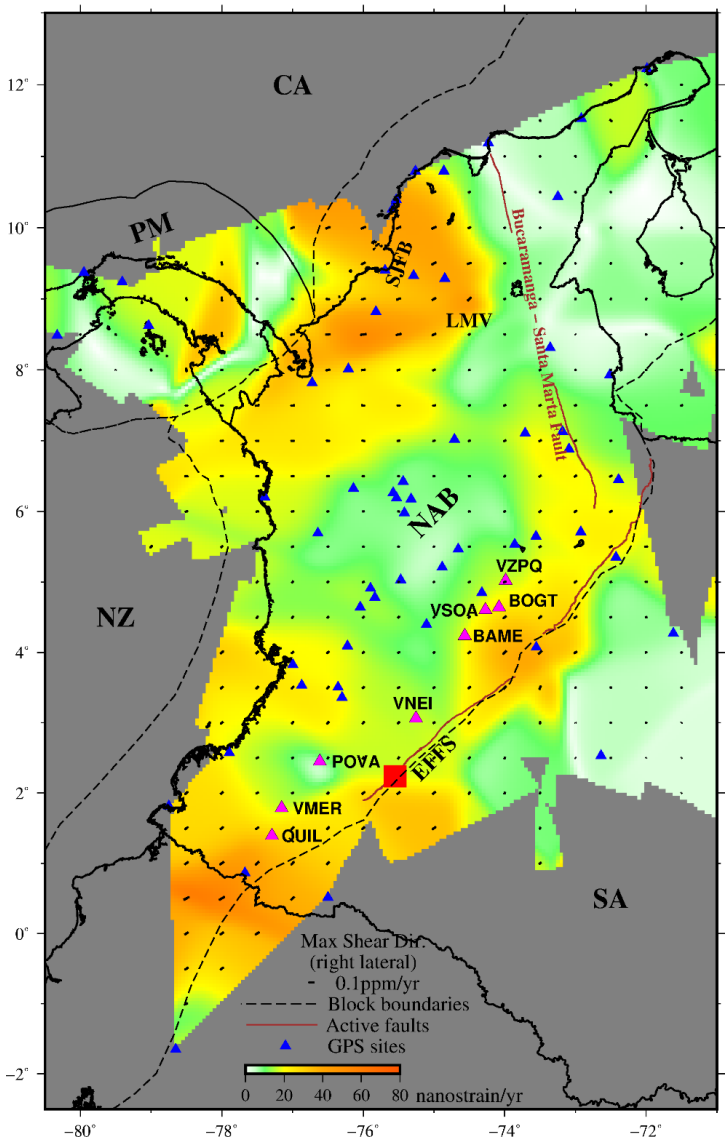

Figure 4.15. *Maximum shear strain rate with a DDC = 75 km. The color bar indicates the amount of shear strain in nanostrain/yr. Black lines show the right lateral direction of the shear. Brown lines are the traces of some geologic faults. Blue triangles show the location of the GPS stations. Magenta triangles denote the stations where right lateral motion along the EFFS was computed and their respective IDs. Red square indicates the location of the paleoseismological trenches named Potrerillos and Miraflores along the EFFS where long-term motions were obtained. Same description of abbreviations as in Figure 4.11.*

4.3. Conclusions

Three-dimensional interseismic velocities were computed based on the GPS network in Colombia and surroundings. They have contributed to clarify the regional kinematics in

northwestern South America which is, in general, compatible to Global Plate Motion Models and previous studies (Bird, 2003; Mora-Páez et al, 2019). It is undeniable that increasing spatial and temporal resolution of the geodetic network in the country and surroundings has been and will continue to be a key aspect to refine the knowledge of a very complex tectonic framework.

The analysis of horizontal velocity data relative to the previously estimated rigid motion of the NAB (Nocquet et al, 2014) allows me to identify that a rigid block assumption for the whole NAB is not appropriate and that the northern part of it behaves independently as a new tectonic block I named Macondo Block (Lizarazo et al, 2021). The southern limit of the Macondo block is not well constrained by the geodetic data due to the limited resolution of the network. Neither geology nor seismotectonics shows clear alignments along the boundary leaving the southern margin of the Macondo block uncertain.

The implications of the newly defined Macondo Block in regional tectonics, as well as the clear definition of its boundaries, is a task to address in future studies with improved datasets. Modification of the traditional tectonic setting presents new potential interpretations of processes taking place at common boundaries of existing plates and blocks. In this case, we propose that the subduction of the Caribbean plate under the Macondo Block, validated by significant compressive strain rates (~65 nanostrain/yr) in NW-SE orientation, is the main process causing the observed crustal deformation at these locations. These results lead me to propose that strain concentration in the Caribbean region of northwestern Colombia could be related to an ignored seismic/tsunami potential. This research hypothesis will be evaluated by GPS data modeling using elastic (Chapter 5) and viscoelastic (Chapter 6) models.

CHAPTER 5
INTERPLATE COUPLING MODEL ALONG THE CARIBBEAN SUBDUCTION ZONE NORTHWESTERN COLOMBIA PART I – ELASTIC MODEL

In this chapter, I discuss three-dimensional crustal deformation in northwestern Colombia based on a geodetic inversion of interseismic GeoRED GPS data to map a potential seismic source region on the subducting Caribbean plate under the Macondo Block based on an elastic half-space model. Findings indicate a shallow fully locked region offshore Cartagena city that was interpreted under two scenarios, a hazardous one, where tectonic stress is being built elastically and might be released in a future earthquake, and a non-hazardous one, where NW-SE contraction is accommodated in a non-reversible plastic way across the SJFB. I debate both possibilities and present available evidence to support the seismogenic case as the most likely one, including a detailed comparison of slow subduction zones worldwide as regions where megathrust earthquakes and tsunamis have occurred in the past.

5.1. Methods

5.1.1. Geodetic inversion method

At the plate interface of subduction zones, the tectonic stress is accumulated during the interseismic period as a result of mechanical locking at intermediate depths and steady slip at shallower and deeper portions. This scheme can be modeled as a superposition of the uniform steady slip at the convergence rate and a slip deficit, also known as backslip, in the locked area (Savage, 1983).

In order to estimate the spatial distribution of the slip deficit along the CSZ, we used the method by Sagiya and Mora-Páez (2020), which followed that of Yabuki and Matsu'ura. (1992) and Yoshioka et al. (1993) with minor modifications. In general terms, the method is described by a highly flexible Bayesian model with unknown hyperparameters. This model combines information provided by the observed data (GPS baselines and vertical velocities) and prior information given by the smoothness of fault slip distribution. The regularization factor is considered in the inversion with a hyperparameter $\alpha^2 = \sigma^2/\rho^2$ (σ^2: scale factor of the covariance matrix and ρ^2: roughness of the slip distribution), which is obtained numerically to minimize the ABIC (Akaike Bayesian Information Criterion) (Akaike, 1980) and allows the computation of the remaining parameters.

Mathematical formulation is as follows: the slip deficit rate (SD) on the plate interface at the location (φ, λ) can be described by a functional expansion:

$$SD(\varphi,\lambda) = V_{pl}(\varphi,\lambda)\psi(\varphi,\lambda) = V_{pl}(\varphi,\lambda)\sum_{k=1}^{K}\sum_{l=1}^{L} a_{kl}B_{kl}(\varphi,\lambda) \tag{5.1}$$

where, $V_{pl}(\varphi,\lambda)$ is the relative plate velocity and $\psi(\varphi,\lambda)$ is the coupling rate; B_{kl} are the 2-dimensional basis functions for the spatial distribution of the coupling rate, and a_{kl} are the functional expansion coefficients; K and L are the number of base functions in the latitude and longitude directions, respectively. We use bicubic B-spline functions (de Boor, 1972; Cox 1972) as the base functions for our analysis. Surface displacement rate due to the interplate coupling at each GPS station is calculated with elastic Green's functions:

$$\begin{aligned} v_j^i\left(\phi,\Lambda\right) &= \int SD(\varphi,\lambda)G^i\left(\varphi,\lambda,\phi,\Lambda\right)d\varphi d\lambda \\ v_j^i\left(\phi,\Lambda\right) &= \sum_{k=1}^{K}\sum_{l=1}^{L} a_{kl}\int V_{pl}(\varphi,\lambda)B_{kl}(\varphi,\lambda)G^i\left(\varphi,\lambda,\phi,\Lambda\right)d\varphi d\lambda \end{aligned} \tag{5.2}$$

where $G^i\left(\varphi,\lambda,\phi,\Lambda\right)$, is the Green's function for the the i-th component of displacement at the surface point ($\phi,\ \Lambda$) due to a unit fault slip at (φ, λ) on the plate interface.

As input data, we analyze the baseline length change rates between GPS sites. The baseline length change rate is determined as following:

$$\dot{L}_{mn} = (\boldsymbol{v}_m - \boldsymbol{v}_n)\cdot\frac{\boldsymbol{r}_m - \boldsymbol{r}_n}{\|\boldsymbol{r}_m - \boldsymbol{r}_n\|} \tag{5.3}$$

where $\boldsymbol{v}_m$ and $\boldsymbol{r}_m$ are the velocity and position vector of the stations m, respectively.

The observation equation can be written as:

$$\boldsymbol{d} = \boldsymbol{H}\boldsymbol{m} + \boldsymbol{e} \qquad \boldsymbol{e}\sim N(0,\sigma^2\boldsymbol{E}) \tag{5.4}$$

The data vector $\boldsymbol{d}$ contains baseline change rate data obtained from GPS observations. The vector of model parameters $\boldsymbol{m}$ represents the functional expansion coefficients a_{kl} shown in Eq. 5.1. σ^2 and $\boldsymbol{E}$ denote the scaling factor of observation errors and the normalized variance-covariance matrix of the observational data, respectively. The observation equation (Eq. 5.4) can be written in the form of a probability density function for the data vector $\boldsymbol{d}$ as:

$$p(\boldsymbol{d}|\boldsymbol{m};\sigma^2) = (2\pi\sigma^2)^{-N/2}\|\boldsymbol{E}\|^{-1/2}\exp\left[-\frac{1}{2\sigma^2}(\boldsymbol{d}-\boldsymbol{H}\boldsymbol{m})^T\boldsymbol{E}^{-1}(\boldsymbol{d}-\boldsymbol{H}\boldsymbol{m})\right] \quad (5.5)$$

N is the number of data and $\|\boldsymbol{E}\|$ is the absolute value of the determinant of $\boldsymbol{E}$.

Because this inversion problem is highly underdetermined, the introduction of a priori constraint related to the smoothness of the coupling coefficients ψ is necessary to find a solution. The smoothness constraint is defined as follows:

$$a_{k-1,l} + a_{k+1,l} + a_{k,l-1} + a_{k,l+1} - 4a_{k.l} = \varepsilon \quad (5.6)$$

and it can be written in vector form,

$$\boldsymbol{0} = \boldsymbol{G}\boldsymbol{m} + \boldsymbol{f} \qquad \boldsymbol{f} \sim N(0, \mu^2\boldsymbol{F}) \quad (5.7)$$

or, equivalently as a probability density function

$$p(\boldsymbol{m};\mu^2) = (2\pi\mu^2)^{-P/2}\|\boldsymbol{\Lambda}_P\|^{-1/2}\exp\left[-\frac{1}{2\mu^2}\boldsymbol{m}^T\boldsymbol{G}^T\boldsymbol{F}^{-1}\boldsymbol{G}\boldsymbol{m}\right] \quad (5.8)$$

Here, P and $\|\boldsymbol{\Lambda}_P\|$ are the rank and the product of nonzero eigenvalues of the matrix $\boldsymbol{G}^T\boldsymbol{F}^{-1}\boldsymbol{G}$. $\boldsymbol{G}$ is a sparse matrix that contains a measure of the roughness of fault slip distribution as a function of the normal vector to each grid point. By combining the probability density functions (Eq. 5.5 and Eq. 5.8) using the Bayes' rule, we obtain a posterior probability distribution for the model parameters $\boldsymbol{m}$.

$$p(\boldsymbol{m};\sigma^2,\mu^2|\boldsymbol{d}) = cp(\boldsymbol{d}|\boldsymbol{m};\sigma^2)p(\boldsymbol{m};\mu^2) \quad (5.9)$$

Here c is a constant to preserve the equality. By combining Eq. 5.5, 5.8, and 5.9, we obtain:

$$p(\boldsymbol{m};\sigma^2,\mu^2|\boldsymbol{d}) = \frac{c}{(2\pi\sigma^2)^{(N+P)/2}}(\alpha^2)^{P/2}\|\boldsymbol{E}\|^{-1/2}exp\left[-\frac{s(\boldsymbol{m})}{2\sigma^2}\right] \quad (5.10)$$

with

$$s(\boldsymbol{m}) = (\boldsymbol{d}-\boldsymbol{H}\boldsymbol{m})^T\boldsymbol{E}^{-1}(\boldsymbol{d}-\boldsymbol{H}\boldsymbol{m}) + \alpha^2\boldsymbol{m}^T\boldsymbol{G}^T\boldsymbol{F}^{-1}\boldsymbol{G}\boldsymbol{m} \quad (5.11)$$

where $\alpha^2 = \sigma^2/\mu^2$ defines the relative weight between the observation equation and the a priori constraint.

If the hyperparameters σ^2 and α^2 are given, the Eq. 5.10 can be maximized by minimizing the sum of weighted residuals $s(m)$ by using least squares. The solution is given by:

$$\boldsymbol{m}^* = (\boldsymbol{H}^T\boldsymbol{E}^{-1}\boldsymbol{H} + \alpha^2\boldsymbol{G}^T\boldsymbol{F}^{-1}\boldsymbol{G})^{-1}\boldsymbol{H}^T\boldsymbol{E}^{-1}\boldsymbol{d} \quad (5.12)$$

The posterior variance-covariance matrix for the model parameter m can be calculated as follows

$$\boldsymbol{C}_{\boldsymbol{m}} = \sigma^2(\boldsymbol{H}^T\boldsymbol{E}^{-1}\boldsymbol{H} + \alpha^2\boldsymbol{G}^T\boldsymbol{F}^{-1}\boldsymbol{G})^{-1} \quad (5.13)$$

Now, the problem is reduced to find the optimal hyperparameters σ^2 and μ^2. We use the ABIC

for this purpose. ABIC is defined by Eq. 5.14

$$ABIC = -2LogL(\sigma^2, \mu^2) \tag{5.14}$$

with

$$L(\sigma^2, \mu^2) = \int p(\boldsymbol{d}|\boldsymbol{m}; \sigma^2) p(\boldsymbol{m}; \mu^2) d\boldsymbol{m} \tag{5.15}$$

The minimum ABIC is obtained by maximizing $L(\sigma^2, \mu^2)$. Thus, the necessary conditions for the minimum ABIC are

$$\frac{\partial L(\sigma^2, \mu^2)}{\partial \sigma^2} = 0 \tag{5.16}$$

$$\frac{\partial L(\sigma^2, \mu^2)}{\partial \mu^2} = 0 \tag{5.17}$$

and solving for σ^2, we obtain

$$\sigma^2 = \frac{s(\boldsymbol{m}^*)}{N + P - M} \tag{5.18}$$

The search for the value of μ^2 which minimizes the ABIC can be carried out numerically. Once it has been defined, we can evaluate Eq. 5.12 to obtain the best estimate for the parameters $\boldsymbol{m}^*$ and compute the calculation of the hyperparameter σ^2 as in Eq. 5.18. *M* is the number of parameters and $s(\boldsymbol{m}^*)$ is defined as in Eq. 5.12.

We explore a variety of inversion models and choose the optimal one by minimizing the ABIC value, which at the same time, reaches the best trade-off between the weight given to the observations and to the prior constraints (Figure 5.1).

To simplify the problem, in this study, we estimate the interseismic coupling ratio (ISC) defined as follows:

$$ISC = slip\ deficit\ rate / convergence\ rate \tag{5.19}$$

ISC is an estimate of the degree of the interaction between the subducting slab and the overriding plate in terms of the ability to build up elastic strain during the interseismic period that can be released in a future earthquake (Métois et al, 2012).

ISC varies from 0 to 1, being 0 a representation of a fully creeping interface and 1 a fully locked one. I assume that the slip deficit occurs in the direction of the relative plate motion predicted from the relative motion between two rigid blocks interacting at the subduction zone.

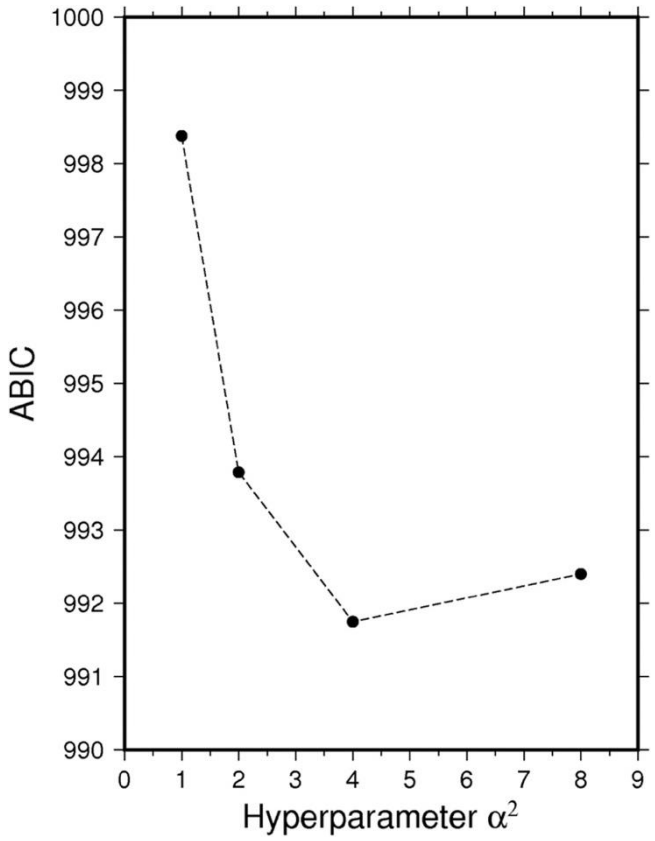

Figure 5.1. *ABIC values as a function of the hyperparameter* α^2. *The ABIC takes the minimum at* $\alpha^2=4$

5.1.2. Caribbean plate configuration

The geometry of the subducting slab affects the pattern of the upper plate deformation (Métois et al, 2012). It is essential to assume an appropriate configuration of the subducting Caribbean plate in order to evaluate the interplate coupling. In this study, we use a geometry by Mora et al. (2017) estimated by integrating seismic reflection data for the shallow part, seismicity for the intermediate part, and seismic tomography for the deeper part of the slab. We digitize the published depth contours and compute a spatial interpolation using the "surface" command of the Generic Mapping Tools (GMT) (Wessel et al, 2013) to obtain a continuous surface configuration (Figure 5.2).

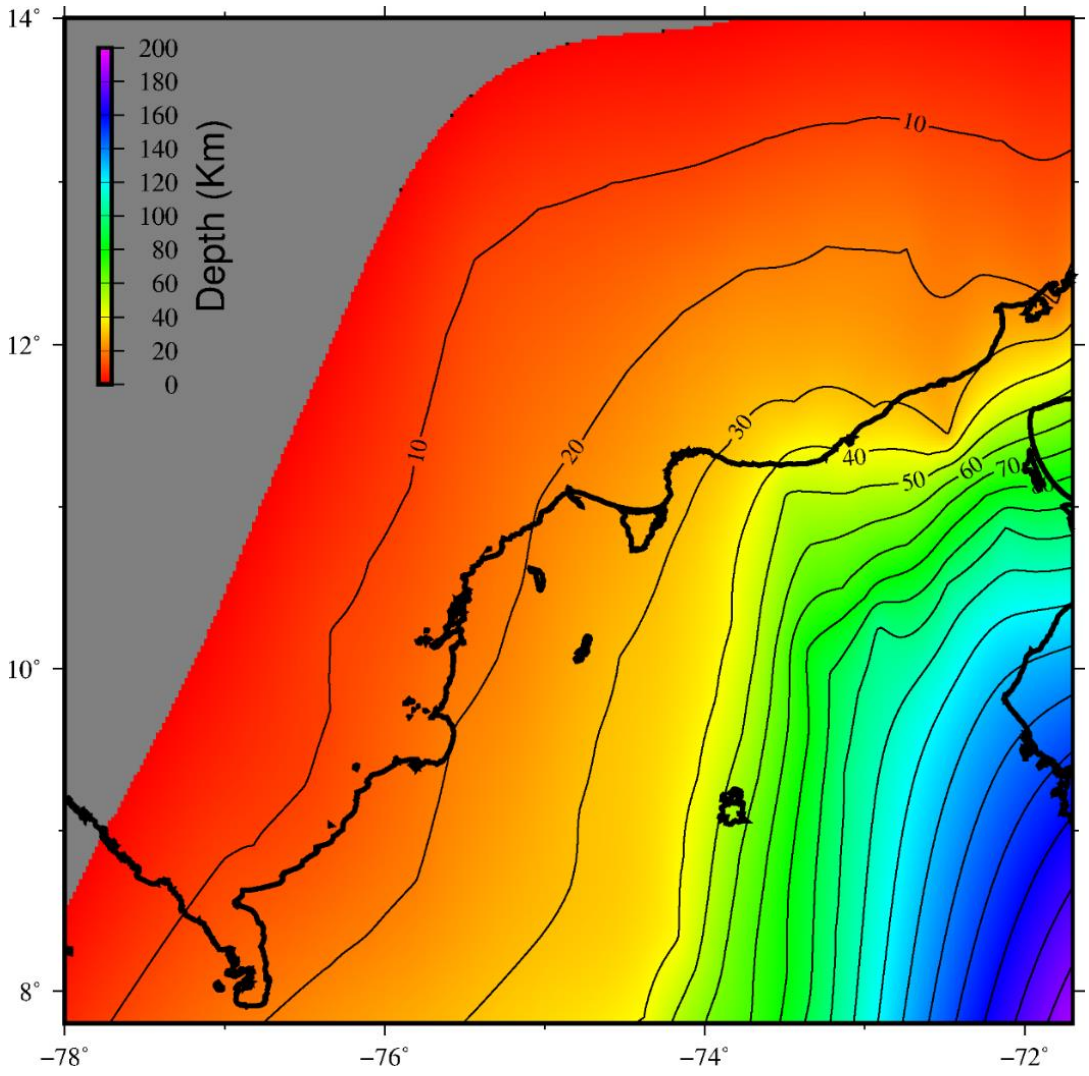

Figure 5.2. *Caribbean subduction zone slab geometry derived from the depth contours defined by Mora et al. (2017). The color bar indicates the depth contours in km which are plotted every 10 km.*

5.1.3. Model setup

The model region is set as 80°W to 71°W in longitude and 7.5°N to 12.5°N in latitude, with a depth range between 0 and 30 km. We introduce a 2-dimensional regular grid on the ground surface with a constant node interval of 0.2˚. This region is subdivided again into 10 smaller regions that can be approximated by a fault plane that represents a curved plate interface on our slab configuration. Then, surface displacements caused by a unit slip on the fault plane are calculated using the elastic dislocation code DC3D (Okada, 1992) for a uniform elastic half-space with a Poisson's ratio of 0.25. Bicubic B-splines (Cox, 1792; De Boor, 1972) cover a region of 4×4 nodes

in latitude and longitude directions. In total, 273 B-splines are used to represent the spatial distribution of interplate coupling.

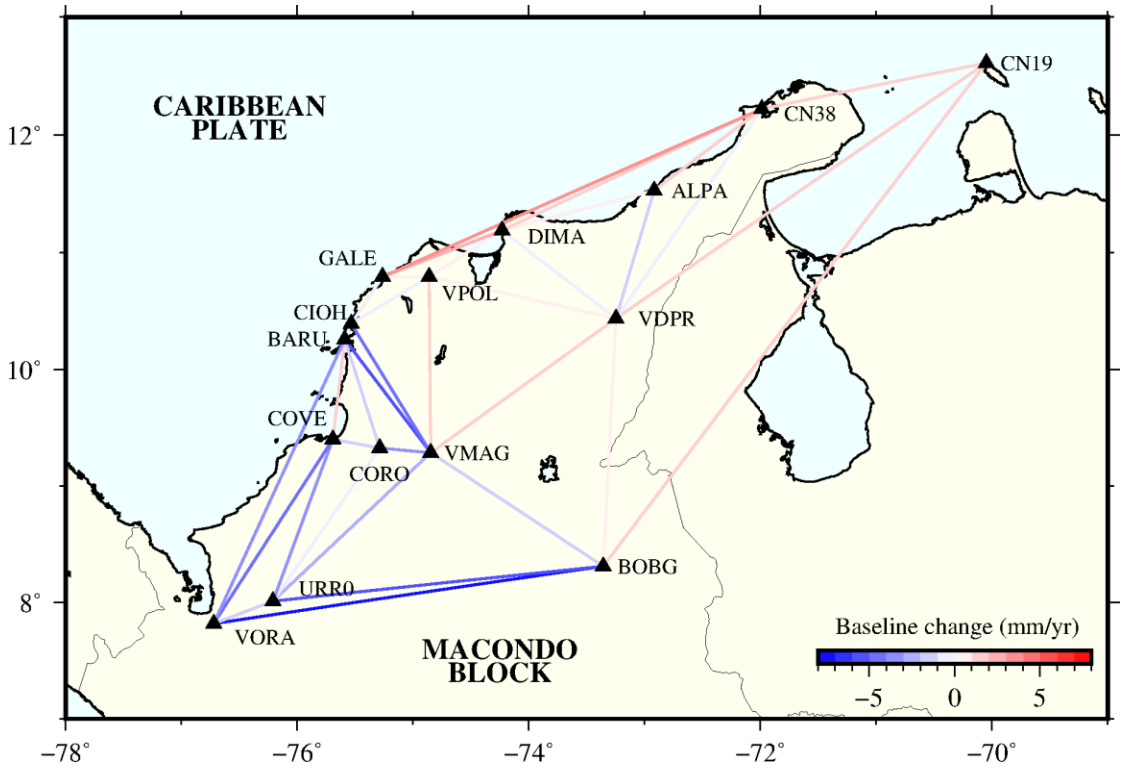

Figure 5.3. *Baseline length change in mm/yr for GPS stations along the Caribbean subduction zone. Blue lines represent shortening and red lines represent extension according to the scale in mm/yr.*

We consider slip deficit in the direction of relative plate motion only. Thus, the number of unknown parameters is 273. As input data, we used 35 baseline change rate data composed of 15 GPS stations located inside the Macondo Block (ALPA, BARU, BOBG, CIOH, CN19, CN38, CORO, COVE, DIMA, GALE, URR0, VDPR, VMAG, VORA and VPOL; Figure 5.3) as well as their vertical velocities. CN36 station is not included due to monument instability related to floods in the vicinity of the site.

Velocities with respect to the Macondo block for the mentioned GPS sites are presented in Table 5.1.

ID	Longitude	Latitude	East	North	Up
ALPA	287.082	11,528	0,885	-0,927	-4.682
BARU(*)	284.410	10,258	3,888	-4,953	-5.575
BOBG	286.642	8,312	-1,183	0,098	2.336
CIOH(*)	284.466	10,391	3,790	-4,164	-3.087
CN19	289.951	12,612	4,037	-1,906	0.010
CN38	288.012	12,222	2,707	-1,250	3.159
CORO(*)	284.712	9,328	3,533	-3,262	-0.833
COVE(*)	284.308	9,402	4,869	-6,568	-4.185
DIMA(*)	285.768	11,188	0,514	0,475	-3.523
GALE(*)	284.737	10,793	-1,137	-1,425	-2.256
URR0	283.790	8,012	4,590	-2,926	-3.504
VDPR	286.752	10,436	0,304	0,469	2.204
VMAG(*)	285.153	9,287	-0,148	-1,030	2.180
VORA	283.278	7,818	6,512	-2,725	-7.754
VPOL(*)	285.139	10,794	-0,246	0,849	3.900

Table 5.1. *GPS velocities expressed with respect to the Macondo Block for the study area (in mm/yr). Stations marked with an asterisk (*) compose the subset of data used in the Chapter 6.*

5.2. Results

5.2.1. Interplate coupling distribution

Our interplate coupling results show an isolated patch of full coupling between 9.6ºN and 10.8ºN and 76.3ºW and 75.3ºW at depths between 9.0 km and 20 km to the south of the city of Cartagena, which tends to decrease homogeneously around this region (Figure 5.4). The uncertainty of the interplate coupling ratio for the main locked region is about 0.11. Considering a mean coupling ratio of 0.9 for the whole patch, the maximum expected backslip rate is ~6.3$\pm$0.7 mm/yr under the slow subduction of the Caribbean plate (~7 mm/yr). Smaller ISC (less than 0.2) was identified around the Golfo de Urabá that can be related to the deceleration of the southeastward convergence of the Caribbean plate due to the collision of the Panamá arc with northwestern Colombia; however, the observed GPS velocities are not explained by the coupling

model. Probably it is not appropriate to interpret deformation in this area simply as a result of the Caribbean plate subduction.

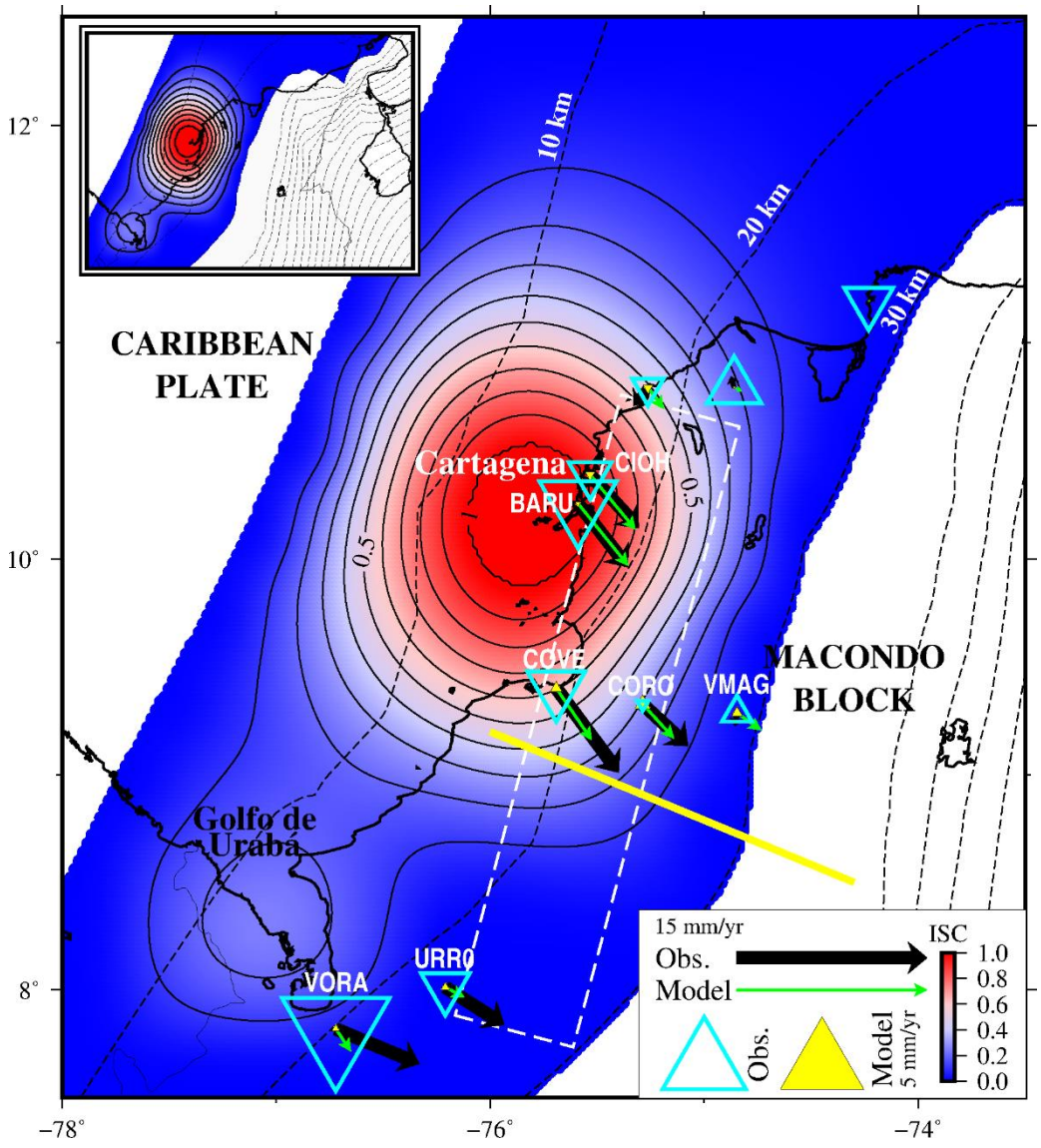

Figure 5.4. *Interplate coupling distribution along the Caribbean subduction zone and adjustment of horizontal and vertical velocities. The inset map includes the whole region used in the inversion and slab configuration. The scale bar denotes the degree of plate coupling (blue: Full creeping, red: Full locking) with coupling ratio contours every 0.1. Black arrows represent horizontal velocities with respect to the Macondo Block. Green arrows represent estimated velocities from the coupling model. Cyan and yellow triangles denote observed and estimated vertical velocities, respectively (inverted triangles indicates subsidence). White broken line box shows the location of the SJFB. Yellow line indicates the location of the analyzed seismic section in Fig. 5.6. Broken black lines are depth contours every 10 km.*

5.2.2. Model fitting

Horizontal velocities with respect to the Macondo Block are well reproduced by the coupling model in their magnitudes and orientations, especially for the GPS stations closer to the locked patch (CIOH, BARU, COVE and CORO). The coupling effect dramatically decreases to the east of 75˚W as well as to the north of 10.8˚N, where significant motion is not observed with respect to the Macondo block. To the south of the model region, observed and estimated velocities in stations VORA and URR0 differ significantly as a consequence of the Panamá arc collision along this boundary.

On the other hand, vertical signals are not explained by the current coupling model. Since the residuals are on the same order of the observed velocities, we consider that these vertical motions are not simply associated with the elastic deformation due to interplate coupling. Other processes such as the steady plate subduction (Fukahata and Matsu'ura, 2016) and viscous relaxation (Sagiya, 2015) may be responsible. Modeling of vertical displacements is a subject of the viscoelastic model implementation to be discussed in Chapter 6.

5.2.3. Source region width validation

While the deeper limit of the coupling region is well constrained by the GPS data, most of the locked area is located offshore and the shallower limit cannot be well resolved due to the limited spatial resolution offered by the GPS network. The result is mainly controlled by the assumption of smoothness of the slip deficit. In order to validate the uncertainty of the fully coupled region, we examine the surface deformation patterns for different extents of a uniform rectangular dislocation using the PSGRN/PSCMP software (Wang et al, 2006). The model calculations are conducted with variable fault widths (40 km, 80 km, and 110 km) dipping 8.0º to the SE, a fixed length of 135 km with an average strike of N20.0ºE and a fixed rake angle of 124º, which indicates the normal motion of the hanging wall in direction of the relative plate motion.

Figure 5.5 shows that GPS velocities at CIOH and BARU are reproduced almost at the same level by the models A (110 km width) and B (80 km width) but predicted velocities with model C (40 km width) are too small. We can conclude that the width of the locked patch should be larger than 80 km.

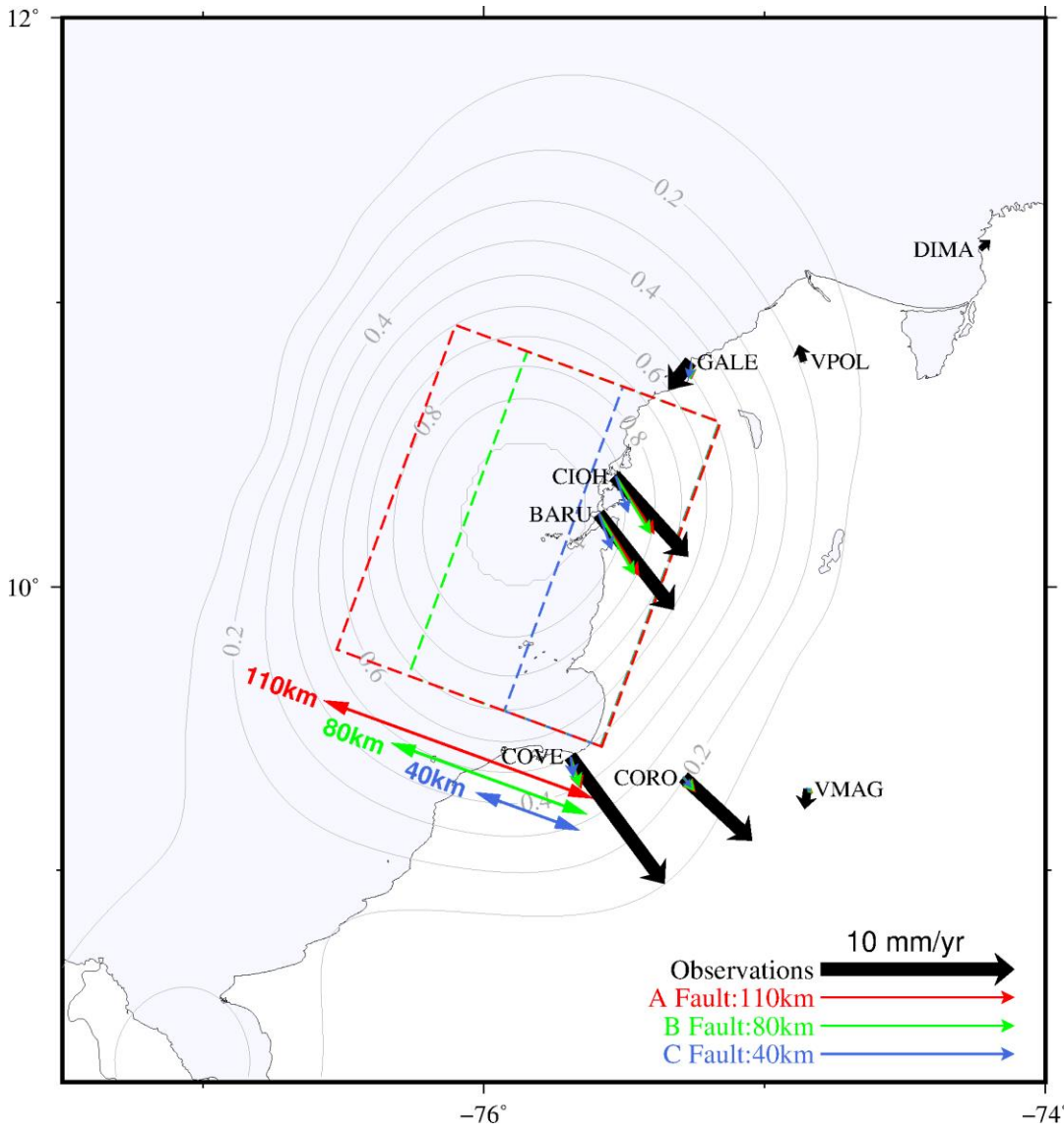

Figure 5.5*. Reproduction of observed velocities in the direction of the Caribbean plate convergence relative to the Macondo Block under the assumption of three rectangular faults with variable widths of A: 110 km (red), B: 80 km (green), and C: 40 km (blue) and fixed length of 135 km. The gray lines represent the coupling ratio contours every 0.1.*

5.3. Discussion

We obtained the interplate coupling distribution along northwestern Colombia as an effect of the mechanical interaction between the subducting Caribbean plate and the overriding Macondo Block. The result indicates a possibility that tectonic stress is being built and may be released in the future as a megathrust earthquake. On the other hand, northwestern Colombia, except for the

Panamá arc itself and the Panamá-Colombia collision region, is characterized by scarce seismicity (Figure 4.7). The only recent historical record of a disastrous earthquake in the Colombian Caribbean region was on May 22nd, 1834, which mainly caused damage such as liquefaction in the city of Santa Marta and neighboring regions as well as landslides on the eastern flank of the SNSM (See Figure 2.4 for location). The epicenter is estimated at (11.24°N, 74.2° W) with a shallow depth, and a magnitude of 6.5 (Cifuentes and Sarabia, 2006). Cotilla (2012) compiled the history of seismology in the northern Caribbean over the past 500 years, and there is no mention of representative earthquakes or tsunamis in the area of our interest. It is to be noted that the seismicity level in the whole Caribbean region is generally high and there exist a number of tsunami records in this area. Thus, the absence of a written document indicates that there was no megathrust earthquake or associated tsunami during the last 500 years. Then, it is an important question what these apparently contradicting observations imply.

Consequently, to interpret the observed surface deformation driven by the interplate coupling between interacting plates and the scarcity of documented large earthquakes along the Caribbean coast of Colombia, we consider the following two opposing scenarios. It is worth noting here that the interpretation is whether the GPS-based strain rate signals represent a short-term elastic deformation or a long-term inelastic one.

5.3.1. Seismogenic strain accumulation – Scenario 1

In the first scenario, the detected strain is elastic and tectonic stress is accumulating, which implies that the stress is going to be released in the future as big earthquakes.

The area of the fully coupled region (ISC ≥ 0.8) is about 11,000 km^2, which we consider as the hypothetical source region of the future earthquake. The average slip deficit rate is evaluated as $\dot{\bar{D}}$==6.3 mm/yr. By assuming the rigidity of the crust as 30 GPa, we obtain a seismic moment accumulation rate of $\dot{M}_0 = 2.0\text{x}10^{18}$ Nm/yr. The extent of the hypothetical source region corresponds to a M_w 8.0 earthquake based on the scaling relationships by Allen and Hayes (2017). According to the definition of moment magnitude by Hanks and Kanamori (1979),

$$logM_0 = 1.5M_w + 9.1 \tag{5.20}$$

the expected seismic moment amounts to $M_0 = 1.3\text{x}10^{21}$ Nm. To accumulate this seismic moment with the estimated rate, the average earthquake recurrence interval would be

approximately 605 years. Considering the large uncertainty of the estimate and randomness of the earthquake phenomena, it is possible that a large earthquake has been absent for over 500 years during which historical documents exist.

As it is discussed, the estimated interplate coupling has a poor resolution for the offshore part and the source area has a large uncertainty. Our calculations indicate that the lower limit of the source region is given by a locked patch with a minimum width of 80 km (area of 10,800 km^2), which could become even wider than 110 km (area of 14,850 km^2) (Figure 5.5). Variations in the size of the source region would implies the expected magnitudes is M_w 8.0 or larger. The seismic moment accumulation rate ($\dot{M}_0$) and the seismic moment (M_0) would increase accordingly with the source region size (from $2.0x10^{18}$ Nm to $2.8x10^{18}$ Nm), but the recurrence interval remains around the value previously estimated (625 ± 12 years).

5.3.2. Plastic deformation – Scenario 2

The previous scenario implicitly assumes that the overriding Macondo Block behaves as an elastic body and there is no dissipation of strain energy. Considering the shallow dip of the Caribbean plate beneath northwestern Colombia obtained by 3D modeling of gravity data and 2D seismic reflection data (Mantilla-Pimiento, 2007; Mantilla-Pimiento et al, 2009), it is necessary to consider a possible plastic deformation that explains the current NW-SE contraction, which could be represented in the SJFB. This fold belt forms a sedimentary wedge of up to 12 km thick that was accreted in the Cenozoic to the South American margin (Toto and Kellogg, 1992, Caro and Spratt, 2003, Kellogg et al, 2019). As the subduction of the Caribbean plate is at a very low angle and thus the overriding plate is thin at the estimated interplate locking depth, it is possible that the overriding plate has significant plastic deformation that is not reversible. If that is the case, there should be geological evidence such as active faulting, folding, and/or other topographic features that reflect the long-term deformation consistent with the geodetic observation.

Mora et al. (2017) analyzed seismic sections that covered our highly coupled area and derived interpretations of tectonostratigraphic sequences to reconstruct the tectonic evolution of northwestern South America and to study the ongoing motion of the Caribbean plate. We analyze the published seismic section presented in Figure 5.6 (See Figure 5.4 for location).

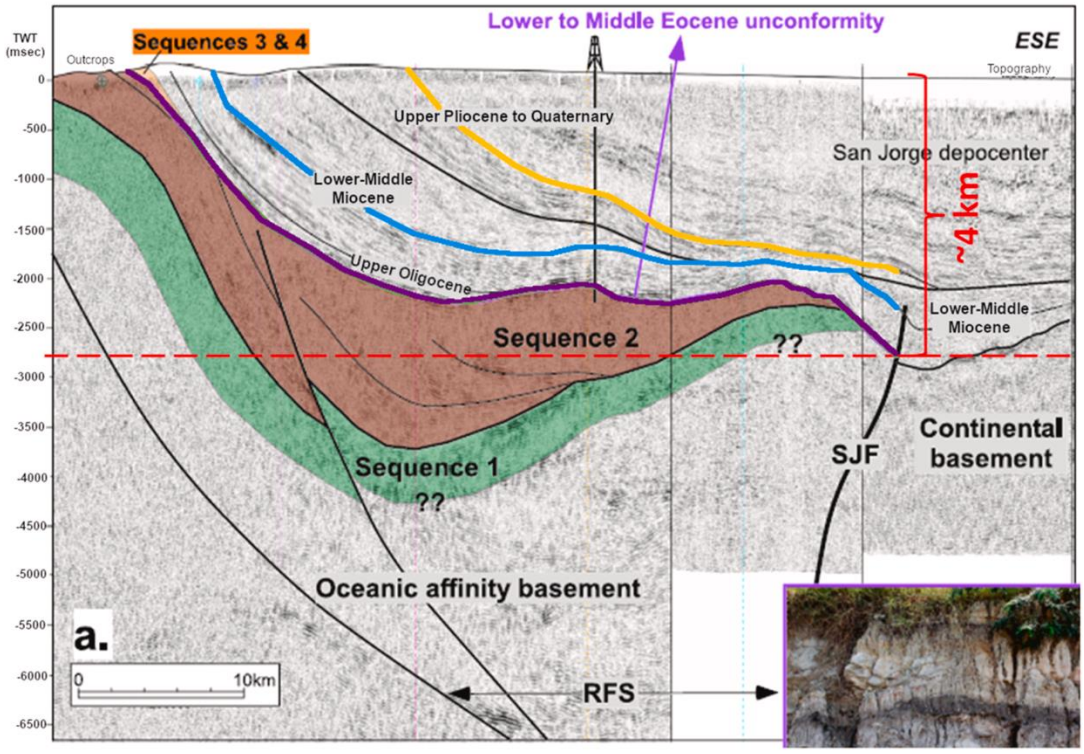

Figure 5.6. *Analyzed seismic section taken and modified from Mora et al. (2017). Its location is presented in Fig. 5.4 as the yellow line. Red line is the limit of ~4 km depth (vertical scale).*

We estimate the average shortening rates at different stages of the deposition based on the configuration of each layer (Upper Pliocene to Quaternary: 2.58 Ma to 3.6 Ma, Lower to Middle Miocene: 15.97 Ma to 23.03 Ma, and Lower to Middle Eocene: 47.8 Ma to 56 Ma). Then, we compare the obtained values with our geodetic estimate of shortening. We measure the length along each deformed geologic layer with a correction for the vertical scale and calculate the strain rate as follows.

$$strain\ rate = \left(\frac{L_1 - L_0}{L_0}\right)/T \tag{5.21}$$

Here, L_1 and L_0 are the current horizontal distance and the original (folded) distance, respectively, and T is the elapsed time to the present for each geological stage. We find that the estimated shortening rate along these profiles is much smaller than the geodetic estimate (~65 nanostrain/yr) by an order of magnitude for the Upper Pliocene - Quaternary horizon and by two orders of magnitude for the Lower to Middle Miocene and the Lower to Middle Eocene as presented in Table 5.2.

Observational data	Time interval	Strain rate (shortening)
GPS data		65 nanostrain/yr
Upper Pliocene - Quaternary	3.6 Ma to 0.012 Ma	9.5 to 6.8 nanostrain/yr
Lower to Middle Miocene	23.03 Ma to 11.63 Ma	0.59 to 0.85 nanostrain/yr
Lower to Middle Eocene	56 Ma to 41.2 Ma	0.18 to 0.22 nanostrain/yr

Table 5.2. *Estimated strain rates (shortening) from observational GPS and seismic profile data across the SJFB.*

The inconsistency between geodetic and geological estimations of the strain rate indicates variable possibilities. A simple explanation is that the geological strain rate has a large uncertainty. Another possibility is a temporal change in strain rate. The geological estimates decrease with the time period lengths, which can be interpreted that the tectonic convergence has been recently accelerated. However, paleotectonic reconstruction studies (Boschman et al, 2014; Matthews et al, 2016) showed that the convergence rate of the Caribbean plate against South America has been decreasing. Therefore, it is not likely that the discrepancy is attributed to a temporal change in tectonic plate motion.

A simple interpretation of the order of magnitude discrepancy in the geodetic and geological strain rate is the elastic strain in the geodetic estimate. Ikeda (2014) interpreted an order of magnitude difference between the geodetic and the geological strain rates in northeast Japan as a result of elastic strain due to interplate coupling, which was validated by the occurrence of the 2011 Tohoku-Oki earthquake. Thus, the strain rate discrepancy would indicate a possibility of elastic strain accumulation unless it is proven to be a matter of uncertainty.

Considering the present evidence, between the two possible scenarios, more careful attention is necessary for the first one with an elastic strain accumulation because of its hazardous implications.

5.3.3. Northwestern Colombia as a case of slow subduction

The scenario of a future megathrust earthquake along the CSZ cannot be neglected considering that the historical record may be too short compared with the expected recurrence interval of large earthquakes. The scarce seismicity along northwestern Colombia may indicate that the plate

interface is perfectly locked such as in the case of Nankai Trough in central and southwestern Japan (Sagiya, 1999; Gutscher, 2001).

An important characteristic of the Caribbean plate in northwestern Colombia is its extremely slow convergence rate. The convergence between the Caribbean plate and the Macondo block is estimated to be ~7.0 mm/yr, which is small enough to be categorized as a "slow subduction zone" (Gutscher and Westbrook, 2009). Although the nature of slow subduction has not been investigated so much, two large historical earthquakes, the 1693 Sicily, Italy, M_w8.0 earthquake (Gutscher et al, 2006; Figure 2.7a) and the 1755 Lisbon M_w8.7 earthquake (Gutscher, 2006 and Gutscher et al, 2012; Figure 2.7b) were reported to occur in the two extremely slow subduction zones of Calabria and Gibraltar, respectively. In both cases, the magnitudes were estimated as M_w8.0 or larger, and the convergence rates are estimated to be less than 10 mm/yr with earthquake recurrence intervals longer than 500 years.

Table 5.3 summarizes slow subduction zones worldwide with several parameters characterizing each of them. Convergence rates are evaluated based on the global plate motion model NNR-MORVEL56 (Argus et al, 2011). Among these areas, northwestern Colombia presents the third smallest convergence rate of 11 mm/yr after Gibraltar (4 mm/yr) and Calabria (9 mm/yr); however, this value becomes even smaller when we consider it relative to the Macondo Block (7 mm/yr).

This summary simply indicates that a small convergence rate does not rule out the possibility of a large megathrust earthquake over magnitude 8. Because of the slow relative motion, the recurrence intervals can be considerably long, making those possible disasters invisible. Thus, although the scenario of a large megathrust earthquake along northwestern Colombia is not conclusive yet, this possibility should be seriously considered. If there exists an elastic strain accumulation due to interplate locking, the seismic quiescence during the last 500 years implies that we are in the latter stage of the interseismic period.

Subduction zone	Plates	Location		NNR-MORVEL56 (mm/yr)	Recurrence interval (yrs)	M_w
	Down-Fixed	Lat (°)	Lon (°)			
NW Colombia	CA-NAB	12	284	11	$625 \pm 12^{(I)}$	$8.0 \pm 0.1^{(I)}$
Gibraltar (*)	NU-EU	34	350	4	1500-2000	8.7
Calabria (*)	NU-EU	36	18	9	500	8.0
Antilles	SA-CA	14	305	20	$80\text{-}400^{(II)}$	$8.0\text{-}8.3^{(II)}$
Hikurangi (*)	PA-KE	-41	180	37	$350\text{-}1725^{(III)}$	8.1
Helenic	NU-AS	33	26	38	$>800^{(IV)}$	$8.0\text{-}8.5^{(V)}$
Makran (*)	AR-EU	22	61	38	$660\text{-}1000^{(VI)}$	8.1
Cascadia (*)	JF-NA	47	233	39	300-1000	9.0

Table 5.3. *Compilation of information related to slow subduction zones worldwide (convergence velocity ≤ 40 mm/yr). Interacting plates as well as velocities are based on the Plate Motion Model NNR-MORVEL56 (Argus et al, 2011) for the respective locations. Abbreviations as follows, CA: Caribbean plate, NAB: North Andean Block, NU: Nubia plate, EU: Eurasia plate, SA: South American plate, PA: Pacific plate, KE: Kermadec plate, AS: Aegean Sea plate, AR: Arabia plate, JF: Juan de Fuca plate and NA: North American plate. Sources: (*) Gutscher and Westbrook (2009), (I) This study (estimations based on the CA plate motion w.r.t. Macondo Block [~7mm/yr]), (II) Hayes et al. (2013), (III) Stiros (2010), (IV) Tselentis et al. (1988), (V) Kovach et al. (2010), (VI) Clark et al. (2019).*

5.4. Conclusions

I conduct the first inversion of 3-dimensional GPS data to estimate the distribution of slip deficit along the CSZ in order to determine the degree and extent of the interplate coupling and their implications in terms of seismic potential. This is the first evidence that this segment of the Caribbean-Macondo boundary can be the locus of a significant earthquake and tsunami hazard.

Along the CSZ, the obtained coupling distribution shows an isolated fully locked patch south of the city of Cartagena, extending from 9.0 to 20 km in depth, with slip deficit rates as large as

7.0 mm/yr. I can attribute the observed geodetic deformation to the stress accumulation along northwestern Colombia as the effect of the subduction of the Caribbean plate beneath the Macondo block. Based on the coupling results along the Caribbean region, I consider two possible accommodation mechanisms for the observed deformation: 1) The stress is building up elastically, implying a future M_w 8.0 megathrust earthquake with a recurrence interval of approximately 600 years, and 2) The strain is being accommodated in a plastic and therefore permanent way, which would not represent a seismic hazard in the area. Considering a larger uncertainty of the geological evidence, any of the scenarios cannot be rejected. However, the scenario of seismogenic strain accumulation seems more likely based on available data. The absence of a large earthquake in the Caribbean can represent atypical long recurrence intervals as a consequence of an extremely slow subduction rate. A comparison with other slow subduction zones indicates a possibility of large megathrust earthquakes should be considered regardless of the convergence rate.

Currently, there is a large gap between geodetic and geological strain rates. This may simply indicate an accumulation of elastic strain or seismic potential, but neotectonics studies along the Caribbean coastal region of Colombia are far from sufficient, and it is of essential importance to precisely evaluate the long-term deformation rate for a time scale of less than 1 Ma with a multidisciplinary approach. Also, through investigation of paleotsunami deposits and paleo-liquefaction, we can evaluate earthquake/tsunami potential over a millennium time scale. In a similar fashion, improvements in the GPS velocity fitting, especially in the vertical component should be addressed to corroborate the hypothesis of a seismogenic scenario for the Caribbean coast of Colombia. This latter part would be presented in Chapter 6 through a viscoelastic model of the earthquake cycle.

CHAPTER 6
INTERPLATE COUPLING MODEL ALONG THE CARIBBEAN SUBDUCTION ZONE NORTHWESTERN COLOMBIA PART II – VISCOELASTIC MODEL

Many studies have shown that the stress state of the crust-mantle system is perturbed by the interseismic fault-locking process, the earthquake itself as well as postseismic afterslip and viscoelastic relaxation. The latter one, in particular, modifies the interseismic deformation, exhibiting a time-dependent pattern in response to the fluid-like behavior of the asthenosphere as supported by several studies, some of them based on geodetic observations (Savage and Prescott, 1978; Wang et al, 2001; Johnson and Segall, 2004; Johnson and Segall, 2005; Wang et al, 2012; Trubienko et al, 2013; Li et al, 2015; Li et al, 2018; Sagiya, 2015; Noda et al, 2018).

Recently, Sagiya (2015) and Noda et al. (2018) demonstrated that the role of viscous relaxation on the interseismic deformation pattern is particularly important when the recurrence interval of earthquakes is much longer than the asthenosphere relaxation time ($\tau = 2\eta/K$, η:viscosity and K:rigidity of the asthenosphere, respectively). This may be the case of the Caribbean of Colombia where the elastic interplate coupling model suggested a recurrence of approximately 600 years (Lizarazo et al, 2021) The expected relaxation time of stress in the asthenosphere is between 0.9 and 9.0 years if we assume a representative steady-state viscosity between $1x10^{18}$ Pas to $1x10^{19}$ Pas of subduction zones (Wang et al, 2012) and a rigidity value of 70 GPa. Hence, postseismic relaxation of the mantle will significantly modify the interseismic deformation patterns.

Until now, there is no concrete evidence of megathrust earthquakes in northwestern Colombia due to a lack of geological investigation (Lizarazo et al, 2021). However, if we assume the above hypothesis, we may be approaching the late stage of the earthquake cycle and therefore, the Caribbean region could be the locus of a M_w8.0 earthquake and subsequent tsunami in the near future. To give a more precise measure of the seismic potential in this area it is necessary to solve problems of the previous elastic coupling model, that is, the inability of reproducing vertical motions. Introducing viscoelastic relaxation into the earthquake cycle modeling is a necessary attempt to model and interpret overall deformation signals under this hypothetical scenario.

6.1. GPS Velocity Data

We analyze GPS velocities of 8 stations located in the northwestern part of Colombia during the period 2008-2017 with respect to the Macondo block (Lizarazo et al, 2021), which was newly defined as an independent tectonic block in the northern part of the NAB (Bird 2003; Nocquet et al, 2014). These stations are BARU, CIOH, CORO, COVE, DIMA, GALE, VMAG, and VPOL and were selected considering their closeness to the identified locked patch offshore Cartagena city based on an elastic interplate coupling model (Figure 6.1). The Euler pole that describes the Caribbean plate motion with respect to the Macondo block is located at 18.9º N, -63.8ºE with the angular velocity 0.2508º/Myr.

Figure 6.1 shows the GPS site velocities w.r.t the Macondo block. Velocities were obtained by a linear fitting of time series data, including step functions for instrumental offsets, periodic functions for seasonal variations, and a combined noise model (white noise plus power law noise) to account for the error component with the Hector software v.1.6 (Bos et al, 2013), and then, they were transformed from ITRF2014 to Macondo block reference with the Euler pole reported by Lizarazo et al. (2021).

Southeastward velocities are observed at BARU, CIOH, CORO, and COVE sites with an average value of 6.2 ± 0.4 mm/yr. GALE and VMAG sites show a southwestward motion of ~1.4 ± 0.6 mm/yr. Both, DIMA and VPOL sites present velocities less than 1 mm/yr in the northeast and northwest directions, respectively. The remaining GPS sites located to the East of 75ºW, represent essentially the rigid motion of the Macondo block with average velocities of less than 1.0 mm/yr.

Observed vertical velocities at BARU, CIOH, CORO, COVE, DIMA, and GALE stations (Figure 6.1) show negative trends between 0.8 and 5.8 mm/yr with average uncertainties of ~1.1 mm/yr. The remaining GPS sites, VMAG and VPOL, present uplifts of 2.2 and 3.9 mm/yr, respectively, with uncertainties of less than 1 mm/yr. In particular, vertical GPS velocities have larger uncertainties than horizontal ones (Mao et al, 1999).

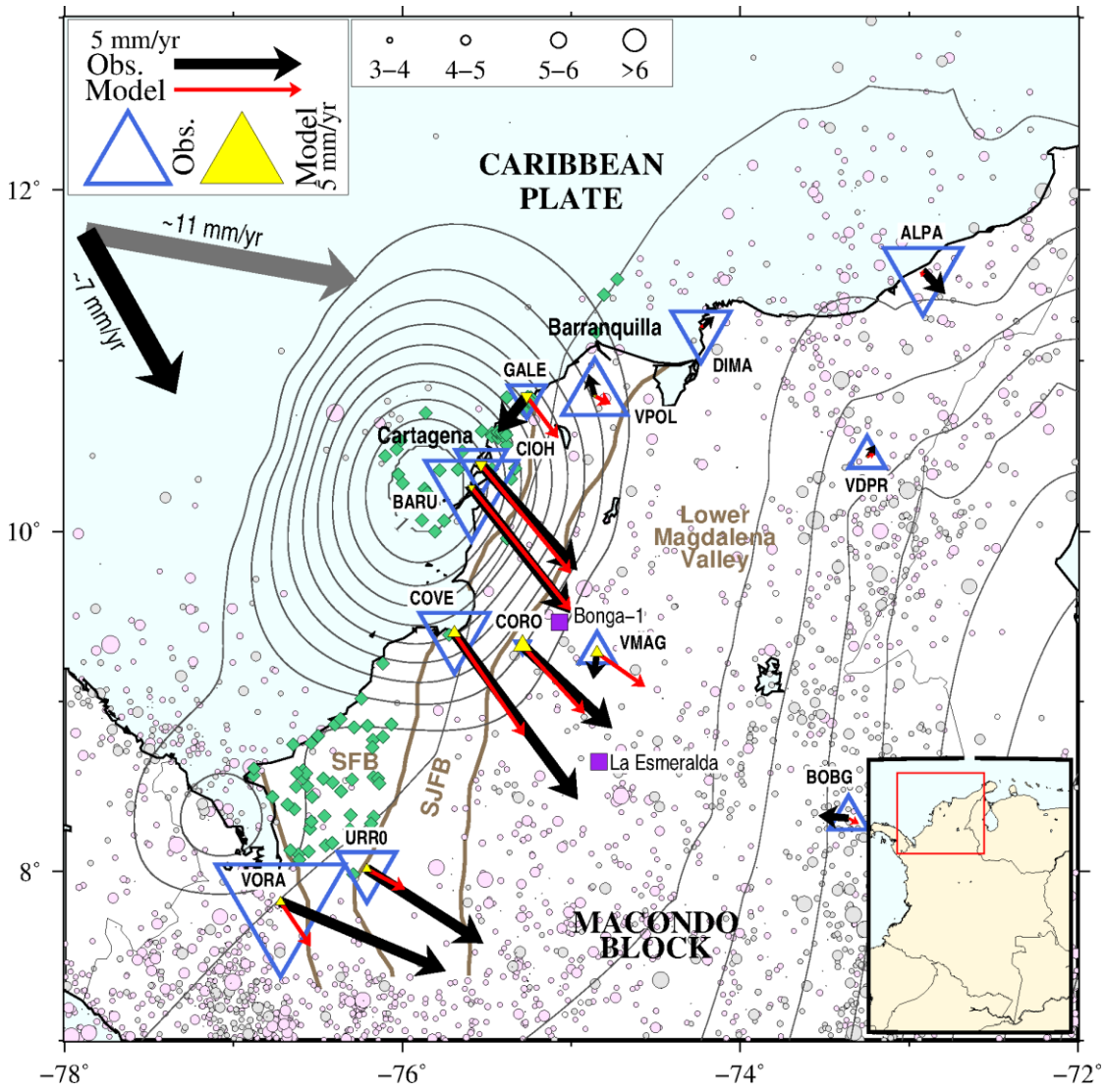

Figure 6.1. *Tectonic setting and seismicity of northwestern Colombia. Pink and gray colors indicate crustal (≤ 40 km) and non-crustal earthquakes. Iso-depth contours (20 km interval) denote the 3D geometry of the plate interface between the Caribbean plate and the Macondo Block. Thick arrows indicate the convergence velocities w.r.t North Andean Block according to the MORVEL-NNR56 model (gray) and w.r.t the Macondo Block (black). Black arrows and blue triangles denote observed horizontal in the Macondo Block reference frame and vertical GPS velocities in mm/yr. Coupling contours from the elastic model by Lizarazo et al. (2021) are presented every 0.1 with its respective estimation of horizontal (red arrows) and vertical (yellow triangles) velocities. Inverted triangles denote subsidence. The distribution of onshore and offshore mud volcanoes is presented as green diamonds (Carvajal, 2000). Representative wells presented in purple squares as in Mora et al. (2018). Brown lines represent the extent of SFB: Sinú Fold Belt, SJFB: San Jacinto Fold Belt, and Lower Magdalena Valley.*

In our study region, the subsidence rate of the DIMA site is not reliable due to the high level of noise and short time series (< 2.5 years), and one at the GALE site was problematic due to several instrumental changes. VMAG and VPOL time series show variation in the interseismic trend for the latest part of the time series between 2016 and 2017, which introduces an additional bias not accounted for during velocity estimation. Then, vertical motions at the mentioned sites are considered less reliable, so we decided to double the standard error in the vertical component in order to reduce their weight in the model selection phase. Appendix A contains the time series plots of these stations in all components with their original uncertainties.

Table 5.1 presents velocity values in east, north, and vertical components and respective uncertainties of the subset of GPS sites in the northwestern corner of Colombia expressed with respect to the Macondo block. Please note that the vertical uncertainties of DIMA, GALE, VMAG, and VPOL are the original ones.

6.2. Methods

6.2.1. Earthquake cycle model formulation

To explain large vertical motions in northwestern Colombia we used a kinematic model to evaluate time-dependent deformation associated with an earthquake cycle. According to Savage and Prescott (1978) and Savage (1983), the representation of the earthquake cycle at subduction zones is given by the linear superposition of the steady-state and the supplemental solutions at the plate interface (Figure 6.2).

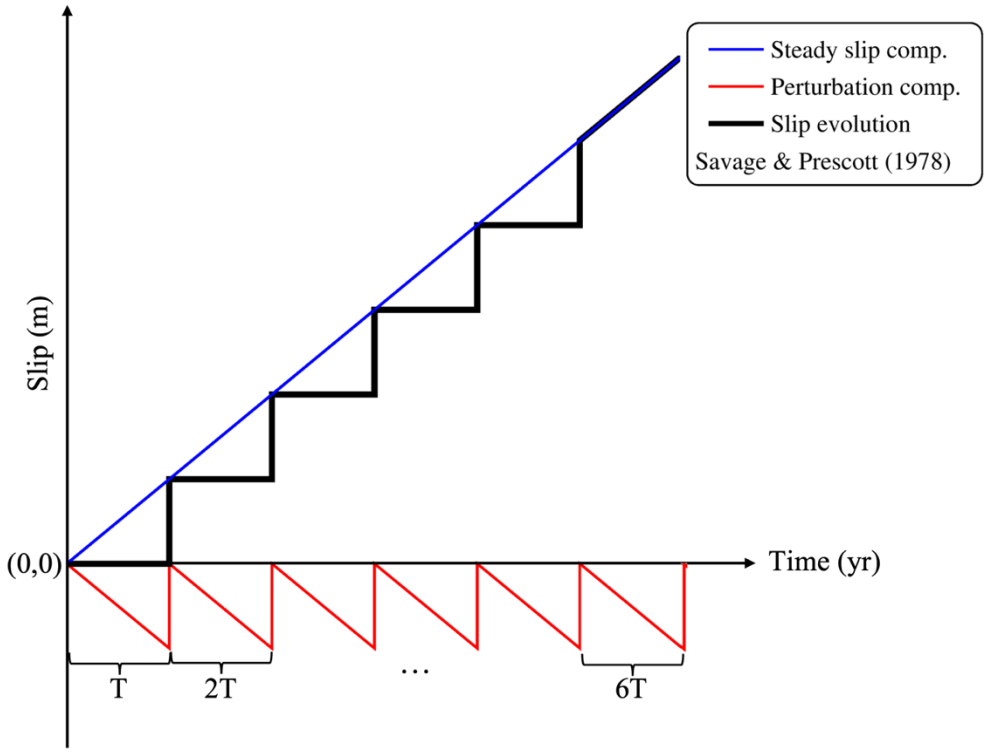

Figure 6.2. *Scheme of the evolution of plate boundary slip over an earthquake cycle and their components according to Savage and Prescott (1978). Steady slip denotes the linear increasing of slip at the subduction velocity, v. The perturbation component is composed by a negative slope that denotes the slip deficit (also known as backslip) and the instantaneous slip (coseismic phase) generated by an earthquake every T in years. The addition of steady and perturbation components produces the earthquake cycle sequence at the plate interface.*

The steady-state slip is characterized by a linear increase in time with a coefficient equal to the plate subduction velocity v as in Eq. 6.1.

$$\Delta u_s(t) = vt \tag{6.1}$$

On the other hand, the supplemental solution, which is a perturbation of the steady state, is defined by the superposition of slip deficit (also known as backslip) and a series of coseismic slips occurring at a regular interval *T*.

Eq. 6.2 (Savage and Prescott, 1978) describes a simplified end-member model where interplate locking is perfect during the entire interseismic period and total accumulated slip deficit is released by earthquakes with a recurrence interval *T*.

$$\Delta u_p(t) = -vt + vT \sum_{k=1}^{\infty} H(t - kT) \tag{6.2}$$

The steady-state subduction contributes mainly to long-term deformation (Matsu'ura and Sato, 1989; Hashimoto et al, 2004; Hashimoto et al, 2008; Fukahata and Matsu'ura, 2016), and as reported by Hashimoto et al. (2004), it amounts only a few mm/yr (<1% of the subduction rate) of uplift in northeast Japan. If we consider this situation and the fact that the subduction velocity of the Caribbean plate relative to the Macondo block is an order of magnitude slower than the one of northeast Japan, it is reasonable to presume that the contribution of the steady-state subduction to contemporary vertical motions is negligible.

On the other hand, the supplemental solution is responsible for time-dependent cyclic changes associated with the earthquake occurrence. In this study, we try to interpret contemporary vertical motions of the GPS sites in terms of cyclic perturbations caused by recurrent interplate earthquakes along the boundary alone. If we consider a single fault patch with a uniform time-dependent slip $\Delta u_p(\tau)$ on the plate interface, the resulting surface deformation $d(\boldsymbol{x}, t)$ is expressed as in Eq. 6.3.

$$\begin{aligned} d(\boldsymbol{x}, t) &= \int_{-\infty}^{t} \Delta \dot{u}_p(\tau)\, G(\boldsymbol{x}, t - \tau) d\tau \\ &= \int_{-\infty}^{t} \left[-v + vT \sum_{k=1}^{\infty} \delta(\tau - kT) \right] G(\boldsymbol{x}, t - \tau) d\tau \end{aligned} \tag{6.3}$$

where $G(\boldsymbol{x}, t)$ represents the viscoelastic Green's functions at a time t and an observation position $\boldsymbol{x}$, and $\Delta \dot{u}_p$, the time derivative of the perturbation component of the fault slip. By assuming that the subduction started at $t = 0$, Eq. 6.3 can be rewritten as follows:

$$d(\boldsymbol{x}, t) = -v \int_{0}^{t} G(\boldsymbol{x}, t - \tau) d\tau + vT \sum_{k=1}^{n} G(\boldsymbol{x}, t - kT) \tag{6.4}$$

Here, n is the total number of earthquakes until the time t.

Due to the viscoelastic nature of the lithosphere-asthenosphere system, the response functions $G(\boldsymbol{x}, t)$ converge to a constant value after time t_0 (Figure 6.3) and the equation can be modified as:

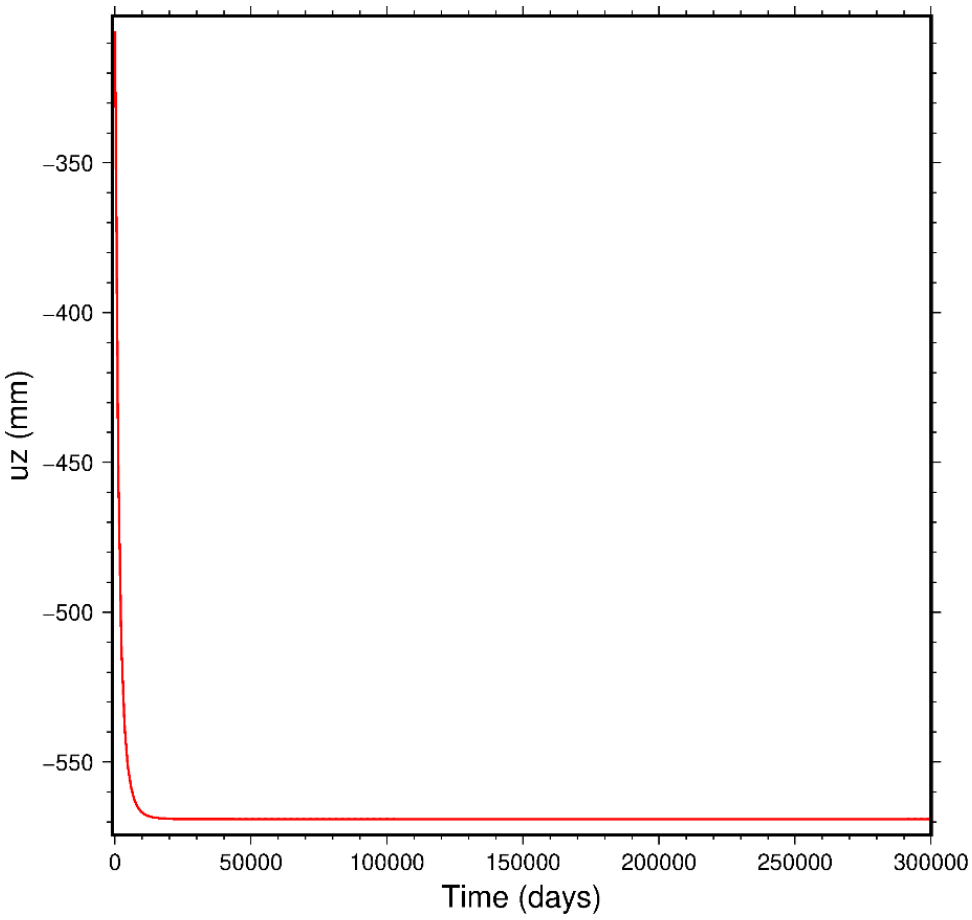

Figure 6.3*. Viscoelastic Green functions pattern for a viscosity value of 1x10^{18} Pa·s in the vertical component. The function reaches a constant value known as the fully relaxed solution $G(\infty)$.*

$$d(\boldsymbol{x},t) = -v\int_{0}^{t-t_0} G(\boldsymbol{x},t-\tau)d\tau - v\int_{t-t_0}^{t} G(\boldsymbol{x},t-\tau)d\tau + vT\sum_{k=1}^{n} G(\boldsymbol{x},t-kT) \qquad (6.5)$$

In Eq. 6.5, the integrand of the first term on the right side is considered to be constant, and the first term increases linearly in time whose rate is equal to the product of the subduction rate v and the fully relaxed Green's function $G(\boldsymbol{x},\infty)$, while the second term is a constant. Then the equation becomes Eq. 6.6 (Sagiya, 2015).

$$d(\boldsymbol{x},t) = -vG(\boldsymbol{x},\infty)t + vT\sum_{k=1}^{n} G(\boldsymbol{x},t-kT) + constant \qquad (6.6)$$

That is, once the displacement response function is obtained, the time-dependent surface deformation due to the earthquake cycle can be evaluated as a finite summation of the response

functions without integration with only two parameters, the subduction velocity v and the earthquake recurrence interval T. It should be noted that Eq. 6.6 is generally applicable to earthquake cycle problems even with structural heterogeneities if we can numerically evaluate the response functions.

6.2.2. Implementation

The calculation of the time-dependent viscoelastic Green's functions $G(\boldsymbol{x}, t)$ with the gravitational effect that describes the surface deformation response to a unit slip on the plate interface was performed using the PSGRN/PSCMP software (Wang et al, 2006). We assumed newtonian Maxwell rheology that represents steady-state viscosity since we do not consider a transient behavior that appears just after the earthquake's occurrence (Wang et al, 2012; Li et al, 2015).

We adopt a four layers earth model consisting of a sedimentary top layer, the oceanic crust, the lithospheric mantle (considered perfectly elastic), and the asthenosphere (Figure 6.4).

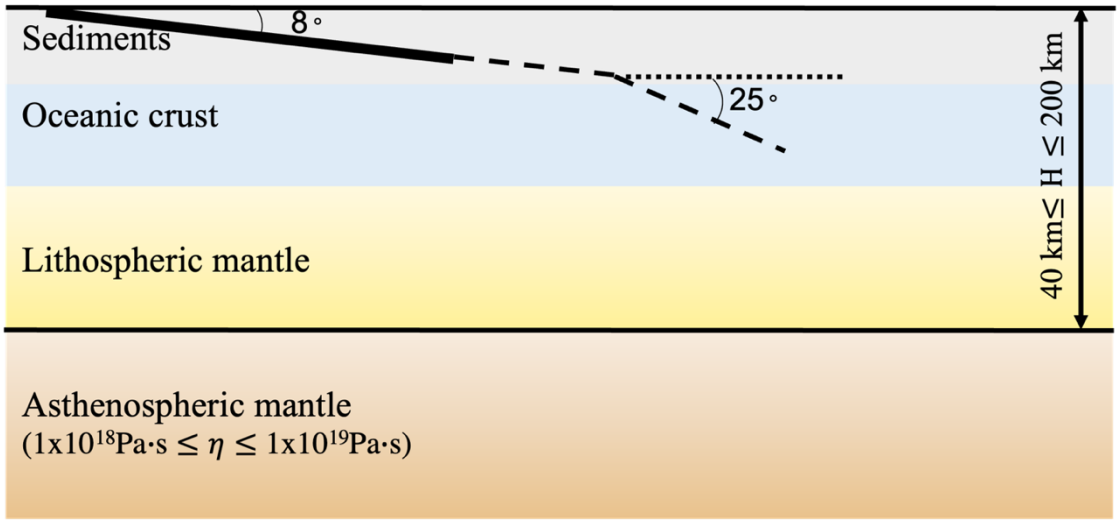

Figure 6.4*. Model configuration for a multilayered earth structure. The thick black line represents the single viscoelastic fault of width on the shallower part of the lithosphere. The broken line represents the geometry of the slab inland. Values of tested elastic lithosphere thickness (H) and asthenospheric viscosity (η) are presented.*

P and S wave velocities (V_p and V_s respectively) and densities (ρ) of each layer are presented in Table 6.1. These values are taken from Bernal-Olaya et al. (2015), Sánchez-Rojas and Palma (2014), and empirical relationships between elastic wave-speeds and density (Brocher, 2005).

Layer	**Thickness (km)**	**V_p (km/s)**	**V_s (km/s)**	**ρ (kg/m^3)**	**η (Pa·s)**
Sediments*	12	5.9	3.1	2500	∞
Oceanic crust*	16	6.9	3.6	2900	∞
Lithospheric mantle*	40	7.7	4.0	3140	∞
	60				
	80				
	100				
	150				
	200				
Asthenospheric mantle	∞	8.1	4.5	3340	$1x10^{18}$
					$3x10^{18}$
					$5x10^{18}$
					$1x10^{19}$

Table 6.1. *Structural model. Layers marked with * compose the elastic lithosphere.*

To check the dependency of estimated interseismic velocities on mechanical and rheological parameters we tested elastic lithosphere thicknesses between 40 and 200 km and viscosity values between $1x10^{18}$ and $1x10^{19}$ Pa·s, typical for subduction zones environments (Wang et al, 2012; Wang, 2017). We also investigate the dependence of the interseismic displacement rate on the earthquake recurrence time for three different intervals such as 300, 600, and 1200 years. Since we assume a perfect interseismic locking and a complete release of interseismic slip deficit by periodic earthquakes, different assumptions of the earthquake recurrence interval per tested fault dimensions correspond to different earthquake sizes at the current subduction rate of 7 mm/yr

following a scaling relationship between area and moment magnitude for subduction earthquakes (Allen and Hayes, 2017).

After obtaining time-dependent Green's functions for our given layered structure, we calculated co- and post-seismic deformation at the GPS site locations for a single rectangular fault with a specific size and geometry imposing a unit slip. We implement a cosine taper of slip distribution at the fault edges to get rid of artificial singularity. We applied different taper values to the four edges of the fault from 0% to 50% of length and width dimensions (Figure 6.5).

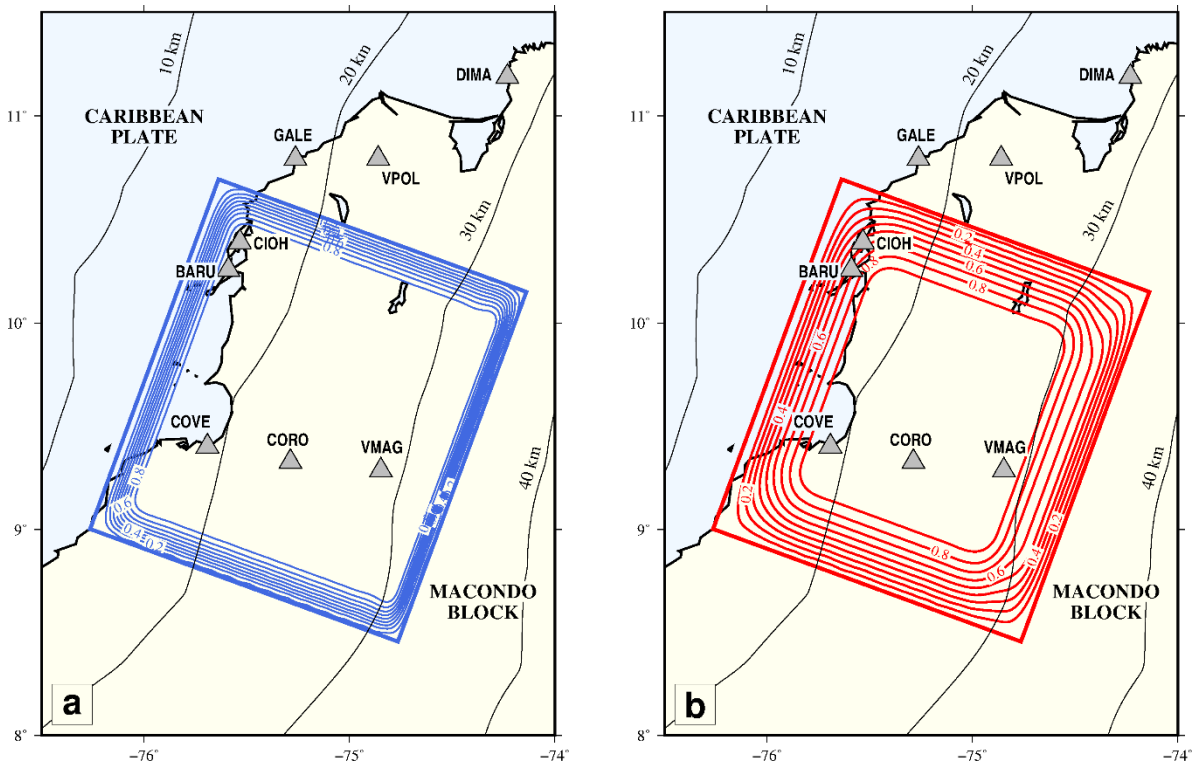

Figure 6.5*. Slip distribution for the viscoelastic source fault for different taper assumptions applied in length and width dimensions for a). 12.5%, b). 25%, c). 37.5%, d). 50% and e). uniform slip.*

(continued on next page)

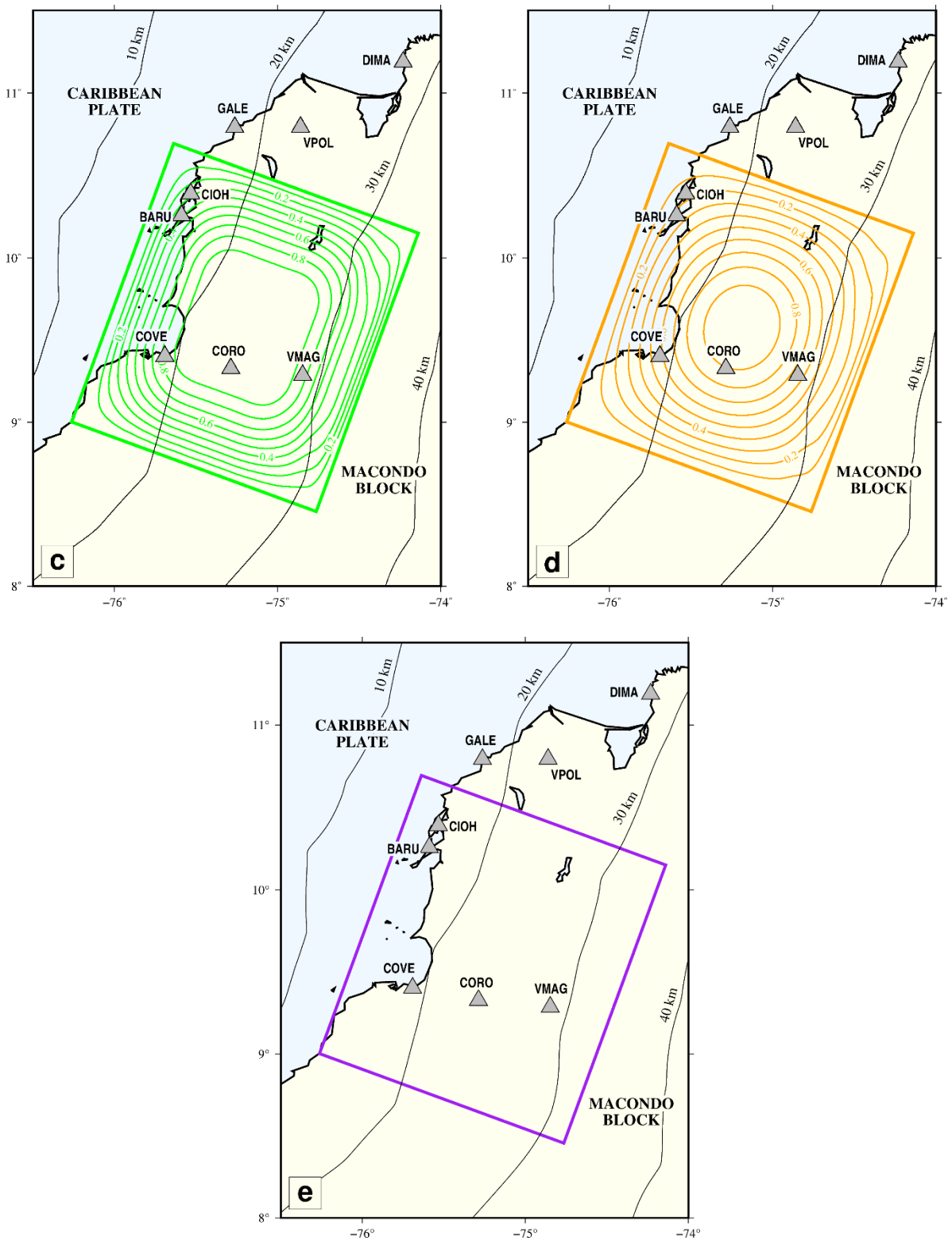

***Figure 6.5**. (continued)*

Based on the minimum 3-dimensional WRMS criteria, 25% of fault length/width was selected for the taper (Figure 6.6).

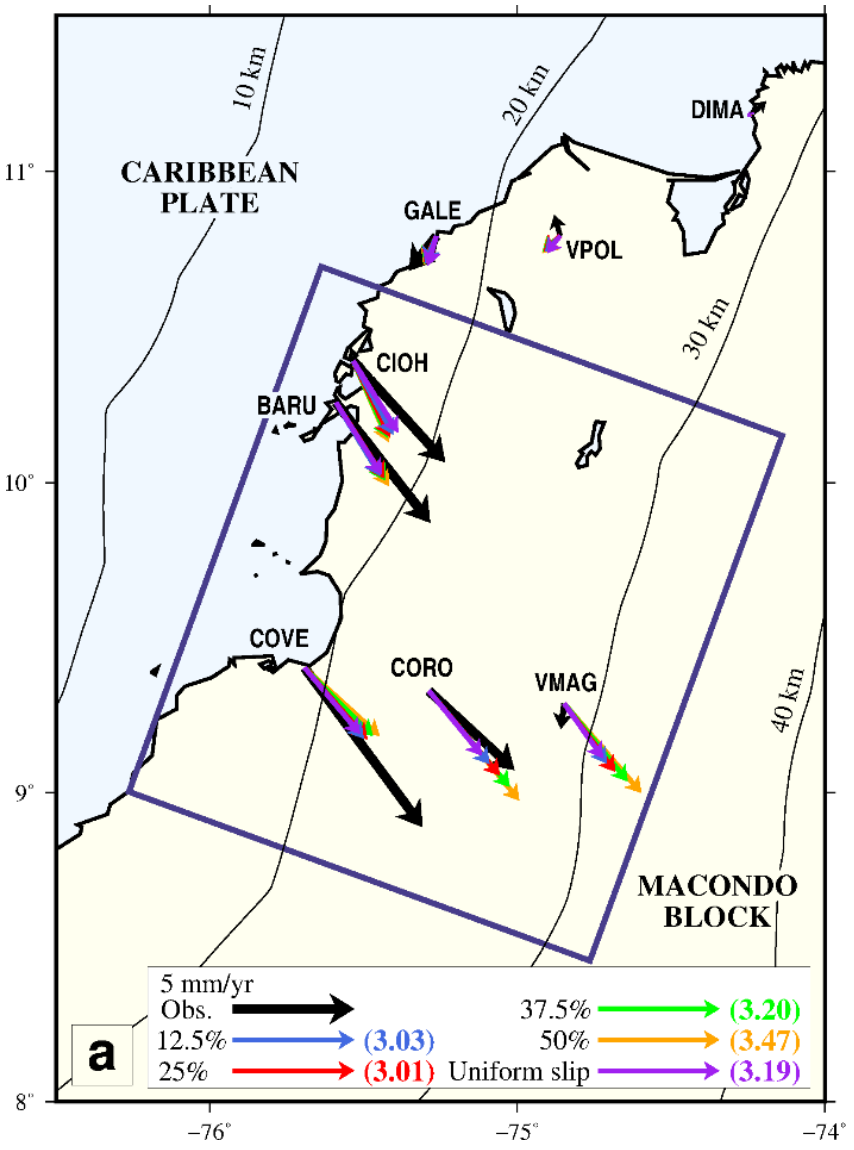

Figure 6.6. *Velocity fitting for different assumptions of slip distribution in a). horizontal and b). vertical components. 3-dimensional WRMS values are presented.*

(continued on next page)

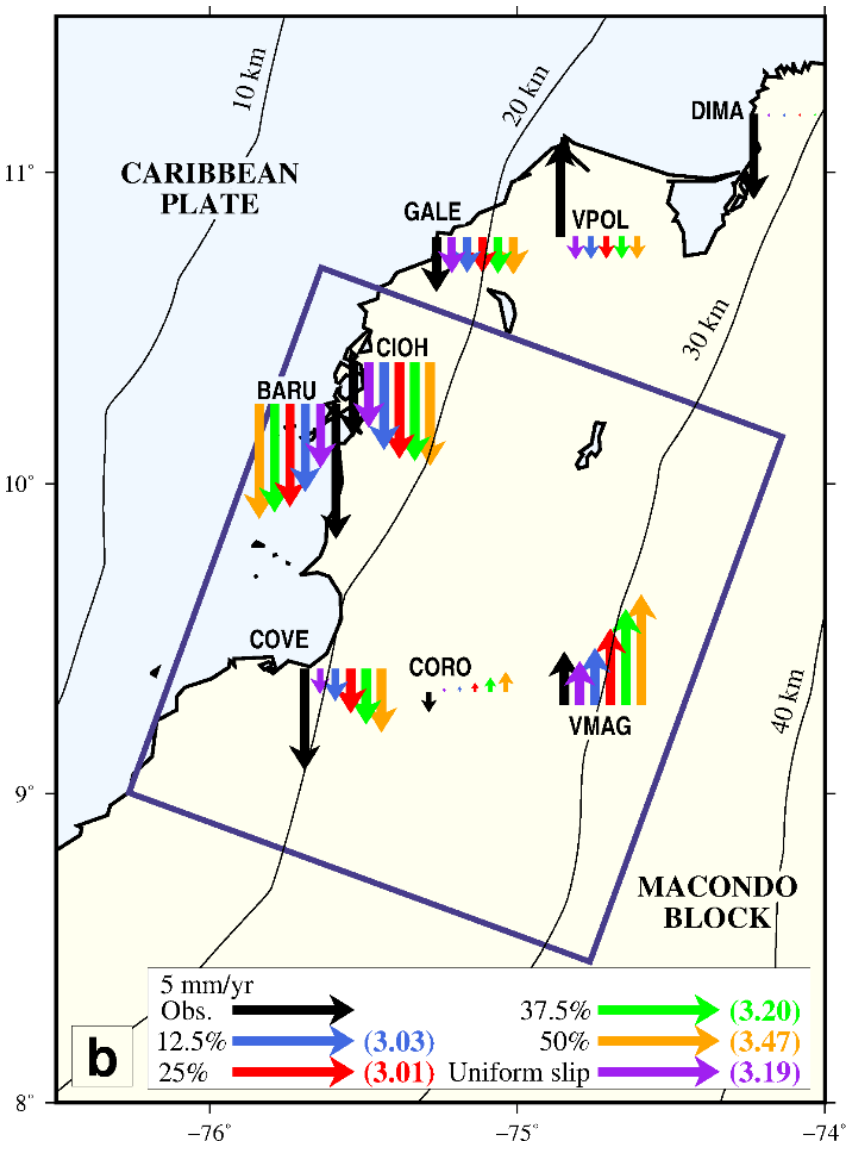

Figure 6.6. *(continued)*

Fault parameters of length, width, strike, dip, and location (longitude, latitude, depth) are optimized by a grid search algorithm. The optimum location is searched every 0.25º between 77ºW to 74ºW in longitude and 8ºN to 11.5ºN in latitude. We did not evaluate latitudes below 8ºN because at these locations the slabs from the Caribbean and Nazca plates are not well differentiated and also, because the effects of the Panamá arc collision are more dominant over the CSZ. The size of the fault is varied from 50 to 400 km in length and from 50 to 250 km in width, evaluated every 25 km in both parameters. A total of 1,895,400 models were tested.

By considering the model described in Eq. 6.6, and assuming a full locking state during the interseismic period and total slip-deficit release at the earthquake occurrence *T*, we calculate horizontal and vertical displacements at the GPS sites over many earthquake cycles. Imposed subduction velocity is 7 mm/yr that produces a maximum coseismic slip of 4.2 m, equivalent to a M_w7.8 earthquake, for the reference recurrence interval of 600 yr. Shorter and longer recurrence intervals, namely 300 and 1200 yr, will generate respectively 2.1 m and 8.4 m of coseismic slip. We evaluate crustal deformation after 9000 years from the beginning at time intervals depending on the viscosity assumption, that is, every 1, 2.5, 3.5, and 6 yr for viscosities equal to $1x10^{18}$, $3x10^{18}$, $5x10^{18}$, and $1x10^{19}$ Pa·s, respectively. Deformation becomes purely periodic after 600 years for the tested viscosity range. The displacement rate for the last 100 years before the next earthquake, representative of the interseismic stage, is computed by linear regression and compared with the observed velocities at GPS stations.

Finally, a selection of the best source fault model including location, geometry and dimensions of the source fault, lithospheric thickness (H) and viscosity value (η) was obtained based on the minimum 3-dimensional weighted root mean square error (3D-WRMS) as in Eq. 6.7 (Kierulf et al, 2014; Li et al, 2015).

$$WRMS = \sqrt{\frac{\sum_{i=1}^{n}\left(\frac{obs_i^N - cal_i^N}{\sigma_i^N}\right)^2}{\sum_{i=1}^{n}\left(\frac{1}{\sigma_i^N}\right)^2} + \frac{\sum_{i=1}^{n}\left(\frac{obs_i^E - cal_i^E}{\sigma_i^E}\right)^2}{\sum_{i=1}^{n}\left(\frac{1}{\sigma_i^E}\right)^2} + \frac{\sum_{i=1}^{n}\left(\frac{obs_i^U - cal_i^U}{\sigma_i^U}\right)^2}{\sum_{i=1}^{n}\left(\frac{1}{\sigma_i^U}\right)^2}} \quad (6.7)$$

Where n is the number of GPS sites, obs_i and cal_i are the observed and predicted velocities, respectively, and σ_i is the velocity uncertainty in north (*N*), east (*E*) and vertical (*U*) components.

6.3. Results

6.3.1. Optimization of location and fault size parameters

Before discussing the source fault model that better reproduces 3-dimensional deformation in the Caribbean of Colombia, it is important to evaluate the spatial distribution of weighted residual values for fault location as well as for fault size parameters, namely length, and width.

Figure 6.7 shows the minimum 3D-WRMS achieved at each position by changing the fault dimensions over the range between 77°W~74°W, and 8°N~11.5°N. The optimal location of the

rectangular fault upper-left corner is at 76.25ºW, 9.0ºN. At this location, the flatter segment of the Caribbean plate slab depths corresponds to 14 km, and therefore, the source region is embedded completely in the elastic lithosphere. The best source fault location is near the southwestern edge of the modeled region and weighted residuals show a progression to larger values to the northeastern and deeper parts of the study region.

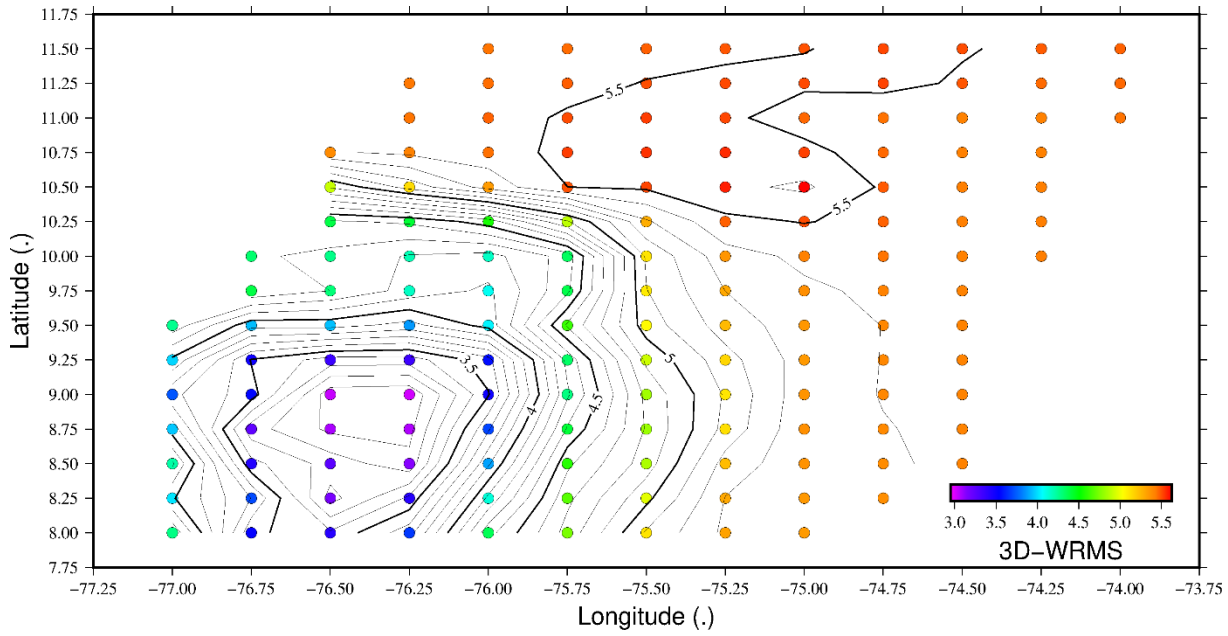

Figure 6.7*. Optimization of fault location in geographic coordinates system. Colors represent the 3-dimensional WRMS values and contours presented every 0.1 mm/yr.*

Regarding the fault size, Figure 6.8 shows the 3D-WRMS contours for different combinations of lengths and widths independent of its location. We assume the modeled fault location is restricted to the flattest part of the slab or above 40 km depth in all cases. A fault of 200x175 km^2 is the most appropriate for reproducing observed crustal motions. The fault width is much better constrained than its length. For fault widths and lengths larger than 225 km, the weighted residual value increases.

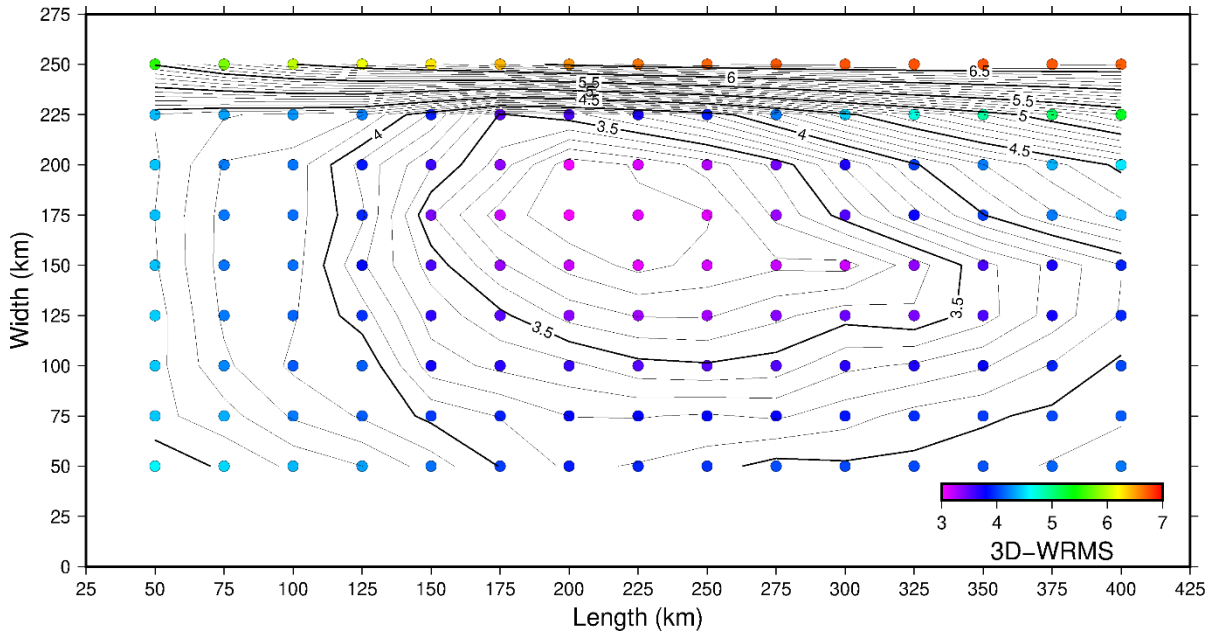

***Figure 6.8**. Optimization of fault dimensions in km. Colors represent the 3-dimensional WRMS values and contours presented every 0.1 mm/yr.*

6.3.2. Best source fault model

Here I present and discuss the time-dependent displacements at the GPS sites obtained from the best fault model for the case with a lithosphere thickness of H=80 km, a viscosity of η=1x10^{18} Pa·s and a recurrence interval between earthquakes of T=600 yr, followed by a comparison with the previous elastic coupling model by Lizarazo et al. (2021).

6.3.2.1. Time-dependent displacement over an earthquake cycle

Deformation responses of the earthquake cycle model at the GPS sites in the vertical component (Figure 6.9a) show an instantaneous coseismic uplift of ~1.35 m, followed by a rapid postseismic uplift of ~1.0 m during the first 20 years of the cycle at coastal sites BARU and CIOH. After transient postseismic effects have vanished, the interseismic subsidence completely recovers the coseismic as well as postseismic uplift by the end of the cycle. The estimated subsidence rate is 4.3 mm/yr at BARU and 3.9 mm/yr at CIOH. Other sites that present a similar deformation pattern throughout the earthquake cycle but with much lower magnitudes are COVE, GALE, and VPOL. At COVE and GALE sites the recovered subsidence rate is 1.8 mm/yr and 1.5 mm/yr in relation to observed velocities of 4.2 mm/yr and 2.3 mm/yr, respectively. For the VPOL site, an estimated 0.9 mm/yr subsidence disagrees not only in the magnitude but also in the sign of the observed

motion. The CORO site calculation shows a coseismic uplift of ~0.5 m followed by an even larger postseismic subsidence of short duration (~40 yr) and interseismic uplift rates of 0.4 mm/yr. Given that the uncertainty of the GPS velocity is larger than the absolute value of subsidence, this station could represent the location of transition from subsidence to uplift inland. The DIMA site, located on the northeastern edge of the study region, shows a very small coseismic and postseismic subsidence recovered by slow constant uplift of ~0.1 mm/yr as opposed to the observed subsidence of 3.5 mm/yr. VMAG presents a slightly larger uplift rate of 3.1 mm/yr in comparison to observed values of 2.2 mm/yr. This site is located at a distance of ~90 km from the coastline, which could indicate that at these locations uplift is predominant.

Figures 6.9b and 6.9c show the time-dependent displacement functions for each GPS site in the East and North components. BARU, CIOH, CORO, COVE, and VMAG sites located above the modeled fault present interseismic southeastward motion with rates between 3.5 mm/yr to 4.6 mm/yr obtained after postseismic effects of short duration (<50 yr) have vanished. DIMA, GALE and VPOL sites at the northernmost part of the study region show southwestward motion varying between 0.3 mm/yr and 1.2 mm/yr.

At the northern part of the study region, 3-dimensional deformation signals produced by the viscoelastic fault model are very weak.

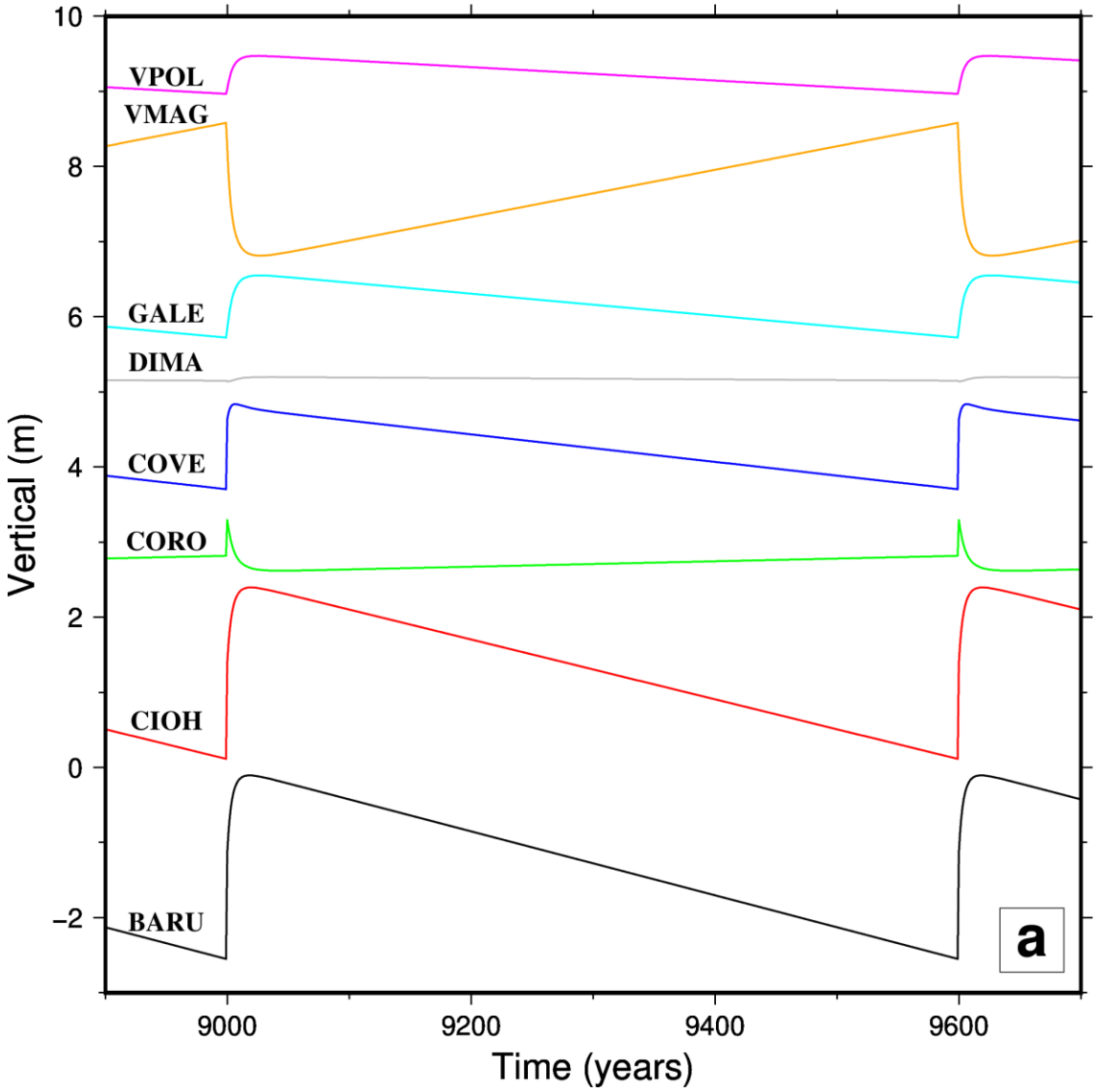

Figure 6.9. *Displacement vs time functions for an earthquake cycle of 600 yr reproduced by the viscoelastic earthquake cycle model at the GPS sites in a). vertical, b). east and c). north components. IDs of GPS stations are presented for reference.*

(continued on next page)

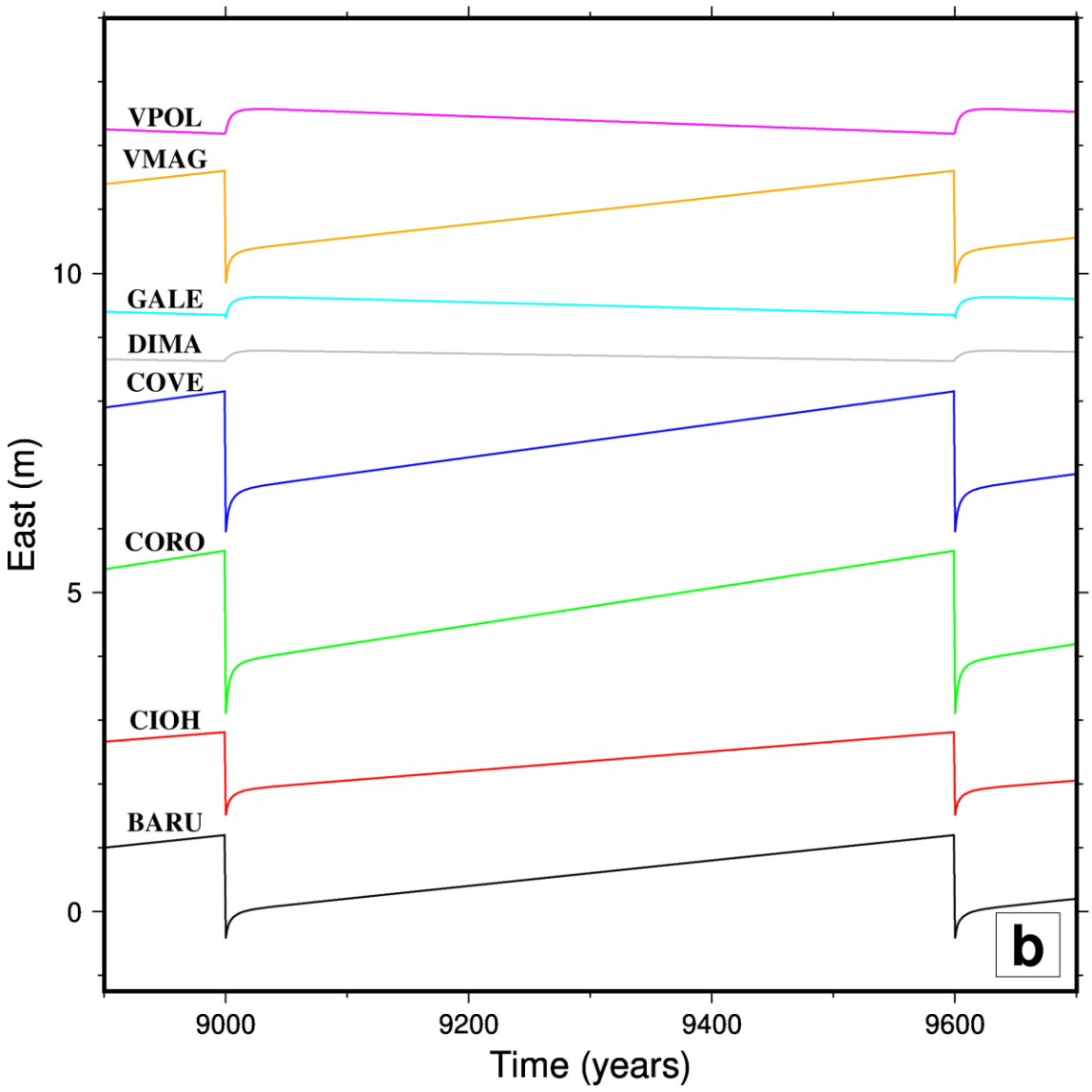

Figure 6.9. *(continued)*

(continued on next page)

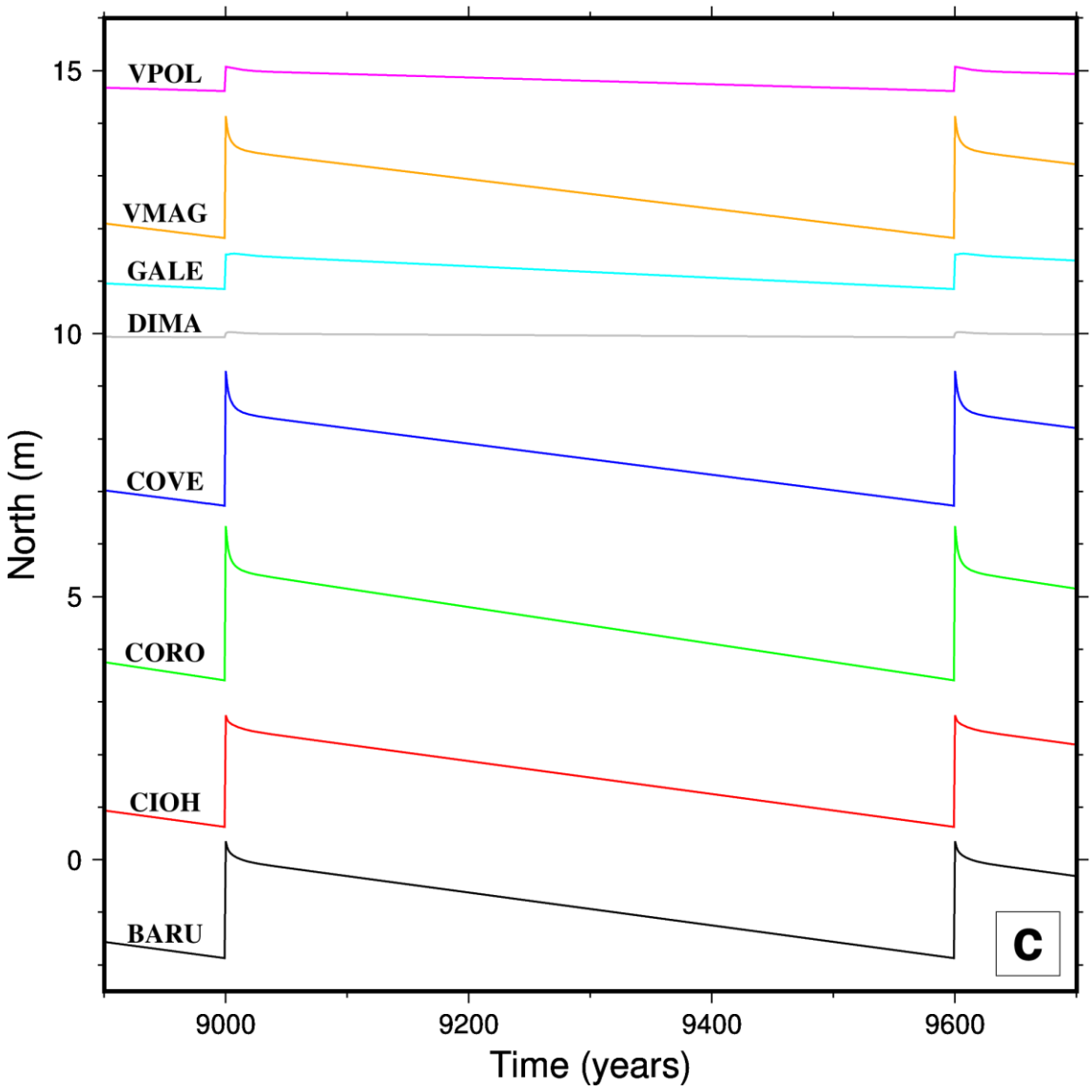

Figure 6.9. *(continued)*

6.3.2.2. Comparison of elastic and viscoelastic models

In our viscoelastic model, the source region is located deeper between 14 km and 35 km depths and shifted to the southeast with respect to the locked area based on the elastic modeling (Figure 6.10). The overall fitting is improved by the viscoelastic model with a 3-dimensional WRMS of 3.0 in comparison with 3.9 from the elastic coupling model, which suggests that viscoelastic effects on the interseismic deformation are important. In particular, these effects are remarkable in the vertical component with an improved WRMS of 1.9 mm/yr in comparison with 3.5 mm/yr from

the elastic coupling model. Regarding the horizontal components, the viscoelastic model fitting is poorer regarding a 2D-WRMS of 2.3 mm/yr in comparison with 1.6 mm/yr from the elastic model.

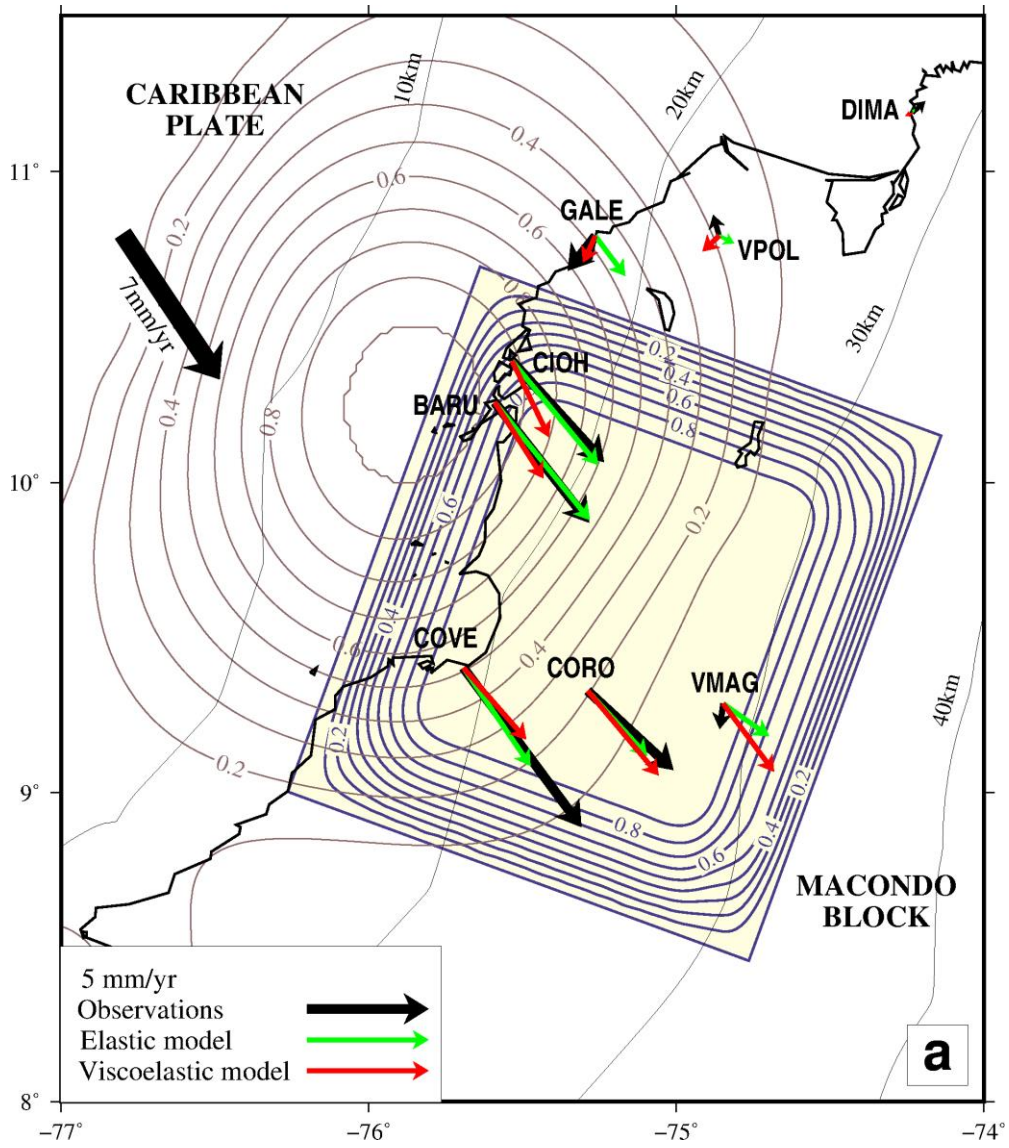

Figure 6.10. *Best source fault models under viscoelastic (light yellow region) and elastic (coupling contours every 0.1) earth structures and velocity fitting from each of them in a). horizontal and b). vertical components. Velocities expressed in mm/yr.*

(continued on next page)

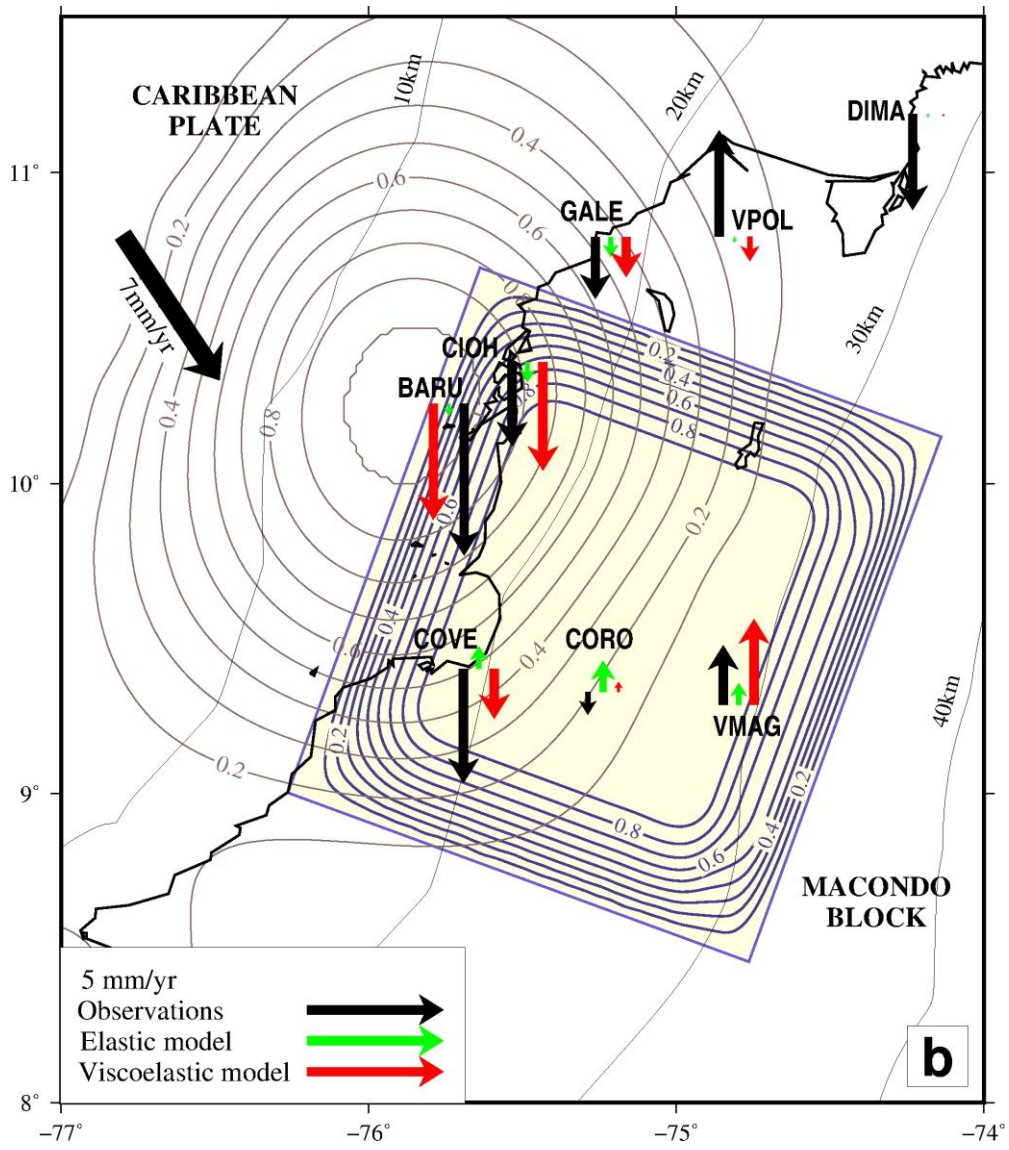

Figure 6.10. *(continued)*

A comparison between the elastic coupling and the viscoelastic models shows important differences regarding the fitting of the horizontal components (Figure 6.10a). First, the offshore locked region from the elastic model reproduces southeastward motion better than the viscoelastic one. At BARU and CIOH sites, the coupling model fits the observations almost perfectly, thanks to the high flexibility of the model (Lizarazo et al, 2021). Noticeable improvement in the velocity fitting is obtained with the viscoelastic model at CORO, COVE, and GALE sites where the prediction level overcomes that of the elastic one. For the latter sites, in particular, the viscoelastic model produces velocities consistent in their directions but smaller in their magnitudes. At the northern GPS sites, DIMA and VPOL, and the innermost site VMAG, none of the models can

reproduce the observed velocities (magnitude nor direction), probably because the effects of the subduction fault are not predominant at these locations and/or due to the imposed geometry simplifications. It is worth noting that computed horizontal velocities at DIMA and VPOL sites are very small (<1 mm/yr), which could also indicate the leading effect of the Macondo block rigid motion over the subduction of the Caribbean plate in the northern part of the study region. In general, the fitting of the north component is slightly better (WRMS=1.5 mm/yr) than the east one (WRMS=1.7 mm/yr).

In the vertical component, the viscoelastic source fault generates vertical velocities closer to the observations improving overall fitting (Figure 6.10b). A possible cause to account for the misfit at DIMA, GALE, VMAG, and VPOL in the vertical component, can be related to the decreasing weighting factor applied on the velocities in relation to their unreliable vertical motion trends as explained in section 6.1.

The viscoelastic model predicts subsidence at BARU, CIOH, COVE, and GALE sites in agreement with observed vertical motions. Predicted subsidence rates at BARU and CIOH sites are close to 4.0 mm/yr, showing a remarkable improvement from the elastic model. At COVE and GALE sites, the polarity of observation is reproduced by the viscoelastic model, but the subsidence rate is underestimated. At the northeasternmost edge of the study region, DIMA and VPOL sites, predicted rates (<1 mm/yr) are much smaller and inconsistent with observations. This situation is expected from the weighting assumptions. Considering that the horizontal motions of these sites are consistent with the rigid motion of the Macondo block, these vertical signals may not be of tectonic origin but local effects. The estimated velocity in CORO (0.4 mm/yr) site is within the uncertainty level of the observed GPS data, pointing out the location of transition from subsidence to uplift. VMAG site estimate, independent of the weight constraints, shows an uplift of 3.1 mm/yr consistent with the observed value, indicating that for distances larger than ~90 km inland, the uplift of the crust is predominant.

6.3.3. Sensitivity test of model parameters

6.3.3.1. Sensitivity to the lithospheric thickness – *H*

Viscoelastic deformation is sensitive to the lithospheric thickness assumption in both, horizontal and vertical components as presented in Figure 6.11. For several values of lithospheric

thickness varying from 40 km to 200 km, it is observed that thicker elastic lithosphere up to 100 km tends to fit better the overall observed 3-dimensional deformation as well as independent displacement components.

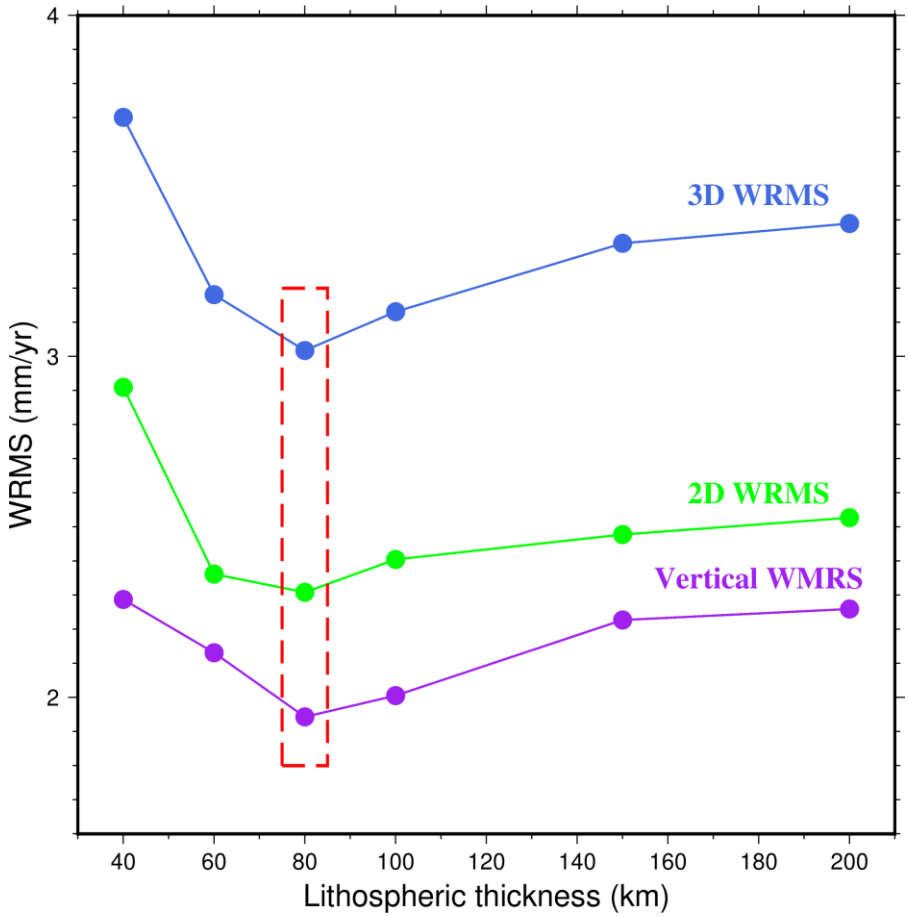

Figure 6.11. *Plot of the vertical, two-dimensional, and 3-dimensional WRMS vs the elastic lithospheric thickness (H). The red box indicates the value of lithospheric thickness (H=80 km) for which WRMS reaches its minimum.*

The minimum WRMS is achieved with the lithospheric thickness of 80 km in all cases for vertical, horizontal (2D), and 3D-dimensional weighted errors. Variation in WRMS is not significant between 60 and 100 km, indicating any value in this range could reproduce similarly observed motions. For values of H>100 km, the statistical value gets worse.

Figure 6.12 presents the map view of the velocity fitting in horizontal and vertical components for different values of the elastic lithosphere thickness.

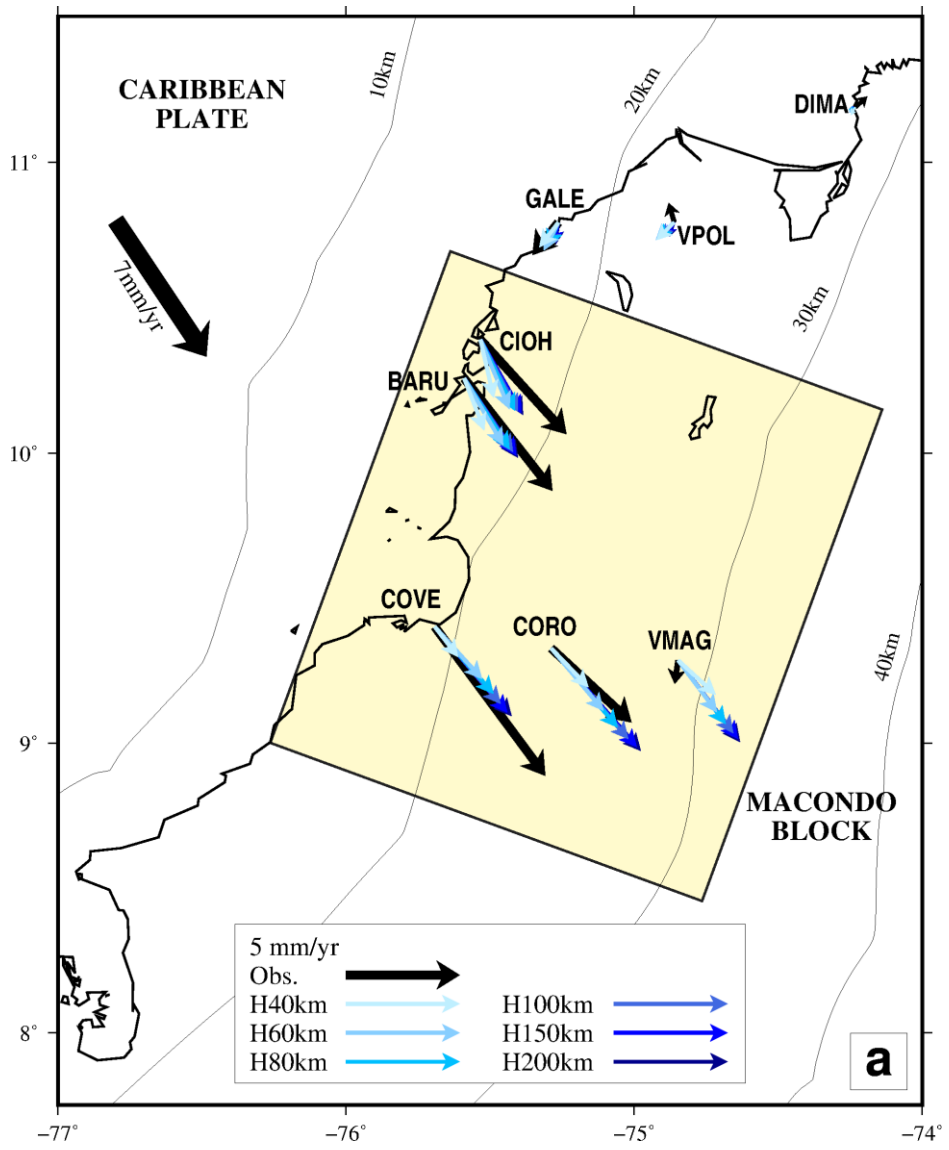

Figure 6.12. *Sensitivity of estimated interseismic velocities to different assumptions of the elastic thickness parameter (H) for the best viscoelastic source fault for a viscosity value of* $1x10^{18}$ *Pa·s in a). horizontal and b). vertical components. Variation from light to dark colors indicate variation from thinner to thicker elastic thickness.*

(continued on next page)

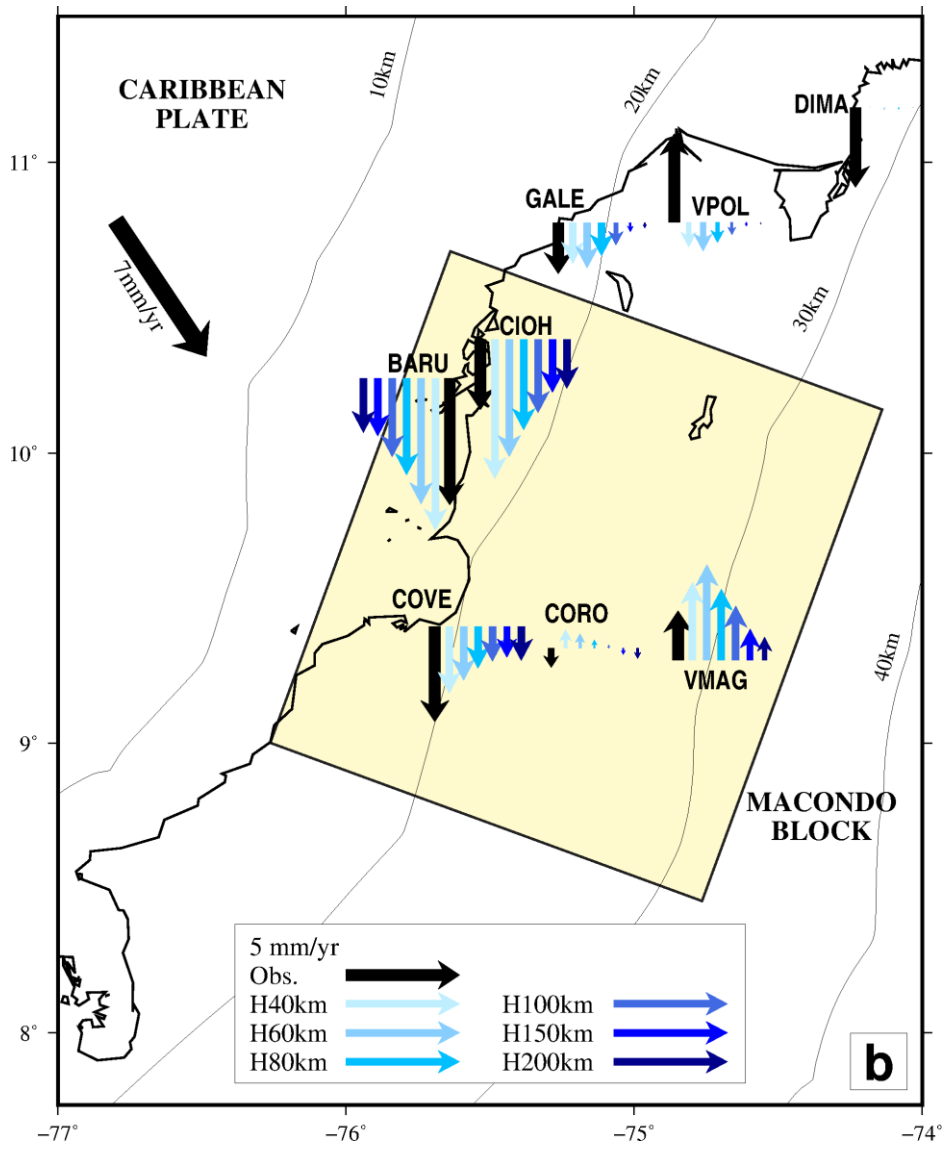

Figure 6.12. *(continued)*

Thicker elastic lithosphere generates larger motions in the horizontal component (Figure 6.12a). These are remarkable at GPS sites BARU, CIOH, COVE, CORO, and VMAG, located above the modeled fault. To the northern extent of the study region, the variation of estimated rates is not significant for the tested range of the parameter.

In the vertical component (Figure 6.12b), larger velocities are produced by thinner elastic lithosphere values such as 40 and 60 km. It can be seen that interseismic vertical motions reduce gradually with the increasing lithosphere thickness. Larger motions are observed at the GPS sites above the fault, where the contrast for different values of *H* is more noticeable. Variations on

estimated rates at the northern sites GALE and VPOL can be observed as well but with a lesser contrast. At the DIMA site, the elastic lithosphere variation does not have any effect on the vertical rate.

6.3.3.2. Sensitivity to the asthenospheric viscosity - η

The optimum fault for the viscoelastic model remains invariable for the analyzed viscosity range, $1x10^{18}$ Pa·s $\leq \eta \leq 1x10^{19}$ Pa·s, which indicates that surface deformation is not sensitive to the assumption of this parameter. For an optimum value of elastic thickness H=80 km, 3D-WRMS presents a minimum change (< 0.03%) for changes in viscosity.

Variations introduced by viscosity assumptions are mostly related to the amplitude and duration of the postseismic transient. For the reference recurrence interval T=600 yr, the displacement vs time plot in the three components is presented in Figure 6.13 for the coastal GPS site CIOH in Cartagena city.

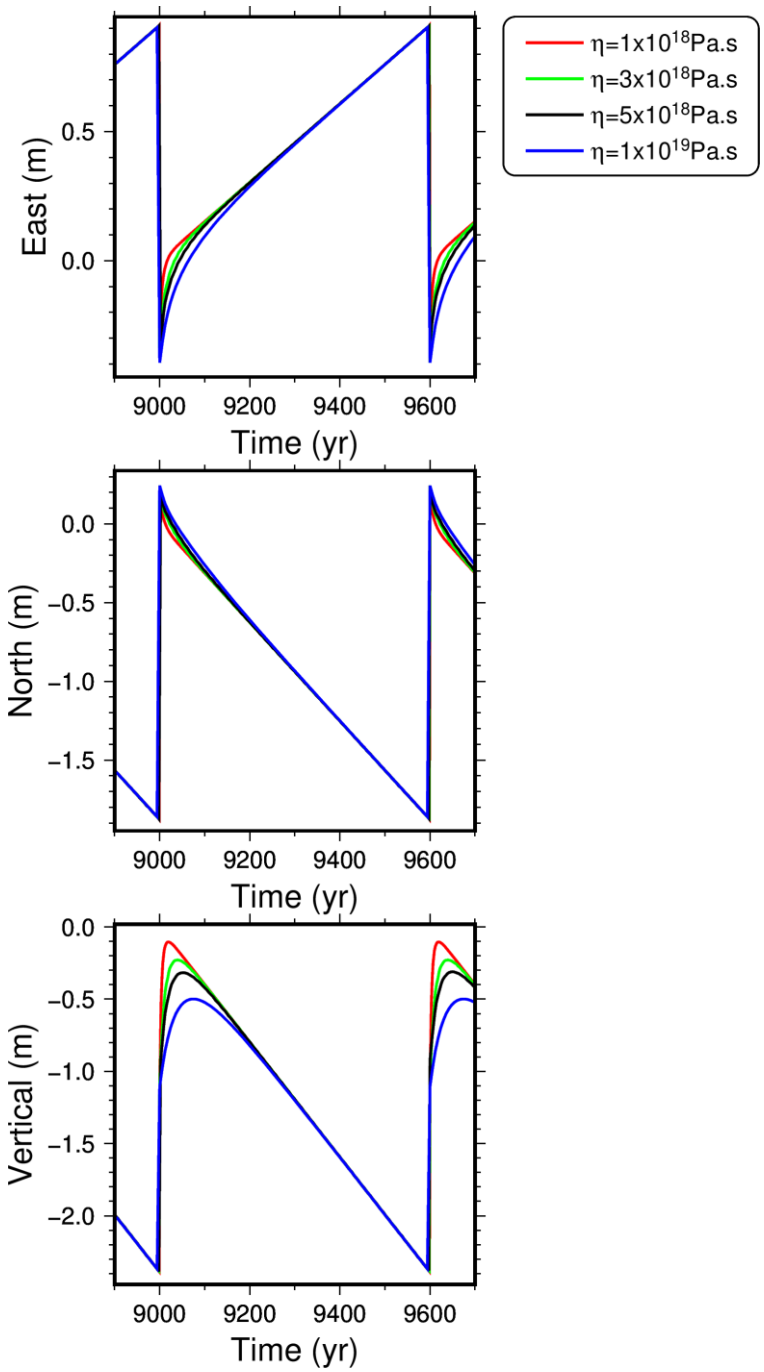

Figure 6.13. *Displacement vs time functions for CIOH site in Cartagena for different values of viscosity (η) in 3-dimensional components. Values of η represented by the colors in the legend.*

Figures 6.14, 6.15 and 6.16 contain plots for the remaining GPS sites in east, north and vertical components.

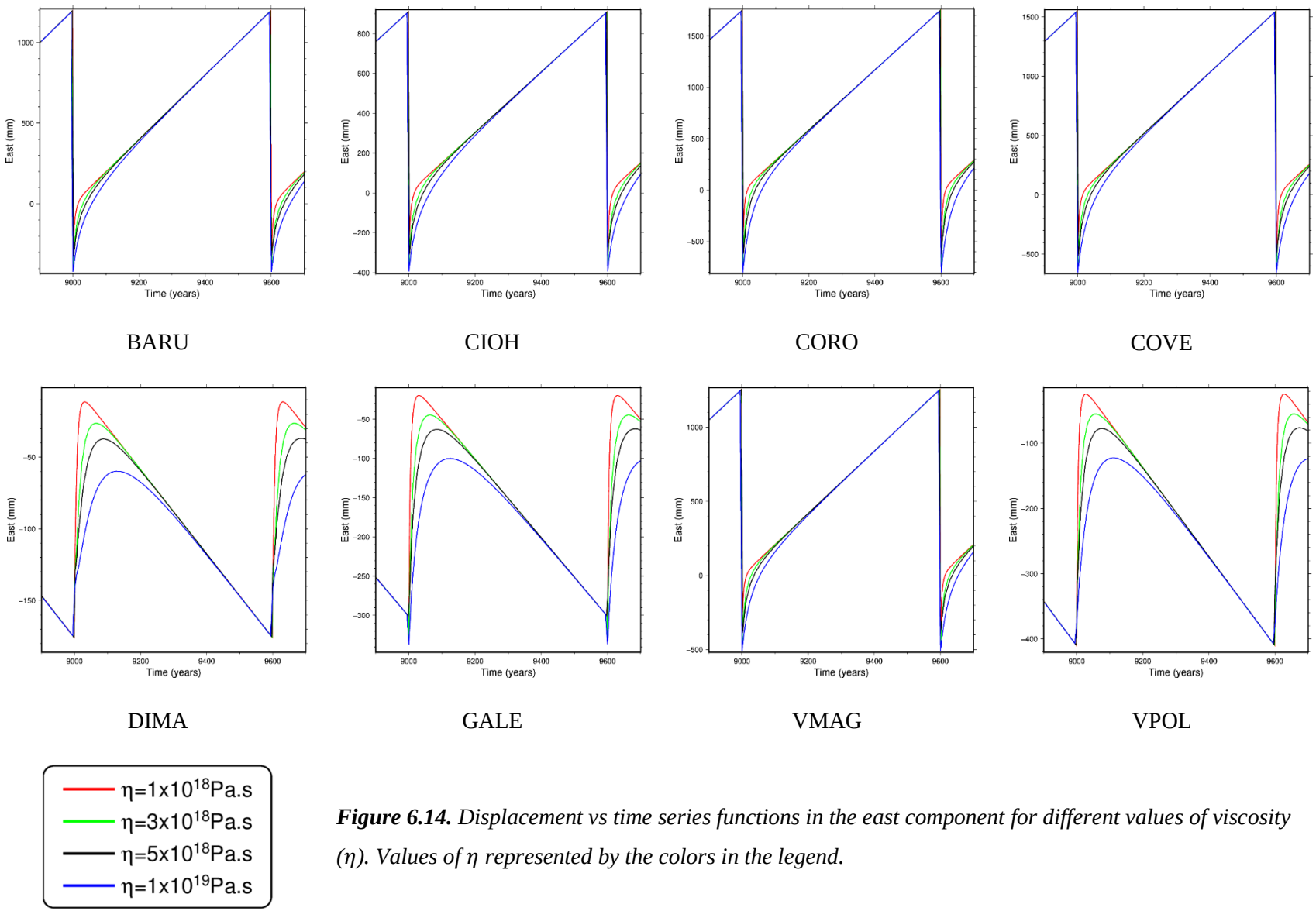

Figure 6.14. *Displacement vs time series functions in the east component for different values of viscosity (η). Values of η represented by the colors in the legend.*

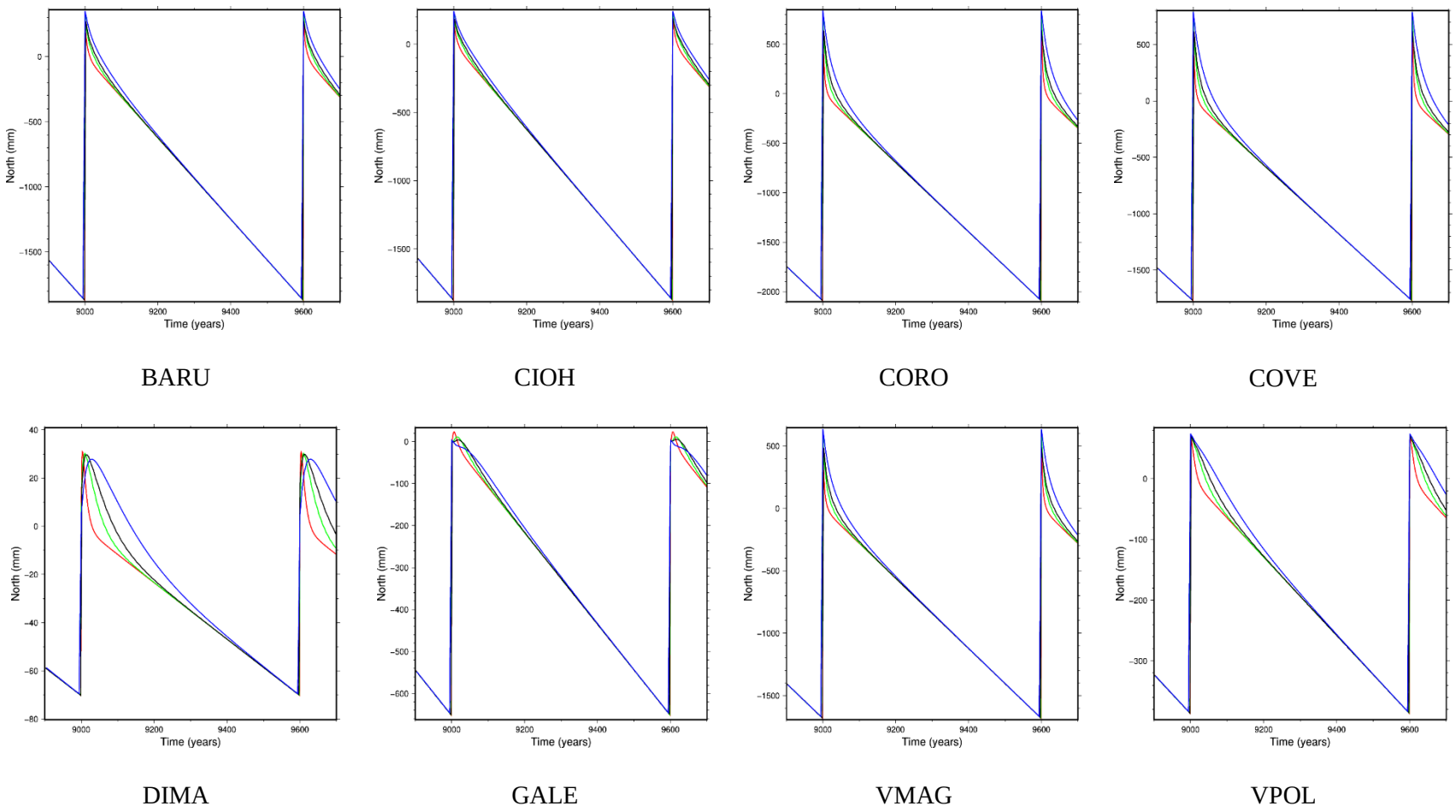

Figure 6.15. *Displacement vs time series functions in the north component for different values of viscosity (η). Values of η represented by the colors in the legend.*

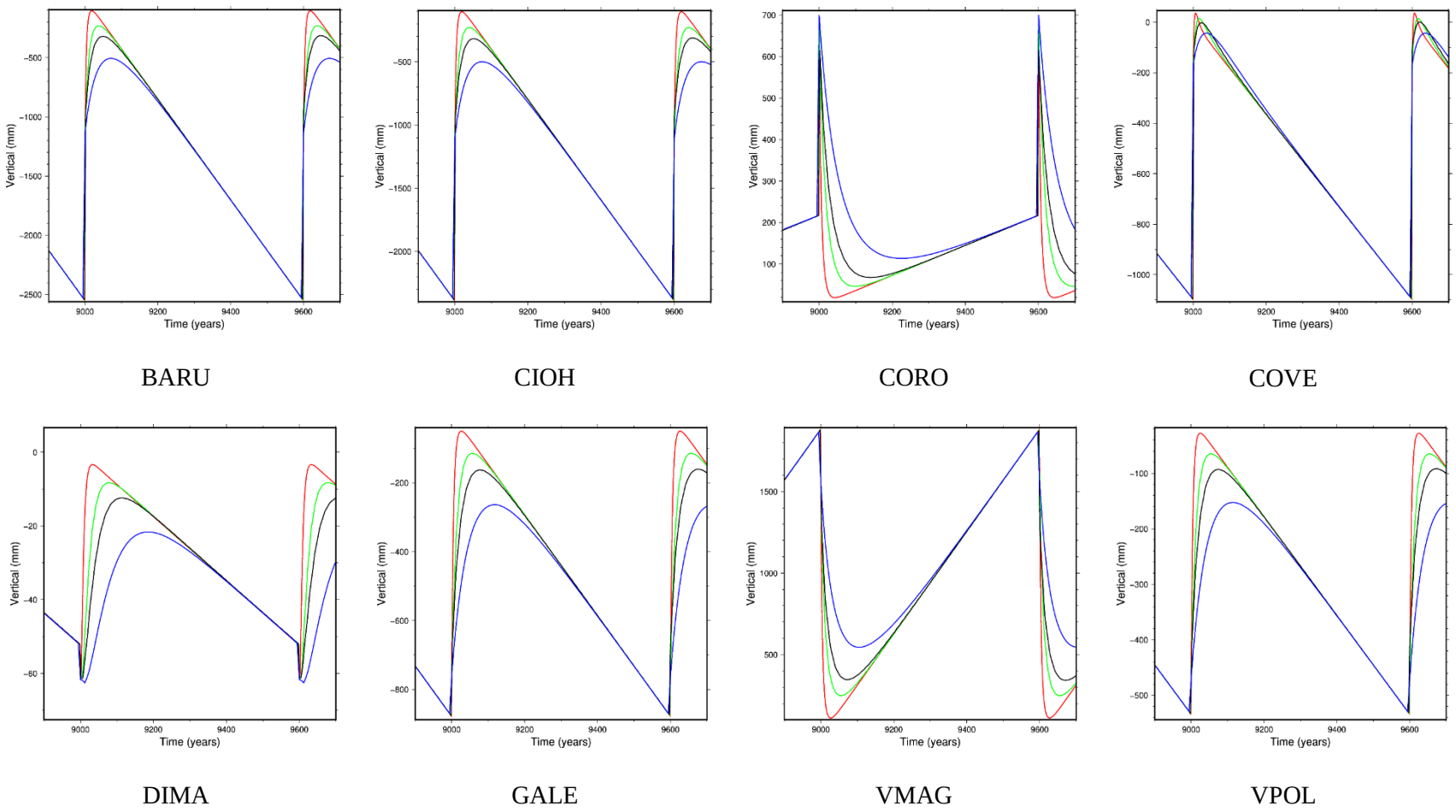

Figure 6.16. *Displacement vs time series functions in the vertical component for different values of viscosity (η). Values of η represented by the colors in the legend.*

For each component, the initial postseismic response generated by a lower viscosity value (η=1x10^{18} Pa·s) is large in size but of short duration at all the analyzed GPS sites, reaching its maximum within the first 50 years from the main shock, irrespective of the sense of the motion. For the largest tested viscosity (η=1x10^{19} Pa·s), postseismic transients are smaller in magnitude but continue for a longer duration. However, the displacement rate in the late stage of the interseismic period is not affected by the viscosity in the tested range. Current GPS velocities are the only available observation data, and they are not useful to constrain the asthenospheric viscosity in the current framework.

6.3.3.3. Sensitivity to the recurrence interval - T

Fixing the viscosity to η=1x10^{18} Pa·s and the lithospheric elastic thickness to H=80 km, we found that calculated overall deformation rates at GPS sites remain unchanged for the last part of the earthquake cycle for different assumptions of the recurrence interval T. Velocity estimations at the GPS sites are computed for T=300 yr and T=1200 yr.

Taking the case of the CIOH site (Figure 6.17), the estimated coseismic uplift displacements are ~0.6 m, ~1.3 m, and ~2.6 m for T=300 yr, T=600 yr, and T=1200 yr, respectively. In the current viscoelastic model, the recurrence interval assumptions determine the amount of coseismic slip and the resulting surface displacements. The magnitude and duration of the postseismic phase uplift, being of ~0.5 m for the first 15 yr after the earthquake for T=300 yr, ~1.0 m for the first 20 yr after the earthquake for the reference interval, T=600 yr, and ~2.0 m for the first 25 yr after the earthquake for T =1200 yr. Larger recurrence intervals generate larger coseismic and early postseismic deformation, while the interseismic rates just before the earthquake occurrence (preseismic) are insensitive to the length of the period of stress build-up. Therefore, the current approach cannot constrain the recurrence interval of the expected earthquakes.

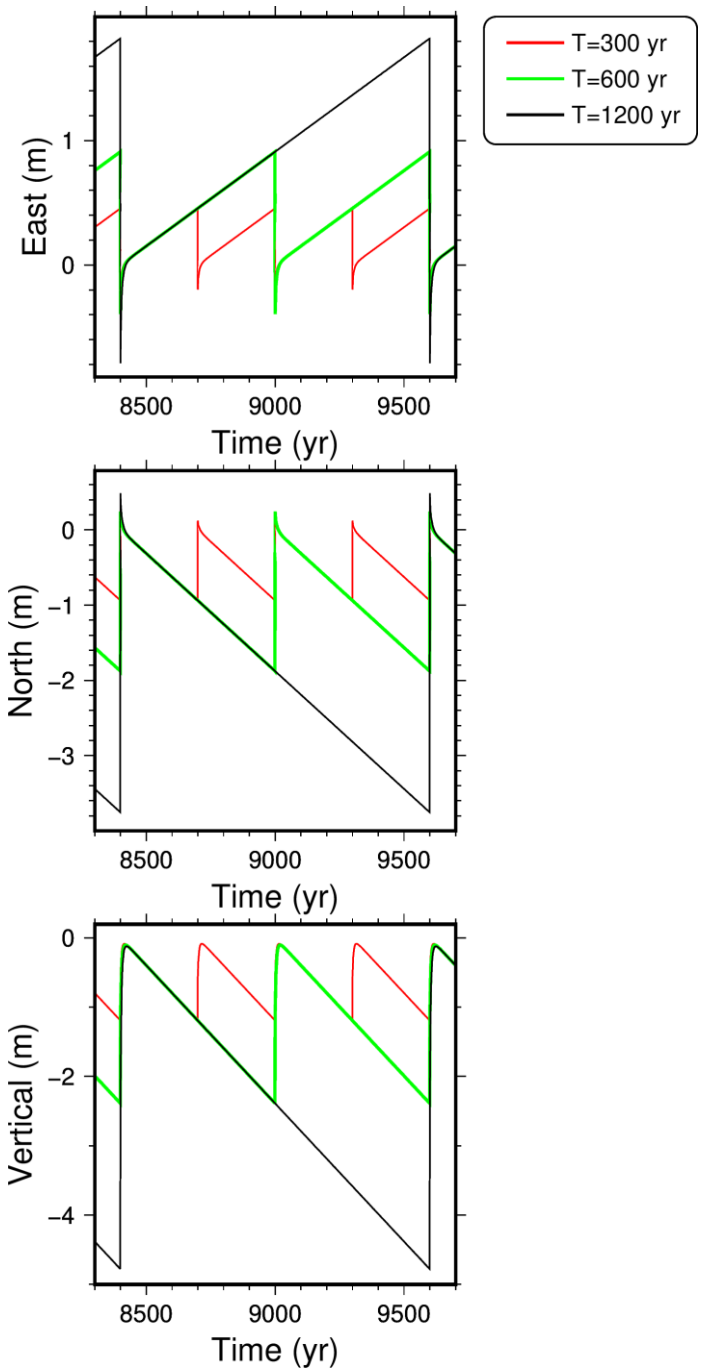

Figure 6.17*. Displacement vs time functions for CIOH site in Cartagena for different assumptions of the recurrence interval (T) in 3-dimensional components. Values of T represented by the colors in the legend.*

Figures 6.18, 6.19 and 6.20 contain plots for the remaining GPS sites in east, north and vertical components.

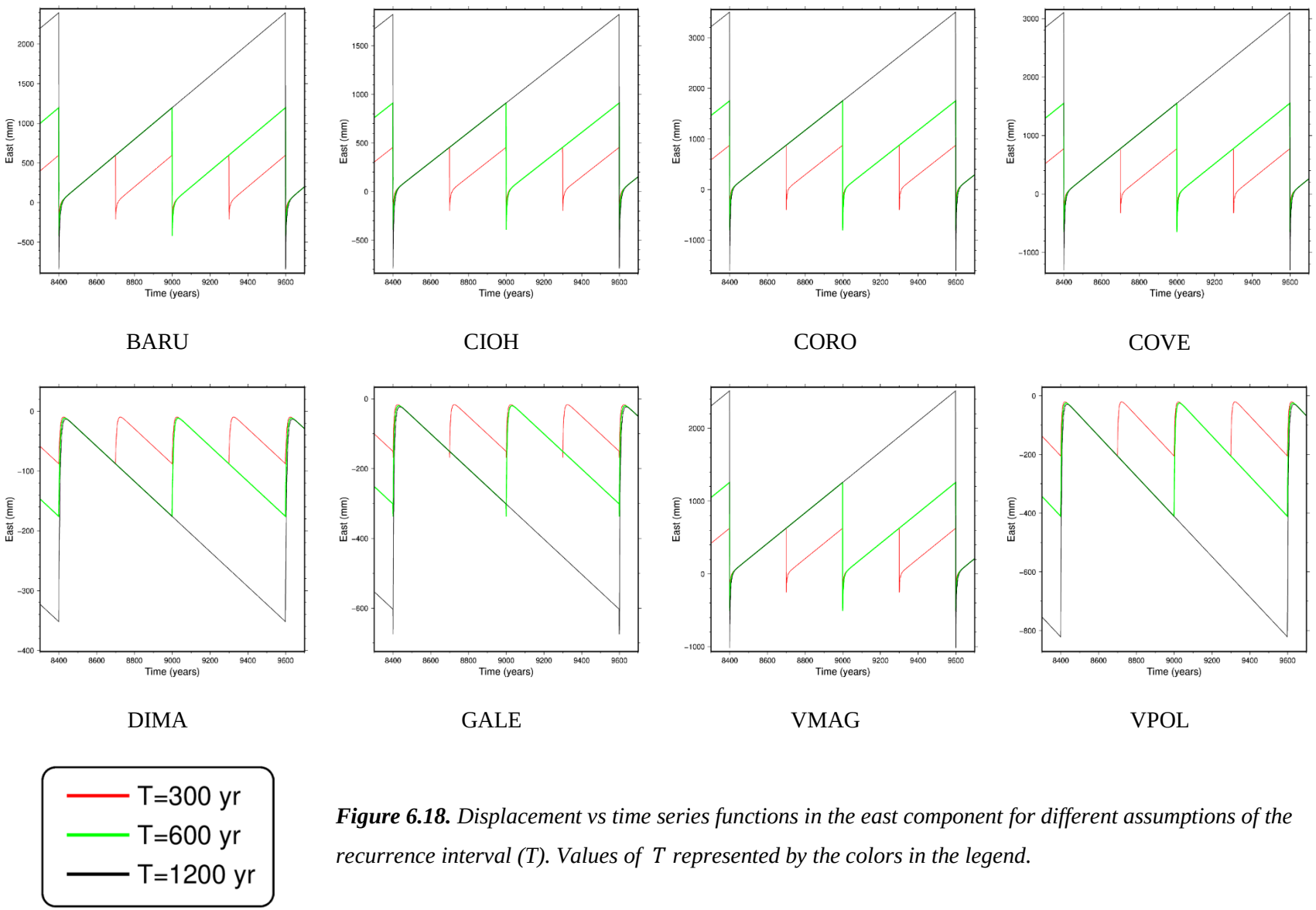

Figure 6.18. *Displacement vs time series functions in the east component for different assumptions of the recurrence interval (T). Values of T represented by the colors in the legend.*

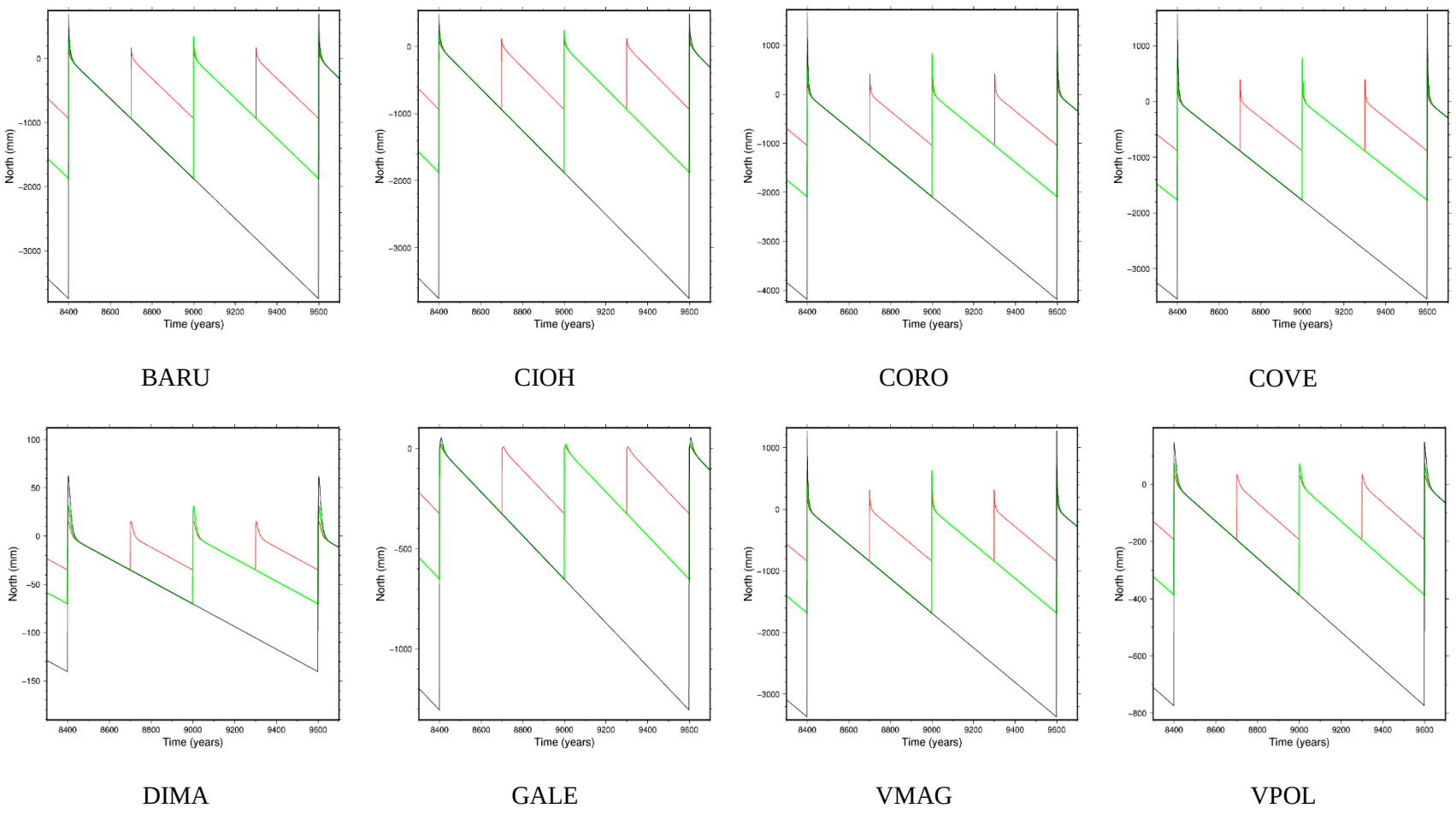

Figure 6.19. *Displacement vs time series functions in the north component for different assumptions of the recurrence interval (T). Values of T represented by the colors in the legend.*

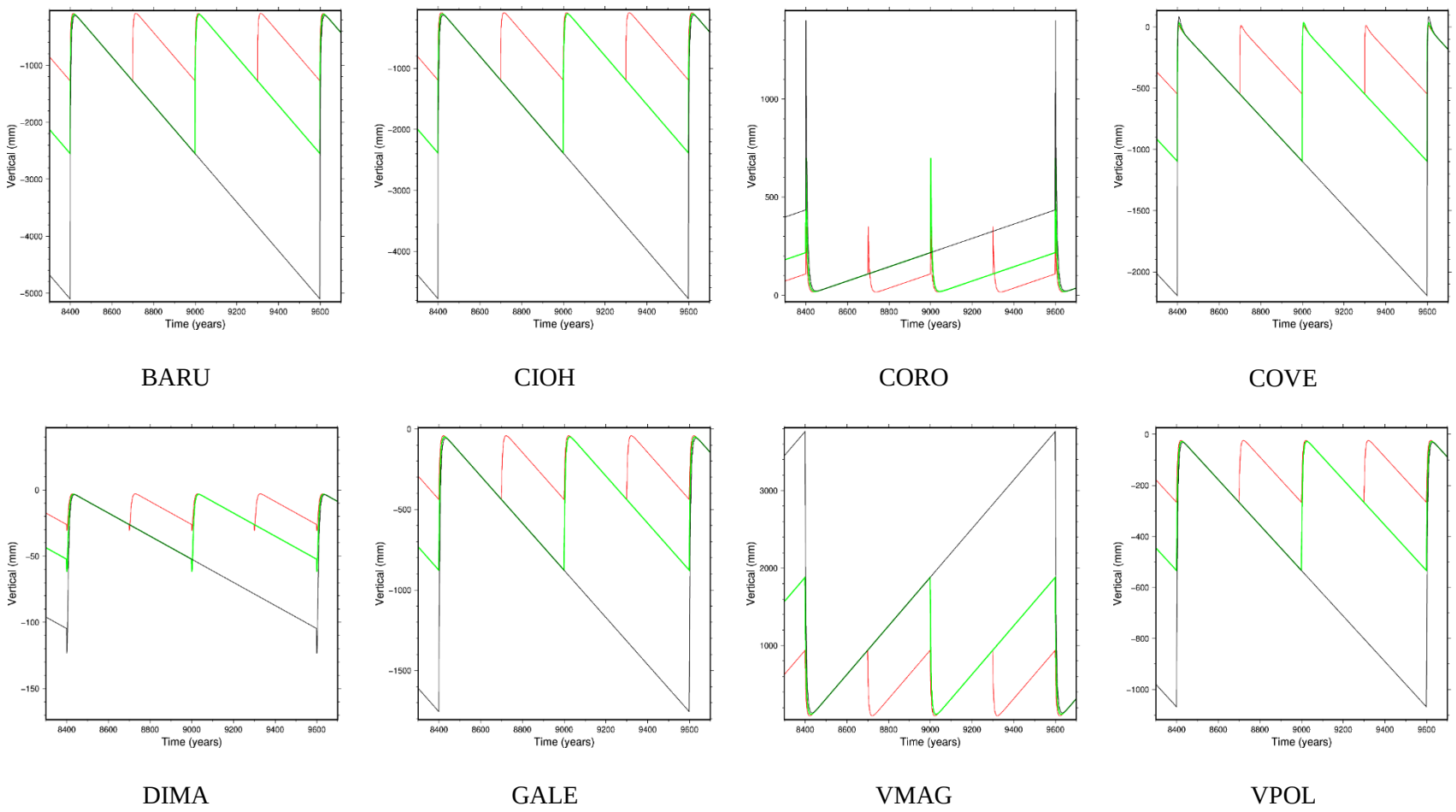

Figure 6.20. *Displacement vs time series functions in the vertical component for different assumptions of the recurrence interval (T). Values of T represented by the colors in the legend.*

6.4.Discussion

6.4.1. Contemporary vertical motions at the Caribbean slow subduction zone

Based on the modeling results, we consider that viscoelastic relaxation in the asthenospheric mantle caused by an earthquake occurring every 600 years contributes significantly to the contemporary vertical deformation observed at the GPS sites in Caribbean northwestern Colombia. This result indicates that large coseismic and postseismic vertical motions >2.4 m can be generated even under the situation of very slow subduction. It is also implied that fast subsidence over a few mm/year at the coastal locations, BARU, CIOH, and COVE (Figure 6.9a and 6.10b), is not restricted to regions with fast subduction rates such as northeast Japan (~80 mm/yr), but they can be also produced at slower subduction settings. Instead, a long recurrence interval over several hundred years is required to accumulate enough strain at the subduction interface.

This is particularly interesting since little information about the vertical crustal motions is known at slow subduction zones. The current results provide an initial hint about how the vertical motions along a slow subduction zone evolve in space and time. It is demonstrated that postseismic transient effects irrespective of their duration can have a significant contribution to the vertical displacement rates at the end of an interseismic period. Viscoelastic deformation then changes the interpretation of interseismic deformation patterns.

6.4.2. Effects of the model configuration

Assumptions about the earth model structure and locking state on the plate interface should be considered for a reasonable interpretation of the deformation patterns. The current model is highly simplified in that it does not take into account a detailed geometry of the subducting slab and assumes fixed strike, dip, and rake angles over the entire fault. In addition, a simple layered structure is assumed and the difference between the continental and oceanic lithosphere was not considered although several authors suggested that vertical motion is sensitive to the contrast in the elastic thickness at the ocean-continent boundary and details of the model structure (Wang et al, 2001; Thatcher, 2009; Trubienko et al, 2014; Sagiya; 2015; Noda et al, 2018; Itoh et al, 2019). These simplifications are reasonable in our study region since the Caribbean slab geometry is very flat with a dip angle of ~8^{o} SE from the trench to distances of ~250 km inland (Figure 5.2). Then, introducing structural heterogeneities by means of more complex approaches such as the Finite Element Method (FEM) seems unnecessary.

Despite the fact the slip distribution on the viscoelastic fault model might be too simple in comparison with the elastic coupling model (Figure 6.10), the surface deformation patterns were successfully reproduced, notably in the vertical component, thanks to the inclusion of long-earthquake recurrence and viscoelastic effects. This leads me to think that an optimization of the fault slip distribution might not be meaningful and that a simple slip tapering assumption as in section 6.2.2, does a better job.

Furthermore, I assume an end-member model where all slip deficit is released at the time of earthquakes. In fact, some other processes can take part in the reduction/increase of the coupling state at the subduction interface influencing the effective slip budget, such as (SSE). At this point, there is no observational evidence that suggests slow slip events in the CSZ in Colombia as a mechanism to accommodate plate motion in an aseismic manner. It is expected that geodetic network improvement (in both space and time) provides better resolution of plate boundary slip or slip deficit that affects the seismic potential in the Caribbean region and leads us to a better understanding of tectonic processes and their relationship with the earthquake occurrence.

As presented in section 6.3.3, I investigated the effects of different parameters, namely elastic lithosphere thickness (H), asthenosphere viscosity (η), and recurrence interval (T), in reproducing deformation signals in the study region. Within the current modeling framework, 3-dimensional interseismic crustal motions are sensitive to the lithospheric thickness (Figures 6.11 and 6.12), while the asthenospheric viscosity and the recurrence interval cannot be resolved with the available observation data.

The estimated range of the lithospheric thickness ($60 \leq H \leq 100$ km) is consistent with the results of Blanco et al. (2017) for the lithosphere-asthenosphere boundary (LAB) depths in the Caribbean-NAB transition region of ~107 ± 11 km. In their study, S-to-P high-quality receiver functions obtained based on broadband seismic waveform data from the National Seismological Network of Colombia (RSNC: Red Sismológica Nacional de Colombia, by its acronym in Spanish) between 2008 to 2015 were analyzed and classified into groups according to different geotectonic settings defined by regional interacting plates and blocks. Receiver functions were corrected to guarantee vertical incidence prior to stacking and then, LAB depths were deduced by a time-to-depth conversion using the iasp91 velocity model.

Analysis of the sensitivity of surface displacement rates to the elastic thickness shows that thicker elastic lithosphere is preferable to fit the horizontal velocity. GNSS sites located above the estimated fault are sensitive to the lithospheric thickness showing an average difference of ~2 mm/yr for values of H between 40 and 100 km (Figure 6.12a). As for the vertical component, the behavior is opposite to the horizontal one. Thinner lithospheres between 40 and 60 km thickness produce larger interseismic rates, resulting in overprediction of the vertical rates at BARU and CIOH, and VMAG (Figure 6.12b). Matsu'ura et al. (1981) and Decriem and Arnadottir. (2012) reported that the amplitude of vertical viscoelastic deformations is larger for thinner values of the elastic layer, which is consistent with these results. It seems that a thicker elastic lithosphere reaches a compromise level between both components improving the overall reproduction of observed motions.

All the above reasons clearly indicate that some components of the deformation are more or less sensitive to the variation of the earth model structure (Milne et al, 2004). However, the identification of an optimal elastic thickness value for the Caribbean is beyond the scope of this study. More important is to highlight the fact that a reasonable value of the elastic thickness between 60 and 100 km is required to interpret both deformation components with the earthquake cycle model scenario, independent of the assumption of other parameters such as viscosity value (η) and recurrence interval (T). The estimated range of the lithospheric thickness is effective at reproducing crustal motions, supporting the initial hypothesis of a megathrust earthquake/tsunami along the Caribbean coast of Colombia.

Regarding the viscosity of the asthenosphere, any of the assumed values reproduce exactly the same interseismic velocities by the end of the earthquake cycle at all the GPS sites (Figures 6.13, 6.14, 6.15 and 6.16). A limiting factor is that we only count with a snapshot of the deformation determined by the temporal resolution of our GPS data, which is insufficient to constrain the value of viscosity in the Caribbean of Colombia. Nevertheless, tested values of viscosity are in agreement with the estimations of Chen et al. (2021) that proposed asthenospheric viscosity of $(3.5\pm1.5)\text{x}10^{18}$ Pa·s for the Caribbean plate based on the analysis of dynamic topography pressure gradient and inversion of free air satellite gravity data and with viscosity estimations at subduction environments worldwide (Khazaradze et al. 2002; Pollitz et al, 2010; Wang et al, 2012; Li et al, 2015; Sagiya, 2015; Hashima and Sato, 2017; Wang, 2017).

Similar to the viscosity effects, changes in the recurrence interval T mainly affect the sizes of the coseismic displacement and the postseismic transient and its duration, which is reduced or increased "proportionally" with respect to the reference recurrence interval, T=600 yr. Then, the recurrence interval reflects the size of the earthquake (Figures 6.15 and 6.16).

6.4.3. Seismic and tsunami potential

Under the viscoelastic modeling, the estimated fully locked region for future earthquake generation with coupling ratios ≥0.8 is more or less the same size as the one estimated with the elastic coupling model (Lizarazo et al, 2021) with an area of ~15,760 km^2. The newly defined fault region corresponds to a M_w8.1 earthquake based on the relationships between the source area and magnitude (Allen and Hayes, 2017) defined by Eq. 6.8:

$$logS_1 = -3.63 + 0.96 \times M_w \quad (6.8)$$

Where S_1 represents the source area in km^2.

This moment magnitude is translated into a seismic moment of M_0=1.78x10^{21} Nm following Hanks and Kanamori (1979) as in Eq. 5.20. The seismic moment accumulation rate for the slow subduction velocity along the Caribbean-Macondo boundary amounts $\dot{M}_0$=2.98x10^{18} Nm/yr for the same parameters as in the elastic model (Chapter 5), which implies a recurrence interval of ~597 yr, still consistent with the absence of historical and instrumental records of megathrust M8-type earthquakes along the CSZ of Colombia, and coherent with previous estimates by Lizarazo et al. (2021).

The validation of the Caribbean of Colombia as a locus of megathrust earthquakes and tsunamis by means of both approaches (elastic and viscoelastic) points out the necessity of local geological studies that involve paleoseismological and paleotsunami data to validate the existence of past events along the coastal area. In the compilation presented by Engel et al. (2016) regarding coastal hazards assessment (Figure 6.21), the lack of tsunami deposits analyzed along northwestern Colombia in comparison with other regions in the Caribbean, represents a handicap to precisely constrain the seismic potential of the region, being this, magnitude and recurrence of subduction earthquakes as well as follow up tsunamis.

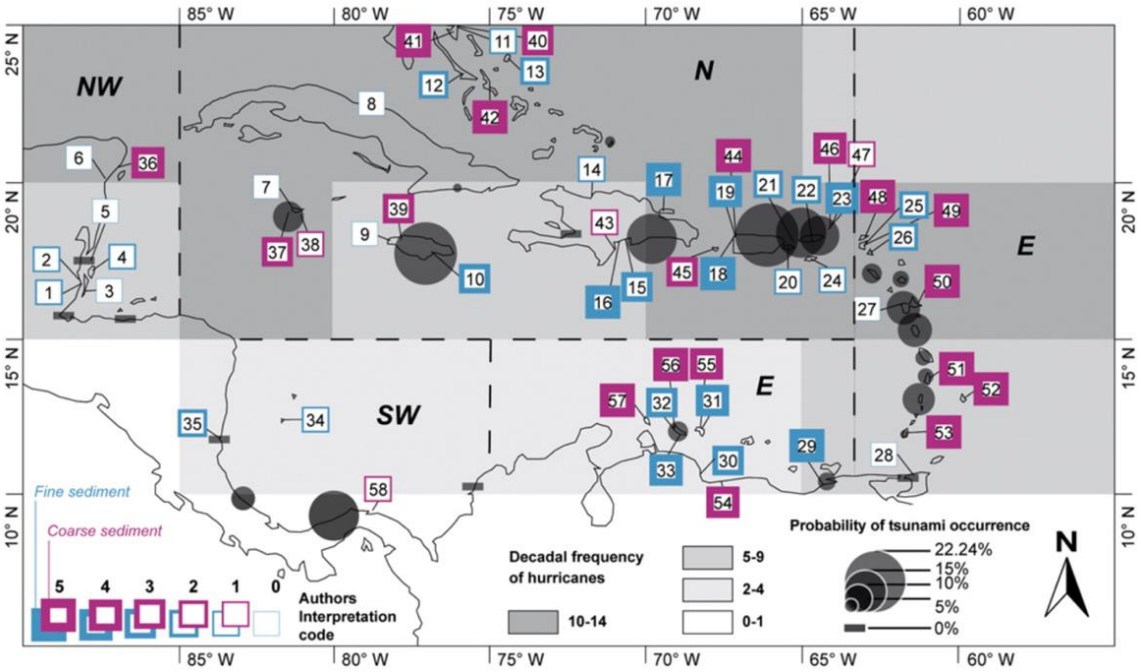

Figure 6.21. *Overview of the Caribbean tsunami potential and tsunami deposit locations. Gray circles indicate modeled probability of tsunami occurrence (run-up>0.5 m) within a period of 30 years. Blue and purple frames represent fine sedimentary records and coarse-clast records, where frame's thicknesses denote the depositional process (storm or tsunami). Greyscale quadrats represent the frequency of decadal tropical cyclones. Taken from Engel et al. (2016).*

6.5. Conclusions

I use a viscoelastic earthquake cycle model to analyze the time-dependent deformation at GPS sites in northwestern Colombia to explain mainly vertical crustal motions characterized by large subsidence on the order of 0.8 to 5.8 mm/yr. Current results indicate that viscoelastic relaxation is critical to explain observed 3-dimensional deformation and therefore, validate the CSZ as a locus of a future M_w8.1 type earthquake/tsunami with a recurrence closer to 600 yr. This also proves that slow and flat subduction settings manage to produce large vertical motions over long earthquake cycles, entailing that this feature is not restricted to normal/faster subduction zones.

Obtained time-dependent deformation functions explain deformation signals in the Caribbean of Colombia, namely, southeastward horizontal motions and generalized subsidence and its transition to uplift inland. It was shown that the postseismic transient phase is effective to increase the interseismic vertical motions at the GPS sites. Then, ignoring the viscoelastic effects triggered

by an earthquake at the Caribbean-Macondo block megathrust may result in a wrong interpretation of observed data and overlooking of the seismic potential of the region.

The analysis of the estimated interseismic deformation to different assumptions of the mechanical, rheological, and temporal parameters of the earthquake cycle model, indicates that the elastic thickness of the lithosphere *H*, is the key controlling parameter of the observed crustal motions in northwestern Colombia. A thicker lithosphere (60 km $\leq H \leq$100 km) balances the GPS velocity fitting in both components. On the other hand, estimated interseismic rates for the latter stage of the earthquake cycle are independent of the viscosity (η) and recurrence interval (T) assumptions.

Given our model simplifications and the omission of the steady part of slip in the calculations, there is no contribution of periodic earthquake occurrence to the formation of marine terraces. Available data of long-term uplift at marine terraces (Martínez et al, 2010) do not help to explain the inconsistency between short- and long-term vertical motions in the region. Further examination on short- and long-term deformation inconsistency is going to be treated in Chapter 7.

CHAPTER 7

DISCUSSION AND IMPLICATIONS

7.1. Implications of the newly defined Macondo block in the regional kinematics

Based on an improved GNSS network in Colombia, I demonstrate the existence of a new tectonic block in the northern NAB that exhibits an independent motion with respect to the main (and southern) part of it. This new block was named Macondo block and it includes two geologically defined blocks known as MB and BB blocks (Audemard, 2014), whose boundaries are not detected within the uncertainty level of the current dataset (Chapter 4). Although the extension of the Macondo block as well as its limits are not entirely defined (Figure 4.5), its implications on the current kinematics are important, especially at the Caribbean-Macondo transition, where the relative motion of the Caribbean plate only amounts to 7 mm/yr in comparison with a faster convergence of 11 mm/yr with respect to the NAB (Mora-Páez et al, 2019). Further improvements regarding the kinematics and boundaries and of the new Macondo block remain a challenge for future studies in which the density of the GNSS network plays a crucial role.

These observations help me to define Caribbean northwestern Colombia as a region where a slow subduction process is taking place in a similar fashion as the regions of Calabria and Gibraltar (Chapter 2) and other locations presented in Table 5.3 (Chapter 5). Such regions have experienced megathrust earthquakes with $M_w \geq 8.0$ followed by tsunamis in the past, which are characterized by long recurrence intervals, in some cases as long as 2000 yr. Due to the absence of instrumental evidence, current knowledge about these subduction zones has been obtained based on preserved written historical documents and/or local geological data, including paleoseismology and paleotsunami records. Along these regions a large seismic and tsunami hazard can exist regardless of the subduction velocity, but the potential can be overlooked due to the long periods of seismic quiescence and totally ignored, in the absence of historical and geological data. In the Caribbean, historical records cover the last 530 years and most of the documented earthquake and tsunami sources during that period are located in the septentrional part (Cotilla, 2012) and the Antilles (Engel et al, 2016). However, no event of such magnitude has been reported along the Caribbean coast of Colombia. Furthermore, there have been almost no geological studies to compile paleoseismological and paleotsunami information in this area. If we consider that slow strain accumulation over very long periods could potentially trigger large earthquakes and tsunamis, as

had been proved for several regions worldwide irrespective of the convergence rate, the Caribbean of Colombia becomes a typical example of a slow subduction zone. As such, the region remains unaware of such "invisible" threat and more efforts to improve alertness on potential natural hazards should be performed.

7.2. Relation between strain distribution and seismicity

The predominance of compressive tectonic strain in Colombia was presented in Chapter 4. Larger strain rates are localized along convergent margins such as the CESZ (~60 nanostrain/yr) and the Panamá-Colombia collision region (~40 nanostrain/yr), where instrumental records of interplate and intraplate seismic activity exist (Figure 4.11). The northwestern boundary of Colombia, where the Caribbean and the Macondo block interact with each other, also presents significant shortening in the NW-SE direction (~65 nanostrain/yr) without direct correspondence in the seismicity level of the region. This new observation calls for a revision of the origin of such deformation, which can be related to permanent deformation features or an ignored seismic and tsunami potential (Chapter 5, section 5.3).

I discarded the possibility that contemporary strain corresponds to permanent deformation given the inconsistency between short- and long-term deformation rates (Table 5.2). It is worth mentioning that the estimation of long-term deformation has significant uncertainty by itself as it was computed on pre-interpreted seismic section data from Mora et al. (2017) without an appropriate processing tool. To resolve the uncertainty, access to the original seismic section data and processing software is required in conjunction with a denser dataset that allows validation of long-term contraction rates along the whole extension of the SFB and the SJFB. Also, not only improvements in the spatial resolution of the GNSS network, but evaluation of different methods to compute the strain distribution and integration of other geodetic datasets such as Synthetic Aperture Radar imagery (SAR), would help to reveal details of the deformation field as well as to constrain contemporary deformation rates in aid for temporal-scale reconciliation. Nonetheless, it is still reasonable to expect that revised geological and geodetic strain rates keep presenting such disparity as the latter one only accounts for inelastic deformation while the first one includes both, elastic and inelastic deformation.

On the other hand, the hypothesis of a seismogenic scenario has been widely investigated in presence of large crustal strain rates along active regions (Shen et al, 2007). Despite the fact that

crustal strain rates along northwestern of Colombia are smaller than those reported at the faster northeast Japan subduction zone by one order of magnitude (>100 nanostrain/yr; Sagiya et al, 2000), the seismic capability of the region cannot be discarded. Carafa et al. (2018), demonstrated that low interseismic strain rates at the Calabrian Arc (~10-20 nanostrain/yr) are indeed a product of conflict between long-term extensional process and transitory interseismic contraction due to a locked interface that have ruptured in the past as supported by turbidites deposits. Then, it would be careless to assume that a seismic/tsunami threat is inexistent along the CSZ without more investigation and that is the reason why an elastic and viscoelastic interplate coupling models (Chapter 5 and Chapter 6) were implemented. Obtained results from both models confirmed the existence of a locked region able to rupture in a M_w8.0-M_w8.1 earthquake every ~600 yr presumably followed by a tsunami. Additional discussion referring to this aspect is given below.

7.3. Implications of the elastic and viscoelastic interplate coupling models on the seismogenic/tsunami potential along the Caribbean coast of Colombia

The elastic interplate coupling model (Chapter 5) was the first attempt to map the interplate locking based on GPS data inversion along the Caribbean coast of Colombia. Results indicated the region of Cartagena and its surroundings as a locus of a M_w8.0 earthquake every ~600 yr potentially followed by a tsunami due to the shallowness of the asperity (Figure 5.4). The elastic model elucidated then, an ignored potential hazard for the region in agreement with significant compressive strain rates and categorization of the region as a slow subduction zone (Lizarazo et al, 2021). The viscoelastic model (Chapter 6) addressed the flaws of the previous elastic model regarding the fitting of vertical crustal motions and reported an equivalent seismic potential (M_w8.1) and recurrence (~597 yr), confirming the seismogenic hypothesis for the Caribbean region.

From both models, the best one to describe the observed motions is the viscoelastic one that takes into account the time-dependency of the deformation over long recurrence intervals as confirmed by the velocity fitting (Figure 6.10) and respective 3-dimensional WRMS values. It is demonstrated that viscoelastic effects over an earthquake cycle of 600 yr change the interpretation of interseismic deformation data and successfully reproduced crustal deformation in northwestern Colombia.

In spite of all the reduction in the model complexity as explained in section 6.4.2, the results show that the viscoelastic approach is capable of reproducing crustal motions in the Caribbean

coast of Colombia to a better level than the elastic interplate coupling model. This successful reproduction of the observation provides a validation of the model and the predicted seismic/tsunami potential. It should be emphasized that there is no other reasonable explanation for the rapid coastal subsidence and landward displacements detected by GPS observation.

To summarize, both models (elastic and viscoelastic) support the potential occurrence of a M8 class megathrust earthquake possibly followed by a tsunami along the Caribbean of Colombia. It is thus urgent to validate or refute the current interpretation with local paleoseismology and paleotsunami data. It is expected that future geological and geomorphological field campaigns contribute to compiling evidence of past earthquakes and tsunami deposits along the Caribbean coast of Colombia, as well as to constraining the time of their occurrence by accurate dating methods such as ^{14}C for example (Ishizawa et al, 2020). With these sources of information alongside the existing ones, a better evaluation of the location, magnitude, and frequency of seismic/tsunami events can be provided to refine current estimates of the seismic budget of the region and reinforce the hazard management policies.

7.4. Long-term vs short-term vertical deformation

Preliminary estimations of long-term strain rates across a seismic section in the SJFB in northwestern Colombia revealed horizontal compressive rates that variate from 9.5 to 6.8 nanostrain/yr at the Upper Pliocene-Quaternary unconformity (See Figure 5.6 and Table 5.2). On the contrary, a much faster deformation was obtained from horizontal GPS data at the same region with average shortening rates of ~65 nanostrain/yr (Figure 4.12). In the vertical component, this situation is also observed. Contemporary GPS data shows general coastal subsidence with rates between 0.8 to 5.8 mm/yr (Figure 6.1), while long-term estimations based on marine terraces stratigraphy and paleontological data show Holocene uplift rates between 1.5 and 3.8 mm/yr (Martínez et al, 2010).

The results of the pair of performed models are useful to interpret current deformation signals. However, inconsistencies between these and long term motions remain unexplained. Particularly, in the viscoelastic model framework of this study, only perturbation effects on the boundary slip were considered, which causes all the coseismic and postseismic deformation to end up being fully recovered by constant interseismic velocities in one earthquake cycle without permanent signature in remaining deformation (Figure 6.9a). The previous result indicated that repeated large

earthquakes are not responsible for marine terraces creation and implied that alternative mechanisms are required to explain the long-term uplift. One of those mechanisms is the steady subduction of the oceanic plate that yields long-term deformation patterns as demonstrated by Sato and Matsu'ura. (1989), Hashimoto et al. (2004), Hashimoto et al. (2008), and Fukahata and Matsu'ura. (2016). Other mechanisms besides steady plate subduction that can take part in the creation of coastal topography are regional active faulting (Martínez et al, 2010), tectonic erosion (Hashima and Sato, 2017), sediment supply, climate and oceanographic dynamics (Martínez et al, 2010), mud volcanism (Duque-Caro, 1984; Vernette, 1989), just to mention a few.

Martínez et al. (2010) argued that the low-level marine terraces of the Cartagena region are a product of tectonic upheaval during the Holocene (between 3.6 and 1.7 Ka) and not a result of a highstand of relative sea-level (RSL). In this regard, the Holocene RSL database for the Caribbean compiled by Khan et al. (2016) supplied validation for Martínez et al. (2010) interpretation by concluding that RSL rates slowdown from mid-Holocene (8 to 4 Ka) and have remained relatively constant until present times in Colombia. Based on this extensive study, it is possible to grant reliability to available long-term uplifting rates in the area of Cartagena. To explain the uplifting rates, steady subduction should cause at least ~1.5 mm/yr of uplift to account for the current terraces' heights within the calibrated ^{14}C ages for dated stratigraphic sections. However, this situation seems very unlikely in view of the slow subduction velocity of the Caribbean plate that might not amount more than 1 mm/yr in the construction of coastal topography. However, if other marine terraces are identified and their formation can be attributed to sea level changes, which is equivalent to say that they correspond to older terraces (probably of Pleistocene origin), the uplift rates will be smaller.

To acquire additional data in the study region will be useful to reduce the uncertainties in each observation. Future improvements on the spatial and temporal resolution of the GPS network would enhance the regional kinematic knowledge providing more reliable velocity determinations. The integration of InSAR analysis to overcome limitations of discrete measurements would supply spatially continuous and consistent deformation features in the region. Regarding the long-term observations, there is room for further investigation by contemplating new geological and geomorphological field observations, the inclusion of more accurate in-situ measurements and the implementation of dating methods that allow deciphering late Quaternary deposits overcoming the

shortcomings of the ^{14}C method that is limited to ~50 Ka, such as Optically Stimulated Luminescence (OSL). Besides, another reason to encouraged OSL dating is to constrain better long-term uplift rates by direct comparison with existing ^{14}C ages of marine terraces in the area of Cartagena and new terraces that might be recognized in northwestern Colombia. Finally, after guarantee the appropriate dataset for analysis, modeling should be the next step to reconcile the short- and long-term discrepancy and to explain the whole deformation patterns at different time scales at the Caribbean-Macondo margin.

CHAPTER 8

CONCLUSIONS

I analyzed the crustal deformation in northwestern Colombia from GeoRED GPS data during the period 2007-2018. Interseismic velocity data from 87 permanent GPS sites allowed me to identify a new tectonic affiliation in the northern part of Colombia, named Macondo Block, that shows a rigid behavior as well as tectonic independency from the NAB (Kellogg and Vega, 1995; Bird, 2003). Under this new tectonic framework, a slow subduction process in northwestern Colombia, in which the Caribbean plate plunges in a flat geometry (~8ºSE dipping angle) below the Macondo block at a rate of ~7 mm/yr was defined. The Macondo Block extension is not completely determined by the current GPS network and some incompatibilities with the traditional tectonic framework, that includes other two regional blocks known as MB and BB blocks (Audemard, 2014), could be clarified in the future with a denser geodetic network in northern Colombia (north of 5.5ºN), along bounding active faults known as the BSMF, OF and the CLT.

The results from the strain rate distribution calculations from horizontal GPS displacement rates, helped me to recognize a predominantly compressive tectonic regime characterized by significant contraction at the CESZ and CSZ, and the intermediate collision region with the Panamá isthmus. These patterns remained even at varying the smoothing factor related to the spacing between GPS stations (75 km) along the mentioned regions, but they might not be well characterized in areas where the spatial resolution of the geodetic network is far from sufficient, such as the northeastern part of the country and along main faults. In order to detect more detailed deformation features and estimate precise strain rates, the densification of the geodetic network is a major task. Further improvement in the determination of strain concentrations in the near field of active faults could be assisted by the combination of the available GPS dataset with satellite imagery through a joint InSAR+GPS analysis.

At the Caribbean-Macondo margin in particular, the slow strain accumulation produced NW-SE compressive strain rates as large as ~65 nanostrain/yr. Similar levels of deformation have resulted in megathrust earthquakes and tsunamis along the CESZ, but do not correspond to the historical absence of these large events in the Caribbean northwestern Colombia.

To explain these peculiar observations, I first investigated the slip distribution along the CSZ with an elastic interplate coupling model. Horizontal GPS baselines and vertical velocities were inverted under a realistic geometry of the Caribbean slab to identify location and extent of locked and creeping regions. I could detect an isolated, shallow and fully coupled region offshore Cartagena city with an area of ~11000 km^2 that could rupture in a M_w8.0 earthquake followed by a tsunami releasing a total seismic moment of $1.3x10^{21}$ Nm. Taking the slow seismic moment accumulation rate of $2.0x10^{18}$ Nm, this kind of events might be repeating every 625 ± 12 yr approximately (Lizarazo et al, 2021).

Since no written records of megathrust earthquakes and/or tsunamis exist during the last 530 years of colonial and post-colonial history, which is in accord to the estimated recurrence interval, I considered an alternative interpretation in which the deformation accommodates permanently across the SJFB with no hazardous outcomes. However, this possibility was rejected given the discrepancy of one order of magnitude between geodetic and Quaternary long-term strain rates with values of -65 nanostrain/yr and -6.8 nanostrain/yr, respectively (Lizarazo et al, 2021). This inconsistency remained as well for the vertical motions. Contemporary GPS data indicates subsidence as large as 5.8 ± 1.0 mm/yr in contradiction of long-term uplifting rates at Holocene marine terraces between 1.5 and 3.8 mm/yr (Martínez et al, 2010). Providing a reconciliation for deformation at different temporal scales would be possible with denser GPS measurements in space and time that produce more precise velocity estimates reducing the uncertainties of current motions. Also, counting with original seismic profiles data across the SFB and SJFB and an adequate processing tool would contribute to refine long-terms estimates of shortening. Furthermore, updated ages for the marine terraces at the Caribbean by means of more accurate dating methods that covers the Pleistocene could suggest slower uplift velocities in agreement with the slow steady subduction of the Caribbean plate.

In view of the available evidence, I favored the megathrust-earthquake/tsunami scenario for its hazardous implications for the Caribbean region. I supported my interpretation by considering the area as a slow subduction setting (Gutscher and Westbrook, 2009). I compared several regions that have reported strong earthquakes with $M_w \geq 8.0$ followed by giant tsunamis under slow subduction velocities with respect to the NNR-MORVEL56 model (Argus et al, 2011). The CSZ moves at one of the three slowest subduction rates in the world (7 mm/yr) together with the regions of Calabria

(9 mm/yr) and Gibraltar (4 mm/yr). In these two regions, written records and paleotsunami/paleoseismology data have suggested recurrence intervals of ~500 yr and ~1500-2000 yr, respectively. Then, the identified locked region northwest Colombia could sustain an invisible seismic/tsunami hazard characterized by long periods of quiescence that would be nearing its end. To aide corroborating the elastic model interpretation, further multidisciplinary studies are required, in particular, the integration of paleoseismic records seems indispensable towards this purpose.

The elastic model provided essential evidence of an overlooked seismic and tsunami potential at the Caribbean coast of Colombia. Although the model itself reproduced horizontal SE velocities, it failed to reproduce vertical motions characterized by fast coastal subsidence as large as ~5.8 mm/yr. To overcome this issue, a viscoelastic model was utilized to incorporate the effects of time-dependent deformation over an earthquake cycle into the interseismic deformation patterns (Sagiya, 2015; Noda et al, 2018). Then, I implemented a viscoelastic cycle model in which the source region, represented by a rectangular fault embedded in an elastic lithosphere overlying a viscoelastic asthenosphere, is loaded at a rate of 7 mm/yr and ruptures every 600 yr.

As a result of the model, a 200x175 km^2 rectangular fault shifted to the SE to a deeper depth than the elastic coupling contours was identified as the source of deformation in the study region. The area would potentially release a seismic moment of $1.78x10^{21}$ Nm every 597 yr at the current slow subduction velocity. These results offer important validation for the Caribbean of Colombia as a as a locus of a M_w8.1 earthquake, possibly followed by a tsunami in agreement with the previous elastic model interpretation. The viscoelastic model was able to reproduce large vertical motions at the coastal GPS sites during the co- and postseismic phases, which generates larger subsidence rates by the end of the earthquake cycle in consistency with observations. On this regard, the early postseismic transient, independent of its duration, contributes effectively to increase interseismic velocities changing the interpretation of the deformation patterns.

It was inferred that the interseismic deformation along the Caribbean was mostly controlled by the elastic lithosphere thickness (H) and did not show sensitive to variations in the asthenospheric viscosity (η) or recurrence interval (T). The latter two parameters generated larger effects on the coseismic displacement, the postseismic transient and its duration. A lithospheric thickness range between 60 and 100 km aided to resolve observed crustal motions, being 80 km the one that

minimizes the 3-dimensional weighted errors. The current dataset, despite its improved spatial and temporal resolution, inhibited to constrain de value of viscosity for the Caribbean region. Denser GPS observations (field and continuous sites) in space and time are needed to refine proposed values of mechanical and rheological parameters in the region.

My modeling attempts indicate the possibility of a megathrust earthquake (M_w8.0 – M_w8.1) and tsunami in the Caribbean northwestern Colombia that have not been observed so far and for which there are no written nor paleoseismic records. Therefore, it becomes vital to strength the current study interpretation in conjunction with additional geological information. Datable paleotsunami deposits would provide factual evidence of past earthquakes/tsunamis enabling a better assessment of the seismic budget along this margin and consequently, contributing to increase the awareness in relation to these events and their effects. To a higher decision level, the presented results can provide elements to ameliorate hazard management in the Caribbean region which include not only the densification of existing GPS and seismic networks, but also, the allocation of resources to carry out multidisciplinary studies that serve to update the current knowledge of the kinematics, tectonics and seismic/tsunami potential of the northern part of Colombia.

BIBLIOGRAPHY

Akaike, H (1980). Likelihood and the Bayes procedure. Trabajos de Estadística y de Investigación Operativa, 31, 143-166. https:// doi.org/10.1007/BF02888350

Allen, T.I., Hayes, G.P (2017). Alternative rupture-scaling relationships for subduction interface and other offshore environments. Bulletin of the Seismological Society of America, 107. https://doi.org/10.1785/0120160255

Altamimi, Z., Collilieux, X., Metivier, L (2011). ITRF2008: an improved solution of the international terrestrial reference frame. Journal of Geodesy, 85, 457–473. https://doi.org/10.1007/s00190-011-0444-4

Altamimi, Z., Metivier, L., Collilieux, X (2012). ITRF2008 plate motion model. Journal of Geophysical Research: Solid Earth, 117 (B7). https://doi.org/10.1029/2011JB08930

Altamimi, Z., Rebischung, P., Metivier, L., Collilieux, X (2016). ITRF2014: A new release of the International Terrestrial Reference Frame modeling nonlinear station motions. Journal of Geophysical Research, 121, 6109-6131. https://doi.org/10.1002/2016JB013098.

Altamimi, Z., Metivier, L., Rebischung, P., Rouby, H., Collilieux, X (2017). ITRF2014 Plate motion model. Geophysics Journal International, 209, 1906-1912. https:// doi.org/10.1093/gji/ggx136

Amelung, F., Galloway, D.L., Bell, J.W., Zebker, H.A., Laczniak. R.J (1999). Sensing the ups and downs of Las Vegas: InSAR reveals structural control of land subsidence and aquifer-system deformation. Geology, 27, 483-486.

Arcila, M., Muñoz-Martín, A (2020). Integrated perspective of the present-day stress and strain regime in Colombia from analysis of earthquake focal mechanisms and geodetic data. The Geology of Colombia, Volume 4: Quaternary. Servicio Geológico Colombiano, Publicaciones Geológicas Especiales, 38, 707-745, Bogotá. https:// doi.org/10.32685/pub.esp.38.2019.17

Argus, D. F., Gordon, R. G., DeMets, C (2011). Geologically current motion of 56 plates relative to the no-net-rotation reference frame. Geochemistry, Geophysics, Geosystems, 12, 1-13. https://doi.org/10.1029/2011GC003751

Audemard, F (2003). Geomorphic and geologic evidence of ongoing uplift and deformation in the Merida Andes, Venezuela. Quaternary International, 101-102, 43-65. https://doi.org/10.1016/S1040-6182(02)00128-3

Audemard, F., Singer, P.A., Soulas, J-P (2006). Quaternary faults and stress regime of Venezuela. Revista de la Asociación Geológica Argentina, 61, 480–491.

Audemard, F (2014). Active block tectonics in and around the Caribbean: A review. Chapter 2 in the Northeastern limit of the South American plate – Lithospheric structures from the surface to the mantle, Schmitz M., Audemard and Urbani F (editors). Facultad de Ingeniería – Universidad Central de Venezuela y FUNVISIS, Caracas, Venezuela. ISBN 978-980-00-2800-1, 29-77.

Baloglanov, E.E., Abbasov, O.R., Akhundov, R.V (2018). Mud volcanoes of the world: classifications, activities and environmental hazard (Informational-Analytical review). European Journal of Natural History, 5, 12-26.

Bermúdez, J.C., Kumagai, H (2020). Repeating earthquakes along the Colombian subduction zone. Journal of Disaster Research, 15 (5). https://doi.org/10.120965/jdr.2020.p0645

Bernal-Olaya, R., Mann, P., Vargas, CA (2015). Earthquake, tomographic, seismic reflection, and gravity evidence or a shallowly dipping subduction zone beneath the Caribbean margin of northwestern Colombia. Petroleum Geology and Potential of the Colombian Caribbean Margin: AAPG Memoir 108, 247-269.

Bevis, M., Brown, A.J (2014). Trajectory models and reference frames for crustal motion geodesy. Journal of Geodesy, 88, 283-311. https://doi.org/10.1007/s00190-013-0685-5.

Bird, P (2003). An updated digital model of plate boundaries. Geochemistry, Geophysics, Geosystems, 4, 1–52. https://doi.org/10.1029/2001GC000252.

Blanco, J.F., Vargas, C.A., Monsalve, G (2017). Lithospheric thickness estimation beneath northwestern South America from and S-wave receiver function analysis. Geochemistry, Geophysics, Geosystems, 18, 1376– 1387, doi:10.1002/2016GC006785

Bos, M.S., Fernandes, R.M.S., Williams, S.D.P., Bastos, L (2013). Fast error analysis of continuous GNSS observations with missing data. Journal of Geodesy, 87, 351-360. doi:10.1007/s00190-012-0605-0.

Boschman, L., van Hinsbergen, D., Torsvik, T., Spakman, W., & Pindell, J. (2014). Kinematic reconstruction of the Caribbean region since the Early Jurassic. Earth-Science Reviews, 138, 102–136. https://doi.org/10.1016/j.earscirev.2014.08.007.

Brocher, T.M (2005). Empirical relation between elastic wavespeeds and density in the Earth's crust. Bulletin of the Seismological Society of America, 95, No.6, 2081-2092. Doi:10.1785/0120050077

Burgmann, R., Ronsen, P.A., Fielding, E.J (2000). Synthetic aperture radar interferometry to measure earth's surface topography and its deformation. Annual Review of Earth and Planetary Sciences, 28: 169-209.

Carafa, M.M.C., Kastelic, V., Bird, P., Maesano, F.E., Valensise (2018). A "geodetic gap" in the Calabrian Arc: Evidence for a locked subduction megathrust? Geophysical Research Letters, 45, 1794-1804. https://doi.org/10.1002/2017GL076554

Caro, M., Spratt, D (2003). Tectonic evolution of the San Jacinto Fold Belt, NW Colombia. CSEG Recorder. 28, 36–43.

Carvajal, J.H (2016). Mud diapirism in the Central Colombian Caribbean coastal zone. In: Landscapes and landforms of Colombia, World geomorphological landscapes. Ed: M.Hermelin. Springer international Publishing. DOI 20.1007/978-3-319-11800-0_3

Carvajal, J.H., Mendivelso, D (2017). Volcanismo de lodo del Caribe Colombiano. Colección Publicaciones Especiales Servicio Geológico Colombiano. Ed: Imprenta Nacional de Colombia. ISBN: 978-958-59782-0-1

Chang, T., Warren, L.M., Prieto, G.A (2017). Precise locations of intermediate-depth earthquakes in the Cauca cluster, Colombia. Bulletin of the Seismological Society of America, 107 (6), 2649-2663. doi: 10.1785/0120170127

Chen, Y-W., Colli, L., Bird, D.E., Wu, J., Zhu, H (2021). Caribbean plate tilted and actively dragged eastwards by low viscosity asthenospheric flow. Nature Communications. https://doi.org/10.1038/s41467-021-21723-1

Chlieh, M., Mothes, P.A., Nocquet, J-M., Jarrin, P., Charvis, P., Cisneros, D., Font, Y., Collot J.-Y., Villegas-Lanza, J.C., Rolandone, F., Vallee, M., Regnier, M., Segovia, M., Martin, X., Yepes, H (2014). Distribution of discrete seismic asperities and aseismic slip along the Ecuadorian Megathrust. Earth and Planetary Science Letters, 400, 292-301. https://doi.org/10.1016/j.epsl.2014.05.027

Chlieh, M., Beauval, C., Yepes, J., Mariniere., Saillard, M and Audin, L (2021). Seismic and aseismic cycle of the Ecuador-Colombia subduction zone. Frontiers in Earth Science, doi: 10.3389/feart.2021.701720

Cifuentes, H. G., Sarabia, A.M (2006). Estudio macrosísmico del sismo del 22 de mayo de 1834, Santa Marta (Magdalena). Instituto Colombiano de Geología y Minería - INGEOMINAS.

Cifuentes, H. G., Sarabia, A.M (2009). Estudio macrosísmico del sismo del 26 de diciembre de 1942, Lorica (Córdoba). Instituto Colombiano de Geología y Minería - INGEOMINAS.

Cifuentes, H. G., Sarabia, A.M (2010). Estudio macrosísmico del sismo ocurrido el 5 de abril de 1975 en la Costa Atlántica. Instituto Colombiano de Geología y Minería - INGEOMINAS.

Clark, K., Howarth, J., Litchfield, N., Cochran, U., Turnbull, J., Dowling, L., Howell, A., Berryman, K., Wolfe, F (2019). Geological evidence for past large earthquakes and tsunamis along the Hikurangi subduction margin, New Zealand. Marine Geology, 412, 139-172. https://doi.org/10.1016/j.margeo.2019.03.00

Coates, A.G., Collins, L.S., Aubry, M-P., Berggren, W.A (2004). The Geology of the Darien, Panamá, and the late Miocene-Pliocene collision of the Panamá arc with northwestern South America. GSA Bull. 116, 1327-1344. https://doi.org/10.1130/B25275.1.

Coates, A.G., Stallard, R.F (2013). How old is the isthmus of Panamá? Bulletin of marine science, 89 (4), 801-813. https://doi.org/10.5343/bms.2012.1076

Cortés, M., Angelier, J., Colletta, B (2005). Paleostress evolution of the northern Andes (Eastern cordillera of Colombia): Implications of plate kinematics of the South Caribbean region. Tectonics, 24 (1). https://doi.org/10.1029/2003TC001551

Cotilla Rodríguez, M.O (2012). Historia sobre la sismología del Caribe Septentrional. Revista de Historia de América, 147, 111-154.

Cox, M.G (1972). The numerical evaluation of B-splines. IMA Journal of Applied Mathematics, 10, 134-149.

De Boor, C (1972). On calculating with B-splines. Journal of Approximation Theory, 6, 50-62.

Decriem, J., Arnadottir, T (2012). Transient crustal deformation in South Iceland Seismic Zone observed by GPS and InSAR during 2000-2008. Tectonophysics. 581, 6-18, doi:10.1016/j.tecto.2011.09.028

Diederix, H., Hernandez M, C., Torres J, E., Alonso Osorio, J., Botero, P (2009). Resultados preliminares del primer estudio paleosismológico a lo largo de la Falla de Bucaramanga, Colombia. I+D, 9, 18-23.

Duque-Caro, H. (1984). Structural style, diapirism, and accretionary episodes of the Sinú-San Jacinto Terrane, southwestern Caribbean borderland. In: W.E. Bonini., R.B. Hargraves., R. Shagam (eds.). The Caribbean-South American plate boundary and regional tectonics. Vol. 162, 303-316. Geological Society of America. https://doi.org/10.1130/MEM162-p303

Duque-Caro, H (1990). The Choco block in the northwestern corner of South America: Structural, tectonostratigraphic and paleographic implications. Journal of South American Earth Sciences, 3 (1), 71-84. https://doi.org/10.1016/0895-9811(90)90019-W

Engel, M., Oetjen, J., May, S.M., Bruckner, H (2016). Tsunami deposits of the Caribbean – Towards an improved coastal hazard assessment. Earth-Science Reviews, 163, 260-296. http://dx.doi.org/10.1016/j.earscirev.2016.10.010

Feaux, K., Braun, J.J, Calais, E., Mattioli, G.S., Miller, M.M., Normandeau, J., Sandru, J., Wang, G (2012). COCONet (Continuously Operating Caribbean GPS Observational Network) - A multihazard GPS/Met observatory: Enhancing geodetic infrastructure and the scientific community in the Caribbean.

Freymueller, J.T., Kellogg, J.N., Vega, V (1993). Plate motions in the north Andean region. Journal of Geophysical Research, 98, 21853-21863. https://doi.org/10.1029/93JB00520.

Fukahata, Y., Matsu'ura, M (2016). Deformation of island-arc lithosphere due to steady plate subduction. Geophysics Journal International, 204, 825-840. https://doi.org/10.1093/gji/ggv482

Gambolati, G., Teatini, P., Ferronato, M (2005). Anthropogenic land subsidence. In: Anderson MG (ed) Encyclopedia of hydrological sciences. Wiley, Wiley Online Library, 17 pp. http://onlinelibrary.wiley.com/book/10.1002/0470848944.,jsessionid=5ECA1E367646E2E75793ACE0CFBFDF11.d02t02

García-Reyes, A., Dyment, J (2021). Structure, age and origin of the Caribbean plate unraveled. Earth and Planetary Science Letters, 571 (117100). https://doi.org/10.1016/j.epsl.2021.117100

Gómez-García, A.M., Le Breton, E., Scheck-Wenderoth, M., Monsalve, G., Anikiev, D (2020). The preserved plume of the Caribbean Large Igneous Plateau revealed by 3D data-integrative methods. Solid Earth, 12, 275-298. https://doi.org/10.5194/se-12-275-2021

Gómez-Hurtado, E., Aguirre-Hoyos, L., Diederix, H., Audemard, F., Mora-Páez, H., Bohórquez-Orozco, O., Muñoz, F., González, D., López-Isaza, J., Escobar-Rey, K., Martínez-Díaz, G., Ramírez-Cadena, J., Idárraga-García, J., López-Herrera, N., Barragán, W., Tique, P., Fonseca,

H., Jiménez, J., Plazas-Ruiz, J (2022). Neotectónica y paleosismología de la Falla de Algeciras, Huila, Colombia. Servicio Geológico Colombiano y Universidad Pedagógica y Tecnológica de Colombia, Publicaciones Especiales vol 44. DOI: https://doi.org/10.32685/9789585399389

Gómez-Martínez, D.M., López, C.M., Monsalve, M.L., Agudelo, A., Cortes, G.P., Calvache, M.L (2021). Active volcanism in Colombia and the role of the Servicio Geológico Colombiano. Volcanica - Special issue collection of volcano observatories in Latin America. 4 (S1), 113-139. https://doi.org/10.30909/vol.04.S1.113139

Goudarzi, MA., Cocard, M., Santerre, R (2014). EPC: Matlab software to estimate Euler pole parameters. GPS Solutions, 18, 153-162. https://doi.org/10.1007/s10291-013-0354-4

[dataset] Grupo de investigación Mapa Geológico de Colombia (2015). Geological Map of Colombia 2015, scale 1:1.000.000. Geological Survey of Colombia – SGC. https://www2.sgc.gov.co/MGC/Paginas/gmc_1M2015.aspx

Gurevich, A.E., Chilingarian, G.V (1993). Subsidence over producing oil and gas fields and gas leakage to the surface. Journal of Petroleum Science and Engineering. 9 (3), 239-250. https://doi.org/10.1016/0920-4105(93)90017-9

Gutscher, M-A (2001). An Andean model of interplate coupling and strain partitioning applied to the flat subduction zone of SW of Japan (Nankai Trough). Tectonophysics, 333, 95-109

Gutscher, M-A (2002). Andean subduction styles and their effect on thermal structure and interplate coupling. Journal of South America Earth Sciences, 15 (1), 3-10. https://doi.org/10.1016/S0895-9811(02)00002-0

Gutscher, M-A., Roger, J., Baptista, M-A., Miranda, J.M., Tinti, S (2006). Source of the 1693 Catania earthquake and tsunami (southern Italy): New evidence from tsunami modeling of a locked subduction fault plane. Geophysical Research Letters, 33, 1-4. https://doi.org/10.1029/2005GL025442

Gutscher, M-A (2006). The great Lisbon earthquake and tsunami of 1755: Lessons from the Sumatra earthquakes and possible link to Plato's Atlantis. European Review, 14, 181-191

Gutscher, M-A., Westbrook, G.K (2009). Great earthquakes in slow-subduction, low taper margins. Subduction zone geodynamics. Frontiers in Earth Sciences, 119-133. https://doi.org/10.1007/978-3-540-87974-9_7

Gutscher, M-A., Dominguez, S., Westbrook, G.K., Le Roy, P., Rosas, R., Duarte, J.C, Terrinha, P., Miranda, J.M., Graindorge, D., Gailler, A., Sallares, V., Bartolome, R (2012). The Gibraltar subduction: A decade of new geophysical data. Tectonophysics, 72-91. http://dx.doi.org/10.1016/j.tecto.1012.08038

Hanks, T.C., Kanamori, H (1979). A moment magnitude scale. Journal of Geophysical Research: Solid Earth, 84, 2348-2350, https://doi.org/10.1029/JB084iB05p02348.

Hayes, G.P, McNamara, D.E., Seidman, L., Roger, J (2013). Quantifying potential earthquake and tsunami hazard in the Lesser Antilles subduction zone of the Caribbean region. Geophysical Journal International, 196, 510-521.

Hashima, A., Sato, T (2017). A megathrust earthquake cycle model for Northeast Japan: bridging the mismatch between geological uplift and geodetic subsidence. Earth, Planets and Space, 69:23, doi: 10.1186/s40623-017-0606-6

Hashimoto, C., Fukui, K., Matsu'ura, M (2004). 3-D modeling of plate interfaces and numerical simulation of long-term crustal deformation in and around Japan. Pure and Applied Geophysics, 161, 2053-2068. Doi: 10.1007/s00024-004-3548-8

Hashimoto, C., Sato, T., Matsu'ura, M (2008). 3-D simulation of steady plate subduction with tectonic erosion: Current crustal uplift and free-air gravity anomaly in Northeast Japan. Pure and Applied Geophysics, 165, 567-583. Doi: 10.1007/s00024-008-0321-0

Hermelin, M (2015). Geomorphological landscapes and landforms of Colombia. In: World Geomorphological Landscapes, Springer. DOI 10.1007/978-3-319-11800-0_1

Herring, T.A., King, R.W., McClusky, S.C (2018). Introduction to GAMIT/GLOBK, release 10.7. Massachusetts Institute of Technology.

Hocol S.A. Map of exploration and production areas. Accessed December 2022, <https://www.hocol.com.co/sites/default/files/transparencia/documentos/mapa_activos_hocol.pdf>

Ikeda, Y (2014). Strain buildup in the Northeast Japan orogen with implications for gigantic subduction earthquakes. Episodes, 37 (4), 234-245.

Ishizawa, T., Goto, K., Yokoyama, Y., Goff, J (2020). Dating tsunami deposits: Present knowledge and challenges. Earth-Science Reviews, 200, 102971. https://doi.org/10.1016/j.earscirev.2019.102971

Itoh, Y., Wang, K., Nishimura, T., He, J (2019). Compliant volcanic arc and backarc crust in southern Kurile suggested by interseismic geodetic deformation. Geophysical Research Letters, 46, 11790-11798. https://doi.org/10.1029/2019GL084656

Jiménez D, G., Speranza, F., Faccena, C., Bayona, G., Mora, A (2015). Magnetic stratigraphy of the Bucaramanga alluvial fan: Evidence for a ≦3 mm/yr slip rate for the Bucaramanga-Santa Marta Fault, Colombia. Journal of South American Earth Sciences, 57, 12-22. https://doi.org/10.1016/j.jsames.2014.11.001

Johnson, K.M., Segall, P (2004). Viscoelastic earthquake cycle models with deep stress driven creep along the San Andreas Fault. Journal of Geophysical Research, 109, B10403. doi:10.1029/2004JB003096

Johnson, K.M., Segall, P (2005). A viscoelastic earthquake cycle model for Taiwan. Journal of Geophysical Research, 110, B10404. doi:10.1029/2004JB003516

Kanamori, H., McNally, K (1982). Variable rupture mode of the subduction zone along the Ecuador-Colombia coast. Bulletin of the Seismological Society of America, 72 (4), 1241-1253, doi: https://doi.org/10.1785/BSSA0720041241

Khan, N., Ashe, E., Horton, B., Duton, A., Kopp, R., Brocard, G., Engelhart, S., Hill, D., Peltier, W.R., Vane, C., Scatena, F (2017). Drivers of Holocene sea-level change in the Caribbean. Quaternary Sciences Review, 115 (1), 13-36. https://doi.org/10.1016/j.quascirev.2016.08.032

Khazaradze, G., Wang, K., Klotz, J., Hu, Y., He, J (2002). Prolonged post-seismic deformation of the 1960 great Chile earthquake and implications for mantle rheology. Geophysical Research Letters, 29, No 22, doi:10.1029/2002GL015986

Kellogg, N. J., Vega, V (1995). Tectonic development of Panamá, Costa Rica, and the Colombian Andes: Constraints from Global Positioning System geodetic studies and gravity. Geological Society of America, Special paper 295, 75-90.

Kellogg, N. J., Franco Camelio, G.B., Mora-Páez, H (2019). Cenozoic tectonic evolution of the North Andes with constraints from volcanic ages, seismic reflection, and satellite geodesy. Andean Tectonics, 69-102. https://doi.org/10.1016/B978-0-12-816009-1.00006-X

Kierulf, H.P., Steffen, H., Ross-Simpson, M.J., Lidberg, M., Wu, P., Wang, H (2013). A GPS velocity field for Fennoscandia and a consistent comparison to glacial isostatic adjustment models. Journal of Geophysical Research: Solid Earth, 119, 6613-6629, doi:10.1002/2013JB010889.

Klotz, J., Khazaradze, G., Angermann, D., Reigber, C., Perdomo, P., Cifuentes, O (2001). Earthquake cycle dominates contemporary crustal deformation in Central and Southern Andes. Earth and Planetary Science Letters, 193, 437-446. https://doi.org/10.1016/S0012-821X(01)00532-5

Kovach, R.L., Grijalva, K., Nur, A (2010). Earthquakes and civilizations in the Indus Valley: A challenge for archaeoseismology. Ancient Earthquakes. Geological Society of America. Special paper 471

Lara, M., Cardona, A., Monsalve, G., Yarce, J., Montes, C., Valencia, V., Weber, M., De la Parra, F., Espitia, D., López-Martínez, M (2013). Middle Miocene near trench volcanism in northern Colombia: A record of slab tearing due to the simultaneous subduction of the Caribbean plate under South America and Central America? Journal of South American Earth. Sciences, 45, 24-41. https://doi.org/10.1016/j.jsames.2012.12.006

Li, S., Moreno, M., Bedford, J., Rosenau, M., Oncken, O (2015). Revisiting viscoelastic effects on interseismic deformation and locking degree: A case study of the Peru-North Chile

subduction zone. Journal of Geophysical Research: Solid Earth, 120, 4522-4538. https://doi.org/10.1002/2015JB011903

Li, S., Wang, K., Wang, Y., Jiang, Y., Dosso, S.E (2018). Geodetically inferred locking state of the Cascadia megathrust based on a viscoelastic model. Journal of Geophysical Research: Solid Earth, 123, 8056-8072. https://doi.org/10.1029/2018JB015620

Lizarazo, S.C (2020). Active deformation and seismic potential in Colombia revealed by GeoRED GPS data. [Master thesis, Nagoya University]

Lizarazo, S.C., Sagiya, T., Mora-Páez, H (2021). Interplate coupling along the Caribbean coast of Colombia and its implications for seismic/tsunami hazards. Journal of South American Earth Sciences, 110, 103332. https://doi.org/10.1016/j.jsames.2021.103332

Lobo-Guerrero, A (2003). Efectos de sobreexplotación del agua subterránea en la infraestructura de superficie de la Sabana de Bogotá (Colombia).

Mantilla-Pimiento, A.M (2007). Crustal structure of the southwestern Colombian Caribbean margin: Geological interpretation of geophysical data. [Doctoral dissertation, Friedrich Schiller University Jena].

Mantilla-Pimiento A.M., Jentzsch G., Kley J., Alfonso-Pava C (2009). Configuration of the Colombian Caribbean Margin: Constraints from 2D Seismic Reflection data and Potential Fields Interpretation. In: Lallemand S., Funiciello F. (eds.) Subduction Zone Geodynamics. Frontiers in Earth Sciences. Springer, Berlin, Heidelberg

Mao, A., Harrison, C.G.A., Dixon, Timothy. (1999). Noise in GPS coordinate time series. Journal of Geophysical Research, 104, 2797-2816.

Marinière, J., Beauval, C., Nocquet, J-M., Chlieh, M., Yepes, H (2021). Earthquake recurrence model for the Colombia-Ecuador subduction zone constrained from seismic and geodetic data, implications for PSHA. Bulletin of the Seismological Society of America, 111 (3): 1508-1528. doi: https://doi.org/10.1785/0120200338

Martínez, J.I., Yokoyama, Y., Gómez, A., Delgado, A., Matsuzaki, H., Rendon, E (2010). Late Holocene marine terraces of the Cartagena region, southern Caribbean: The product of neotectonism or a former high stand in sea-level? Journal of South American Earth Sciences, 29, 214-224. doi:10/1016/j.jsames.2009.08.010

Matsu'ura, M., Tanimoto, T., Iwasaki, T (1981). Quasi-static crustal deformation due to a surface load: rheological structure of the earth's crust and upper mantle. Journal of Physics of the Earth, 30, 469-508. https://doi.org/10.4294/jpe1952.30.469

Matsu'ura, M., Sato, T (1989). A dislocation model for the earthquake cycle at convergent plate boundaries. Geophysical Journal International, 96, 23-32. https://doi.org/10.1111/j.1365-246X.1989.tb05247.x

Matthews, K., Maloney, K., Zahirovic, S., William, S., Seton, M., & Muller, D. (2016). Global plate boundary evolution and kinematics since the Late Paleozoic. Global and Planetary Change, 146, 226–250. https://doi.org/10.1016/j.gloplacha.2016.10.002

Mencin, D (2018). Periodic and static strain investigations with borehole strainmeters and GPS. [Doctoral dissertation, University of Colorado].

Mendoza, C., Dewey, J.W (1984). Seismicity associated with the great Colombia-Ecuador earthquakes of 1942, 1958, and 1979: Implications for barrier models of earthquake rupture. Bulletin of the Seismological Society of America, 74 (2): 577–593. doi: https://doi.org/10.1785/BSSA0740020577

Meneses-Gutierrez, A., Segall, P., Sagiya, T (2022). How steady is interseismic crustal deformation in northeast Japan? Evidence from an integrated analysis of centennial geodetic data. Journal of Geophysical Research: Solid Earth, 127, e2021JB023100. https://doi.org/101029/2021JB023100

Métois, M., Socquet, A., Vigny, C (2012). Interseismic coupling, segmentation and mechanical behavior of the central Chile subduction zone. Journal of Geophysical Research: Solid Earth, 117, B03406, doi:10.1029/2011JB008736.

Milne, G.A., Mitrovica, J.X., Scherneck, H-G., Davis, J.L., Johansson, J.M., Koivula, H., Vermeer, M (2004). Continuous GPS measurements of postglacial adjustment in Fennoscandia. Journal of Geophysical Research, 109, B-02412, doi:10.1029/2003JB002619

Mora, J.A., Oncken, O., Le Breton, E., Ibañez-Mejia, M., Faccenna, C., Veloza, G., Velez, V., de Freitas, M., Mesa, A (2017). Linking late Cretaceous to Eocene Tectonostratigraphic of the San Jacinto Fold Belt of NW Colombia with Caribbean Plateau collision and flat subduction. Tectonics, 36, 2599-2629.

Mora, J.A., Oncken, O., Le Breton, E., Mora, A., Veloza, G., Velez, V., de Freitas, M., Mesa, A (2018). Controls on forearc basin formation and evolution: Insights from Oligocene to recent tectono-stratigraphy of the Lower Magdalena Valley basin northwest Colombia. Marine and Petroleum Geology, 97, 288–310. https://doi.org/10.1016/j.marpetgeo.2018.06.032

Mora-Páez, H (2006). "Red Nacional de Estaciones Geodésicas Satelitales GPS para estudios e investigaciones geodinámicas". Documento BPIN y Fichas de Proyecto, MGA para Departamento Nacional de Planeación. INGEOMINAS, 63 p. Bogotá.

Mora-Páez, H., Peláez-Gaviria, J-R, Diederix, H., Bohorquez-Orozco, O., Cardona-Piedrahita, L., Corchuelo-Cuervo, Y., Ramirez-Cadena, J., Diaz-Mila, F (2018a). Space geodesy infrastructure in Colombia. Seismological Research Letters, 89, 446-452. https: //doi.org/10.1785/0220170185.

Mora-Páez, H., Carvajal, H., Ferrero, A., León, H., Andrade, C (2018b). On natural gas venting and preliminary results on subsidence in the Cartagena Bay (Colombia). Boletin Cientifico CIOH, 38, 35-51. DOI: 10.26640/22159045.448

Mora-Páez, H., Kellogg, J.N., Freymueller, J.T., Mencin, D., Fernandes, R.M.S., Diederix, H., LaFemina, P., Cardona-Piedrahita, L., Lizarazo, S., Peláez Gaviria, J-R., Diaz-Mila, F., Bohórquez-Orozco., O., Giraldo-Londoño, L., Corchuelo-Cuervo, Y (2019). Crustal deformation in the Northern Andes: A new velocity field. Journal of South American Earth Sciences, 89, 76-91, https://doi.org/10.1016/j.jsames.2018.11.002

Mora-Páez, H (2020). Crustal movements in Colombia based on GPS space geodesy with the GeoRED network. [Doctoral dissertation, Nagoya University].

Mothes, P.A., Nocquet, J-M., Jarrin, P (2013). Continuos GPS network operating throughout Ecuador. EOS 94, 229-231, https://doi.org/10.1002/2013EO260002

Muller, D., Sdrolias, M., Gaina, C., Roest, W.R (2008). Age, spreading rates and spreading asymmetry of the world's ocean crust. Geochemistry, Geophysics, Geosystems, 9 (4). Q04006, doi:10.1029/2007GC001743. ISSN: 1525-2027

Nishimura, T., Sagiya, T., Stein, R.S (2005). Crustal Block kinematics and seismic potential of the northernmost Philippine Sea plate and Izu microplate, central Japan, inferred from GPS and levelling data. Journal of Geophysical Research, 112, 1-22. https://doi.org/10.1029/2005JB004102

[Dataset] NOAA National Geophysical Data Center. 2009: ETOPO1 1 Arc-Minute Global Relief Model. NOAA - National Oceanic and Atmospheric Administration. https://www.ngdc.noaa.gov/mgg/global/

Nocquet, J-M., Villegas-Lanza, J.C., Chlieh, M., Mothes, P.A., Rolandone, F., Jarrin, P., Cisneros, D., Alvarado, A., Audin, L., Bondoux, F., Martin, X., Font, Y., Regnier, M., Vallee, M., Tran, T., Beauval, C., Maguina Mendoza, J.M., Martínez, W., Tavera, H., Yepes, H (2014). Motion of continental slivers and creeping subduction in the northern Andes. Nature Geosciences 7, 287-291, doi:10.1038/ngeo2099

Noda, A., Sato, T., Fukuyama, E (2018). Slip-deficit rate distribution along the Nankai trough, southwest Japan, with elastic lithosphere and viscoelastic asthenosphere. Journal of Geophysical Research: Solid Earth. 123, 8125-8241. https://doi.org/10.1029/2018JB15515

O'Dea, A., Lessios, H.A ., Coates, A.G ., Eytan, R.I ., Restrepo-Moreno, S.A ., Cione, A.L., Colings, L.S., De Queiroz, A., Farris, D.W, Norris, R.D., Stallard, R.F., Woodburne, M.O., Aguilera, O., Aubry, M-P, Berggren, W.A., Budd, A.F., Cozzuol, M.A., Coppard, S.E., Duque-Caro, H., Finnegan, S., Gasparini, G.M., Grossman, E.L., Johnson, K.G., Keiwin, L.D., Knowlton, N., Leigh, E.G., Leonard-Pingel, J.S., Marko, P.B., Pyenson, N.D., Rachello-Dolmen, P.G.,

Soibelzon, E., Soibelzon, L., Todd, J.A., Vermeji, G.J., Jackson, J.B.C (2016). Formation of the isthmus of Panamá. Science Advances, 2 (8), e1600883. https://doi.org/10.1126/sciadv.1600883

Okada, Y (1992). Internal deformation due to shear and tensile faults in a half-space. Bulletin of the Seismological Society of America, 82, 1018-1040.

Paris, G., Romero, J.A (1993). Fallas activas de Colombia. Boletin de Geologia, 34 (2-3), Insitituto de Geologia y Mineria de Colombia – INGEOMINAS.

Paris, G., Machette, M.N., Dart, R.L., Haller, K.M (2000). Mapa and database of quaternary faults and folds in Colombia and its offshore regions. A project of the international lithosphere program task group II-2, major active faults in the world. USGS – National Earthquake Hazard Reduction Program.

Pennington, W (1981). Subduction of the Eastern Panamá basin and seismotectonics of northwestern South America. Journal of Geophysical Research, 86 (B11), 10753-10770. https://doi.org/10.1029/JB086iB11p10753

Pérez, O.J., Jaimes, M.A., Garcíacaro, E (1997). Microseismicity evidence for the subduction of the Caribbean plate beneath the South American plate in northwestern Venezuela. Journal of Geophysical Research: Solid Earth, 102 (B8), 17875-17881. https://doi.org/10.1029/96JB03174

Pérez, O.J., Bilham, R., Bendick, R., Velandia, J.R., Hernandez, N., Moncayo, C., Hoyer, M., Kozuch, M (2001). Velocity field across the southern Caribbean plate boundary and estimates of Caribbean/South American plate motion using GPS geodesy 1994-2000. Geophysical Research Letters, 28 (15), 2987-2990. https://doi.org/10.1029/2001GL013183

Pérez, O.J., Wesnousky, S.G., De La Rosa, R., Márquez, J., Uzcategui, R., Quintero, C., Liberal, L., Mora-Páez, H., Szeliga, W (2018). On the interaction of the North Andes plate with the Caribbean and South American plates in northwestern South America from GPS geodesy and seismic data. Geophysical Journal International, 214, 1986-2001.

Pollitz, F.F., McCroy, P., Wilson, D., Svarc, J., Puskas, C., Smith, R. B (2010). Viscoelastic-cycle model of interseismic deformation in the northwestern United States. Geophysical Journal International, 181, 665-696. doi: 10.1111/j.1365-246X.2010.04546.x

Pulido, N (2003). Seismotectonics of the northern Andes (Colombia) and the development of seismic networks. Bulletin of the International Institute of Seismology and Earthquake Engineering, Special Edition, 69-76.

[Dataset] Red Sismológica Nacional de Colombia (2022). Instrumental seismicity data of Colombia from 1993 to 2022. Geological Survey of Colombia – SGC. http://bdrsnc.sgc.gov.co/paginas1/catalogo/Consulta_Experta/consultaexperta_2.php

Restrepo-Angel, J.D., Mora-Páez, H., Diaz, F., Govorcin, M., Wdowinski, S., Giraldo-Londono, L., Tosic, M., Fernandez, I., Paniagua-Arroyave, J.F., Duque-Trujillo, J.F (2021). Coastal subsidence increases vulnerability to sea level rise over twenty first century in Cartagena, Caribbean Colombia. Scientific Reports. https://doi.or/10.1038/s41598-021-98428-4

Robertson, K., Flórez, A, Ceballos L, J.L (2002). Geomorfología volcánica, actividad reciente y clasificación en Colombia. Cuadernos de Geografía: Revista Colombiana de Geografía, 11 (1-2), 37-76.

Rolandone, F., Nocquet, J-M., Mothes, P., Jarrin, P., Vallee, M., Cubas, N ., Hernandez, S ., Plain, M ., Vaca, S., Font, Y (2018). Areas prone to slow slip events impede earthquake rupture propagation and promote afterslip. Science Advances, 4 (1). DOI: 10.1126/sciadv.aao6596

Rossello, E., Cossey, S (2012). What is the evidence for subduction in the Caribbean margin of Colombia? XI Simposio Bolivariano: Petroleum exploration in subandean basins “Knowledge Integration –The key to success”.

Sagiya, T (1999). Interplate coupling in the Tokai District, Central Japan, deduced from continuous GPS data. Geophysical Research Letters, 26, 2315-2318.

Sagiya, T., Miyazaki, S., Tada, T (2000). Continuos GPS array and present-day crustal deformation of Japan. Pure Applied Geophysics, 157, 2303-2322, doi :10.1007/PL00022507

Sagiya, T (2015). Paradoxical vertical crustal movement along the Pacific Coast of northeast Japan. In: Hashimoto M. (eds.) International Symposium on Geodesy for Earthquake and Natural Hazards (GENAH). International Association of Geodesy Symposia, 145. Springer, Cham. https://doi.org/10.1007/1345_2015_189

Sagiya, T., Mora-Páez, H (2020). Interplate coupling along the Nazca subduction zone on the Pacific Coast of Colombia deduced from GeoRED GPS observation data. The Geology of Colombia, Volume 4 Quaternary. Servicio Geológico Colombiano, Publicaciones Geológicas Especiales 38, p. 615-661, Bogotá. https//doi.org/10.32685/pub.esp.38.2019.15

Salcedo-Hurtado, E., Alvarado-Florez, C (2007). Intensidades del sismo de Pizarro-Choco del 15 de noviembre de 2004 en Cali-Colombia. Revista Epsilon, 9, 57-72.

Sanabria, O., Ordoñez, M., Idarraga, J., Chacón, Z., Peña, J (2021). Informe técnico-operativo de la actividad volcánica, segmento volcánico norte de Colombia. Servicio Geológico Colombiano – SGC, Manizales.

Sánchez-Rojas, J., Palma, M (2014). Crustal density structure in northwestern South America derived from analysis and 3-D modeling of gravity and seismicity data. Tectonophysics, 634, 97-115. https://dx.doi.org/10.1016/j.tecto.2014.07.026.

Savage, J.C., Prescott, W.H (1978). Asthenosphere readjustment and the earthquake cycle. Journal of Geophysical Research, 83, 3369-3376.

Savage, J.C (1983). A dislocation model of strain accumulation and release at a subduction zone. Journal of Geophysical Research: Solid Earth, 88, 4984-4996, https://doi.org/10.1029/JB088iB06p04984

Schellart, W.P (2008). Overriding plate shortening and extension above subduction zones: A parametric study to explain formation of the Andes Mountains. GSA Bulletin, 120 (11/12), 1441-1454. doi: 10.1130/B26360.1

Sepúlveda-Jaimes, F.J., Cabrera-Zambrano, F.H (2018). Tomografía sísmica 3D del nido sísmico de Bucaramanga (Colombia). Boletín de Geología, 40 (2), 15-33. DOI: 10.18273/revbol.v40n2-2018001

Shen, Z-K., Jackson, D.D., Ge, B.X (1996). Crustal deformation across and beyond the Los Angeles basin from geodetic measurements. Journal of Geophysical Research: Solid Earth, 101, 27957-27980, https://doi.org/10.1029/96JB02544

Shen, Z-K., Jackson, D.D., Kagan, Y.Y (2007). Implications of Geodetic Strain Rate for Future Earthquakes, with a Five-Year Forecast of M5 Earthquakes in Southern California. Seismological Research Letters, 78 (1).

Stiros, S.C (2010). The 8.5+ magnitude, AD365 earthquake in Crete: Coastal uplift, topography changes, archaeological and historical signature. Quaternary International, 216, 54-63.

Syracuse, EM., Abers, G.A (2003). Global compilation of variation in slab depth beneath arc volcanoes and implications. Geochemistry, Geophysics, Geosystems, 7 (5). https://doi.org/10.1029/2005GC001045

Syracuse, EM., Maciera, M., Prieto, GA., Zhang, H., Ammon, C.J (2016). Multiple plates subducting beneath Colombia, as illuminated by seismicity and velocity from the joint inversion of seismic and gravity data. Earth and Planetary Science Letters 444, 139-149, https://doi.org/10.1016/j.epsl.2016.03.050.

Taboada, A., Dimate, C., Fuenzalida, A (1998). Sismotectonica de Colombia: deformation continental activa y subducción. Fisica de la Tierra, 10, 111-147. ISSN: 0214-4557

Taboada, A., Rivera, L.A., Fuenzalida, A., Cisternas, A., Phillip, H., Bijwaard, H., Olaya, J., Rivera, C (2000). Geodynamics of the northern Andes: Subductions and intracontinental deformation (Colombia). Tectonics 19, 787-813. https://doi.org/10.1029/2000TC900004

Thatcher, W (2009). How the continents deform: The evidence from tectonic geodesy. Annual Review of Earth and Planetary Sciences, 37, 237-262, doi: 10.1146/annurev.earth.031208.100035

Toto, E.A., Kellogg, N.J (1992). Structure of the Sinú-San Jacinto fold belt – An active accretionary prism in northern Colombia. Journal of South American Earth Sciences, 5, 211-222.

Trenkamp, R., Kellogg, J.N., Freymueller, J.T., Mora P, H (2002). Wide plate margin deformation, southern Central America and northwestern South America, CASA GPS observations. Journal of South American Earth Sciences 15, 157-171, https://doi.org/10.1016/S0895-9811(02)00018-4.

Trubienko, O., Fleitout, L., Garaud, J-D., Vigny, C (2013). Interpretation of interseismic deformations and the seismic cycle associated with large subduction earthquakes. Tectonophysics. 589, 126-141. http://dx.doi.org/10.1016/j.tecto.2012.12.027

Trubienko, O., Garaud, J-D., Fleitout, L (2014). Models of postseismic deformation after megathrust earthquakes: the role of various rheological and geometrical parameters of the subduction zone. Solid Earth Discussions. 6, 427-466. doi:10.5194/sed-6-427-2014

Tselentis, G-A., Stravakakis, G., Makropoulos, K., Latousakis, J., Drakopoulos, J (1988). Seismic moments of earthquakes at the western Hellenic arc and their application to the seismic hazard of the area. Tectonophysics, 148, 73-82.

United States Geological Survey – USGS (2022). Land subsidence, accessed December 2022, <https://www.usgs.gov/mission-areas/water-resources/science/land-subsidence#overview>

Vaca, S., Vallée, M., Nocquet, J-M., Battaglia, J., Regnier, M (2018). Recurrent slow slip event as barrier to the northward rupture propagation of the 2016 Pedernales earthquake (Central Ecuador). Tectonophysics, 724-725, 80-92. https://doi.org/10.1016/j.tecto.2017.12.012

Vallée, M., Nocquet, J-M., Battaglia, J., Font, Y., Segovia, M., Regnier, M., Mothes, P., Jarrin, P., Cisneros, D., Vaca, S., Yepes, H., Martin, X., Bethoux, N., Chlieh, M (2013). Intense interface seismicity triggered by a shallow slow slip event in the Central Ecuador subduction zone. Journal of Geophysical Research, 118 (6), 2965-2981. https://doi.org/10.1002//jgrb.50216

Van Der Hilst, R., Mann, P (1994). Tectonic implications of tomographic images of subducted lithosphere beneath northwestern Colombia. Geology, 22 (5), 451-454. https://doi.org/10.1130/0091-7613(1994)022<0451:TIOTIO>2.3.CO.,2

Vargas, C.A., Duran, J (2005). State of strain and stress in northwestern of South America. Earth Sciences Research Journal, 9, (1), 43-50. ISSN 1794-6190

Vargas, C.A., Mann, P (2013). Tearing and breaking off of subducted slabs as result of collision of the Panamá arc-indenter with Northwestern South America. Bulletin of Seismological Society of America 103, 2025-2046, https://doi.org/10.1785/0120120328.

Vargas, C.A., Caneva, A., Monsalve, H., Salcedo, E., Mora, H (2015). Geophysical networks in Colombia. Seismological Research Letters, 89, 440–445. Doi: https://doi.org/10.1785/0220170168

Vargas, C.A (2020). Subduction geometries in northwestern South America. The Geology of Colombia, Volume 4: Quaternary. Servicio Geológico Colombiano, Publicaciones Geológicas Especiales, 38, 397-422, Bogotá. https:// doi.org/10.32685/pub.esp.38.2019.11

Veloza, G., Styron, R., Taylor, M., Mora, A (2012). Active Tectonics of the Andes – ATA: An open-source archive for active faults in northwestern South America. GSA Today, 22 (10), 4-10, doi: 10.1130/GSAT-G156A.1.

Vernette, G. (1989). Examples of diapiric control on shelf topography and sedimentation patterns on the Colombian Caribbean continental shelf. Journal of South American Earth Sciences, 2 (4), 391-400. https://doi.org/10.1016/0895-9811(89)90017-5

Wang, K., He, J., Dragert, H., James, T.S (2001). Three-dimensional viscoelastic interseismic deformation model for the Cascadia subduction zone. Earth, Planets and Space. 53, 295-306. https://doi.org/10.1186/BF03352386

Wang, R., Martin, F.L., Roth, F (2006). PSGRN/PSCMP – A new code for calculating co- and post-seismic deformation, geoid and gravity changes based on the viscoelastic gravitational dislocation theory. Computers and Geosciences, 32, 527-541.

Wang, K., Hu, Y., He, J., 2012. Deformation cycles of subduction earthquakes in a viscoelastic earth. Nature. 484, 327-332. https://doi.org/10.1038/nature11032

Wang, K., 2017. Elastic and viscoelastic models of crustal deformation in subduction earthquake cycles. In: The seismogenic zone of subduction thrust faults, edited by Timothy H Dixon and Casey Moore, New York Chichester, West Sussex: Columbia University Press, 2007, pp. 540-575. https://doi.org/10.7312/dixo13866-017

Wells, D.L., Coppersmith, K.J (1994). New empirical relationships among magnitude, rupture length, rupture width, rupture area, and surface displacement. Bulletin of the Seismological Society of America, 84, 974-1002.

Wessel, P., Smith, W.H.F., Scharroo, R., Luis, J., Wobbe, F (2013). Generic Mapping Tools: Improved version released. EOS, 94, 409-420, https://doi.org/10.1002/2013EO450001.

White, S.M., Trenkamp, R., Kellogg, J.N (2003). Recent crustal deformation and the earthquake cycle along the Ecuador-Colombia subduction zone. Earth and Planetary Science Letters, 231-242, doi:10.1016/S0012-821X(03)00535-1

Yabuki, T., Matsu'ura, M (1992). Geodetic data inversion using a Bayesian information criterion for spatial distribution of fault slip. Geophysical Journal International, 109, 363-375, https://doi.org/10.1111/j.1365-246X.1992.tb00102.x

Yamanaka, Y., Tanioka, Y (2017). Large amplification of the 1906 Colombia–Ecuador earthquake tsunami in Hilo Bay induced by bay-scale resonance. Geophysical Journal International, 214, 1937-1946, https://doi.org/10.1093/gji/ggy244

Ye, L., Kanamori, H., Avouac, J-P., Li, L., Cheung, K.F., Lay, T (2016). The 16 April 2016, MW 7.8 (MS 7.5) Ecuador earthquake: A quasi-repeat of the 1942 MS 7.5 earthquake and partial re-rupture of the 1906 MS 8.6 Colombia–Ecuador earthquake. Earth and Planetary Science Letters, 454, 248-258. https://doi.org/10.1016/j.epsl.2016.09.006.

Yoshimoto. M., Kumagai, H., Acero, W., Ponce, G., Vasconez, F., Arrais, S., Ruiz, M., Alvarado, A., Pedraza García, P., Dionicio, V., Chamorro, O., Maeda, Y., Nakano, M (2017). Depth-dependent rupture mode along the Ecuador-Colombia subduction zone. Geophysical Research Letters 44, 2203-2210, doi:10.1002/2016GL071929.

Yoshioka, S., Yabuki, T., Sagiya, T., Tada, T., Matsu'ura, M (1993). Interplate coupling and relative plate motion in the Tokai district, central Japan, deduced from geodetic data inversion using ABIC. Geophysical Journal International, 113, 607–621, https://doi.org/10.1111/j.1365-246X.1993.tb04655.x

Zarifi, Z., Havskiv, J., Hanyga, A (2007). An insight into the Bucaramanga nest. Tectonophysics, 443, 93-105. doi:10.1016/j.tecto.2007.06.004

Zhang, J., Bock, Y., Johnson, H., Fang, P., Williams, S., Genrich, J., Wdowinski, S., Behr, J (1997). California permanent GPS geodetic array: Error analysis of daily position estimates and site velocities. Journal of Geophysical Research, 102, 18305-18055

APPENDICES

APPENDIX A: TIME SERIES OF THE GPS DATA IN COLOMBIA W.R.T ITRF2014

Estimated 3-dimensional velocities are presented in the upper right part of each plot with their respective uncertainties in mm/yr. Black dots represent the daily solutions obtained with GAMIT-GLOBK software, vertical red lines denote instrumental changes, and the green line represents the fitting obtained with the Hector software v1.6**.**

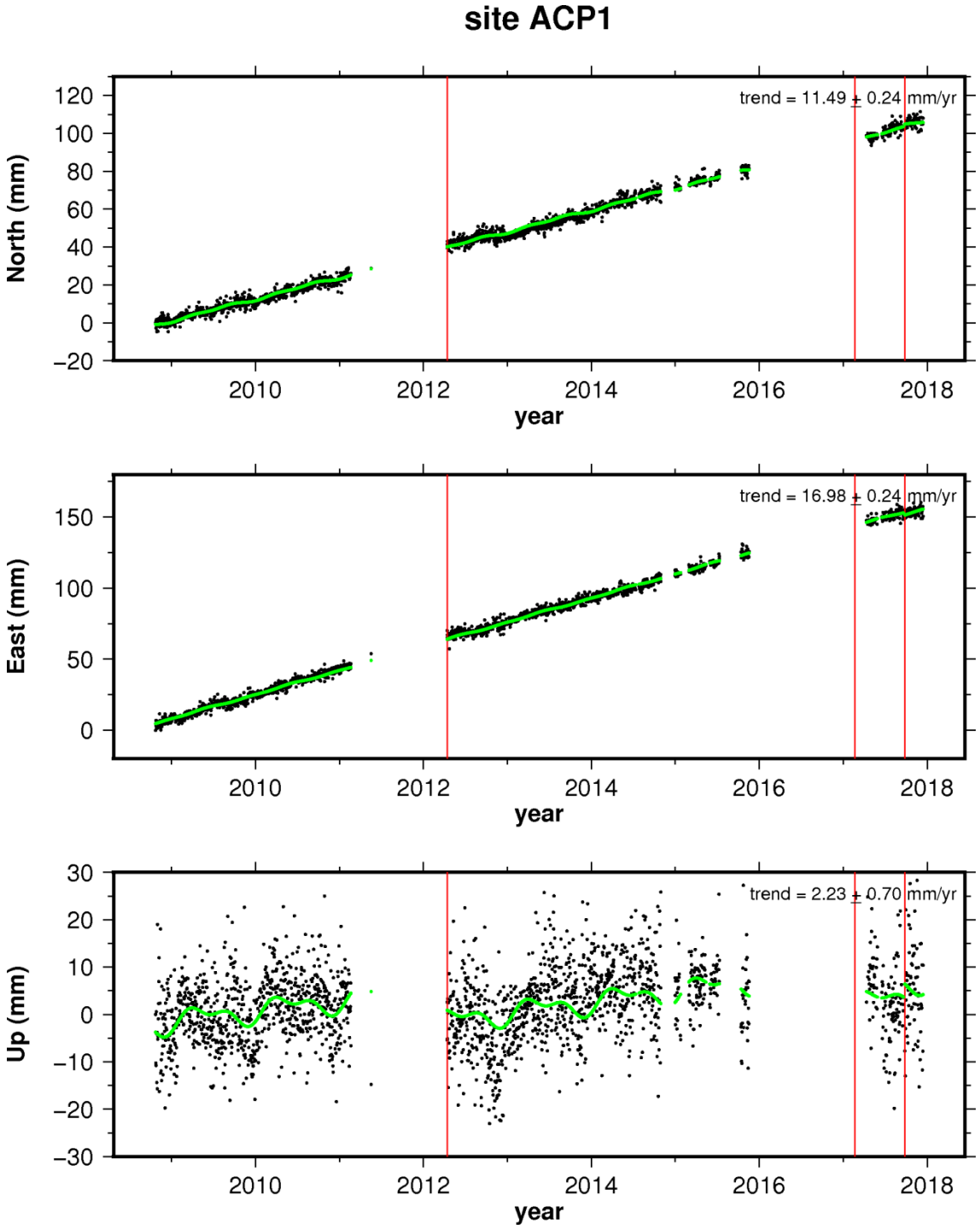
site ACP1
trend = 11.49 ± 0.24 mm/yr
North (mm)
120
100
80
60
40
20
0
−20
2010
2012
2014
2016
2018
year
trend = 16.98 ± 0.24 mm/yr
East (mm)
150
100
50
0
2010
2012
2014
2016
2018
year
trend = 2.23 ± 0.70 mm/yr
Up (mm)
30
20
10
0
−10
−20
−30
2010
2012
2014
2016
2018
year

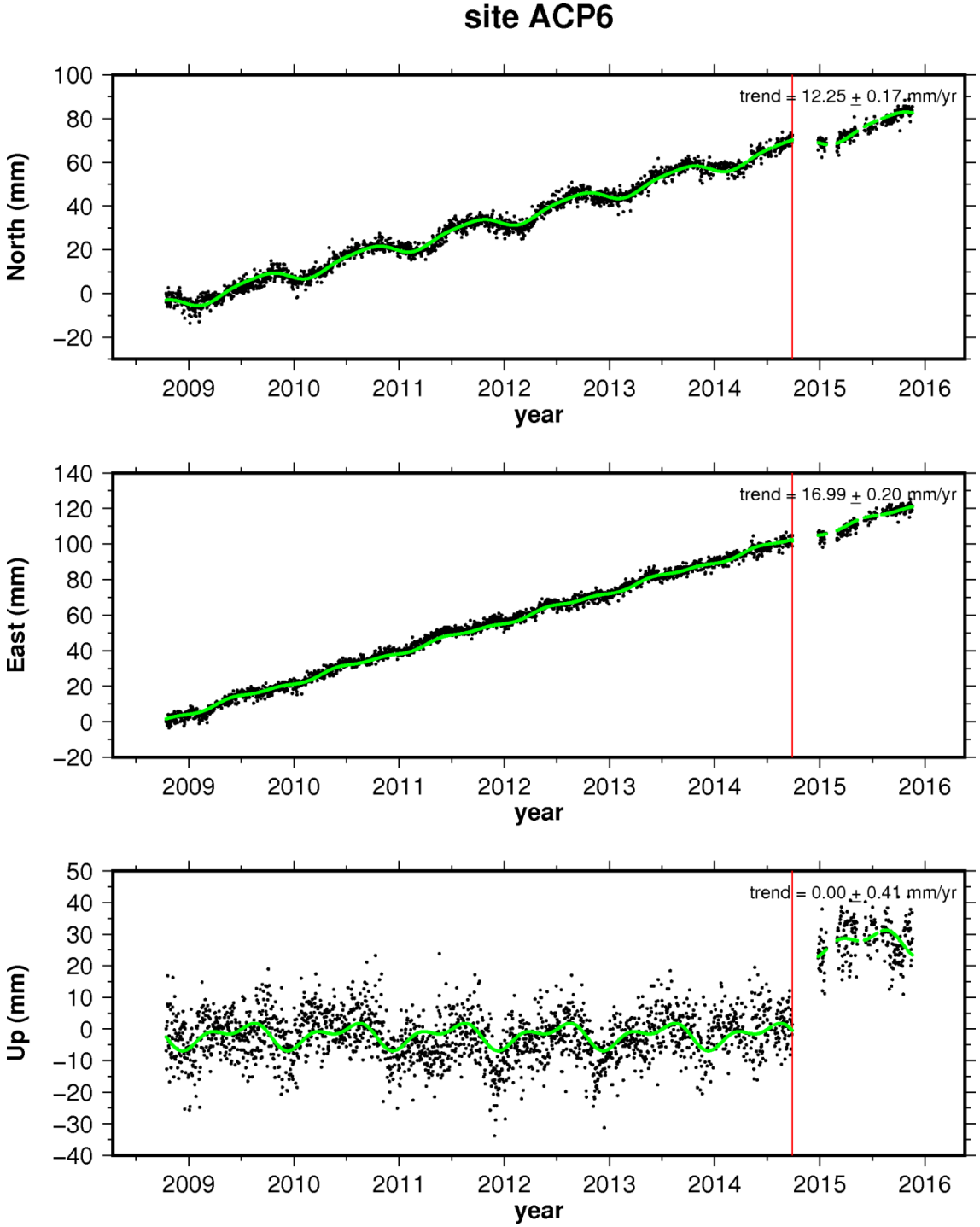
site ACP6
North (mm)
trend = 12.25 ± 0.17 mm/yr
East (mm)
trend = 16.99 ± 0.20 mm/yr
Up (mm)
trend = 0.00 ± 0.41 mm/yr
year
2009
2010
2011
2012
2013
2014
2015
2016

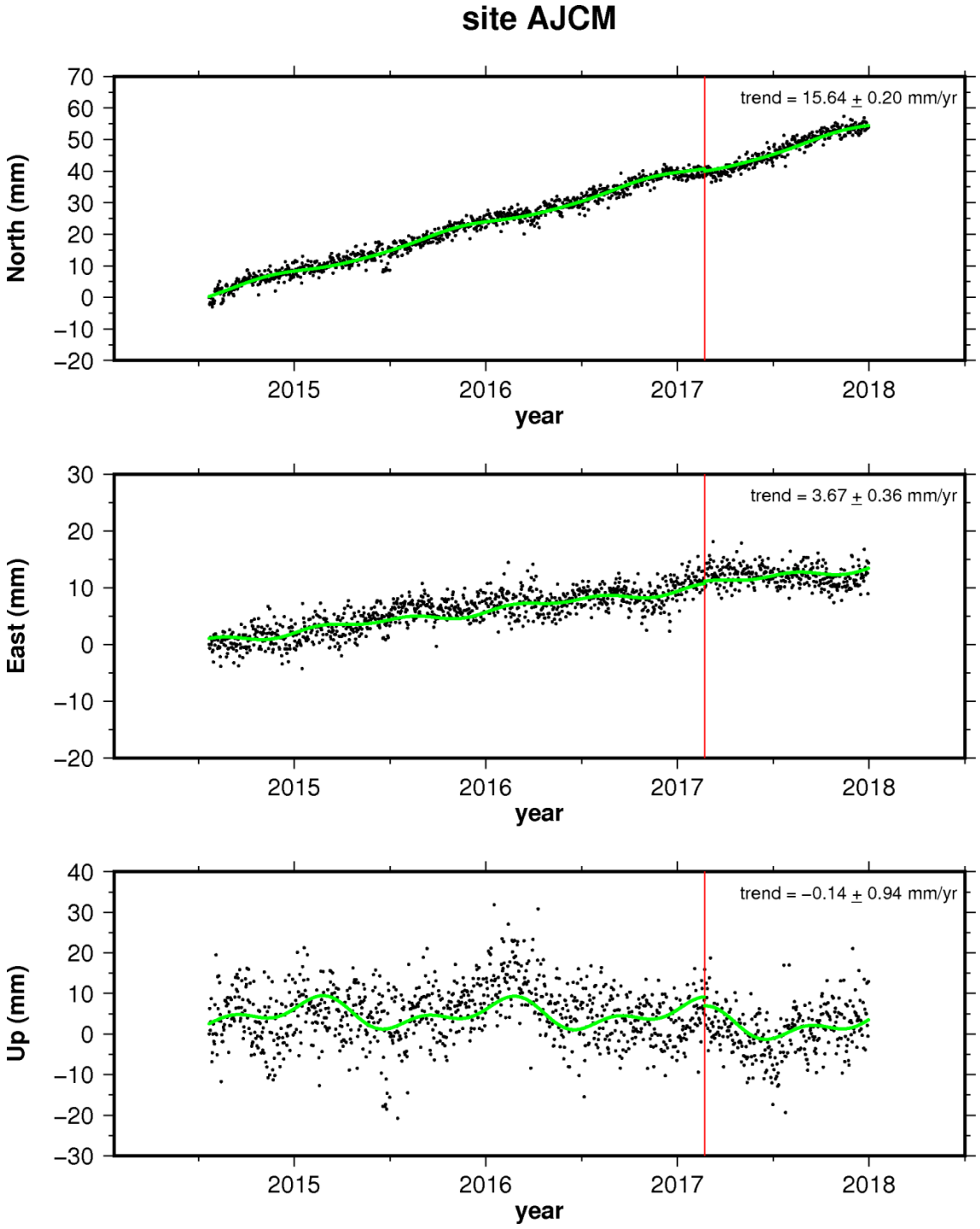
site AJCM
North (mm)
trend = 15.64 ± 0.20 mm/yr
year
East (mm)
trend = 3.67 ± 0.36 mm/yr
year
Up (mm)
trend = −0.14 ± 0.94 mm/yr
year
2015
2016
2017
2018

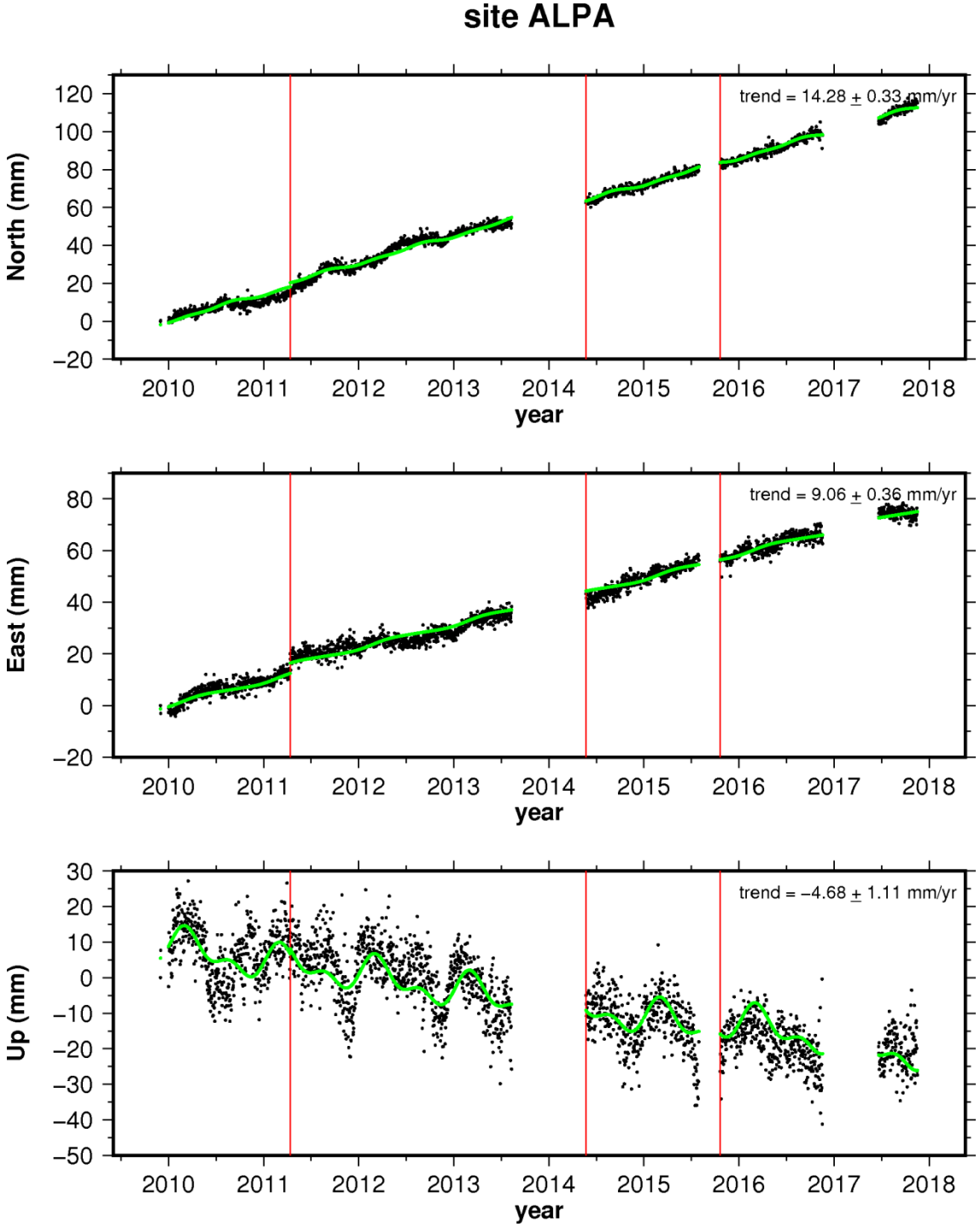
site ALPA
North (mm)
trend = 14.28 ± 0.33 mm/yr
East (mm)
trend = 9.06 ± 0.36 mm/yr
Up (mm)
trend = −4.68 ± 1.11 mm/yr
year
2010
2011
2012
2013
2014
2015
2016
2017
2018

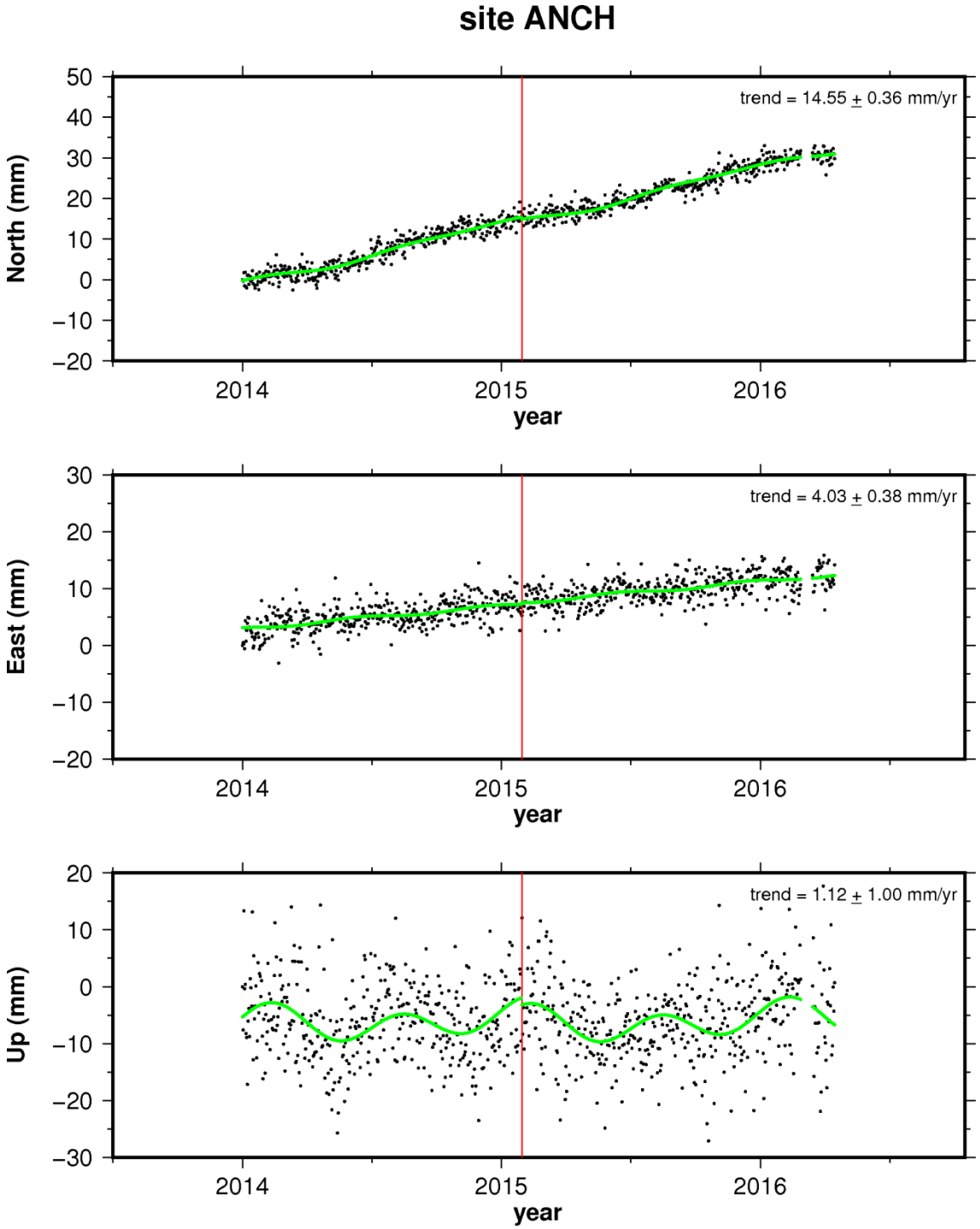
site ANCH
North (mm)
trend = 14.55 ± 0.36 mm/yr
year
East (mm)
trend = 4.03 ± 0.38 mm/yr
year
Up (mm)
trend = 1.12 ± 1.00 mm/yr
year
2014
2015
2016

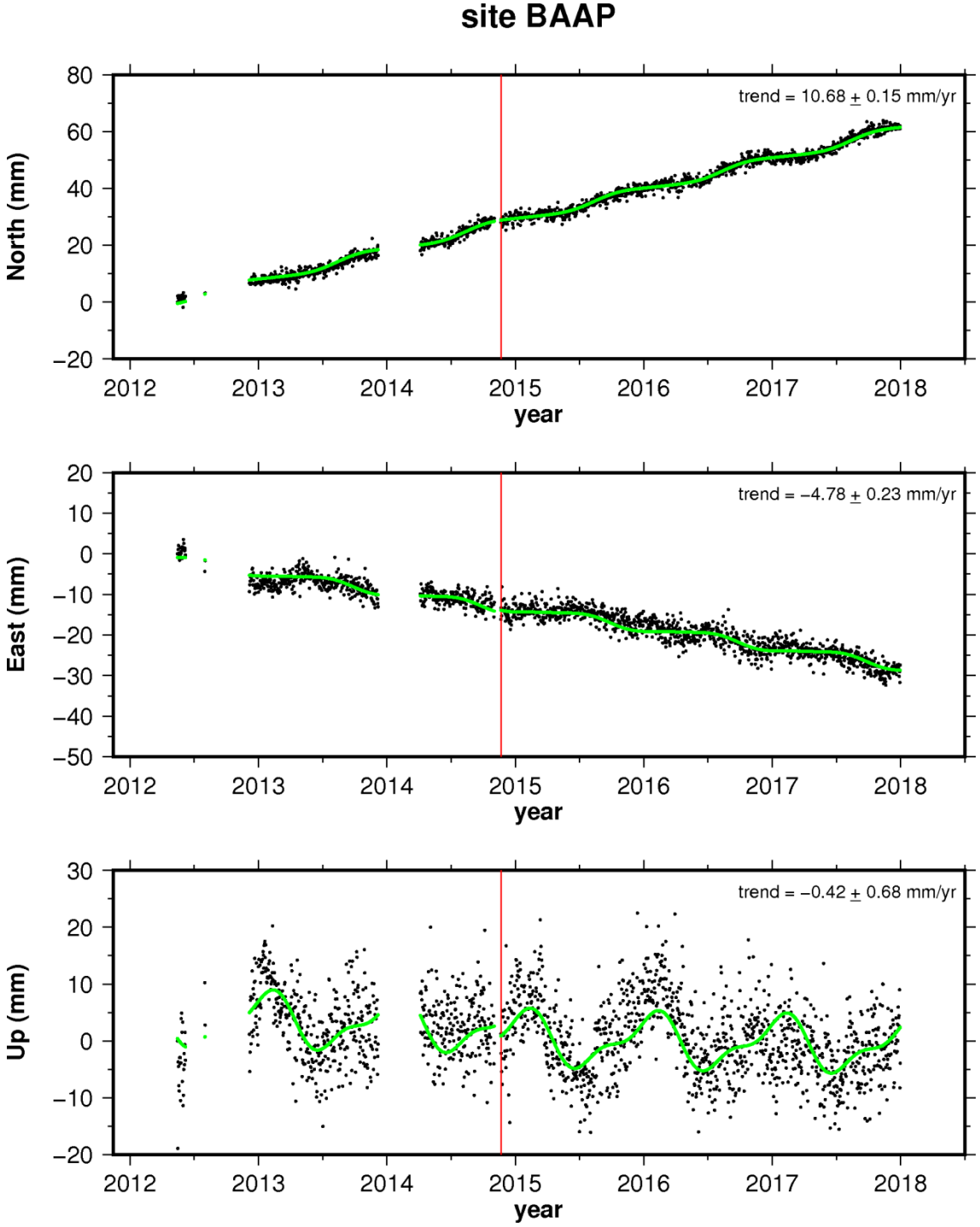
site BAAP
trend = 10.68 ± 0.15 mm/yr
North (mm)
80
60
40
20
0
−20
2012
2013
2014
2015
2016
2017
2018
year
trend = −4.78 ± 0.23 mm/yr
East (mm)
20
10
0
−10
−20
−30
−40
−50
year
trend = −0.42 ± 0.68 mm/yr
Up (mm)
30
20
10
0
−10
−20
year

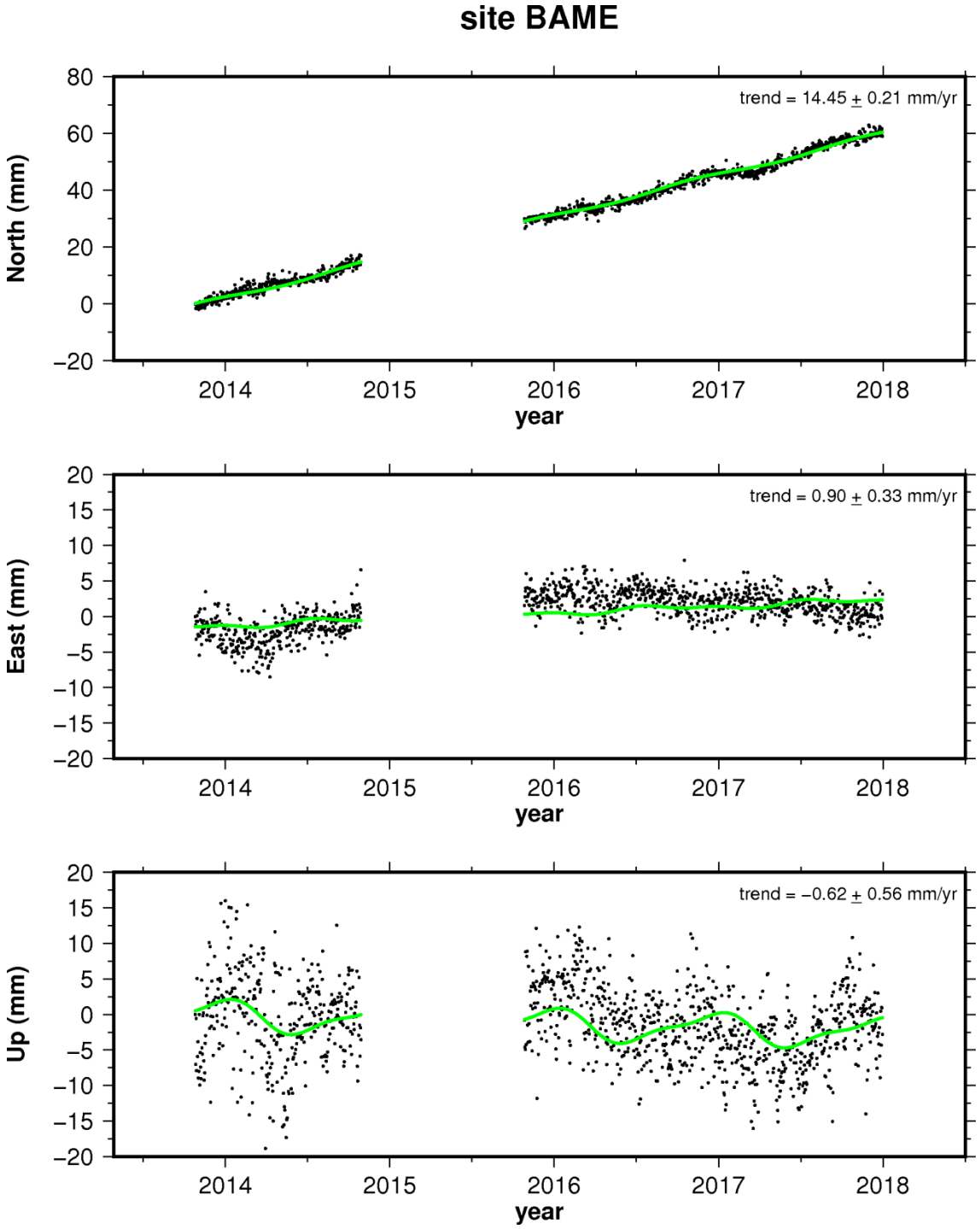
site BAME
trend = 14.45 ± 0.21 mm/yr
North (mm)
80
60
40
20
0
−20
2014
2015
2016
2017
2018
year
trend = 0.90 ± 0.33 mm/yr
East (mm)
20
15
10
5
0
−5
−10
−15
−20
2014
2015
2016
2017
2018
year
trend = −0.62 ± 0.56 mm/yr
Up (mm)
20
15
10
5
0
−5
−10
−15
−20
2014
2015
2016
2017
2018
year

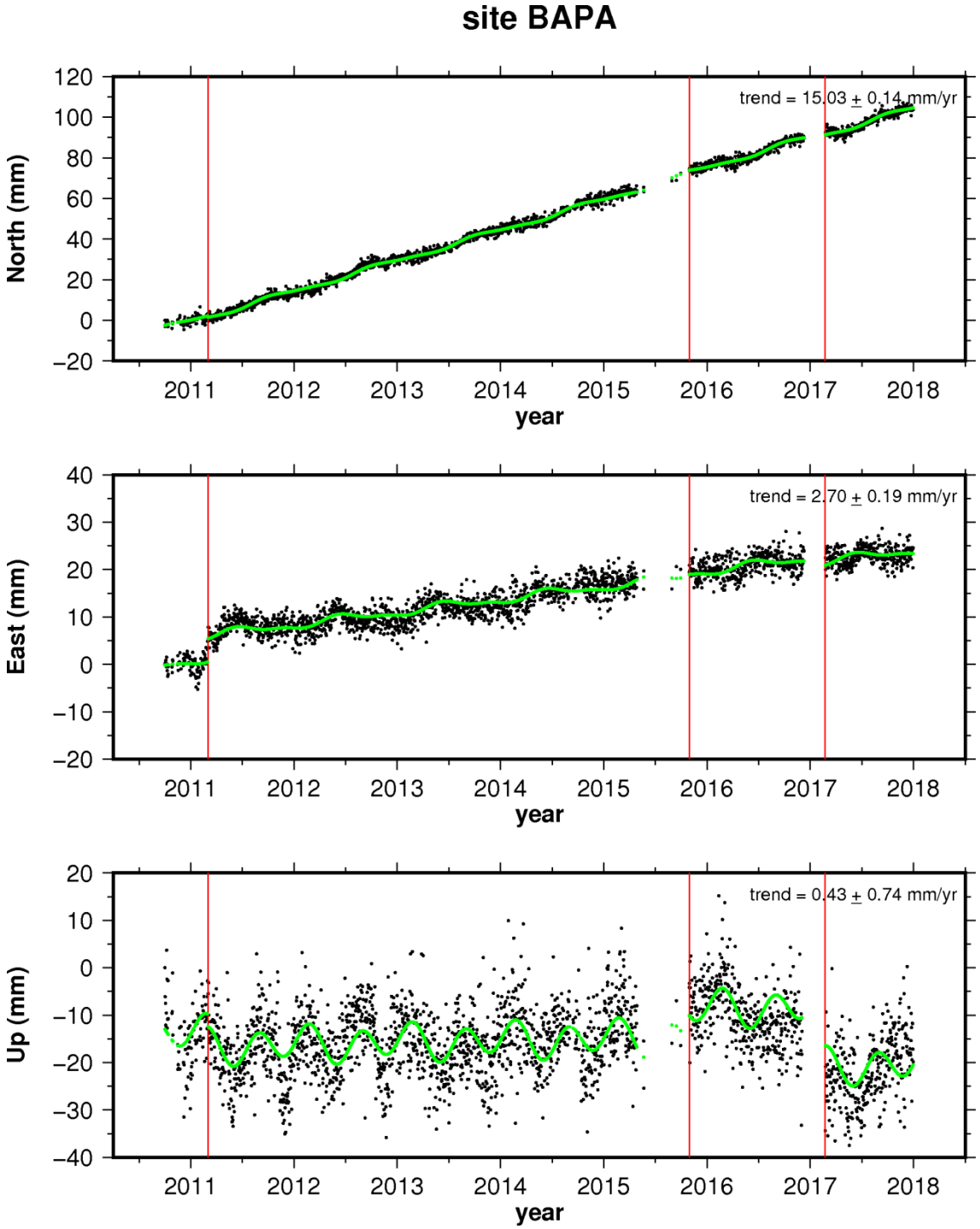
site BAPA
North (mm)
trend = 15.03 ± 0.14 mm/yr
East (mm)
trend = 2.70 ± 0.19 mm/yr
Up (mm)
trend = 0.43 ± 0.74 mm/yr
year
2011
2012
2013
2014
2015
2016
2017
2018

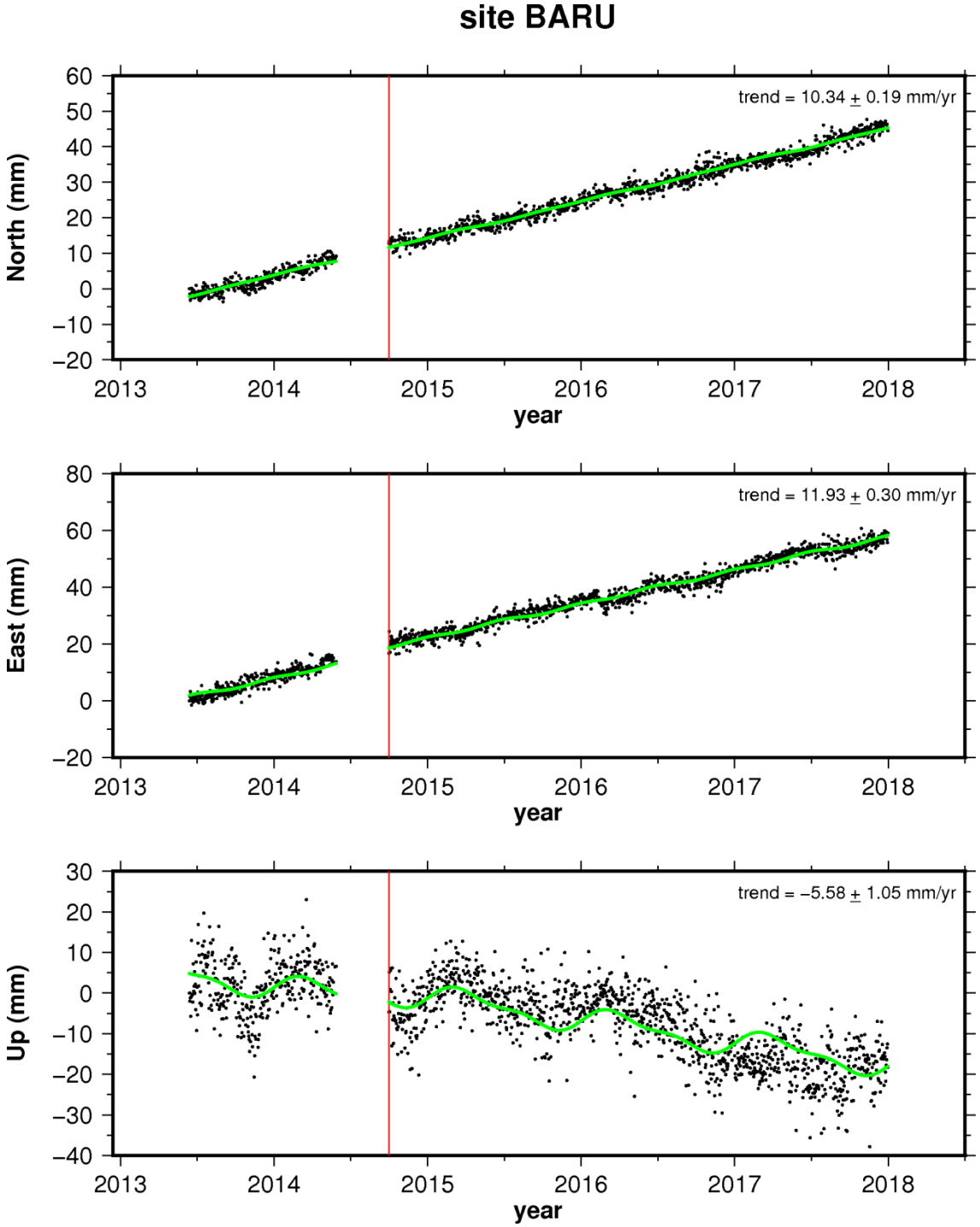
site BARU
North (mm)
trend = 10.34 ± 0.19 mm/yr
East (mm)
trend = 11.93 ± 0.30 mm/yr
Up (mm)
trend = −5.58 ± 1.05 mm/yr
year
2013
2014
2015
2016
2017
2018

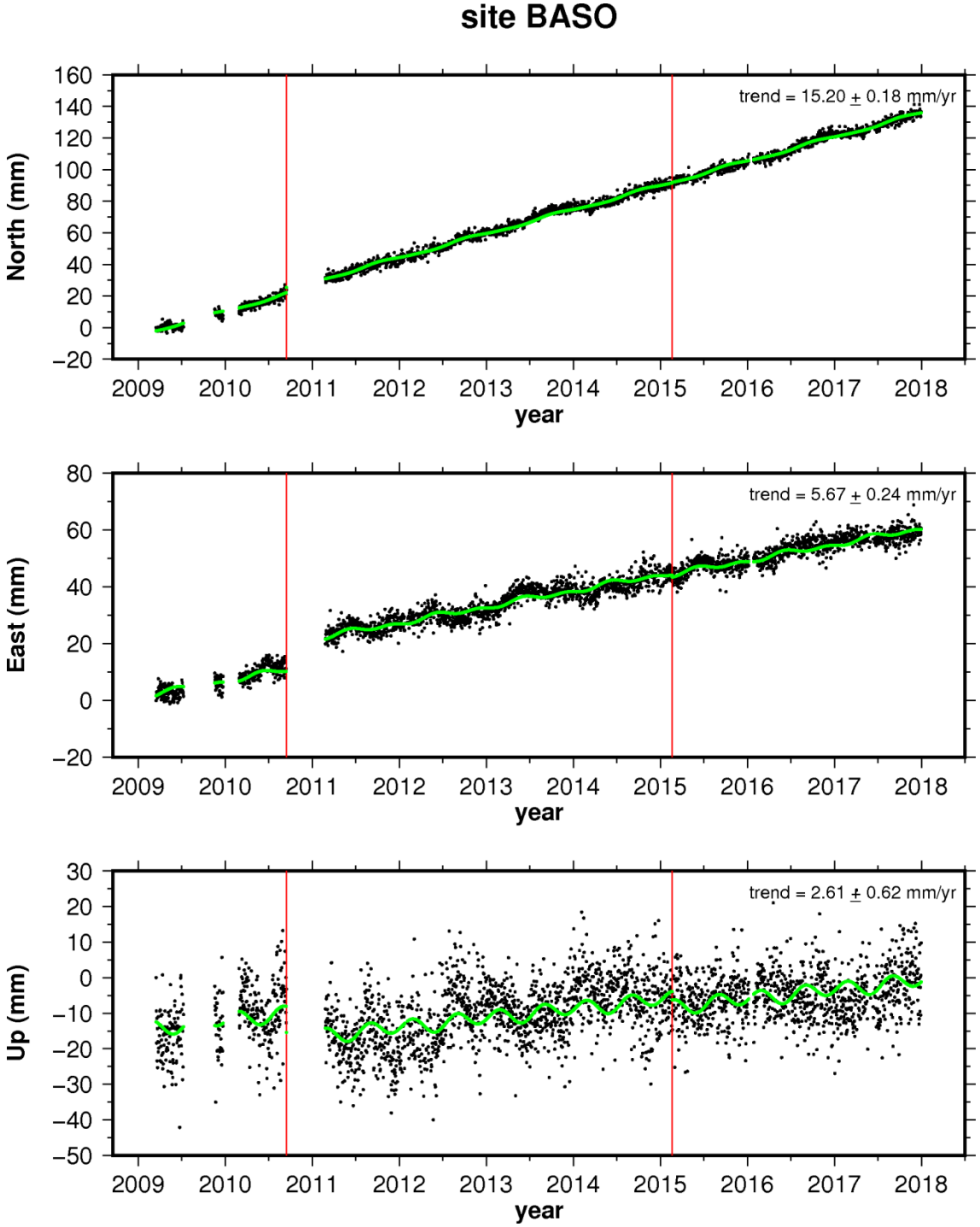
site BASO
North (mm)
trend = 15.20 ± 0.18 mm/yr
East (mm)
trend = 5.67 ± 0.24 mm/yr
Up (mm)
trend = 2.61 ± 0.62 mm/yr
year
2009
2010
2011
2012
2013
2014
2015
2016
2017
2018

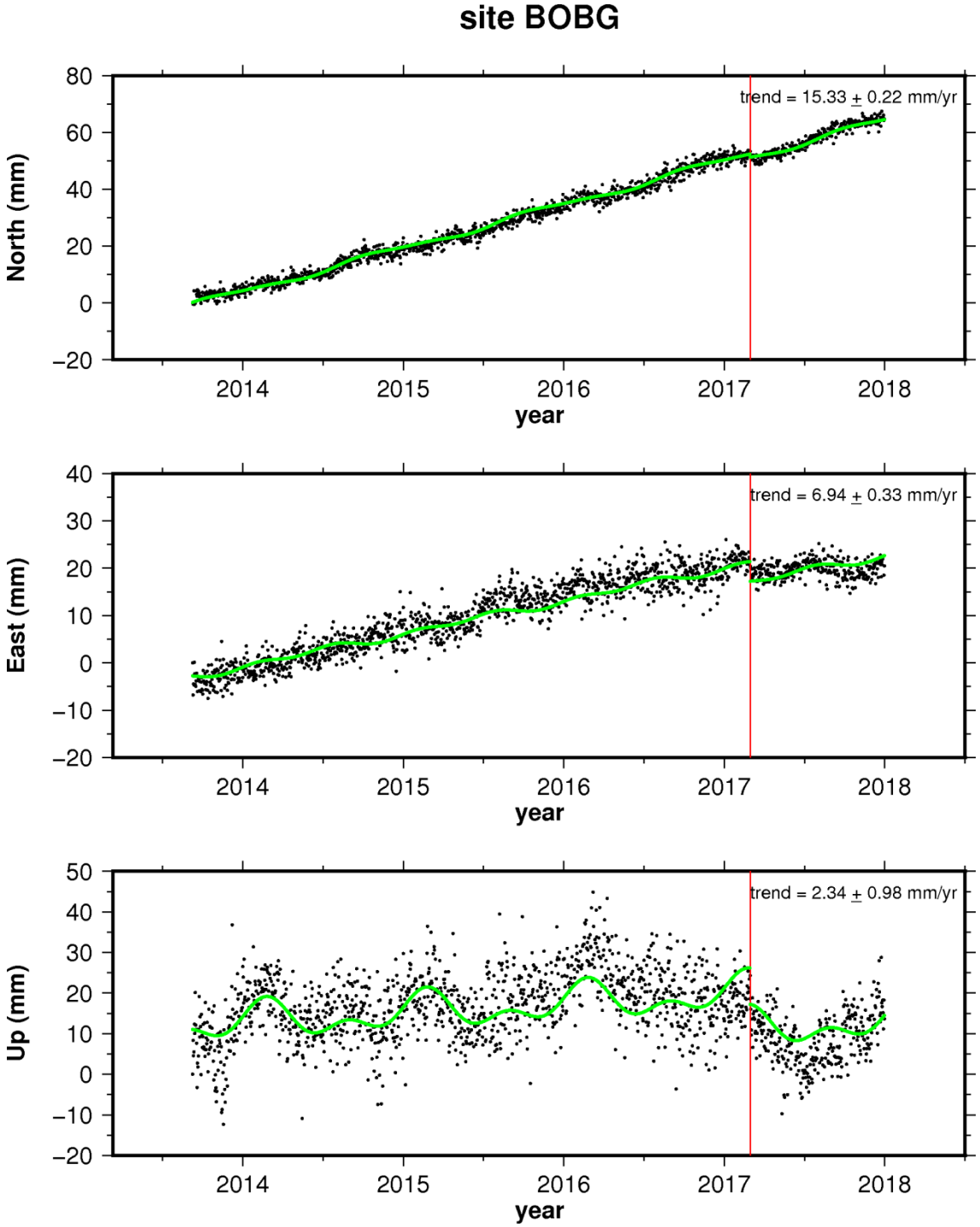
site BOBG
North (mm)
trend = 15.33 ± 0.22 mm/yr
East (mm)
trend = 6.94 ± 0.33 mm/yr
Up (mm)
trend = 2.34 ± 0.98 mm/yr
year
2014
2015
2016
2017
2018

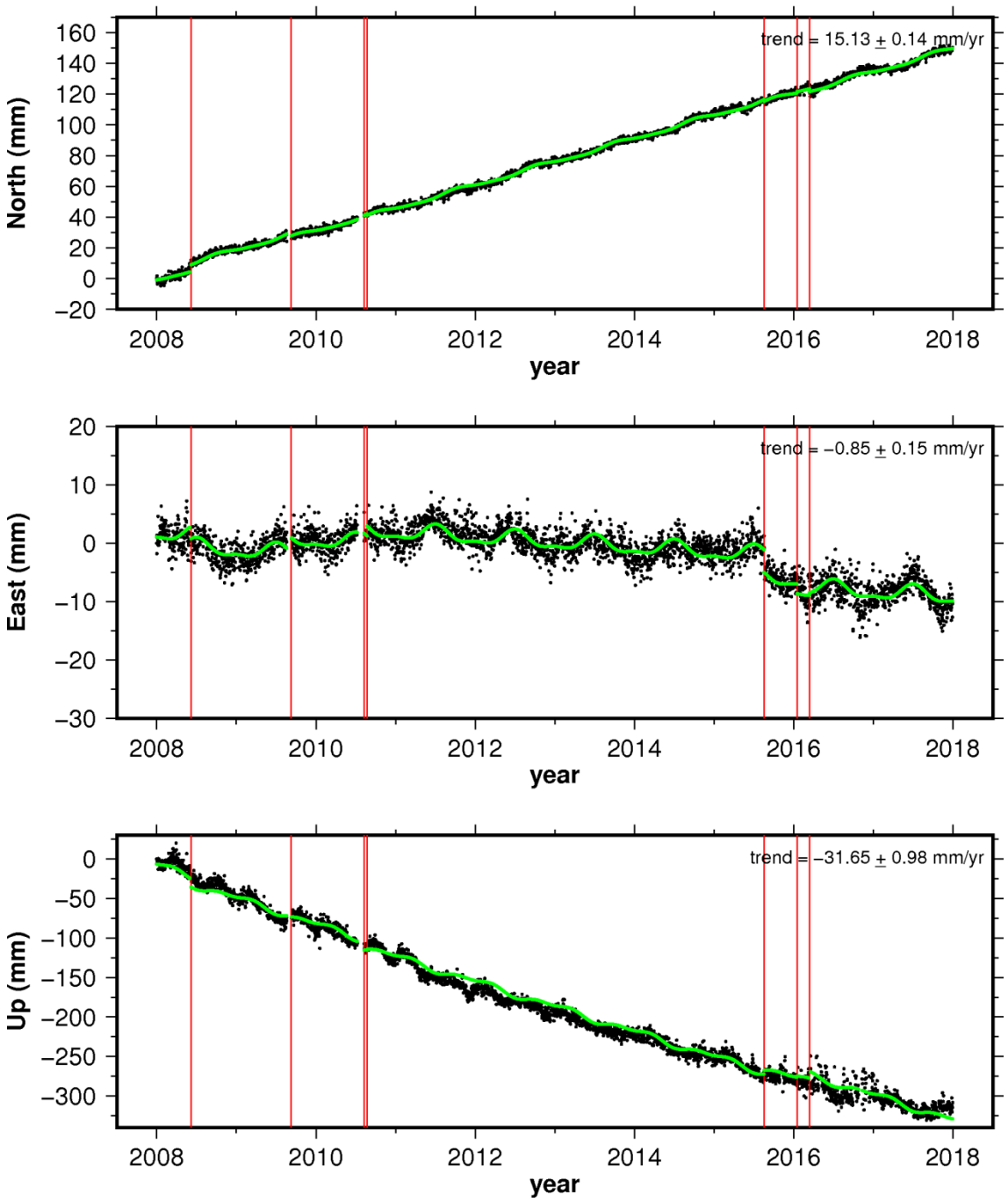
site BOGT
North (mm)
trend = 15.13 ± 0.14 mm/yr
year
East (mm)
trend = −0.85 ± 0.15 mm/yr
year
Up (mm)
trend = −31.65 ± 0.98 mm/yr
year

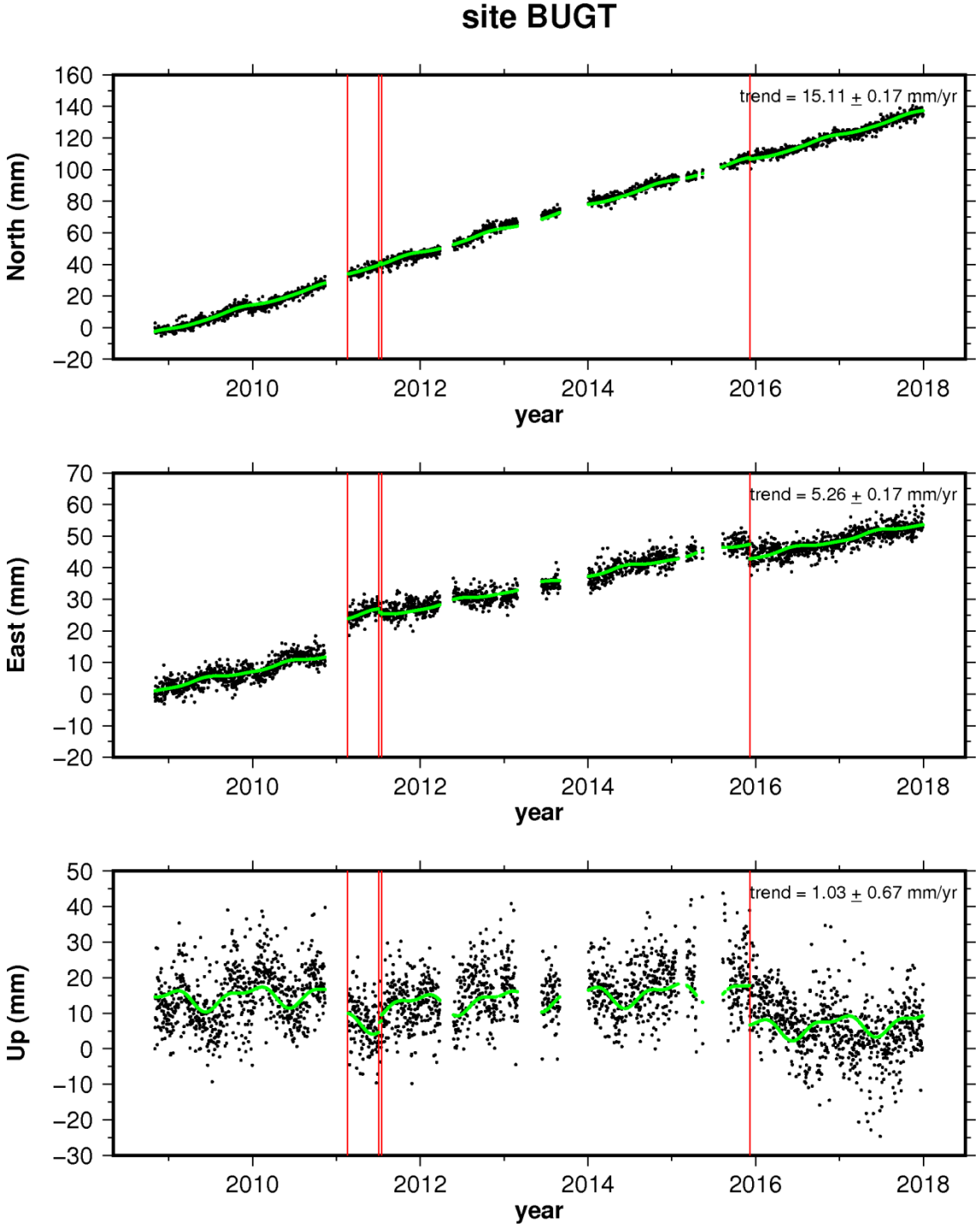
site BUGT
North (mm)
trend = 15.11 ± 0.17 mm/yr
East (mm)
trend = 5.26 ± 0.17 mm/yr
Up (mm)
trend = 1.03 ± 0.67 mm/yr
year
2010
2012
2014
2016
2018

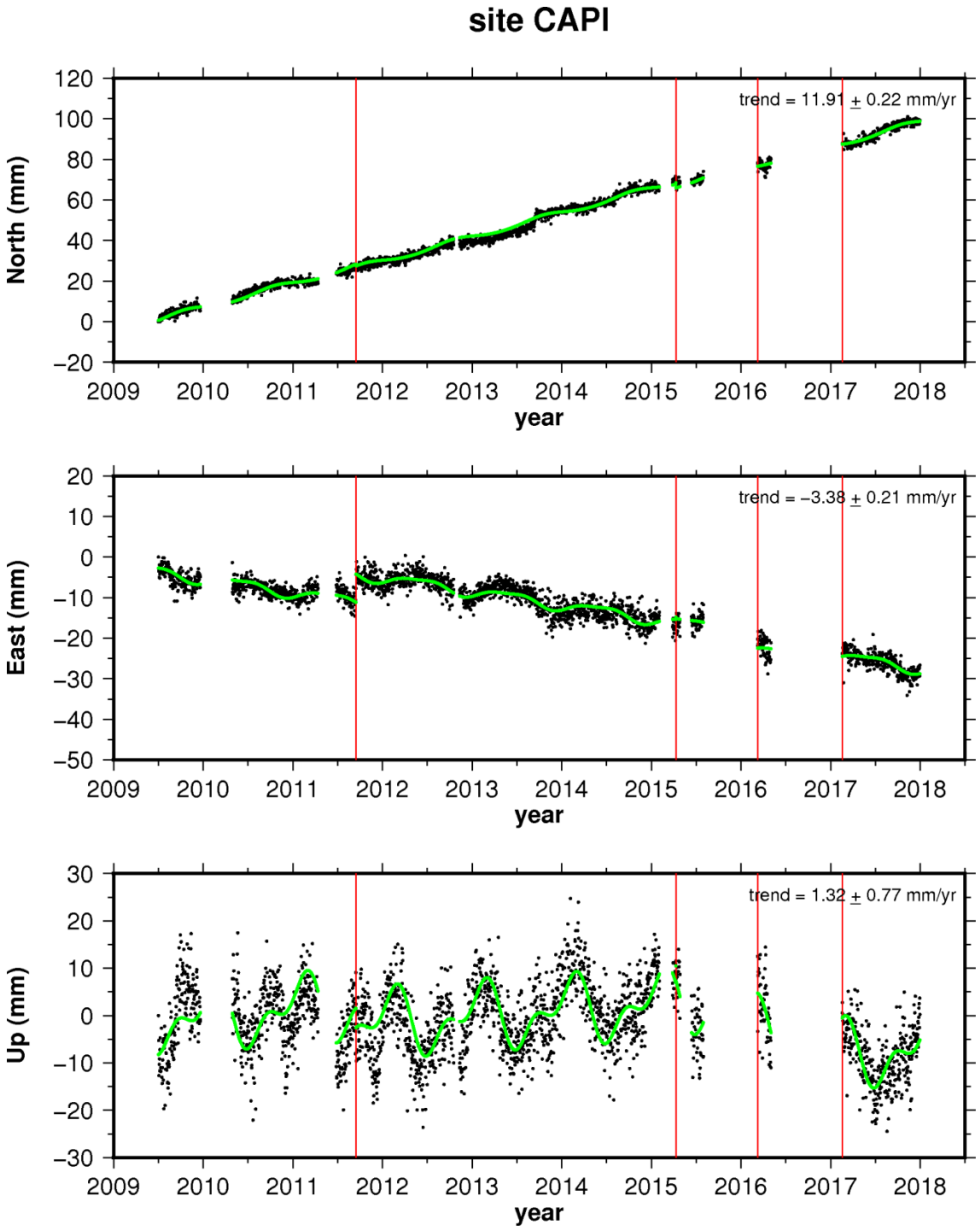
site CAPI
trend = 11.91 ± 0.22 mm/yr
North (mm)
120
100
80
60
40
20
0
−20
2009
2010
2011
2012
2013
2014
2015
2016
2017
2018
year
trend = −3.38 ± 0.21 mm/yr
East (mm)
20
10
0
−10
−20
−30
−40
−50
year
trend = 1.32 ± 0.77 mm/yr
Up (mm)
30
20
10
0
−10
−20
−30
year

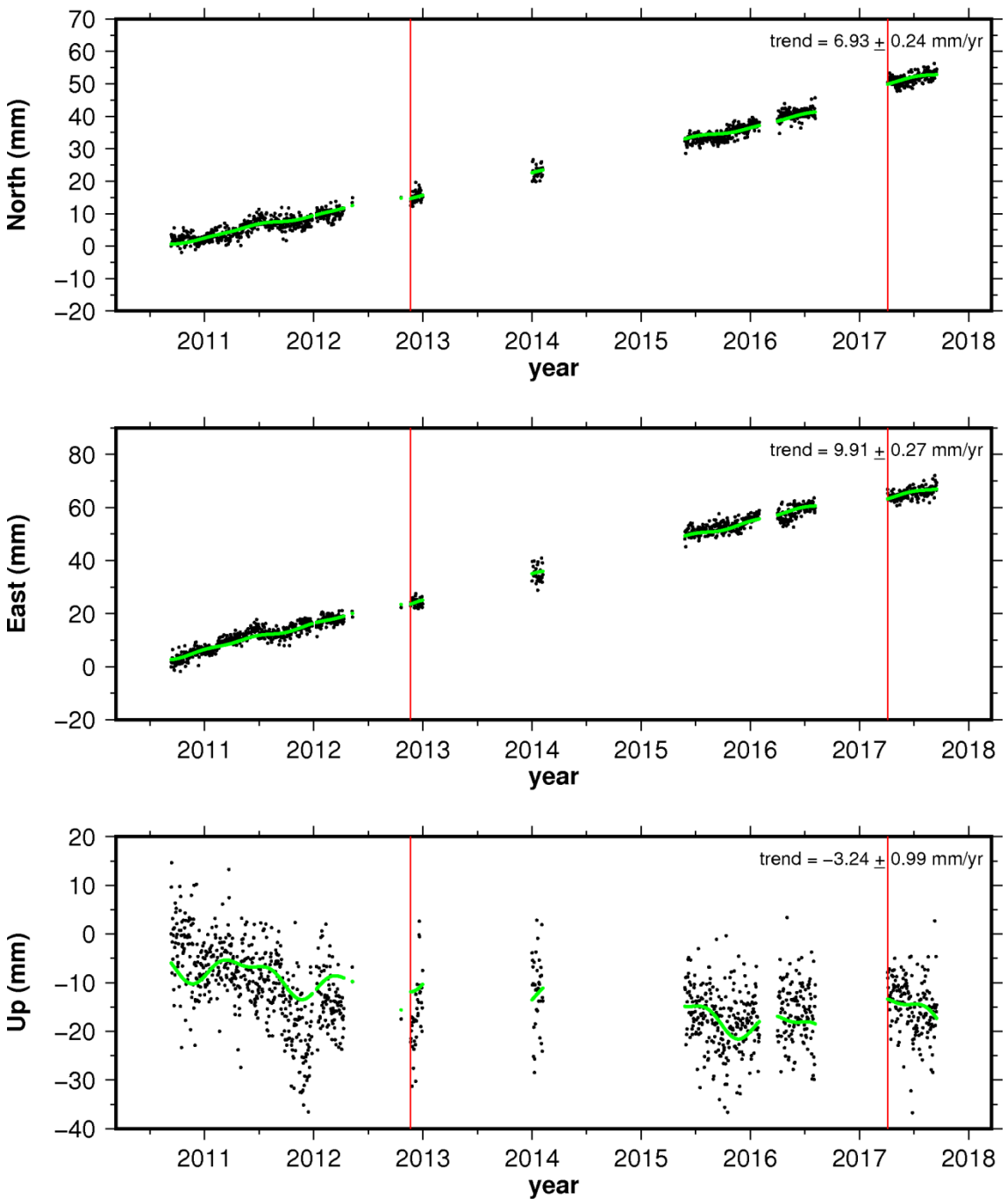
site CAYS
North (mm)
trend = 6.93 ± 0.24 mm/yr
East (mm)
trend = 9.91 ± 0.27 mm/yr
Up (mm)
trend = −3.24 ± 0.99 mm/yr
year
2011
2012
2013
2014
2015
2016
2017
2018

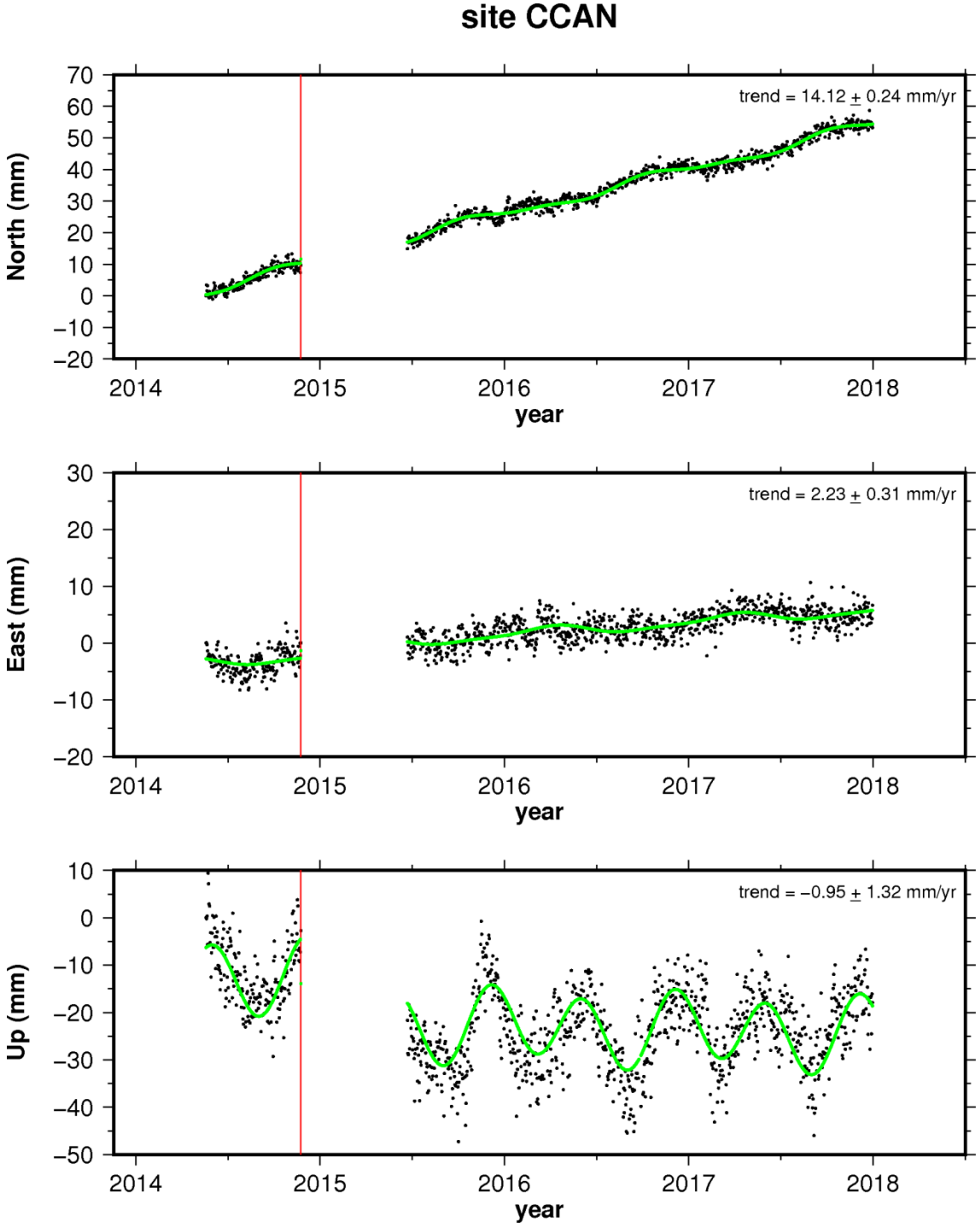
site CCAN
North (mm)
trend = 14.12 ± 0.24 mm/yr
East (mm)
trend = 2.23 ± 0.31 mm/yr
Up (mm)
trend = −0.95 ± 1.32 mm/yr
year
2014
2015
2016
2017
2018

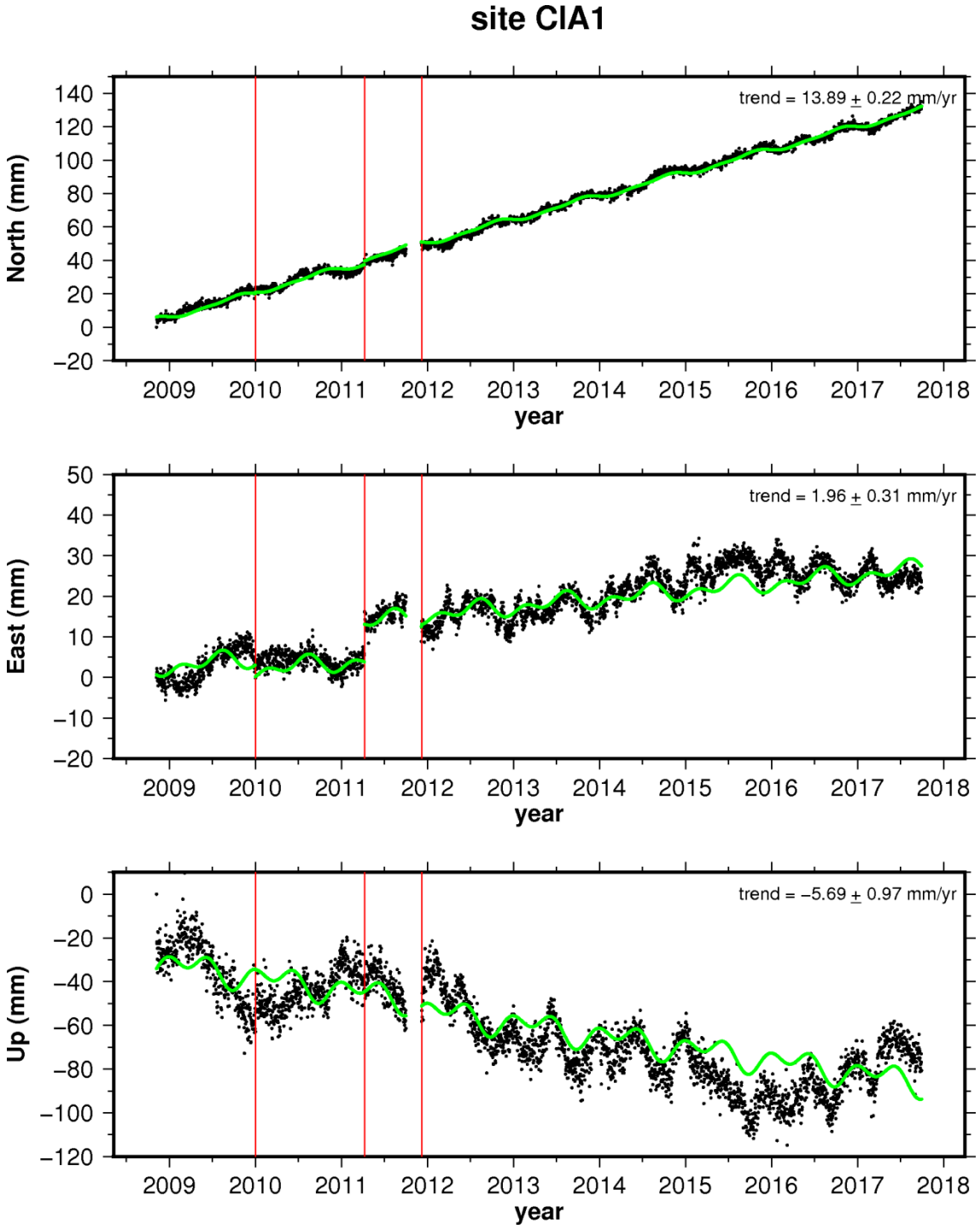
site CIA1
trend = 13.89 ± 0.22 mm/yr
North (mm)
140
120
100
80
60
40
20
0
−20
2009
2010
2011
2012
2013
2014
2015
2016
2017
2018
year
trend = 1.96 ± 0.31 mm/yr
East (mm)
50
40
30
20
10
0
−10
−20
year
trend = −5.69 ± 0.97 mm/yr
Up (mm)
0
−20
−40
−60
−80
−100
−120
year

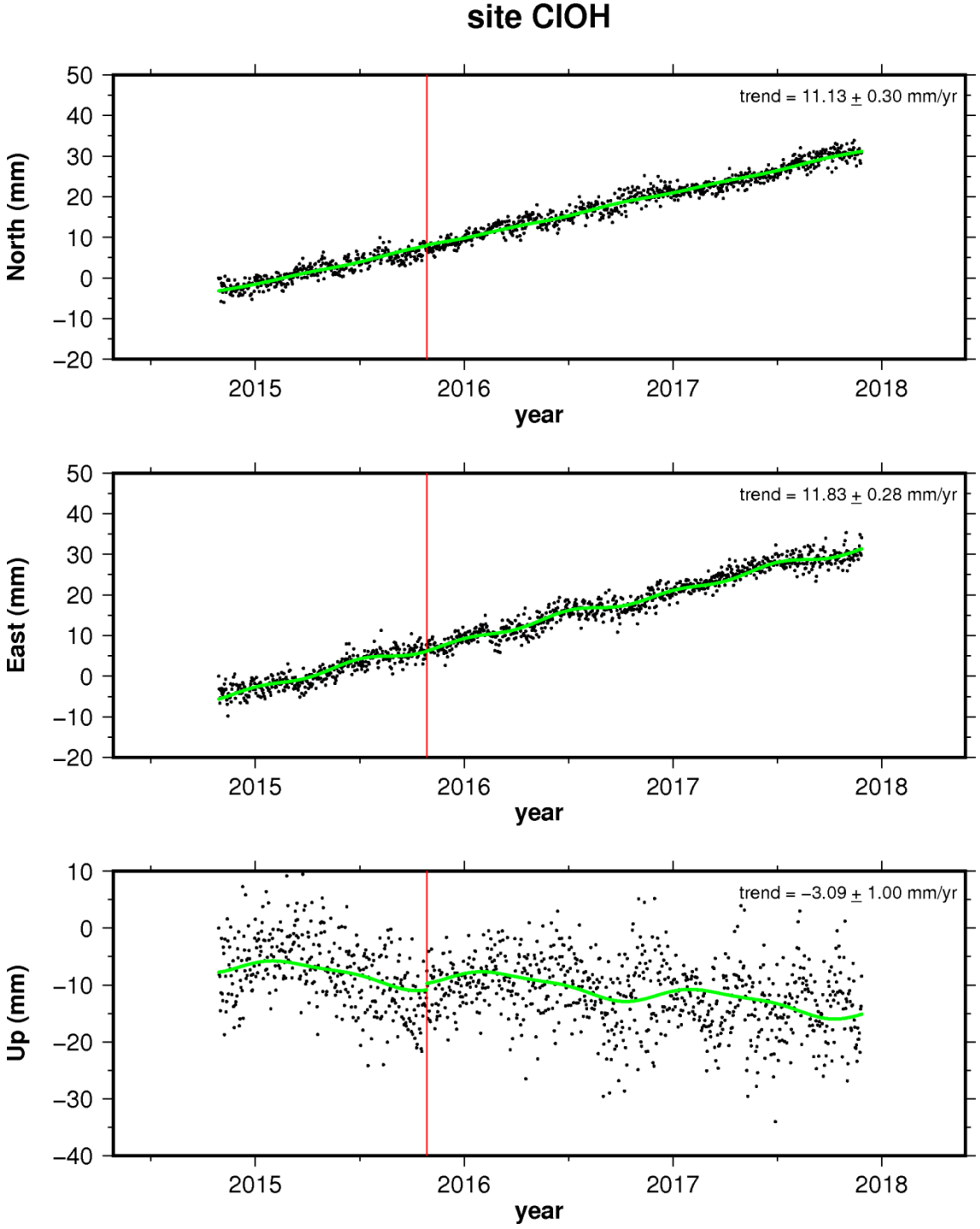
site CIOH
North (mm)
trend = 11.13 ± 0.30 mm/yr
East (mm)
trend = 11.83 ± 0.28 mm/yr
Up (mm)
trend = −3.09 ± 1.00 mm/yr
year
2015
2016
2017
2018

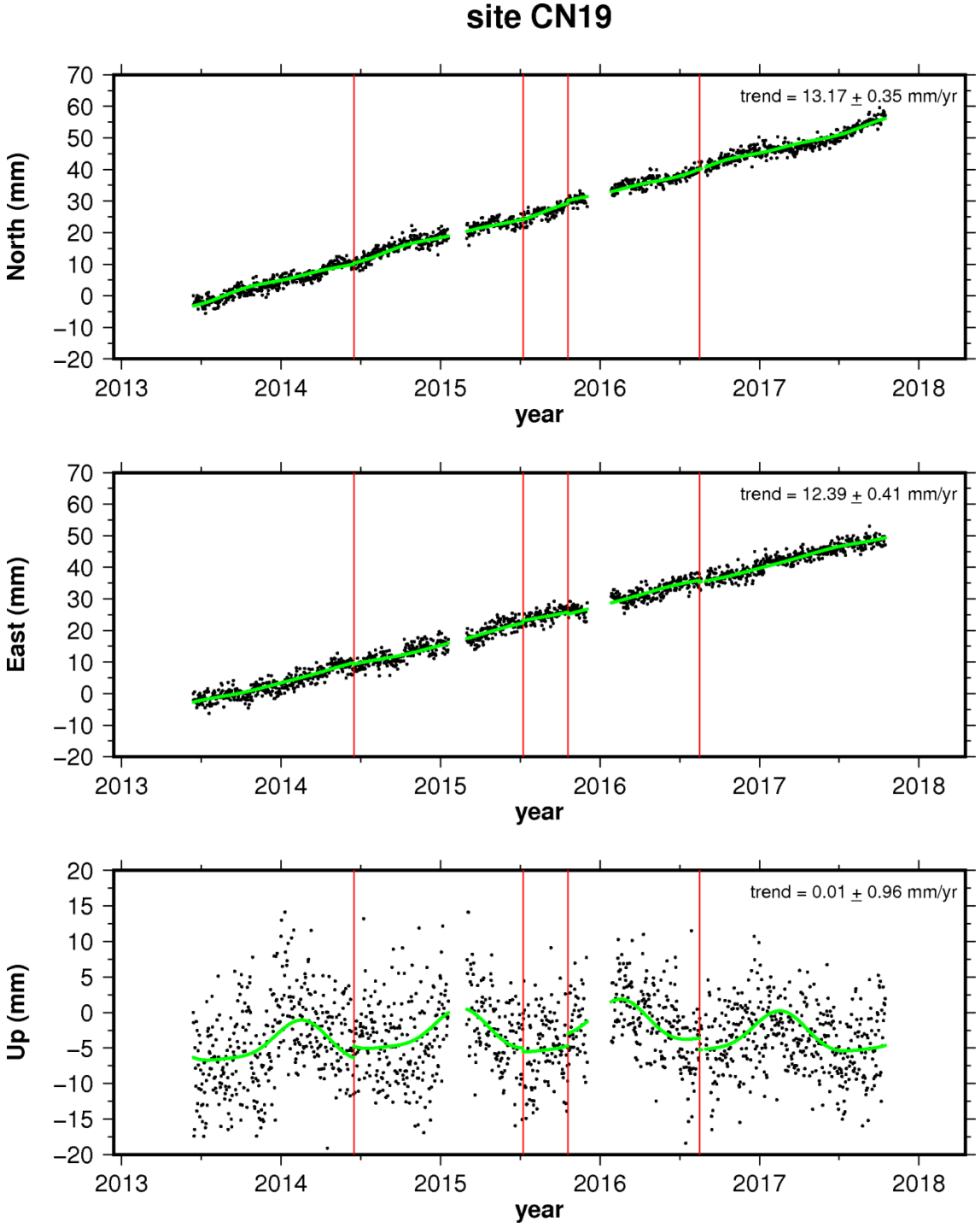
site CN19
North (mm)
East (mm)
Up (mm)
year
trend = 13.17 ± 0.35 mm/yr
trend = 12.39 ± 0.41 mm/yr
trend = 0.01 ± 0.96 mm/yr
2013
2014
2015
2016
2017
2018

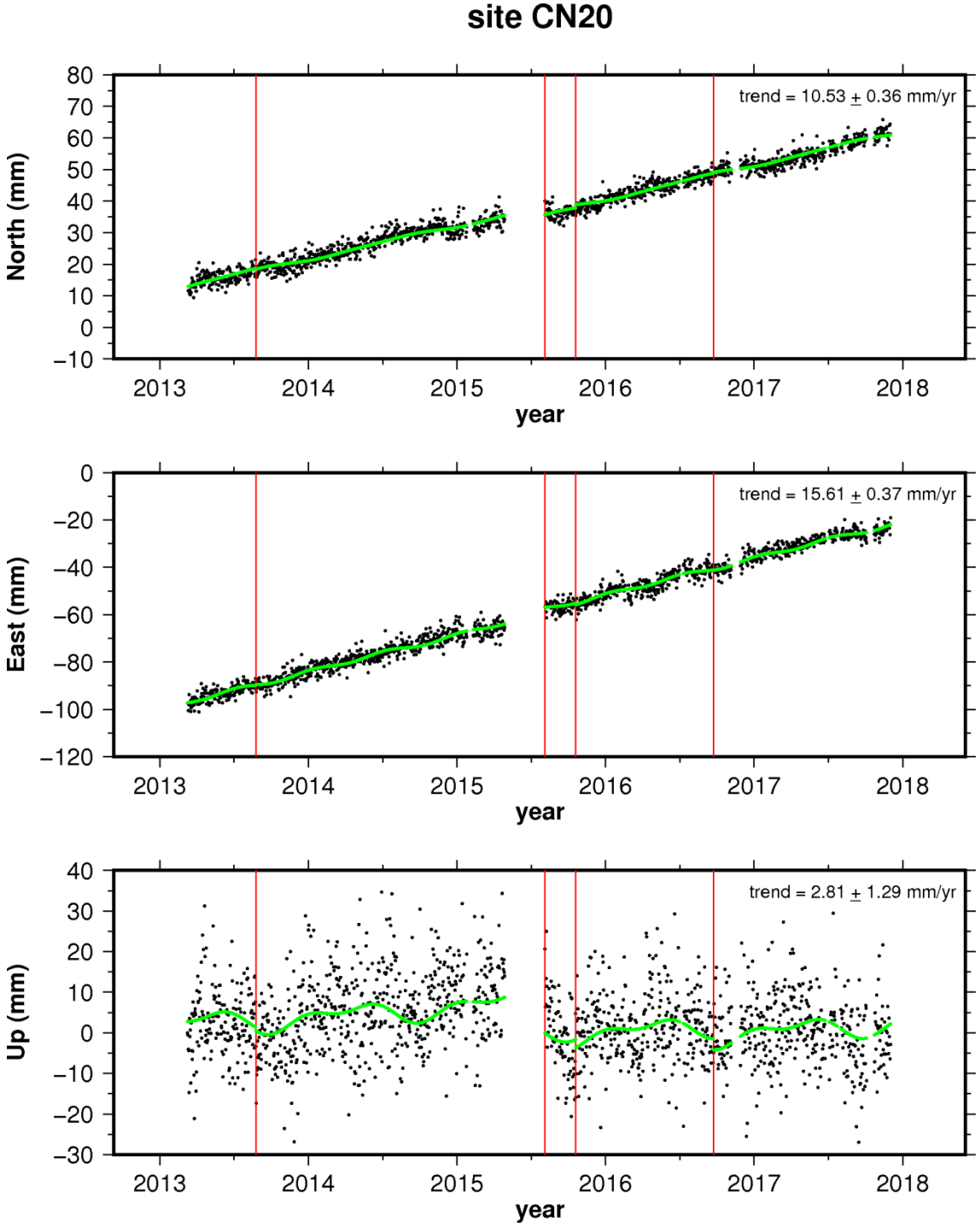
site CN20
North (mm)
trend = 10.53 ± 0.36 mm/yr
East (mm)
trend = 15.61 ± 0.37 mm/yr
Up (mm)
trend = 2.81 ± 1.29 mm/yr
year
2013
2014
2015
2016
2017
2018

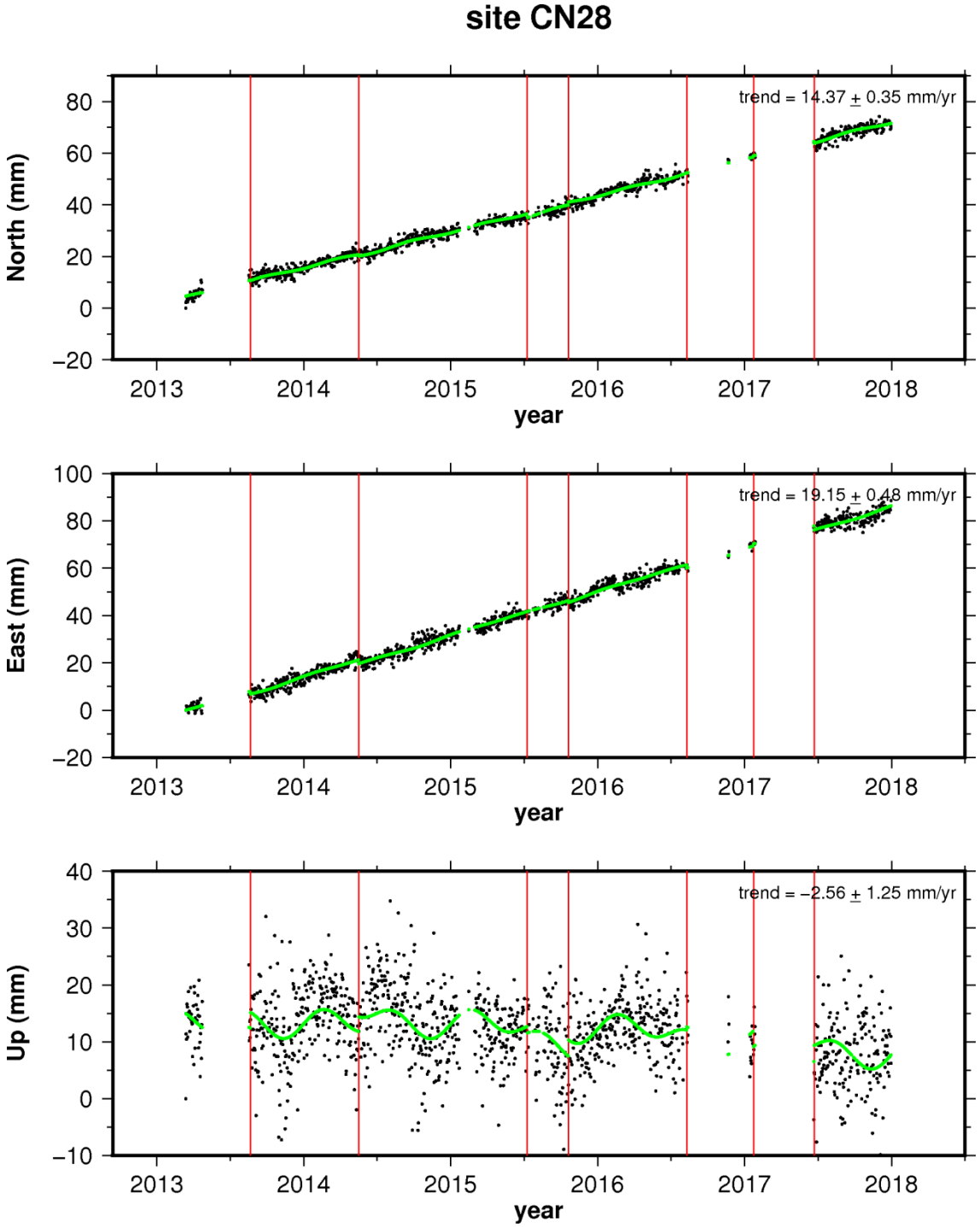
site CN28
trend = 14.37 ± 0.35 mm/yr
North (mm)
80
60
40
20
0
−20
2013
2014
2015
2016
2017
2018
year
trend = 19.15 ± 0.48 mm/yr
East (mm)
100
80
60
40
20
0
−20
2013
2014
2015
2016
2017
2018
year
trend = −2.56 ± 1.25 mm/yr
Up (mm)
40
30
20
10
0
−10
2013
2014
2015
2016
2017
2018
year

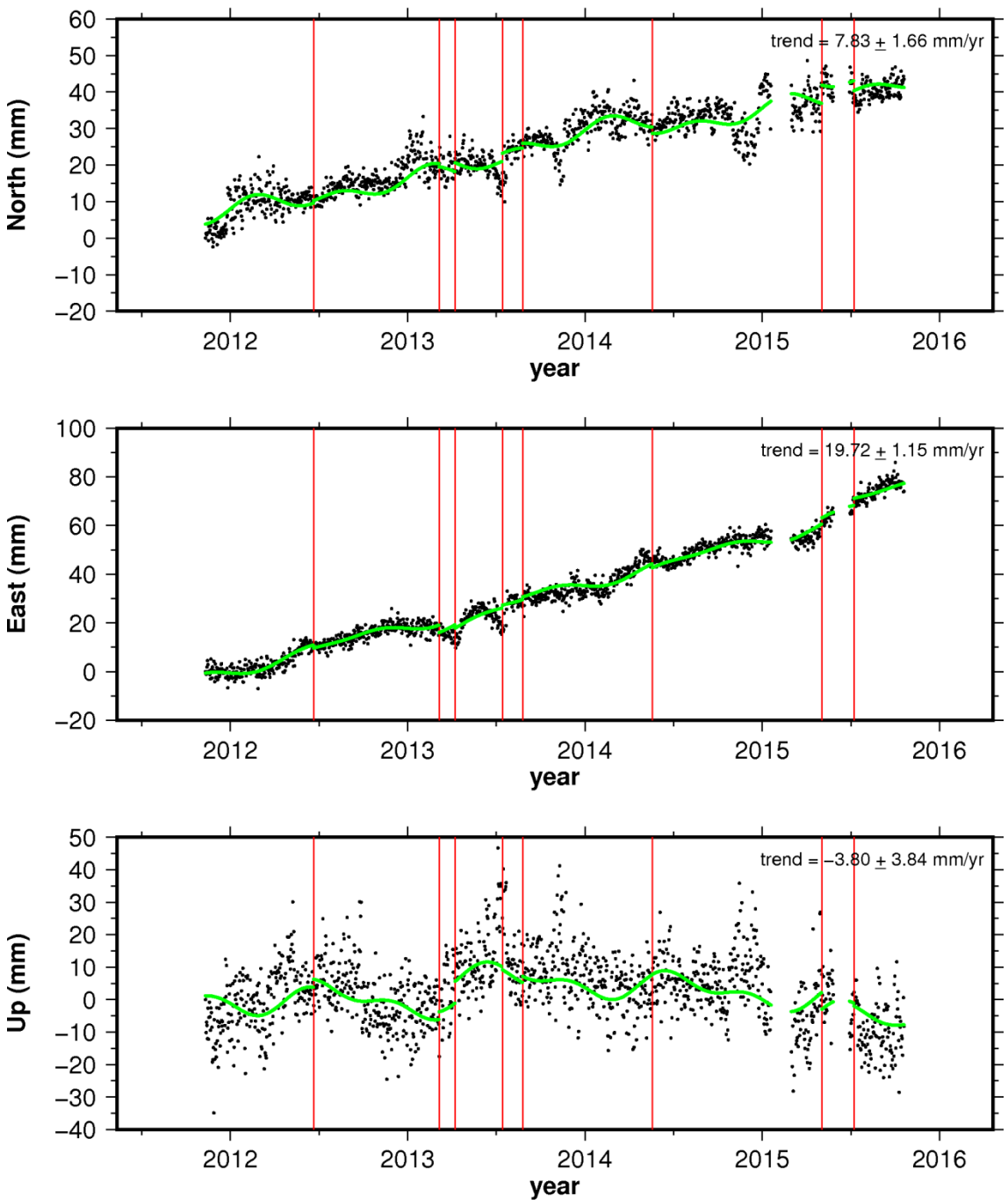
site CN33
trend = 7.83 ± 1.66 mm/yr
North (mm)
60
50
40
30
20
10
0
−10
−20
2012
2013
2014
2015
2016
year
trend = 19.72 ± 1.15 mm/yr
East (mm)
100
80
60
40
20
0
−20
2012
2013
2014
2015
2016
year
trend = −3.80 ± 3.84 mm/yr
Up (mm)
50
40
30
20
10
0
−10
−20
−30
−40
2012
2013
2014
2015
2016
year

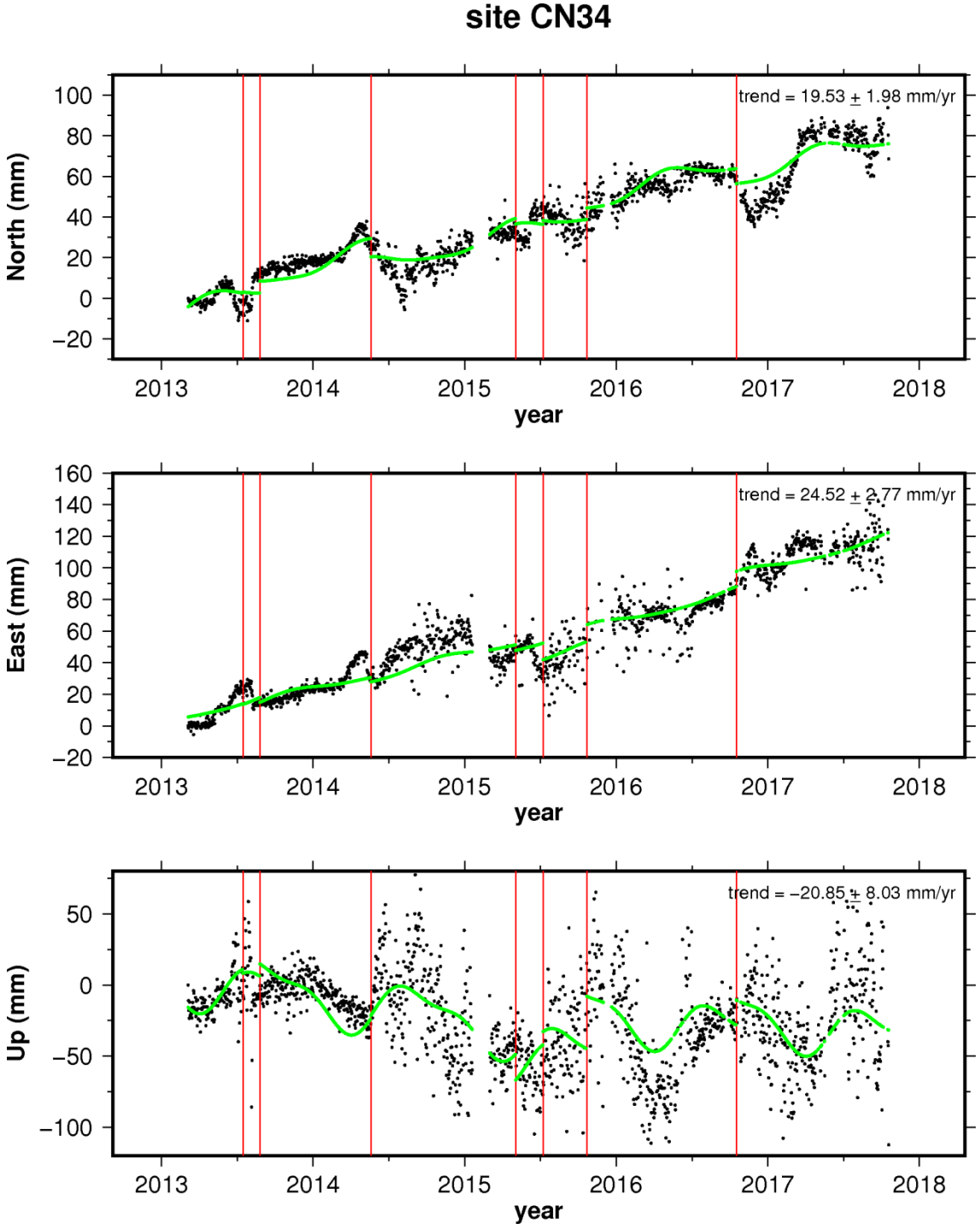
site CN34
trend = 19.53 ± 1.98 mm/yr
North (mm)
100
80
60
40
20
0
−20
2013
2014
2015
2016
2017
2018
year
trend = 24.52 ± 2.77 mm/yr
East (mm)
160
140
120
100
80
60
40
20
0
−20
2013
2014
2015
2016
2017
2018
year
trend = −20.85 ± 8.03 mm/yr
Up (mm)
50
0
−50
−100
2013
2014
2015
2016
2017
2018
year

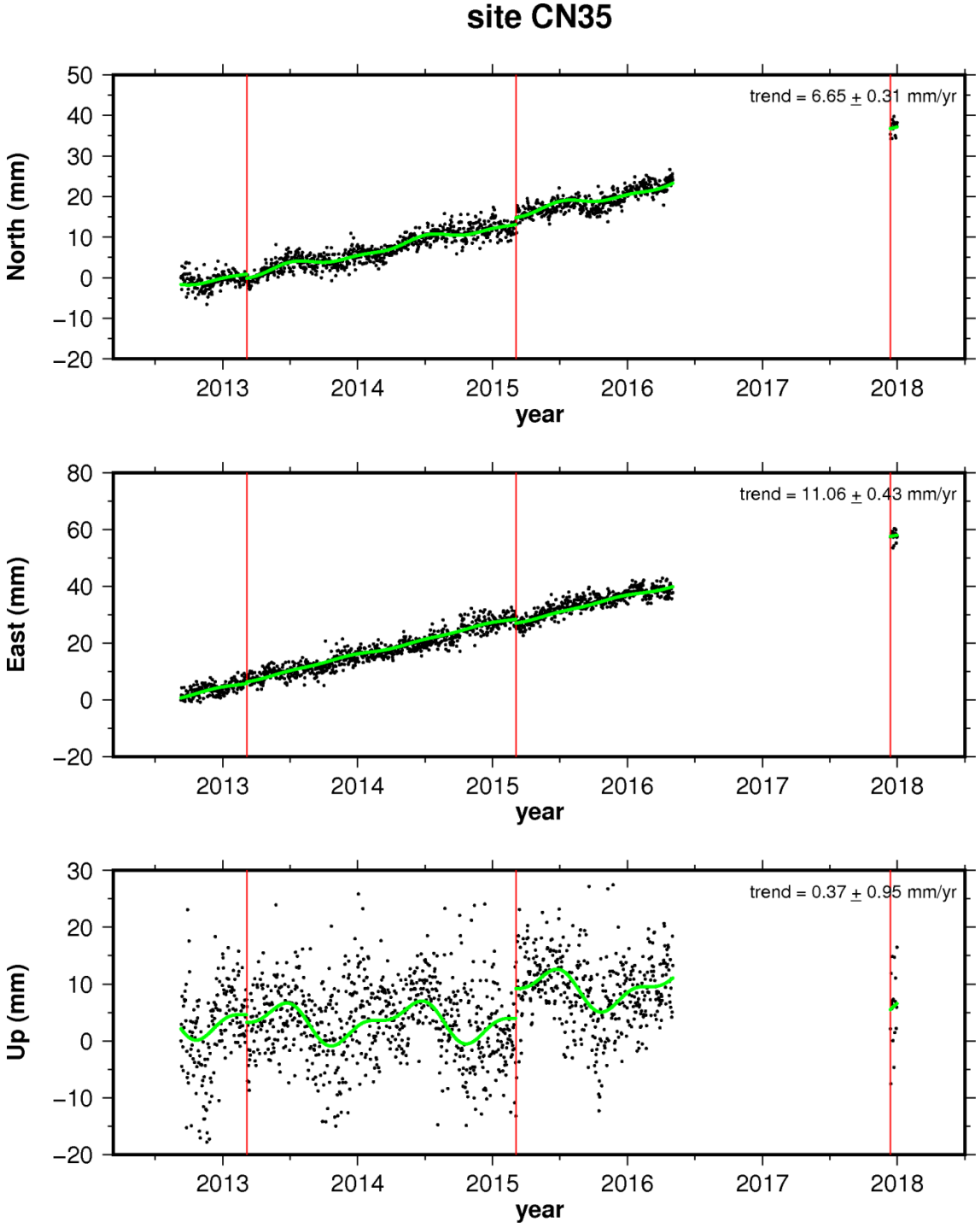
site CN35
North (mm)
trend = 6.65 ± 0.31 mm/yr
East (mm)
trend = 11.06 ± 0.43 mm/yr
Up (mm)
trend = 0.37 ± 0.95 mm/yr
year
2013
2014
2015
2016
2017
2018

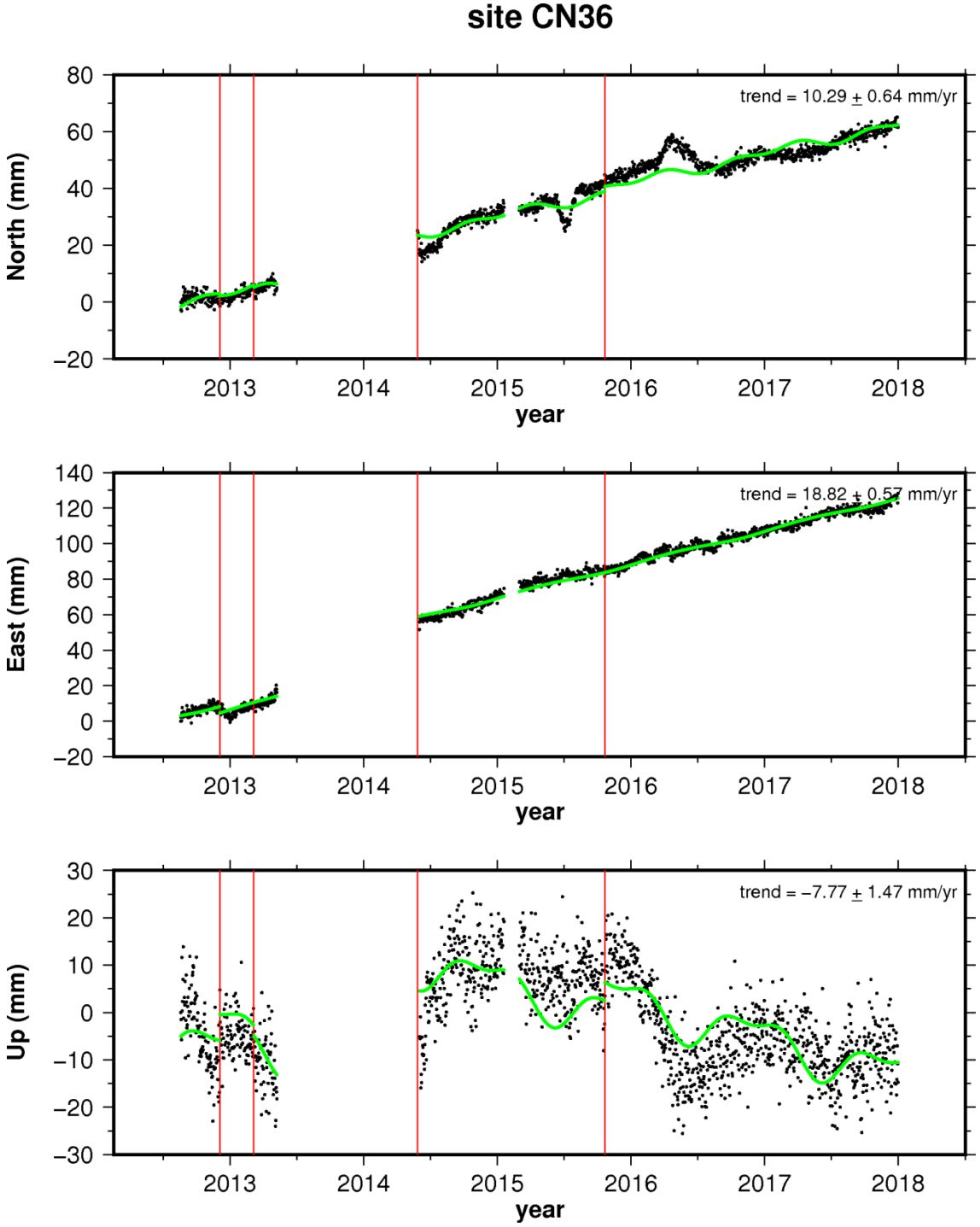
site CN36
trend = 10.29 ± 0.64 mm/yr
North (mm)
80
60
40
20
0
−20
2013
2014
2015
2016
2017
2018
year
trend = 18.82 ± 0.57 mm/yr
East (mm)
140
120
100
80
60
40
20
0
−20
2013
2014
2015
2016
2017
2018
year
trend = −7.77 ± 1.47 mm/yr
Up (mm)
30
20
10
0
−10
−20
−30
2013
2014
2015
2016
2017
2018
year

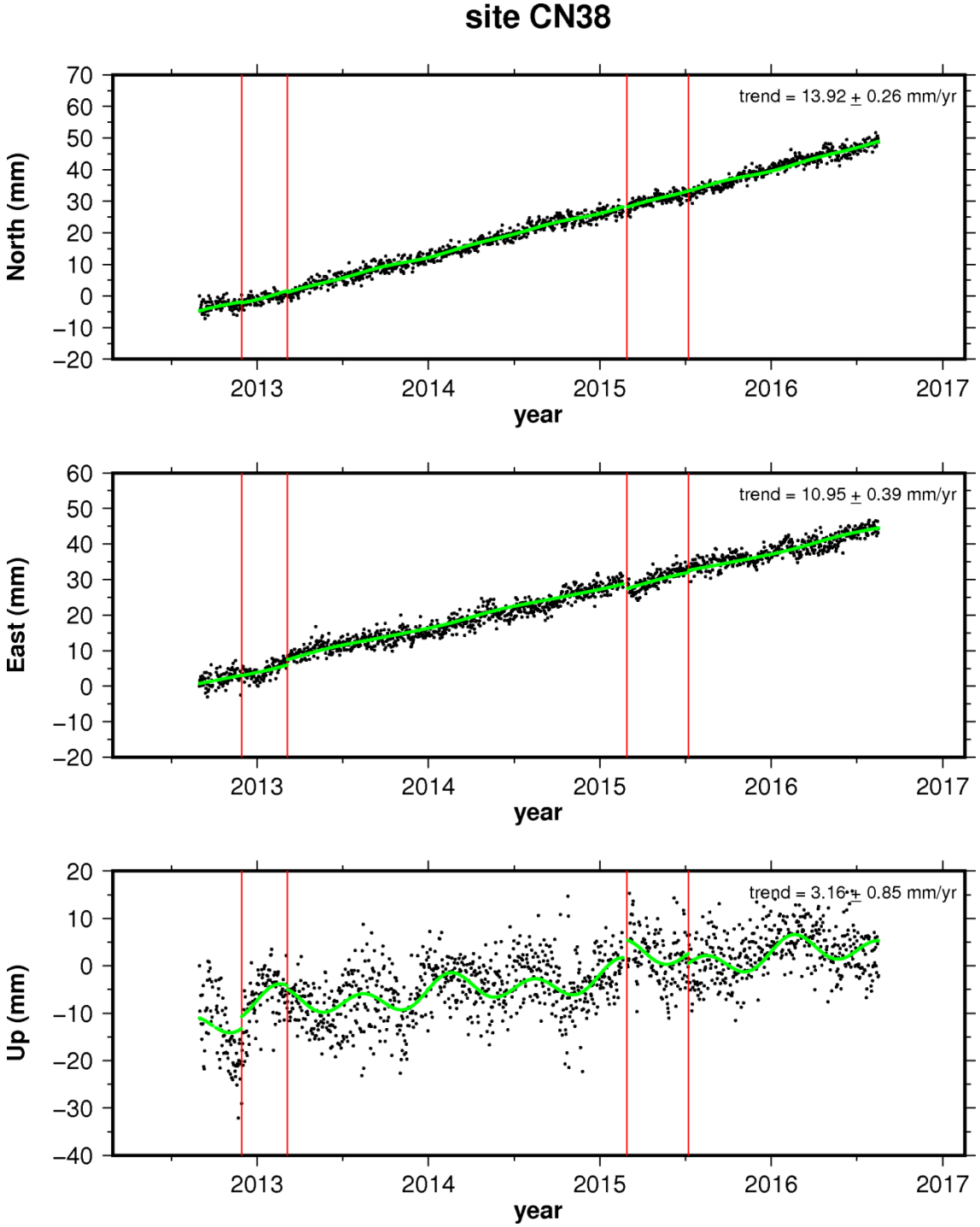
site CN38
North (mm)
trend = 13.92 ± 0.26 mm/yr
year
East (mm)
trend = 10.95 ± 0.39 mm/yr
year
Up (mm)
trend = 3.16 ± 0.85 mm/yr
year
2013
2014
2015
2016
2017

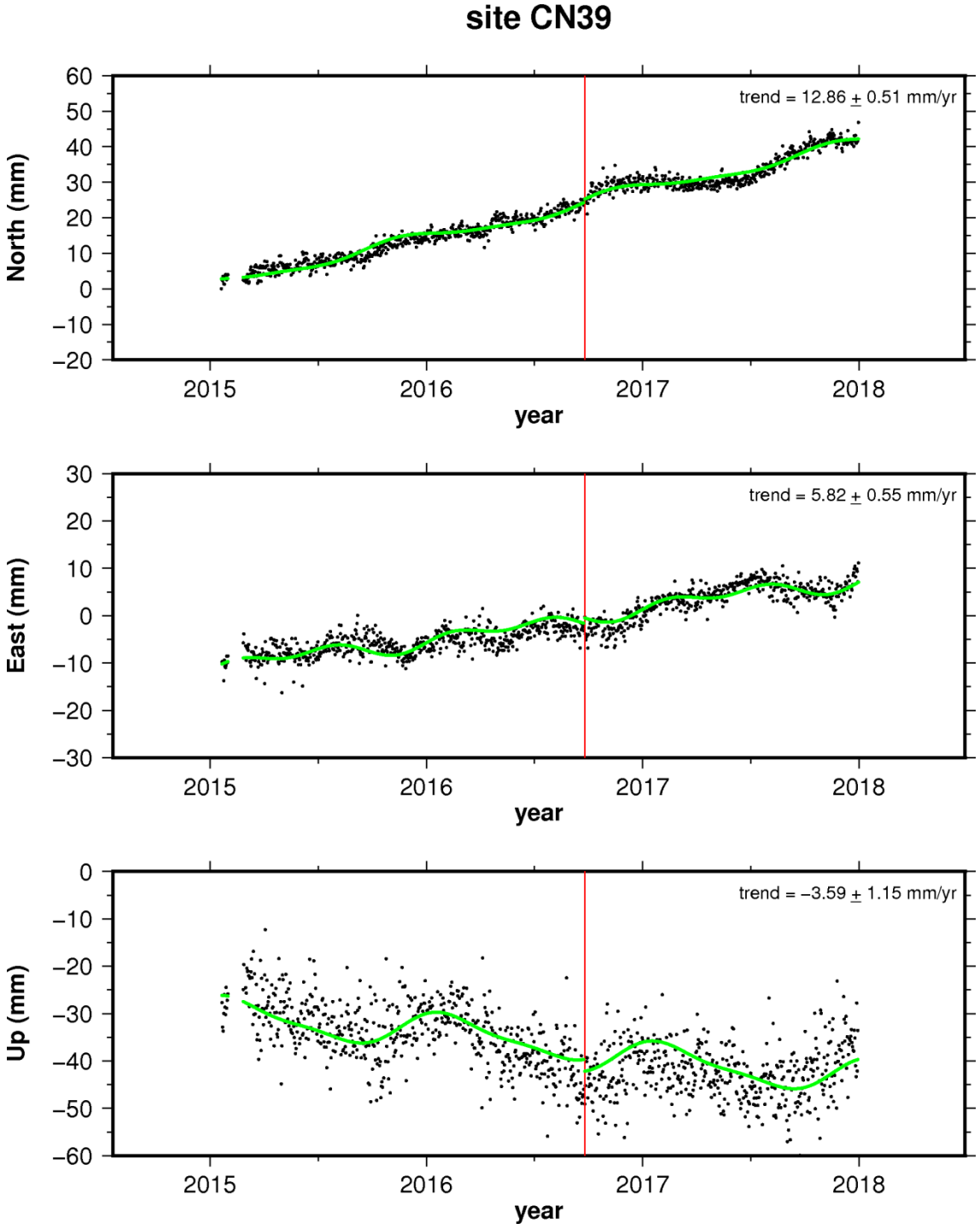
site CN39
trend = 12.86 ± 0.51 mm/yr
North (mm)
60
50
40
30
20
10
0
−10
−20
2015
2016
2017
2018
year
trend = 5.82 ± 0.55 mm/yr
East (mm)
30
20
10
0
−10
−20
−30
2015
2016
2017
2018
year
trend = −3.59 ± 1.15 mm/yr
Up (mm)
0
−10
−20
−30
−40
−50
−60
2015
2016
2017
2018
year

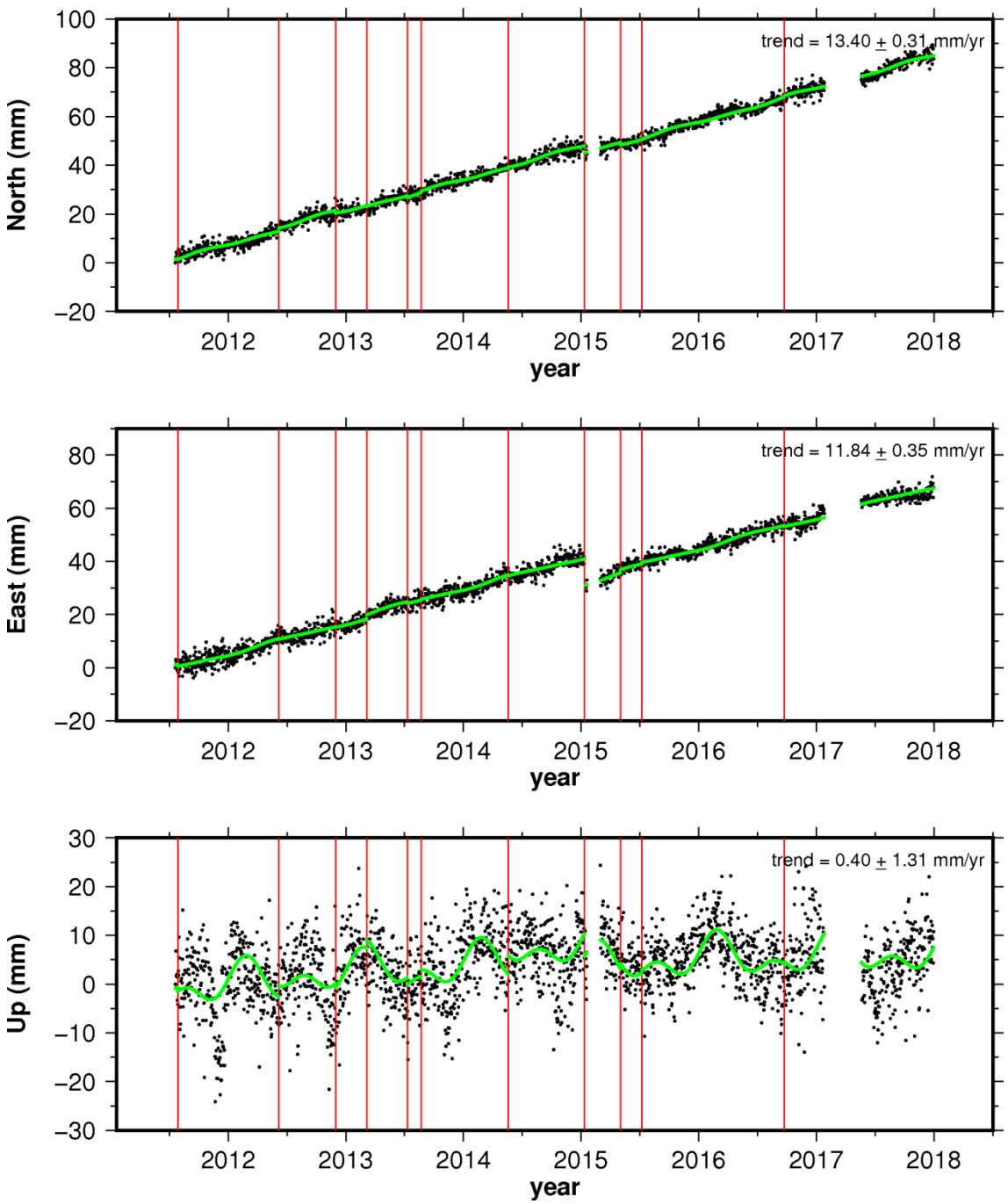
site CN40
trend = 13.40 ± 0.31 mm/yr
North (mm)
100
80
60
40
20
0
−20
2012
2013
2014
2015
2016
2017
2018
year
trend = 11.84 ± 0.35 mm/yr
East (mm)
80
60
40
20
0
−20
2012
2013
2014
2015
2016
2017
2018
year
trend = 0.40 ± 1.31 mm/yr
Up (mm)
30
20
10
0
−10
−20
−30
2012
2013
2014
2015
2016
2017
2018
year

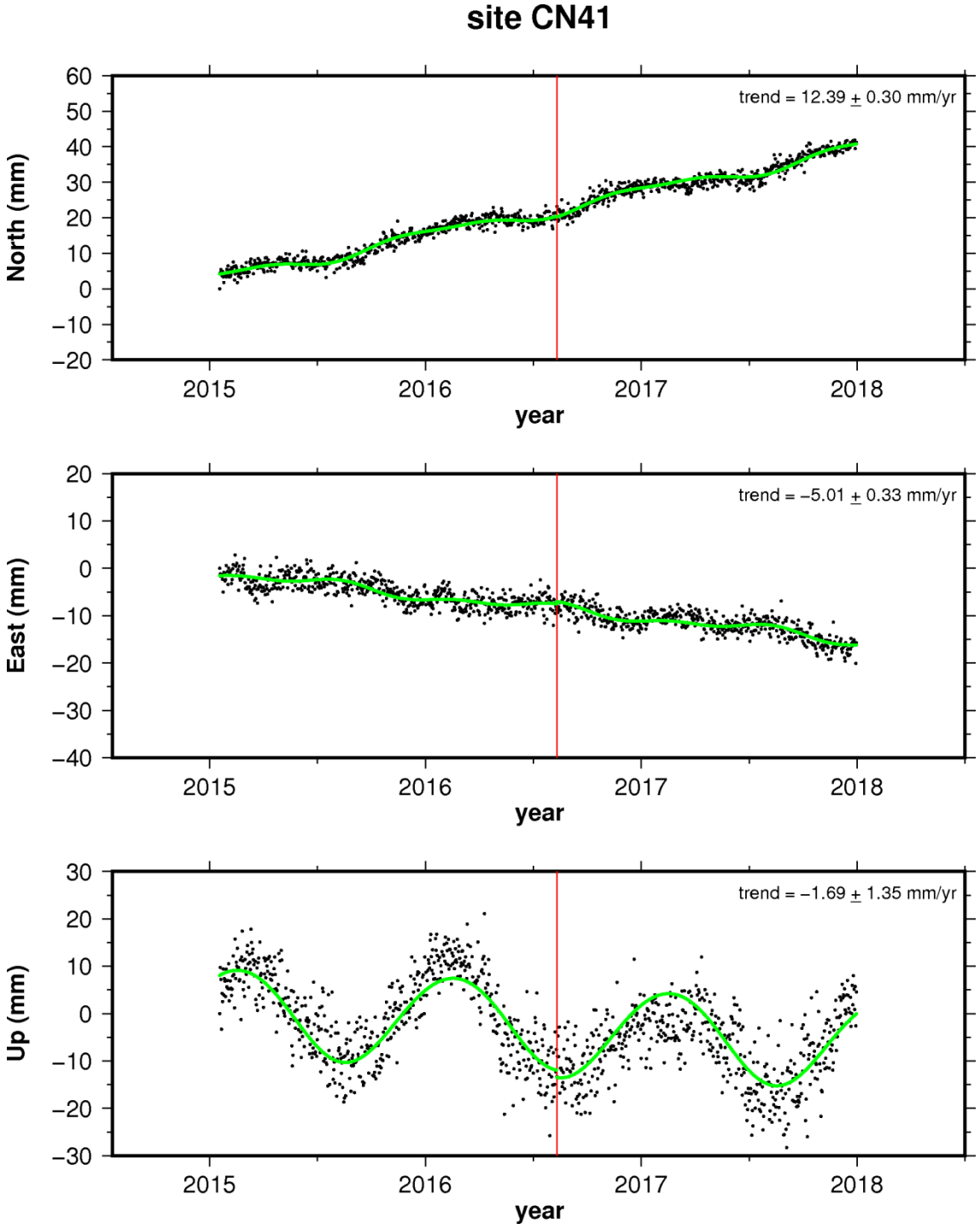
site CN41
trend = 12.39 ± 0.30 mm/yr
North (mm)
60
50
40
30
20
10
0
−10
−20
2015
2016
2017
2018
year
trend = −5.01 ± 0.33 mm/yr
East (mm)
20
10
0
−10
−20
−30
−40
2015
2016
2017
2018
year
trend = −1.69 ± 1.35 mm/yr
Up (mm)
30
20
10
0
−10
−20
−30
2015
2016
2017
2018
year

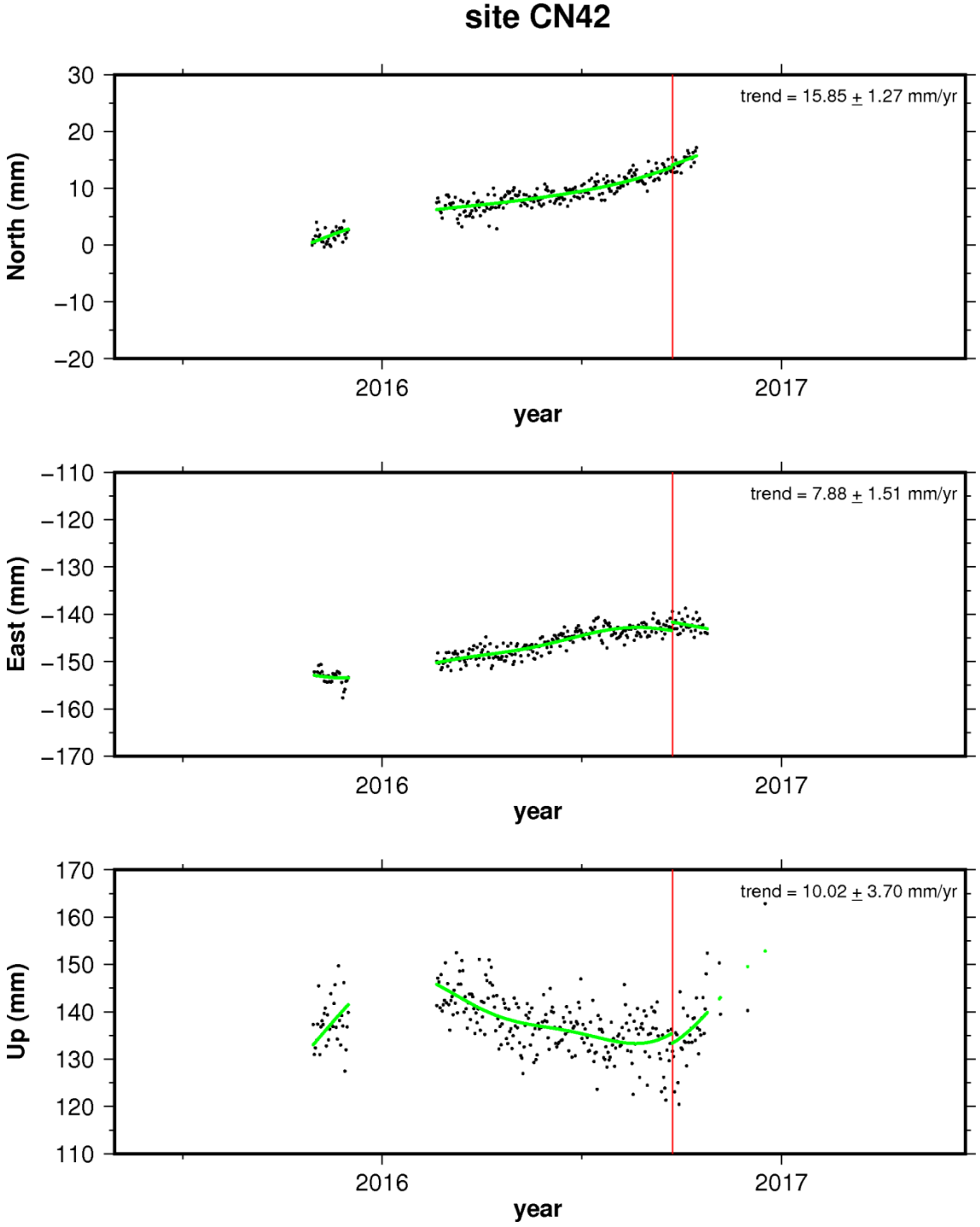
site CN42
trend = 15.85 ± 1.27 mm/yr
North (mm)
30
20
10
0
−10
−20
2016
2017
year
trend = 7.88 ± 1.51 mm/yr
East (mm)
−110
−120
−130
−140
−150
−160
−170
2016
2017
year
trend = 10.02 ± 3.70 mm/yr
Up (mm)
170
160
150
140
130
120
110
2016
2017
year

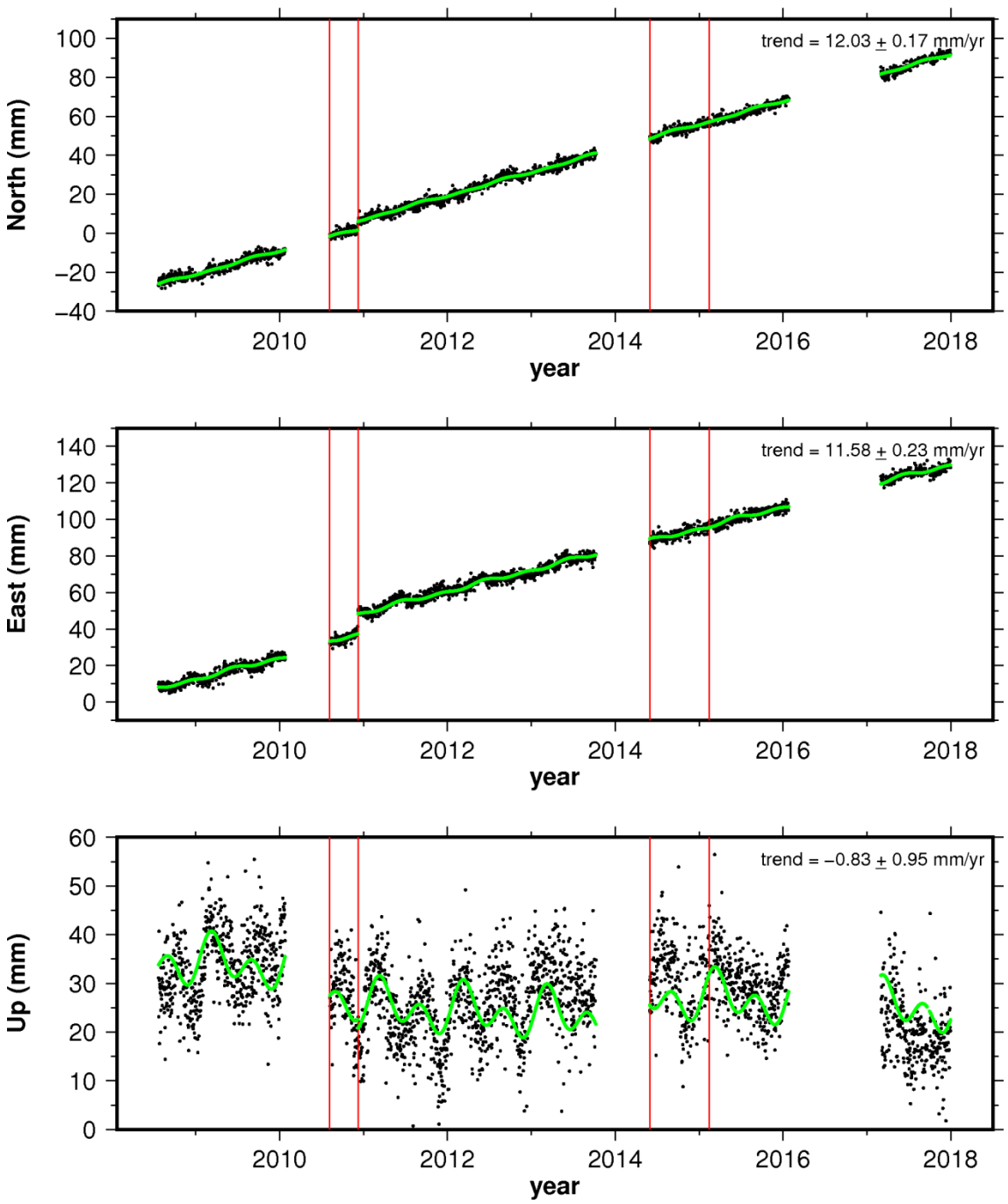
site CORO
trend = 12.03 ± 0.17 mm/yr
North (mm)
100
80
60
40
20
0
−20
−40
2010
2012
2014
2016
2018
year
trend = 11.58 ± 0.23 mm/yr
East (mm)
140
120
100
80
60
40
20
0
2010
2012
2014
2016
2018
year
trend = −0.83 ± 0.95 mm/yr
Up (mm)
60
50
40
30
20
10
0
2010
2012
2014
2016
2018
year

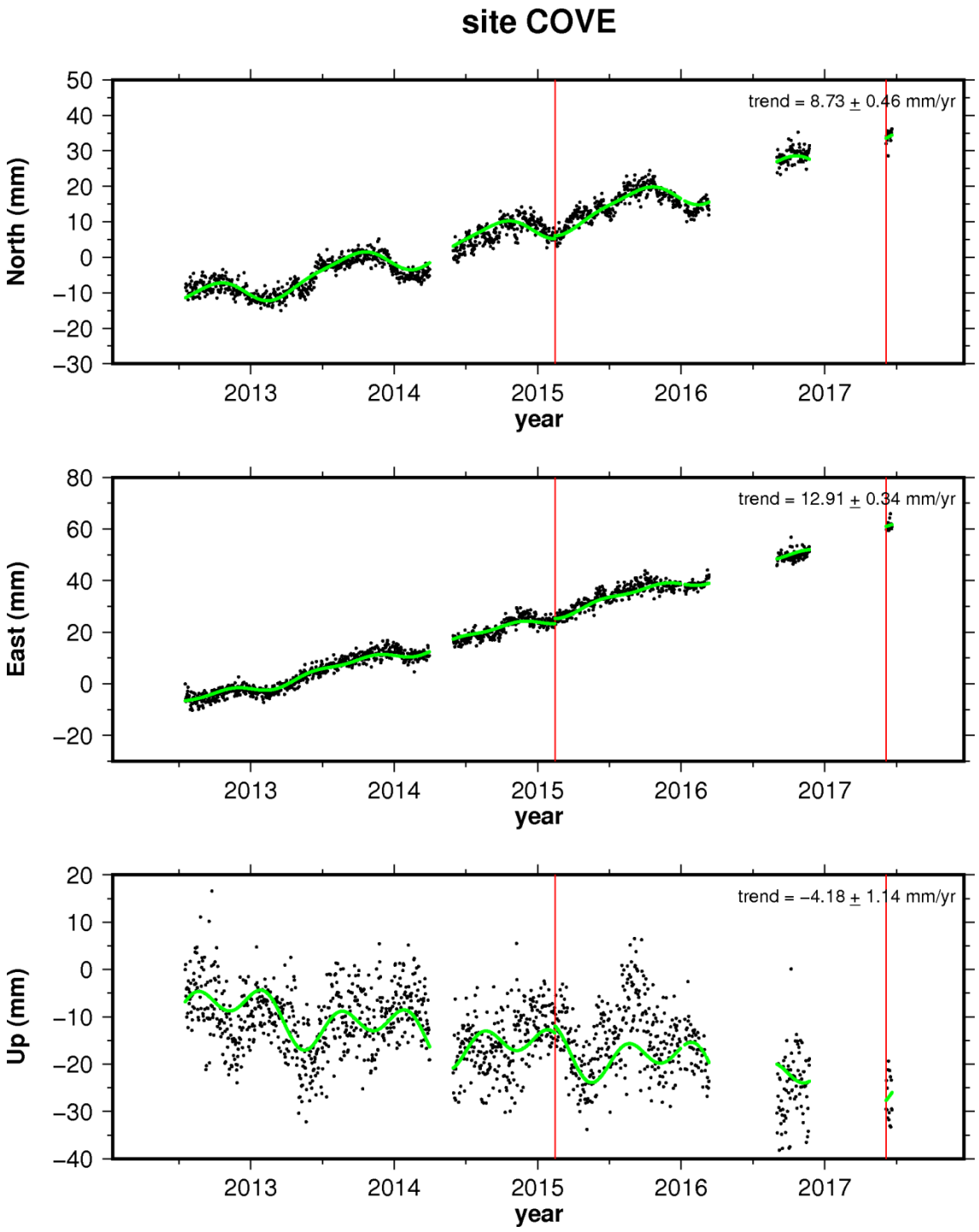
site COVE
trend = 8.73 ± 0.46 mm/yr
North (mm)
50
40
30
20
10
0
−10
−20
−30
2013
2014
2015
2016
2017
year
trend = 12.91 ± 0.34 mm/yr
East (mm)
80
60
40
20
0
−20
2013
2014
2015
2016
2017
year
trend = −4.18 ± 1.14 mm/yr
Up (mm)
20
10
0
−10
−20
−30
−40
2013
2014
2015
2016
2017
year

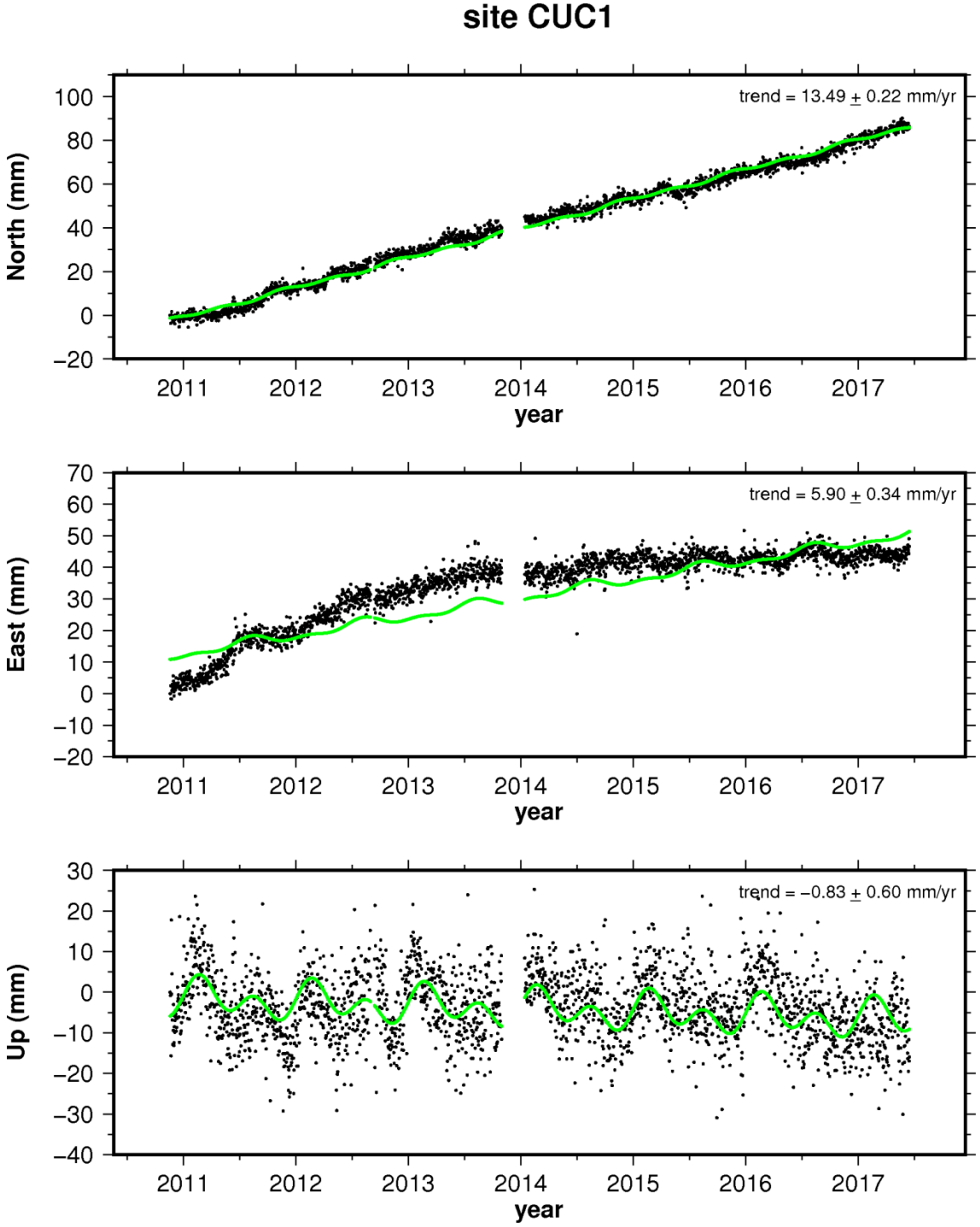
site CUC1
trend = 13.49 ± 0.22 mm/yr
North (mm)
100
80
60
40
20
0
−20
2011
2012
2013
2014
2015
2016
2017
year
trend = 5.90 ± 0.34 mm/yr
East (mm)
70
60
50
40
30
20
10
0
−10
−20
year
trend = −0.83 ± 0.60 mm/yr
Up (mm)
30
20
10
0
−10
−20
−30
−40
year

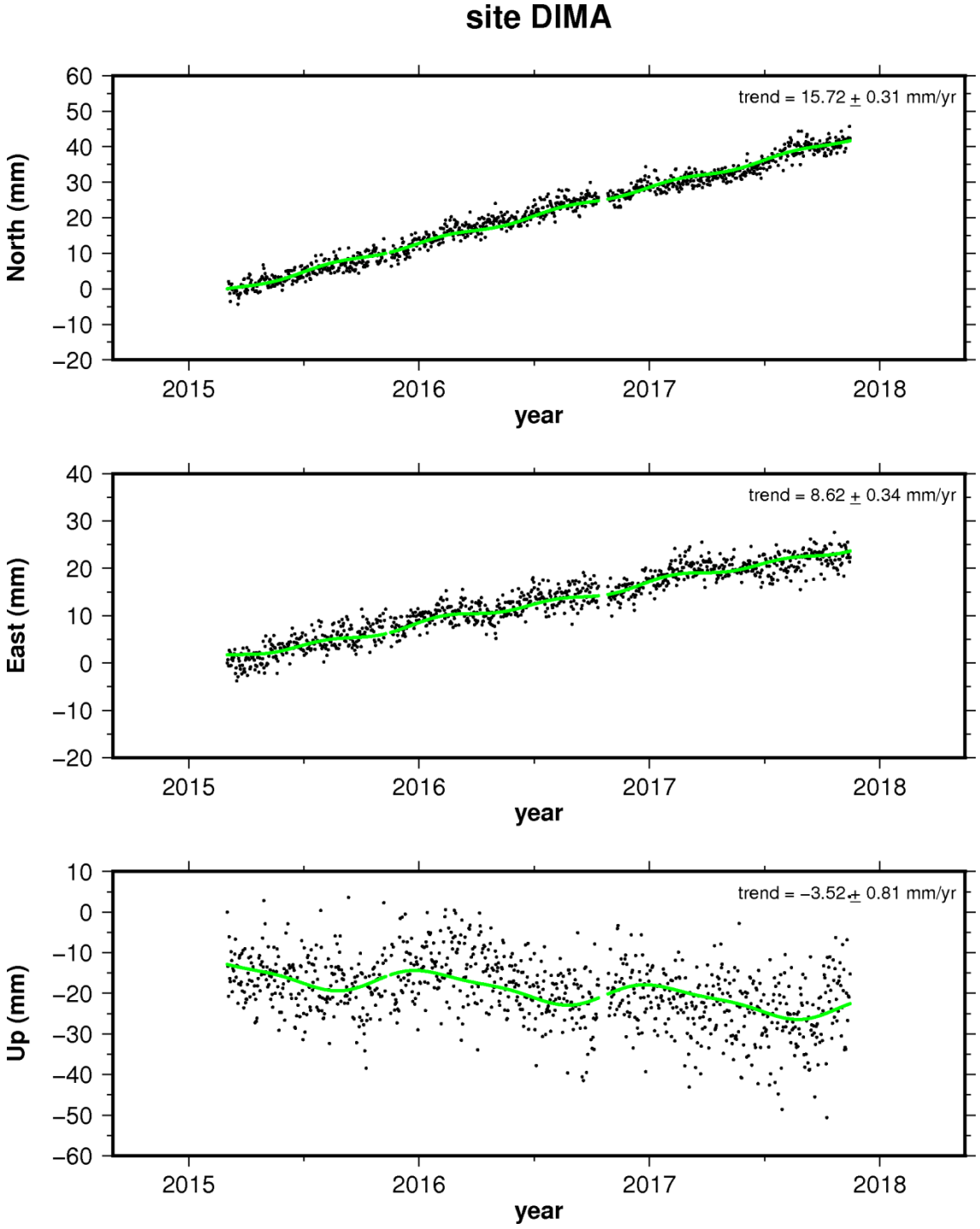
site DIMA
trend = 15.72 ± 0.31 mm/yr
North (mm)
60
50
40
30
20
10
0
−10
−20
2015
2016
2017
2018
year
trend = 8.62 ± 0.34 mm/yr
East (mm)
40
30
20
10
0
−10
−20
2015
2016
2017
2018
year
trend = −3.52 ± 0.81 mm/yr
Up (mm)
10
0
−10
−20
−30
−40
−50
−60
2015
2016
2017
2018
year

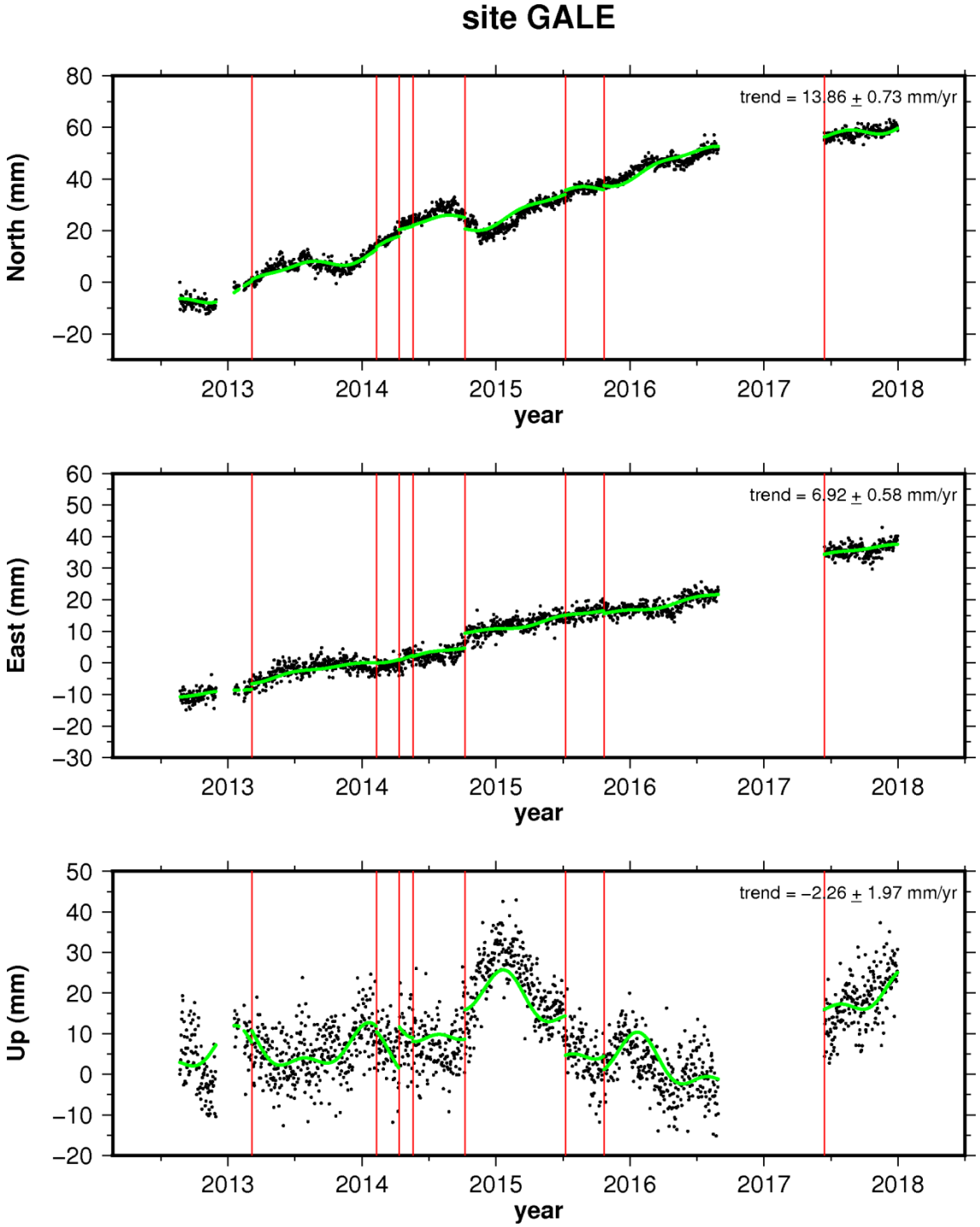
site GALE
trend = 13.86 ± 0.73 mm/yr
North (mm)
80
60
40
20
0
−20
2013
2014
2015
2016
2017
2018
year
trend = 6.92 ± 0.58 mm/yr
East (mm)
60
50
40
30
20
10
0
−10
−20
−30
2013
2014
2015
2016
2017
2018
year
trend = −2.26 ± 1.97 mm/yr
Up (mm)
50
40
30
20
10
0
−10
−20
2013
2014
2015
2016
2017
2018
year

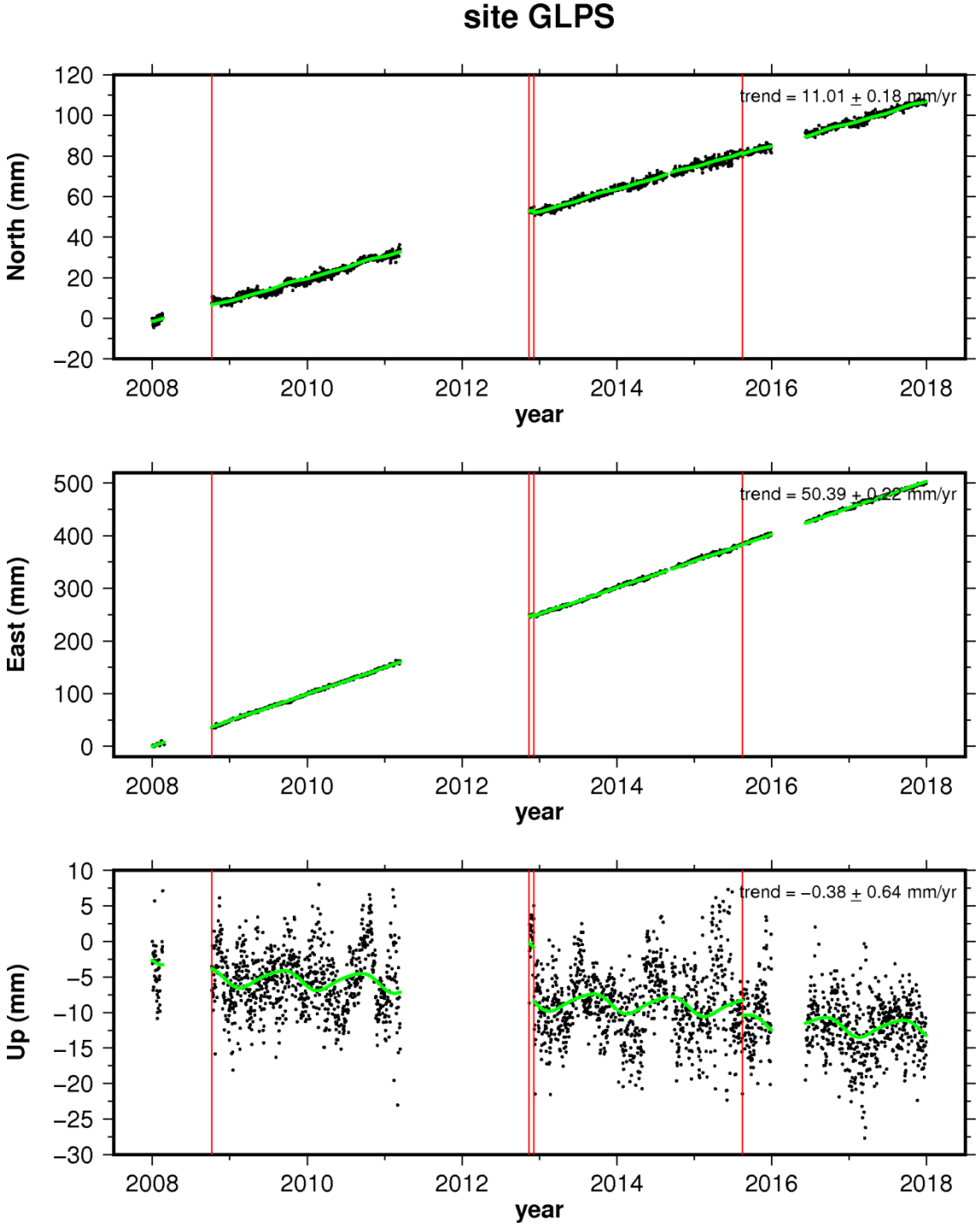
site GLPS
North (mm)
trend = 11.01 ± 0.18 mm/yr
East (mm)
trend = 50.39 ± 0.22 mm/yr
Up (mm)
trend = −0.38 ± 0.64 mm/yr
year
2008
2010
2012
2014
2016
2018

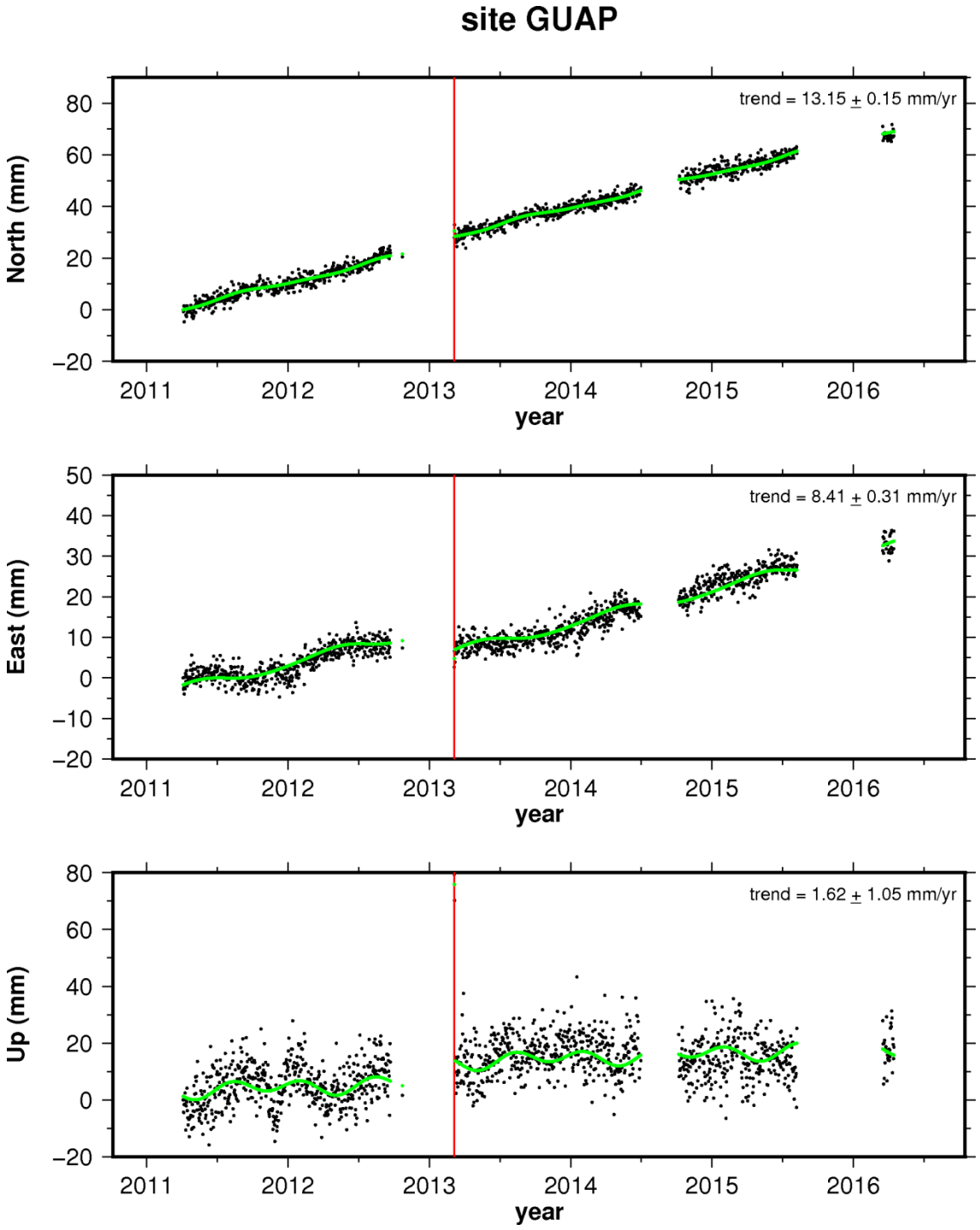
site GUAP
trend = 13.15 ± 0.15 mm/yr
North (mm)
80
60
40
20
0
−20
2011
2012
2013
2014
2015
2016
year
trend = 8.41 ± 0.31 mm/yr
East (mm)
50
40
30
20
10
0
−10
−20
2011
2012
2013
2014
2015
2016
year
trend = 1.62 ± 1.05 mm/yr
Up (mm)
80
60
40
20
0
−20
2011
2012
2013
2014
2015
2016
year

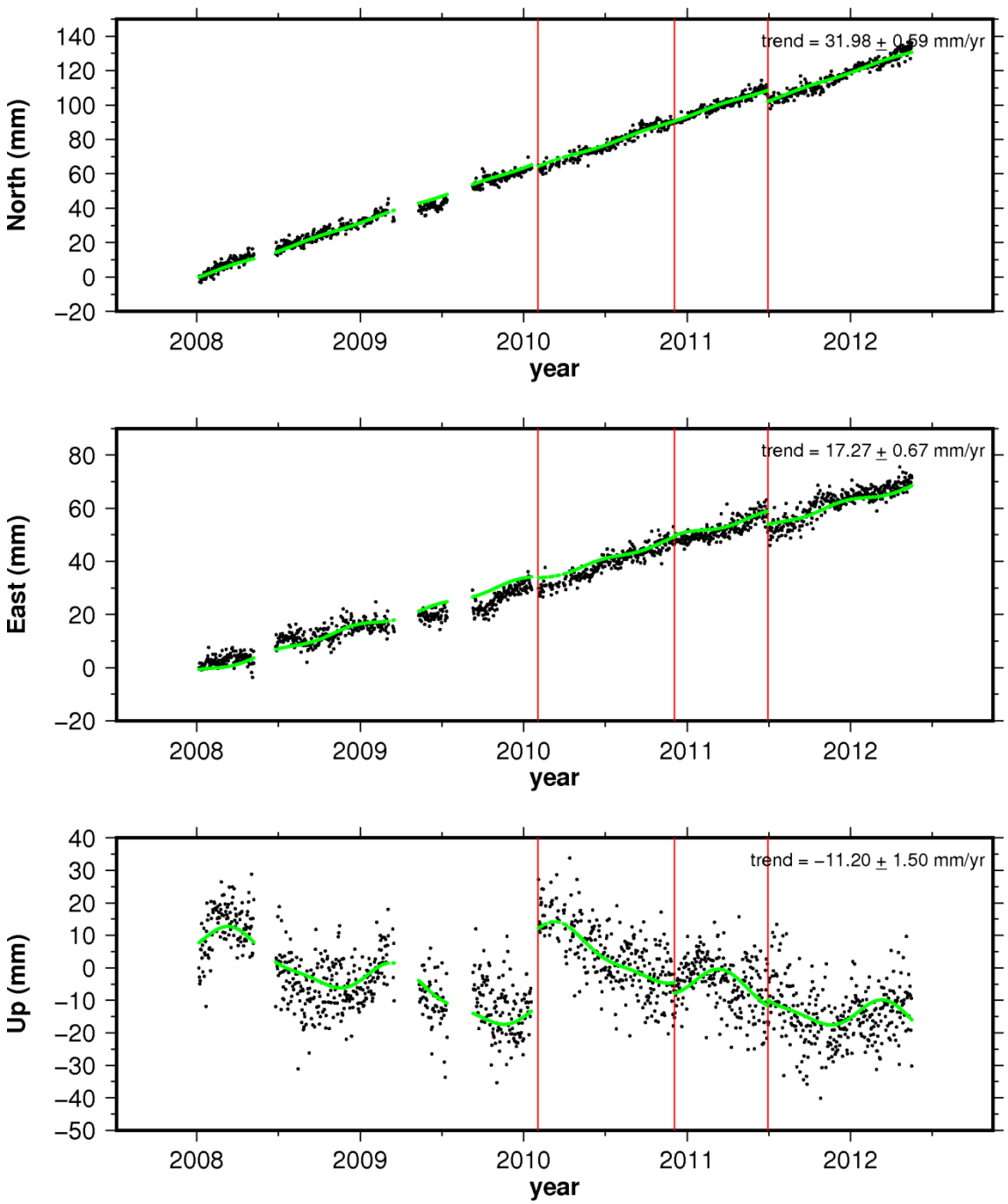
site IND1
North (mm)
trend = 31.98 ± 0.59 mm/yr
East (mm)
trend = 17.27 ± 0.67 mm/yr
Up (mm)
trend = −11.20 ± 1.50 mm/yr
year
2008
2009
2010
2011
2012

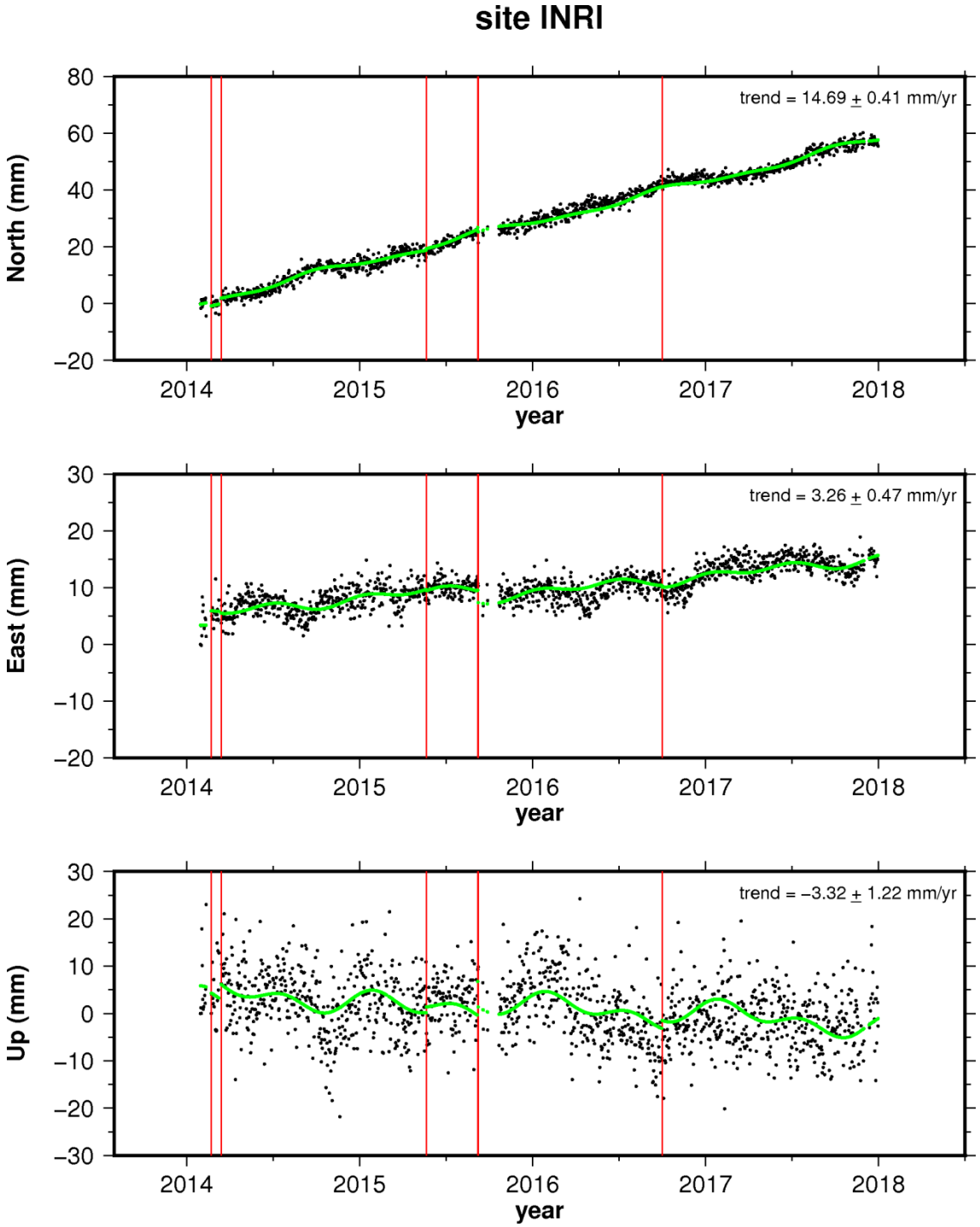
site INRI
North (mm)
trend = 14.69 ± 0.41 mm/yr
East (mm)
trend = 3.26 ± 0.47 mm/yr
Up (mm)
trend = −3.32 ± 1.22 mm/yr
year
2014
2015
2016
2017
2018

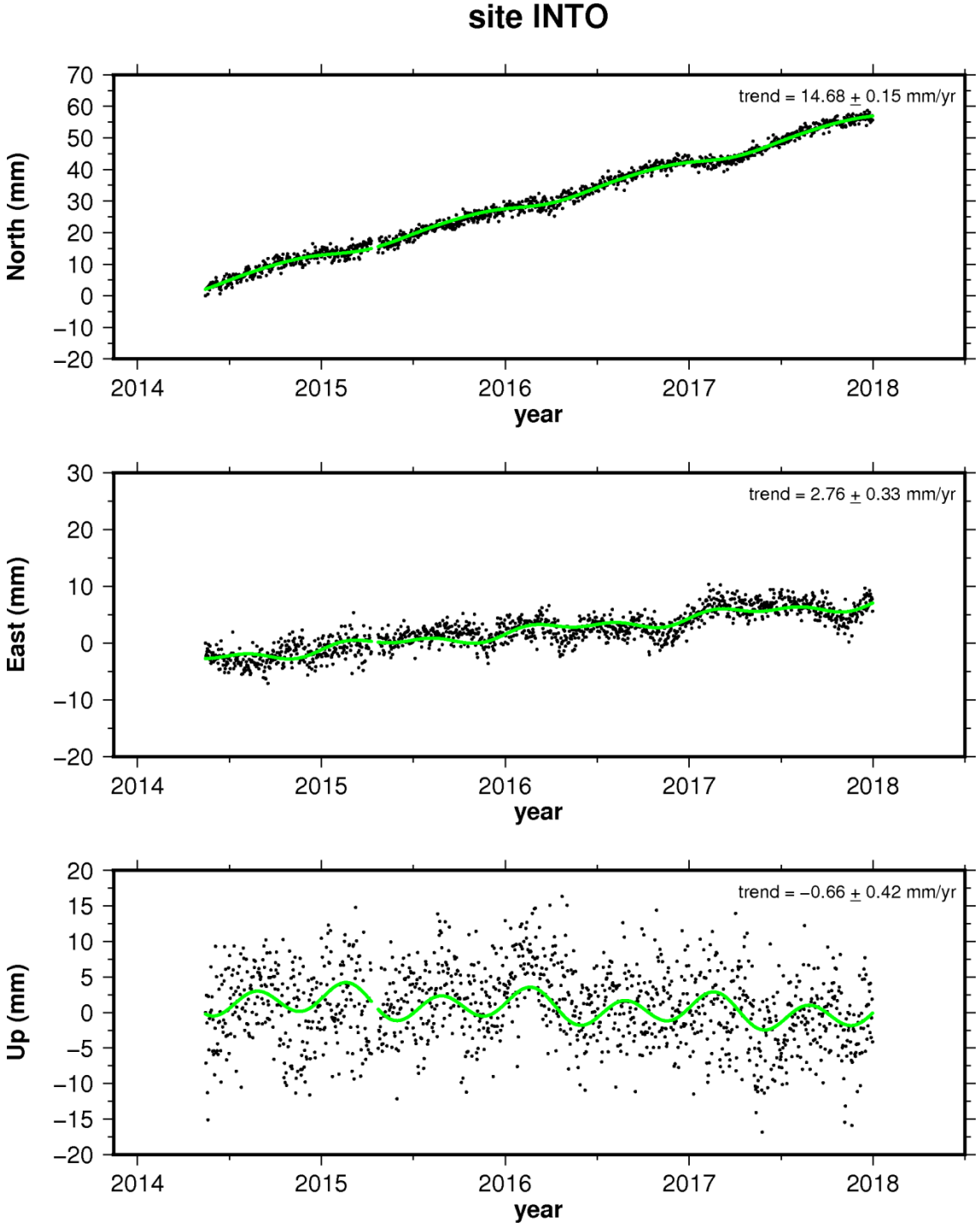
site INTO
trend = 14.68 ± 0.15 mm/yr
North (mm)
70
60
50
40
30
20
10
0
−10
−20
2014
2015
2016
2017
2018
year
trend = 2.76 ± 0.33 mm/yr
East (mm)
30
20
10
0
−10
−20
2014
2015
2016
2017
2018
year
trend = −0.66 ± 0.42 mm/yr
Up (mm)
20
15
10
5
0
−5
−10
−15
−20
2014
2015
2016
2017
2018
year

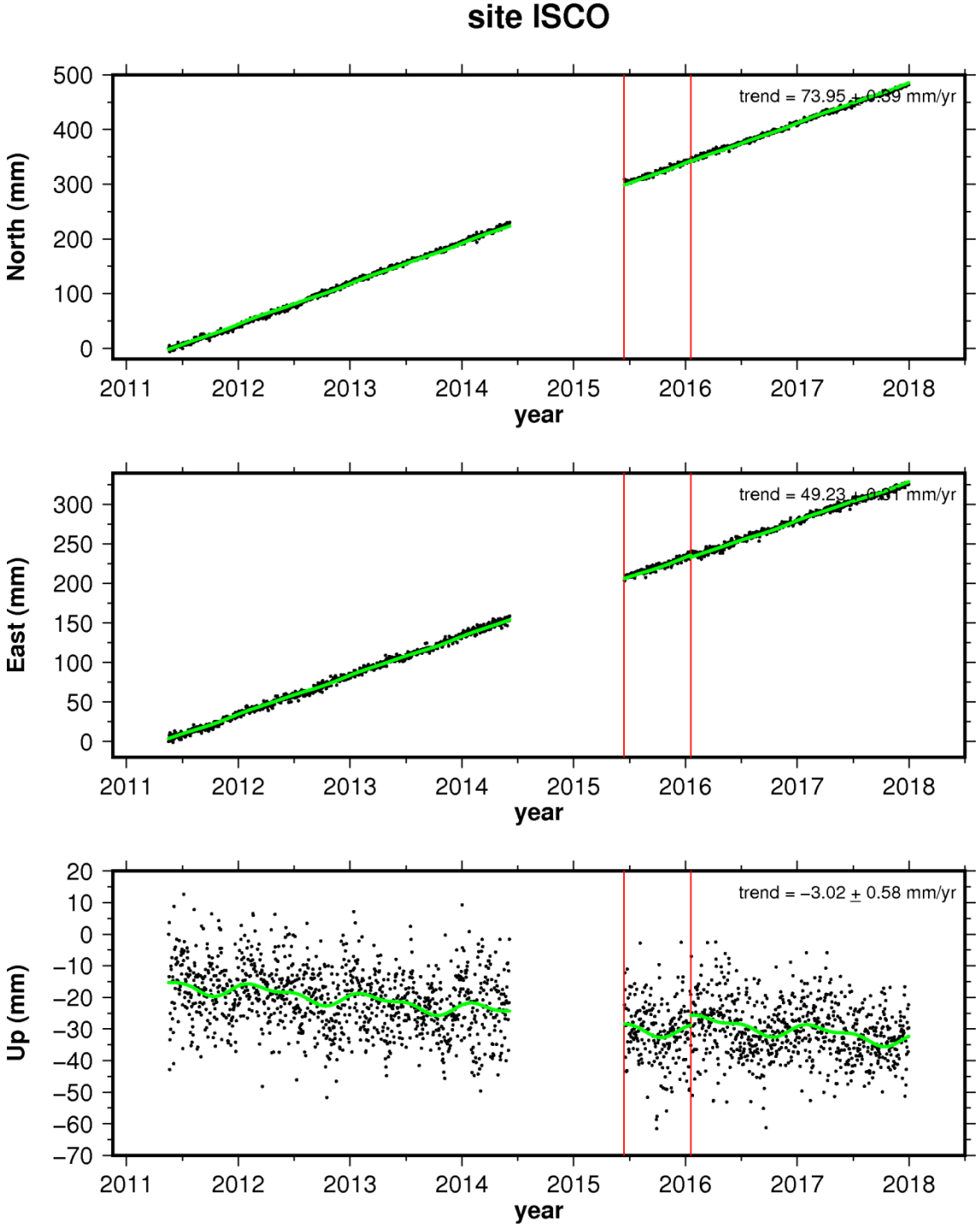
site ISCO
North (mm)
East (mm)
Up (mm)
year
trend = 73.95 ± 0.89 mm/yr
trend = 49.23 ± 0.81 mm/yr
trend = −3.02 ± 0.58 mm/yr

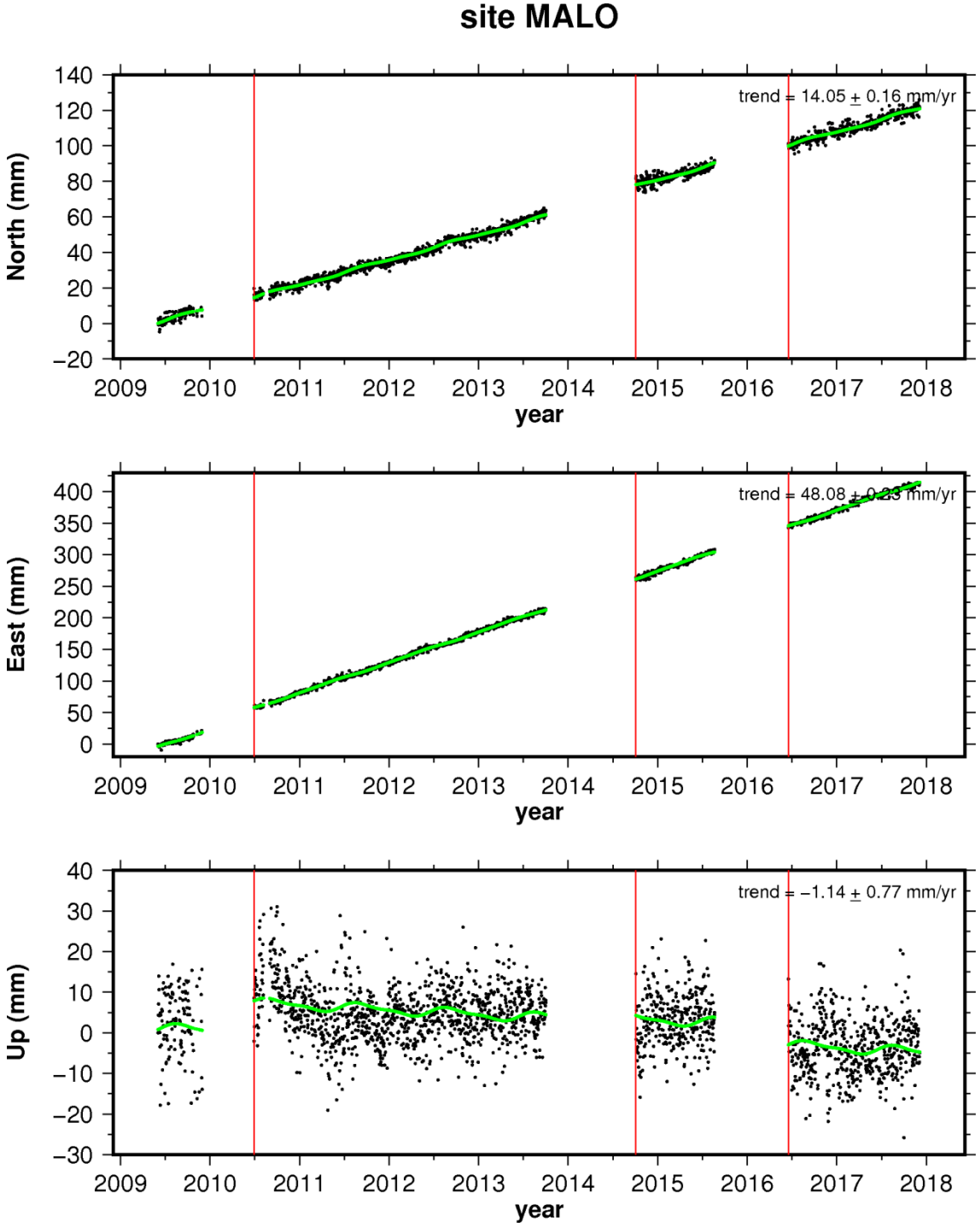
site MALO
North (mm)
trend = 14.05 ± 0.16 mm/yr
East (mm)
trend = 48.08 ± 0.23 mm/yr
Up (mm)
trend = −1.14 ± 0.77 mm/yr
year
2009
2010
2011
2012
2013
2014
2015
2016
2017
2018

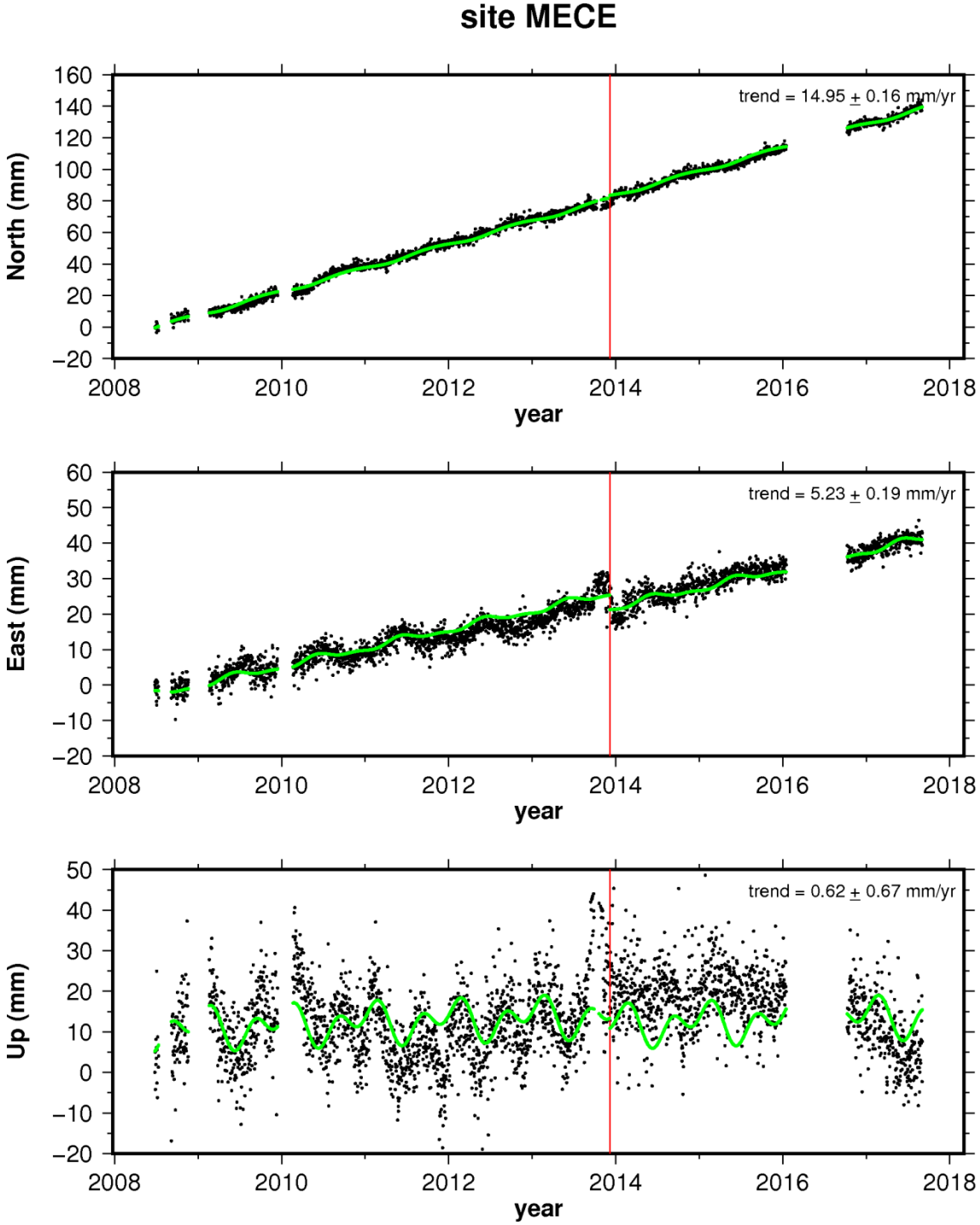
site MECE
North (mm)
trend = 14.95 ± 0.16 mm/yr
East (mm)
trend = 5.23 ± 0.19 mm/yr
Up (mm)
trend = 0.62 ± 0.67 mm/yr
year
2008
2010
2012
2014
2016
2018

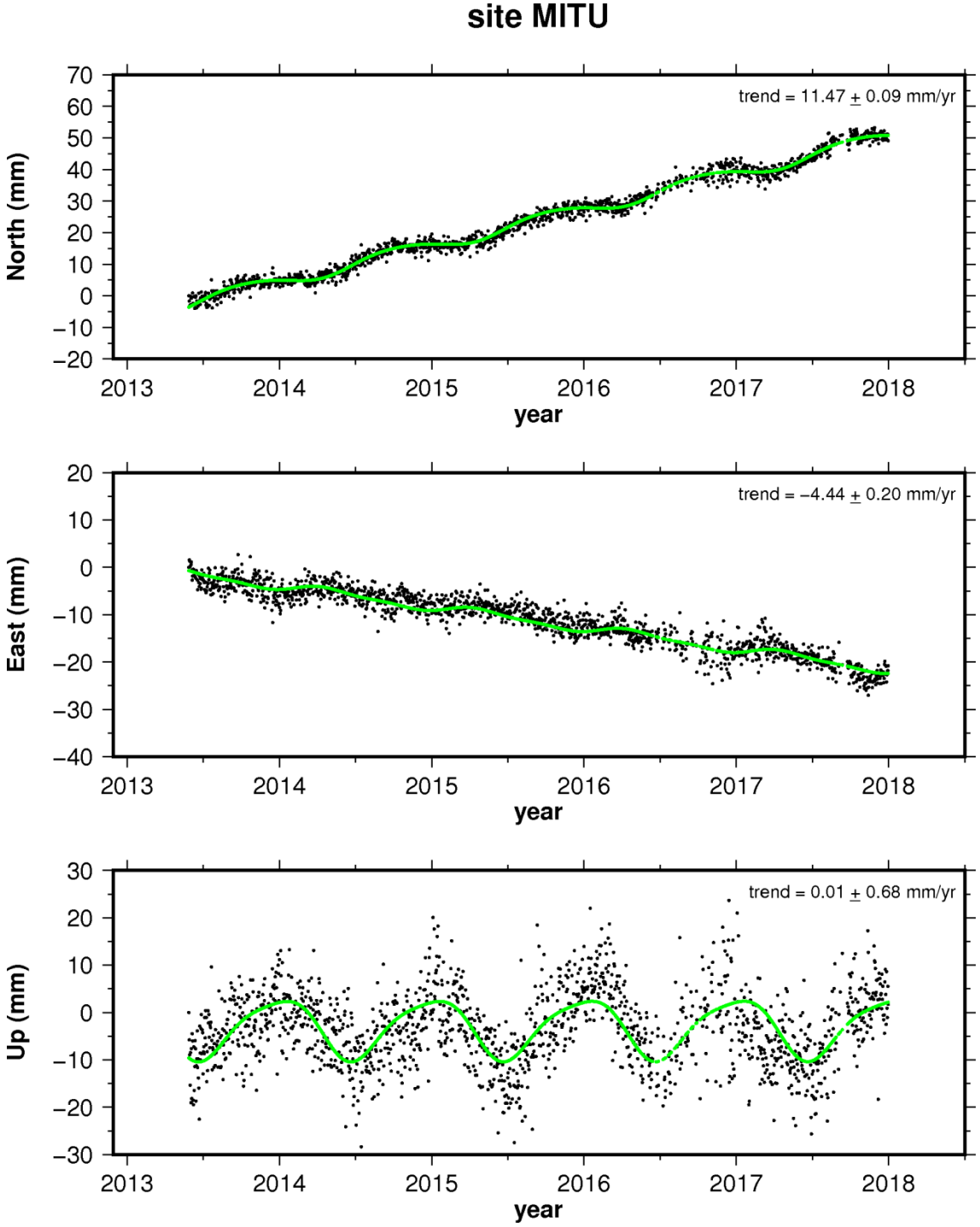
site MITU
trend = 11.47 ± 0.09 mm/yr
North (mm)
70
60
50
40
30
20
10
0
−10
−20
2013
2014
2015
2016
2017
2018
year
trend = −4.44 ± 0.20 mm/yr
East (mm)
20
10
0
−10
−20
−30
−40
2013
2014
2015
2016
2017
2018
year
trend = 0.01 ± 0.68 mm/yr
Up (mm)
30
20
10
0
−10
−20
−30
2013
2014
2015
2016
2017
2018
year

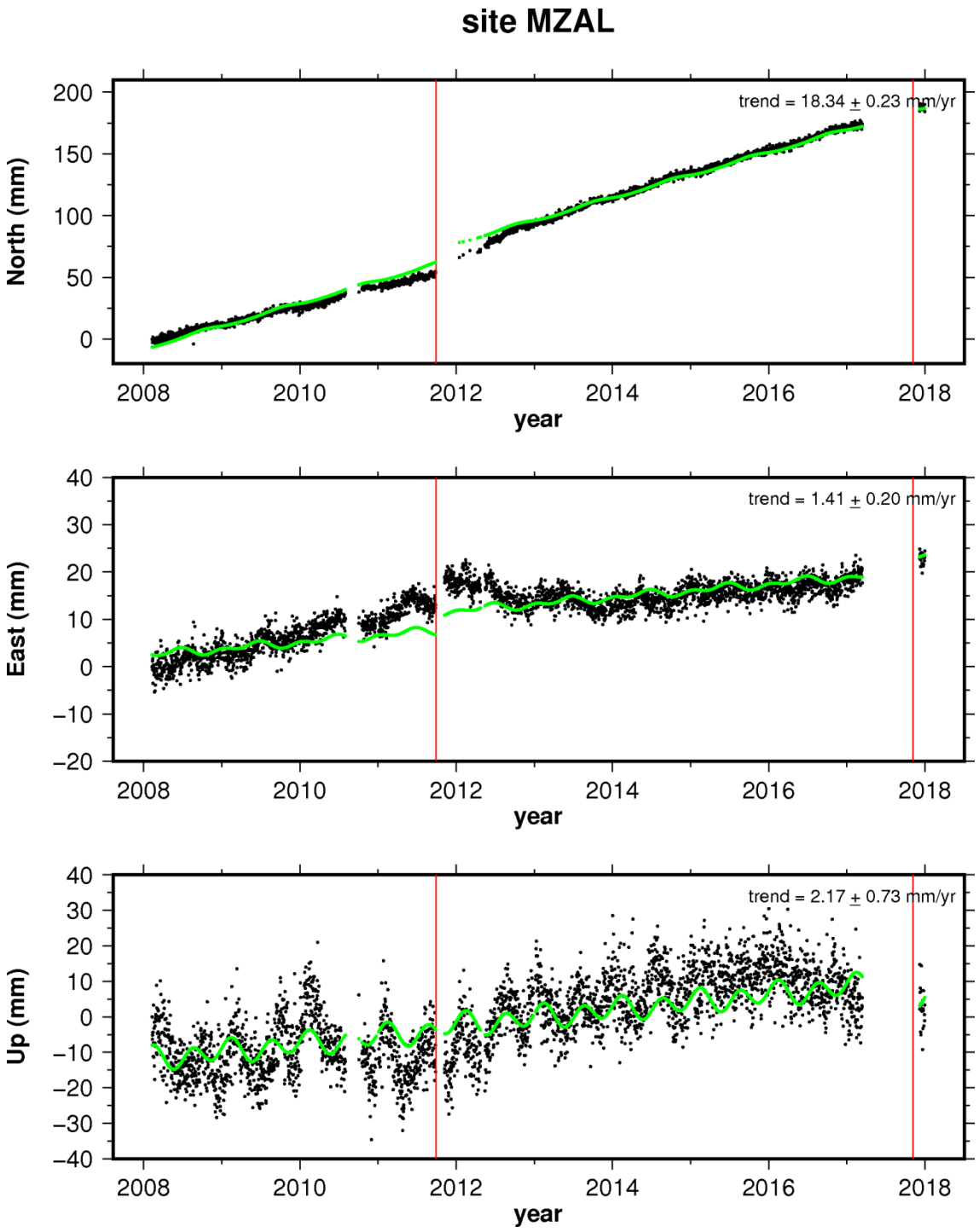
site MZAL
trend = 18.34 ± 0.23 mm/yr
North (mm)
200
150
100
50
0
2008
2010
2012
2014
2016
2018
year
trend = 1.41 ± 0.20 mm/yr
East (mm)
40
30
20
10
0
−10
−20
year
trend = 2.17 ± 0.73 mm/yr
Up (mm)
40
30
20
10
0
−10
−20
−30
−40
year

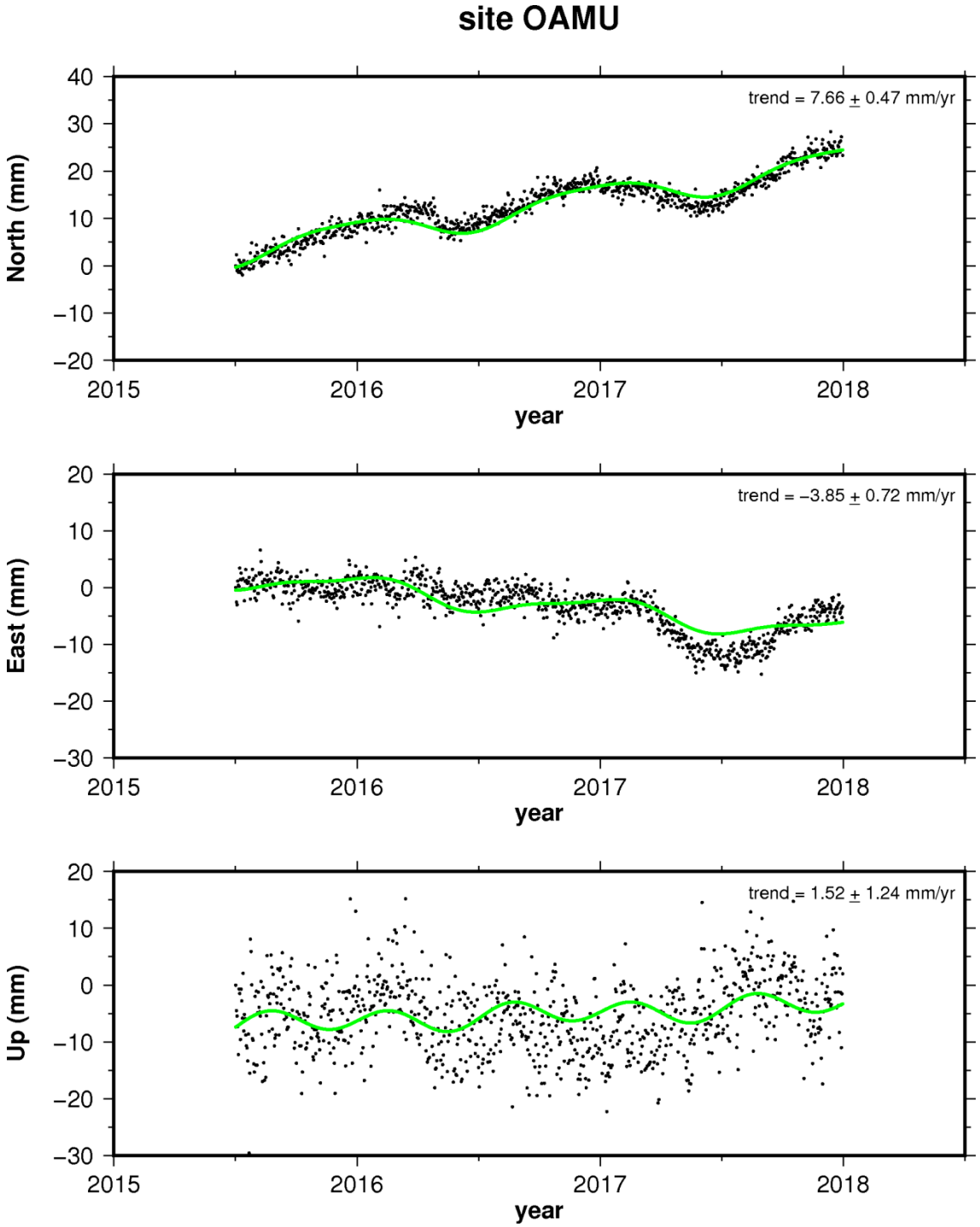
site OAMU
trend = 7.66 ± 0.47 mm/yr
North (mm)
40
30
20
10
0
−10
−20
2015
2016
2017
2018
year
trend = −3.85 ± 0.72 mm/yr
East (mm)
20
10
0
−10
−20
−30
2015
2016
2017
2018
year
trend = 1.52 ± 1.24 mm/yr
Up (mm)
20
10
0
−10
−20
−30
2015
2016
2017
2018
year

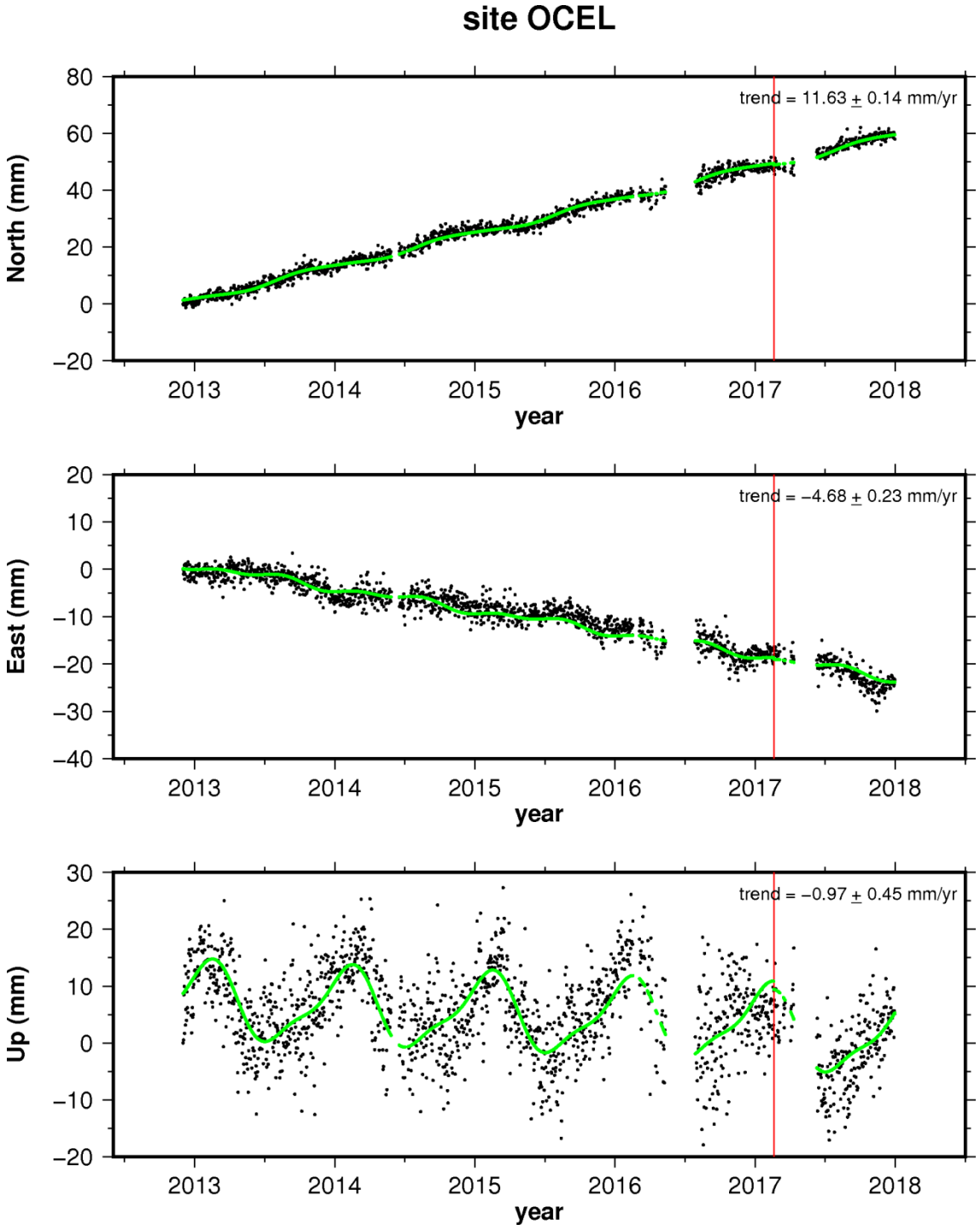
site OCEL
trend = 11.63 ± 0.14 mm/yr
North (mm)
80
60
40
20
0
−20
2013
2014
2015
2016
2017
2018
year
trend = −4.68 ± 0.23 mm/yr
East (mm)
20
10
0
−10
−20
−30
−40
2013
2014
2015
2016
2017
2018
year
trend = −0.97 ± 0.45 mm/yr
Up (mm)
30
20
10
0
−10
−20
2013
2014
2015
2016
2017
2018
year

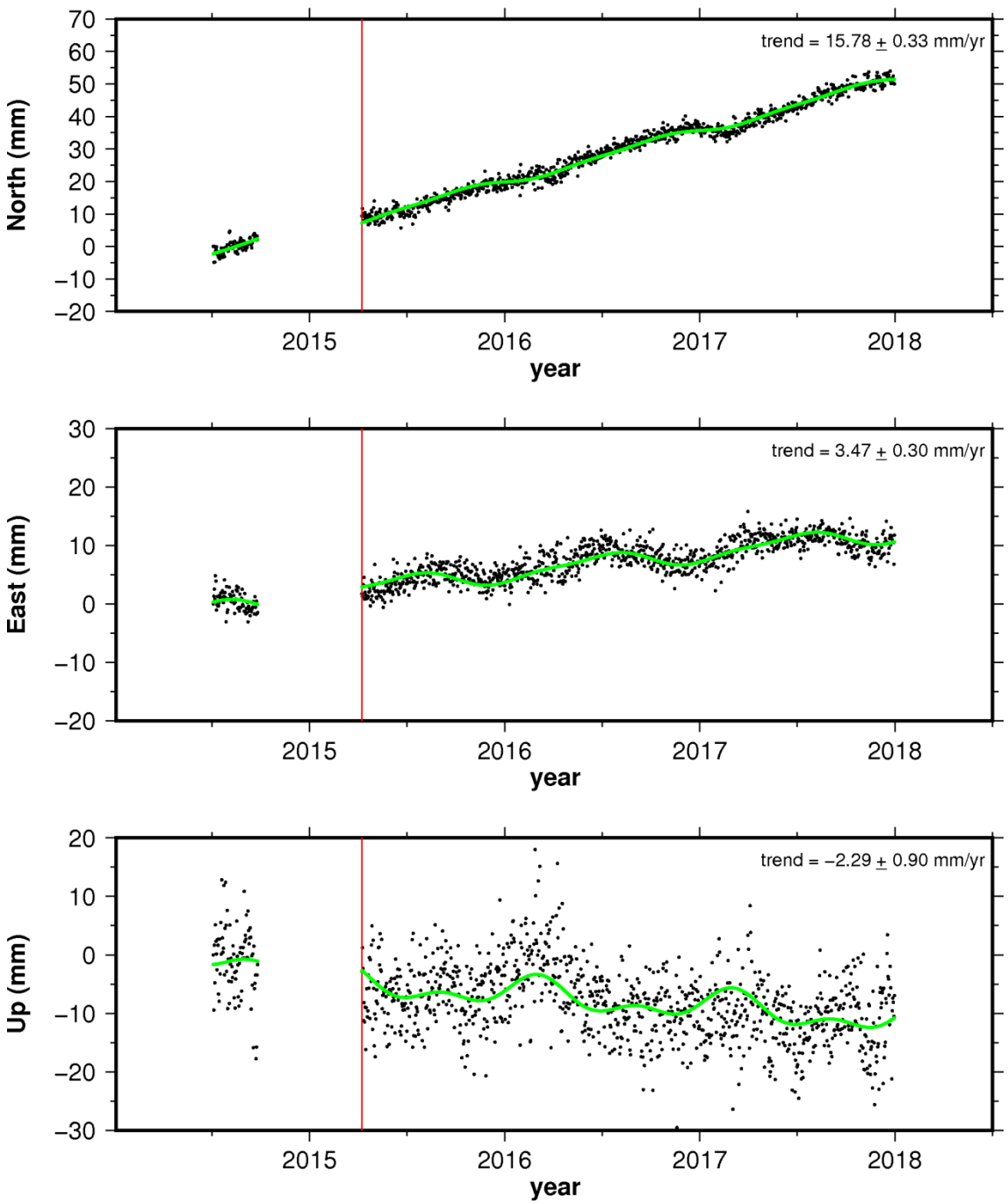
site PAL2
trend = 15.78 ± 0.33 mm/yr
North (mm)
70
60
50
40
30
20
10
0
−10
−20
2015
2016
2017
2018
year
trend = 3.47 ± 0.30 mm/yr
East (mm)
30
20
10
0
−10
−20
2015
2016
2017
2018
year
trend = −2.29 ± 0.90 mm/yr
Up (mm)
20
10
0
−10
−20
−30
2015
2016
2017
2018
year

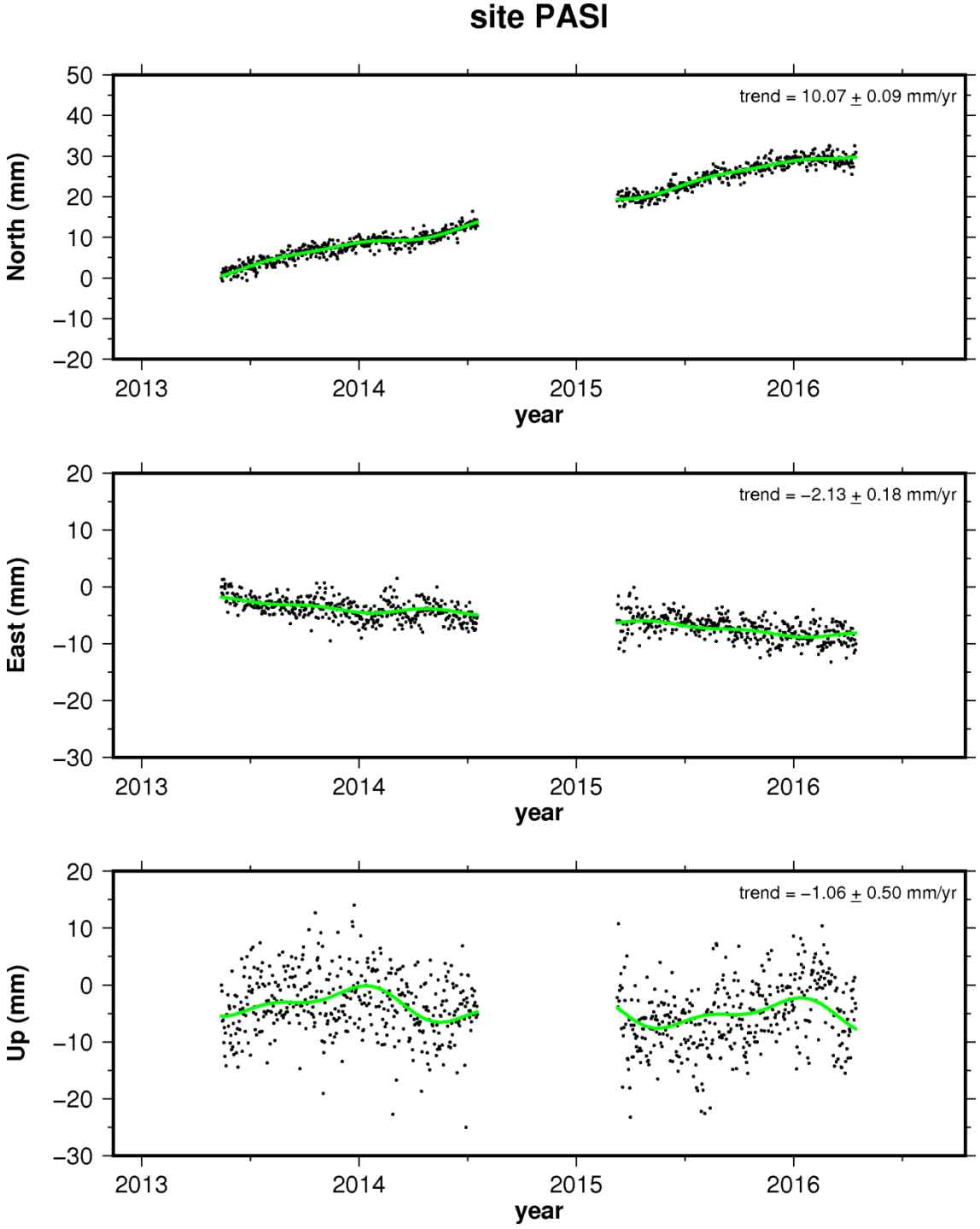
site PASI
trend = 10.07 ± 0.09 mm/yr
North (mm)
50
40
30
20
10
0
−10
−20
2013
2014
2015
2016
year
trend = −2.13 ± 0.18 mm/yr
East (mm)
20
10
0
−10
−20
−30
2013
2014
2015
2016
year
trend = −1.06 ± 0.50 mm/yr
Up (mm)
20
10
0
−10
−20
−30
2013
2014
2015
2016
year

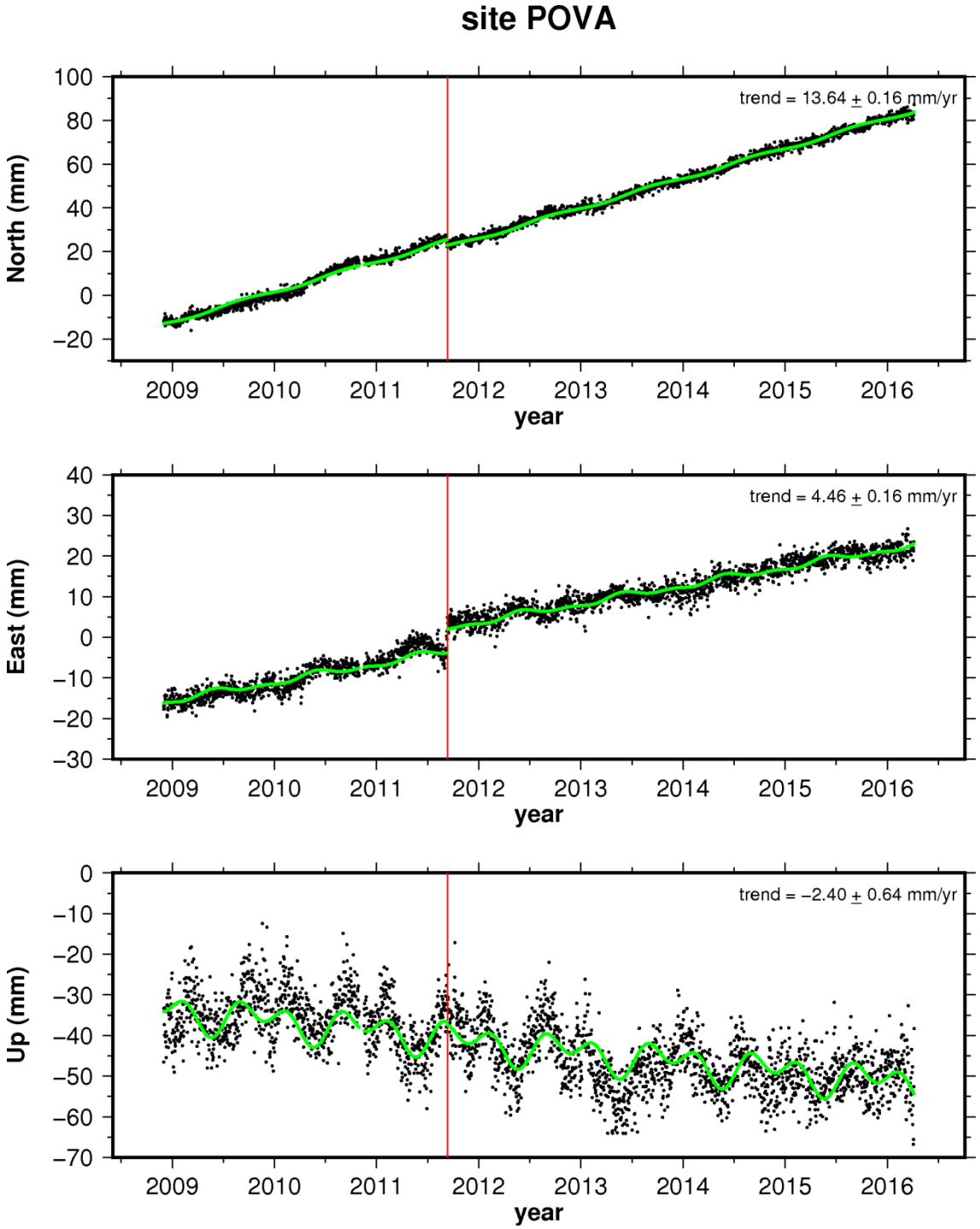
site POVA
North (mm)
trend = 13.64 ± 0.16 mm/yr
East (mm)
trend = 4.46 ± 0.16 mm/yr
Up (mm)
trend = −2.40 ± 0.64 mm/yr
year
2009
2010
2011
2012
2013
2014
2015
2016

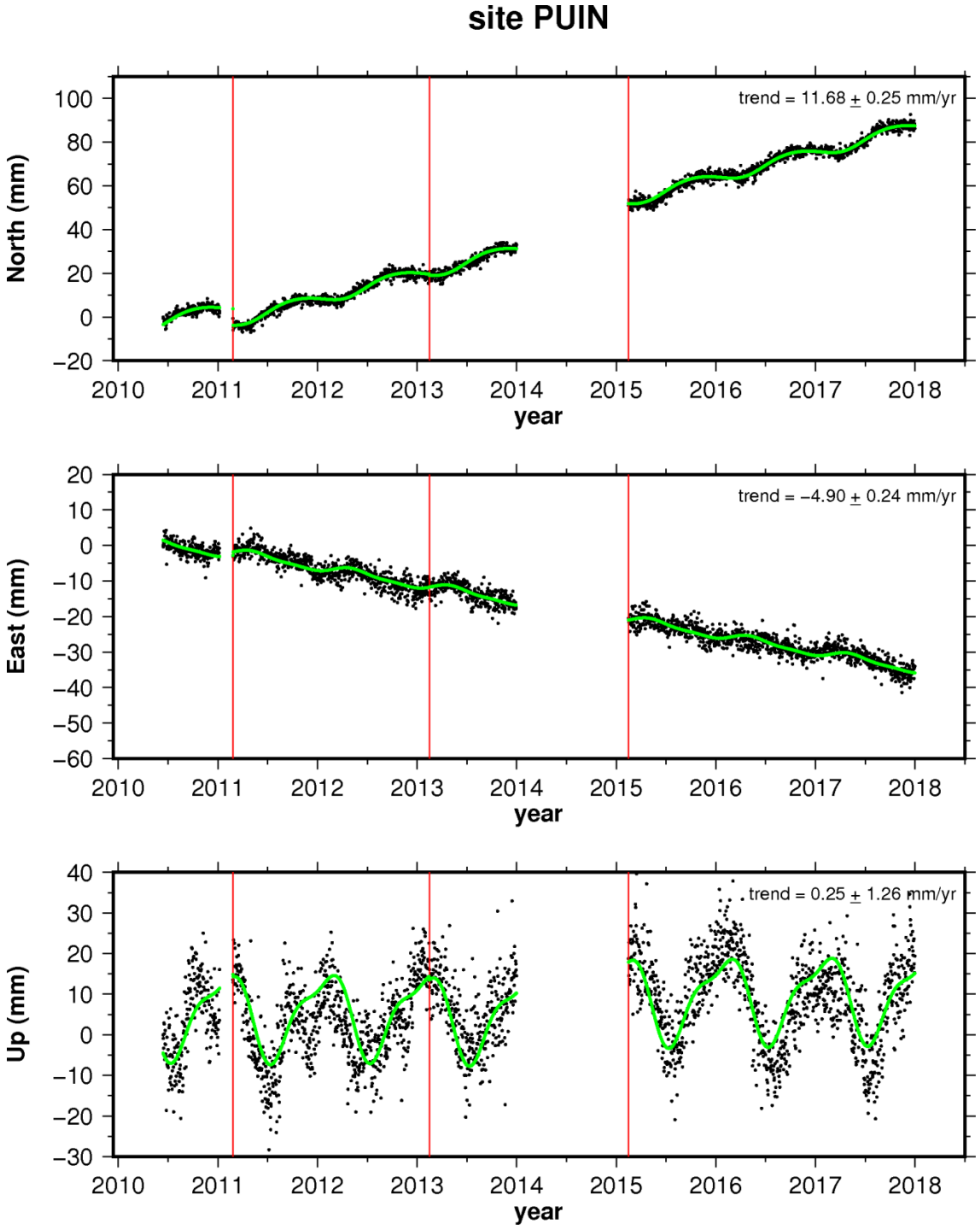
site PUIN
North (mm)
trend = 11.68 ± 0.25 mm/yr
East (mm)
trend = −4.90 ± 0.24 mm/yr
Up (mm)
trend = 0.25 ± 1.26 mm/yr
year
2010
2011
2012
2013
2014
2015
2016
2017
2018

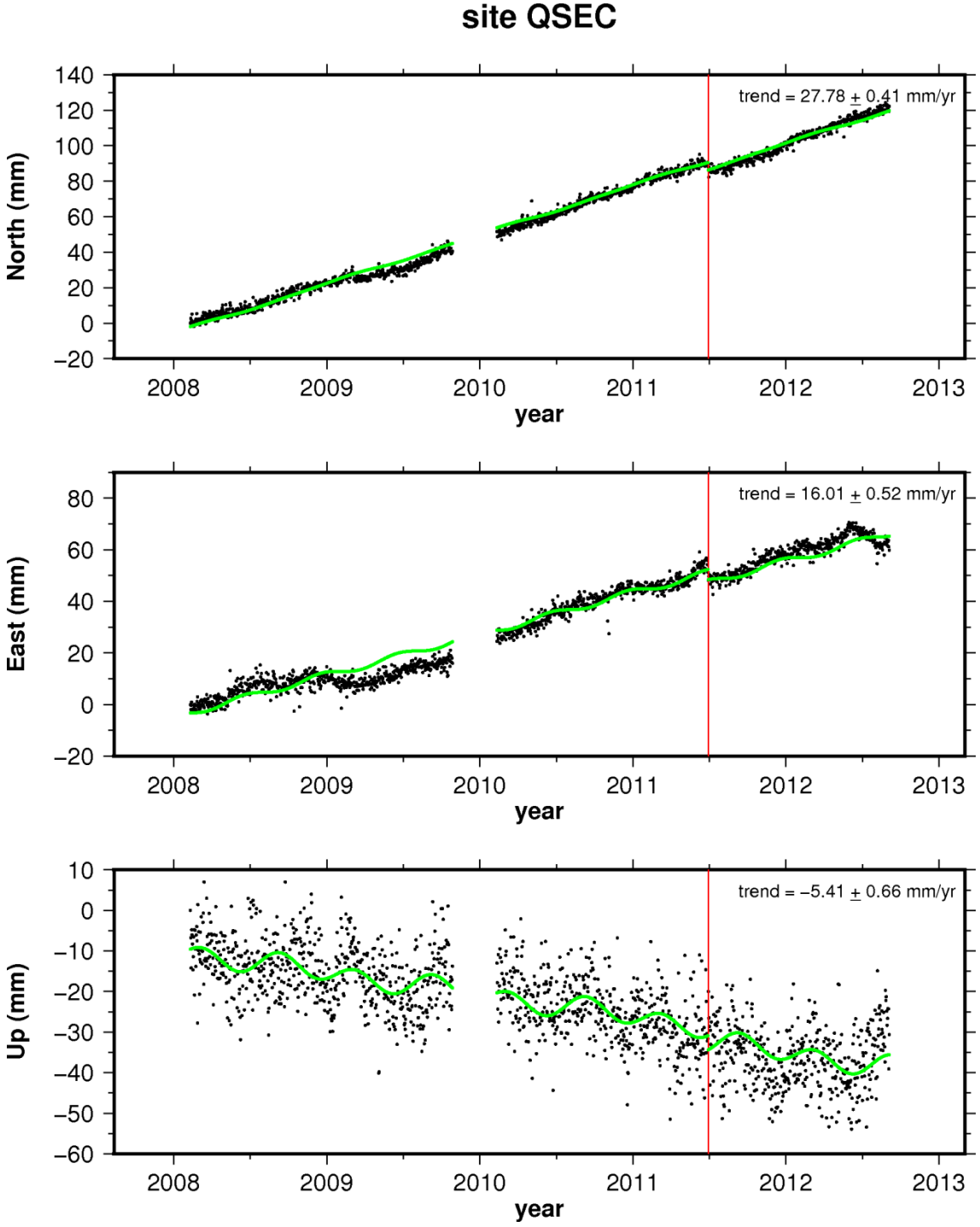
site QSEC
trend = 27.78 ± 0.41 mm/yr
North (mm)
140
120
100
80
60
40
20
0
−20
2008
2009
2010
2011
2012
2013
year
trend = 16.01 ± 0.52 mm/yr
East (mm)
80
60
40
20
0
−20
2008
2009
2010
2011
2012
2013
year
trend = −5.41 ± 0.66 mm/yr
Up (mm)
10
0
−10
−20
−30
−40
−50
−60
2008
2009
2010
2011
2012
2013
year

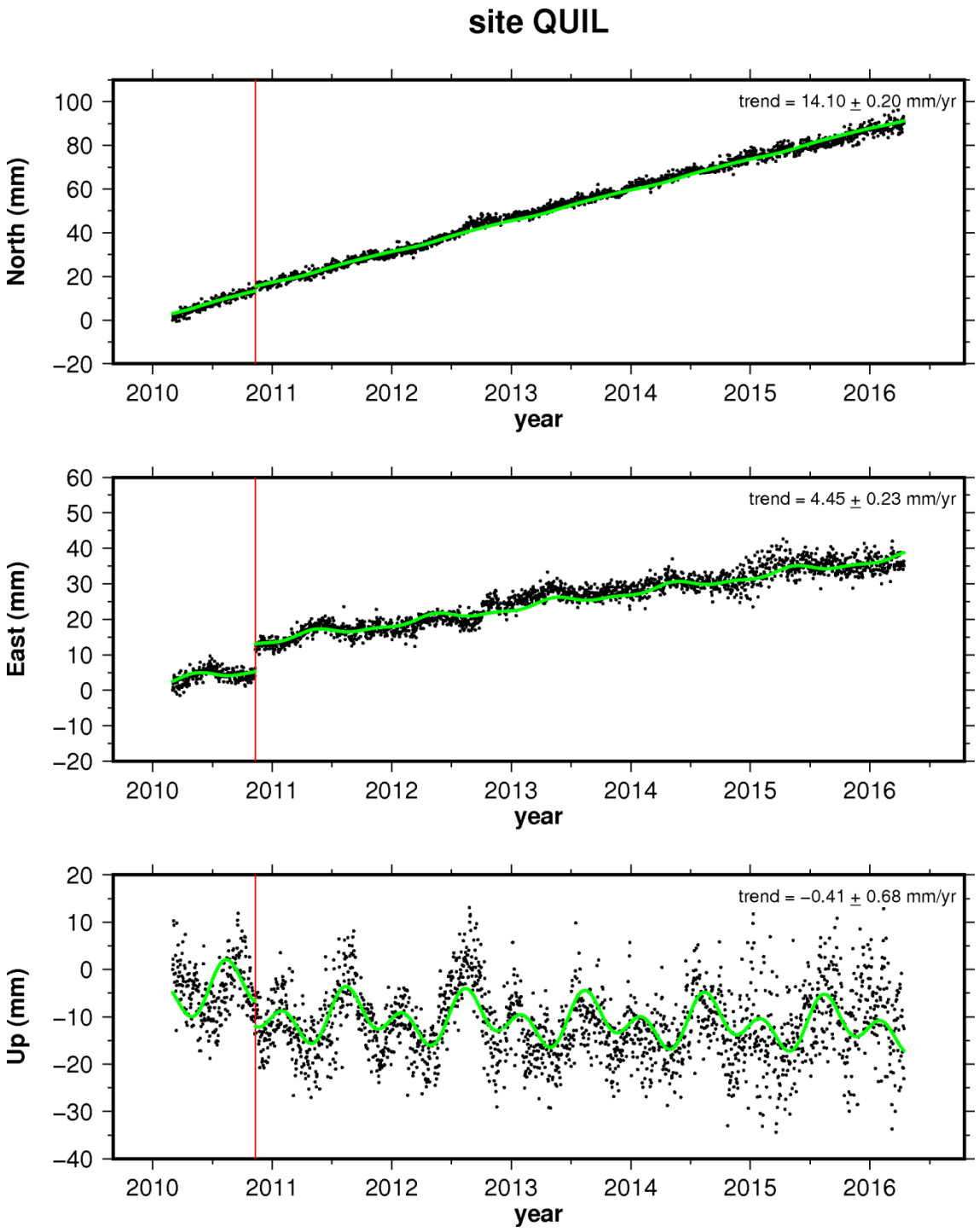
site QUIL
trend = 14.10 ± 0.20 mm/yr
North (mm)
100
80
60
40
20
0
−20
2010
2011
2012
2013
2014
2015
2016
year
trend = 4.45 ± 0.23 mm/yr
East (mm)
60
50
40
30
20
10
0
−10
−20
2010
2011
2012
2013
2014
2015
2016
year
trend = −0.41 ± 0.68 mm/yr
Up (mm)
20
10
0
−10
−20
−30
−40
2010
2011
2012
2013
2014
2015
2016
year

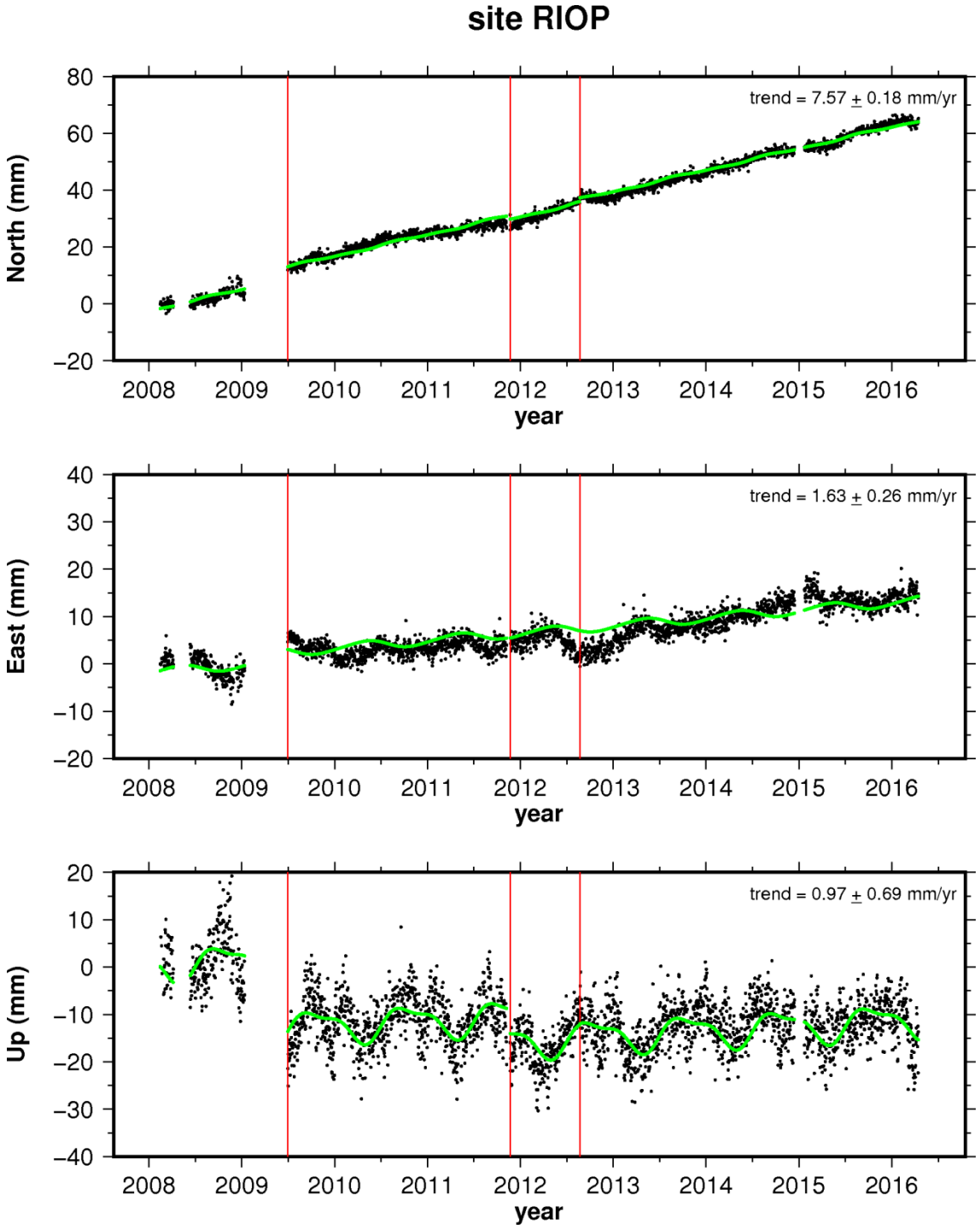
site RIOP
trend = 7.57 ± 0.18 mm/yr
North (mm)
80
60
40
20
0
−20
2008
2009
2010
2011
2012
2013
2014
2015
2016
year
trend = 1.63 ± 0.26 mm/yr
East (mm)
40
30
20
10
0
−10
−20
year
trend = 0.97 ± 0.69 mm/yr
Up (mm)
20
10
0
−10
−20
−30
−40
year

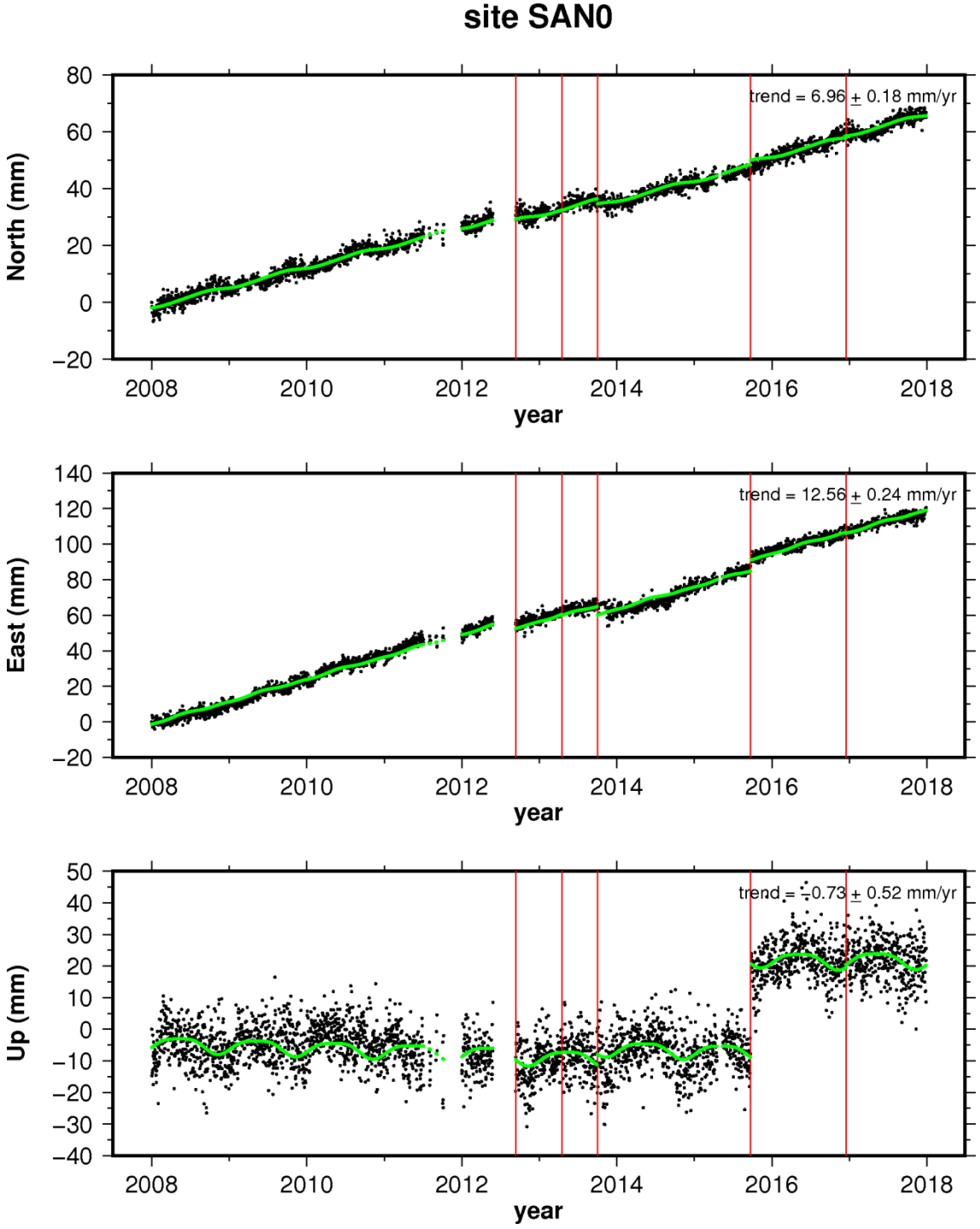
site SAN0
North (mm)
East (mm)
Up (mm)
year
trend = 6.96 ± 0.18 mm/yr
trend = 12.56 ± 0.24 mm/yr
trend = -0.73 ± 0.52 mm/yr
2008
2010
2012
2014
2016
2018

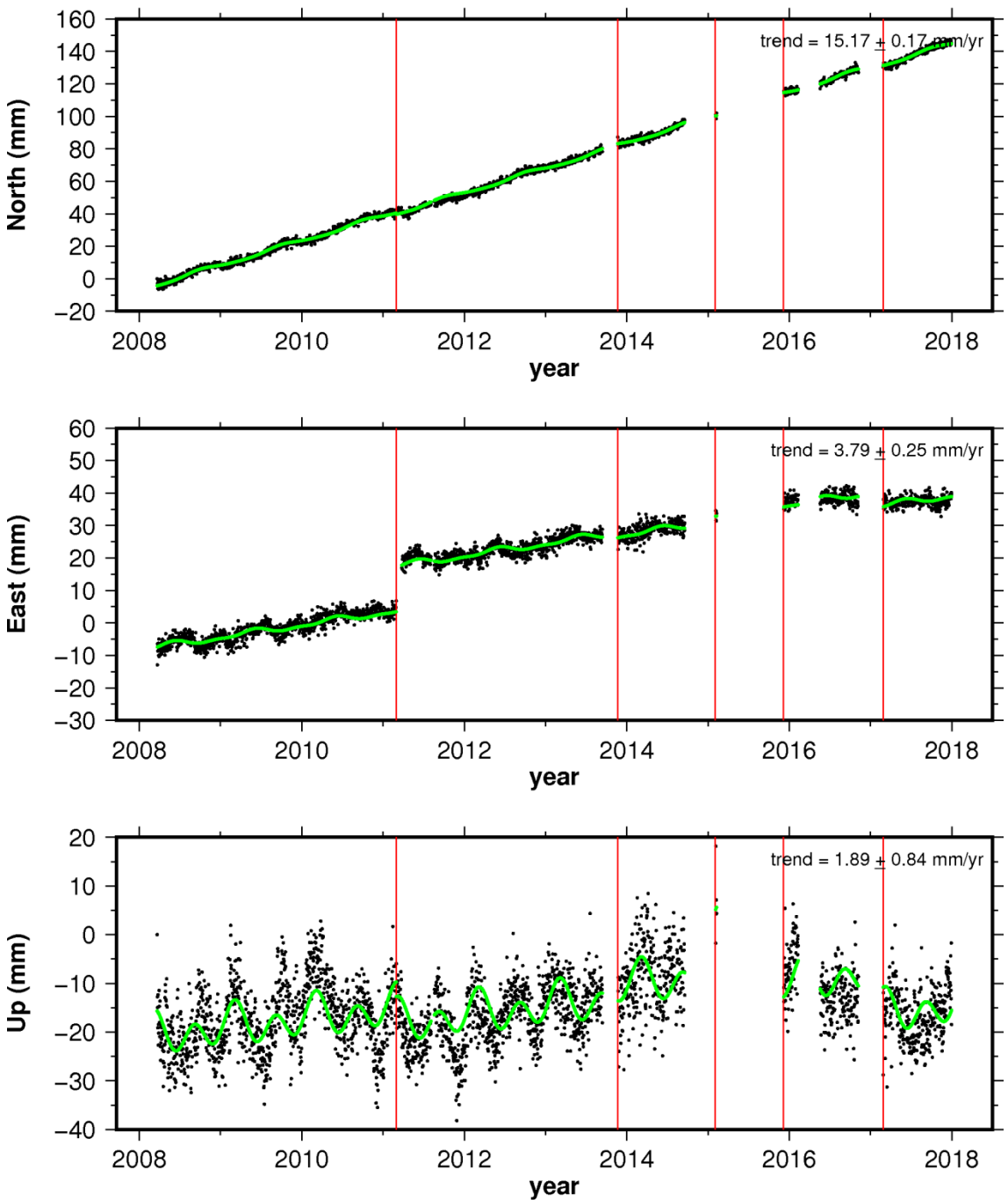
site SEL1
North (mm)
trend = 15.17 ± 0.17 mm/yr
year
East (mm)
trend = 3.79 ± 0.25 mm/yr
year
Up (mm)
trend = 1.89 ± 0.84 mm/yr
year

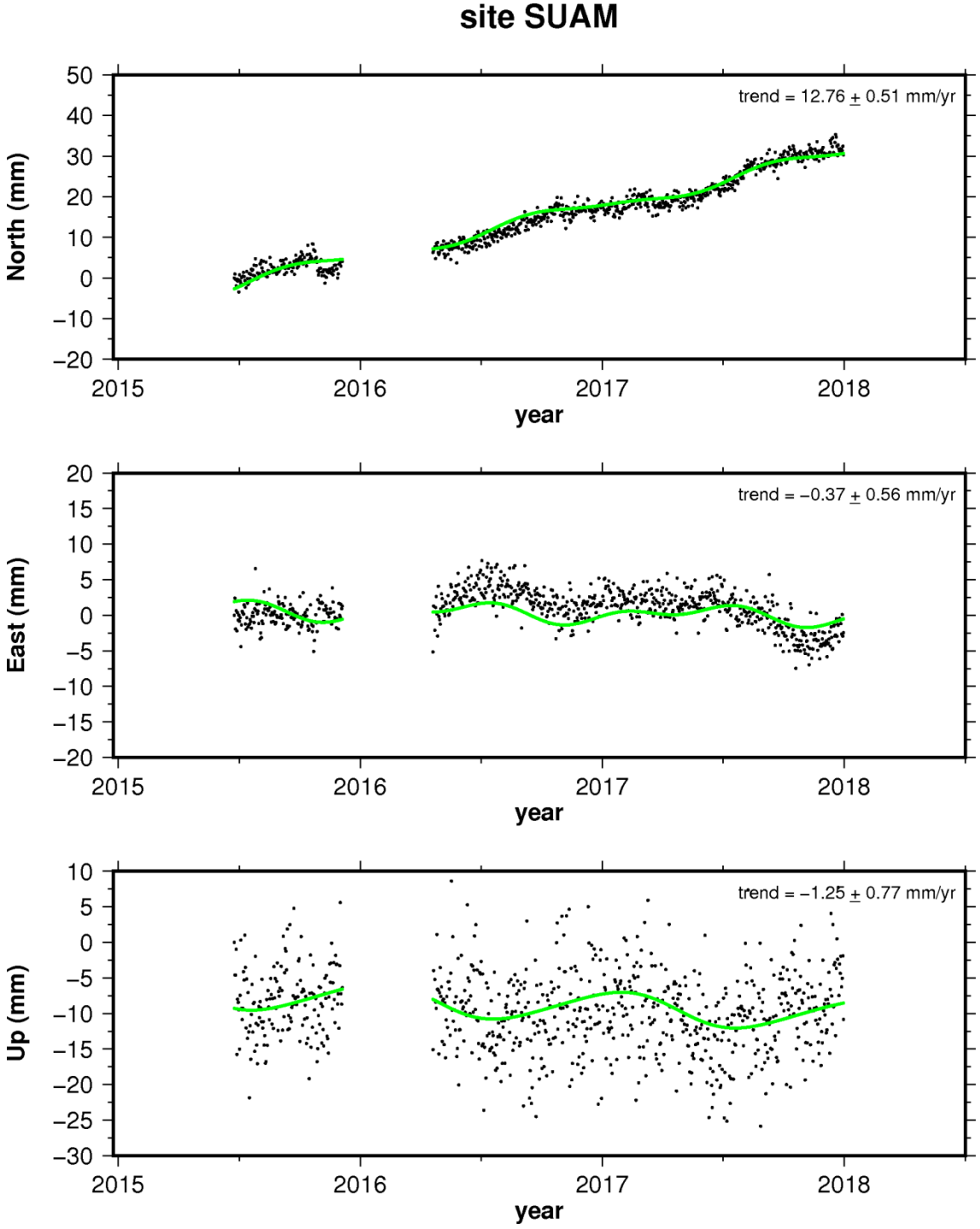
site SUAM
trend = 12.76 ± 0.51 mm/yr
North (mm)
50
40
30
20
10
0
−10
−20
2015
2016
2017
2018
year
trend = −0.37 ± 0.56 mm/yr
East (mm)
20
15
10
5
0
−5
−10
−15
−20
2015
2016
2017
2018
year
trend = −1.25 ± 0.77 mm/yr
Up (mm)
10
5
0
−5
−10
−15
−20
−25
−30
2015
2016
2017
2018
year

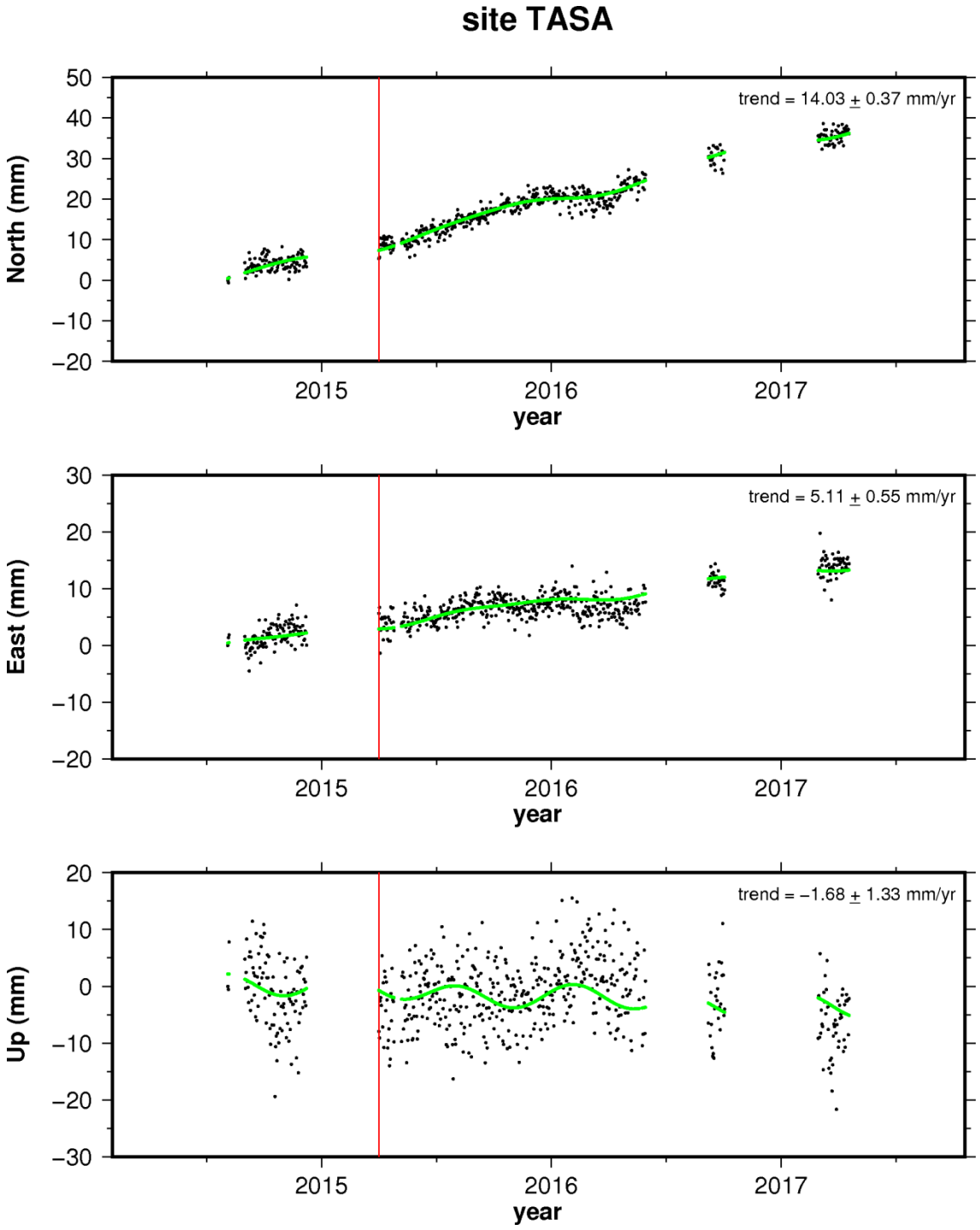
site TASA
trend = 14.03 ± 0.37 mm/yr
North (mm)
50
40
30
20
10
0
−10
−20
2015
2016
2017
year
trend = 5.11 ± 0.55 mm/yr
East (mm)
30
20
10
0
−10
−20
2015
2016
2017
year
trend = −1.68 ± 1.33 mm/yr
Up (mm)
20
10
0
−10
−20
−30
2015
2016
2017
year

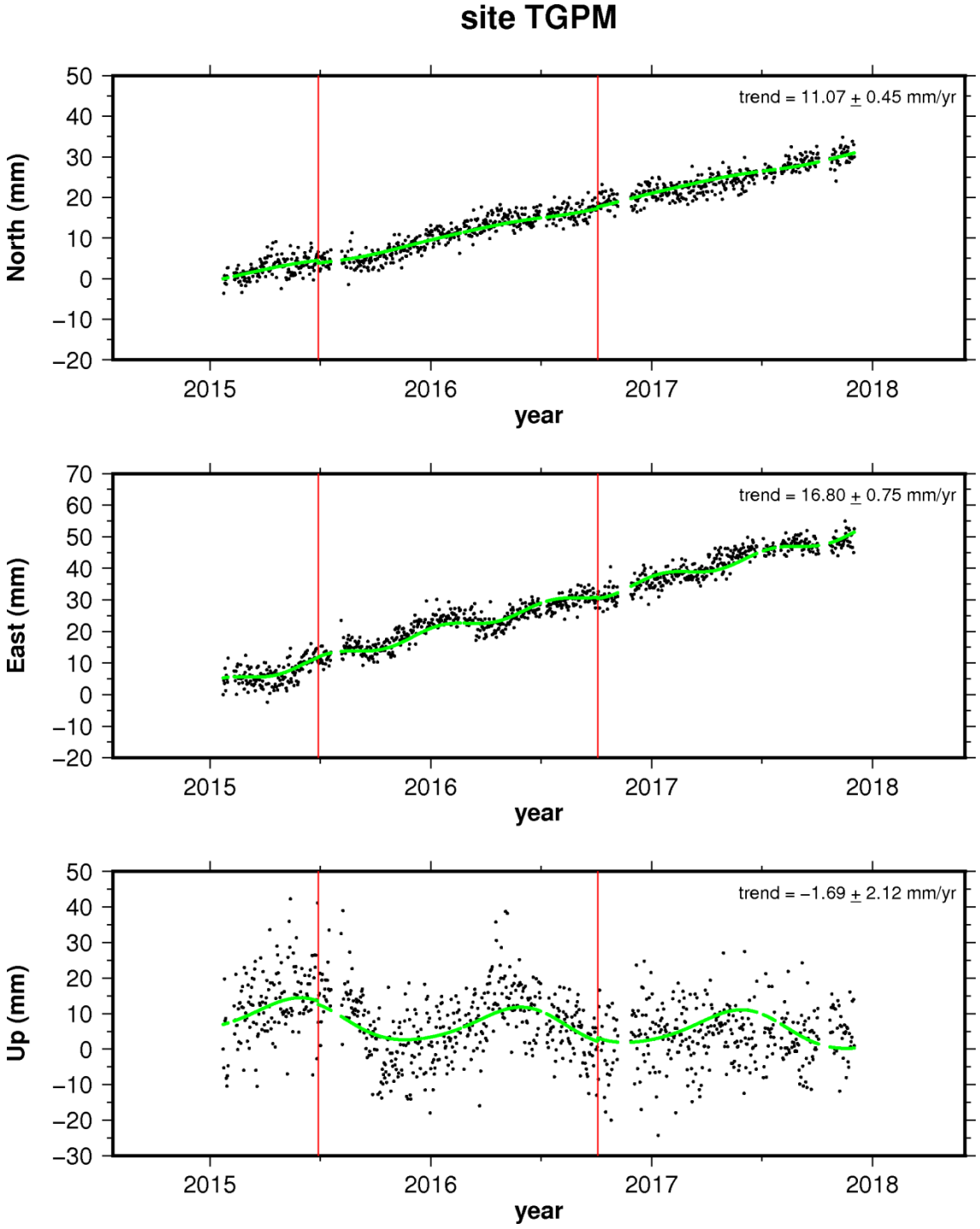
site TGPM
trend = 11.07 ± 0.45 mm/yr
North (mm)
year
trend = 16.80 ± 0.75 mm/yr
East (mm)
year
trend = −1.69 ± 2.12 mm/yr
Up (mm)
year
2015
2016
2017
2018

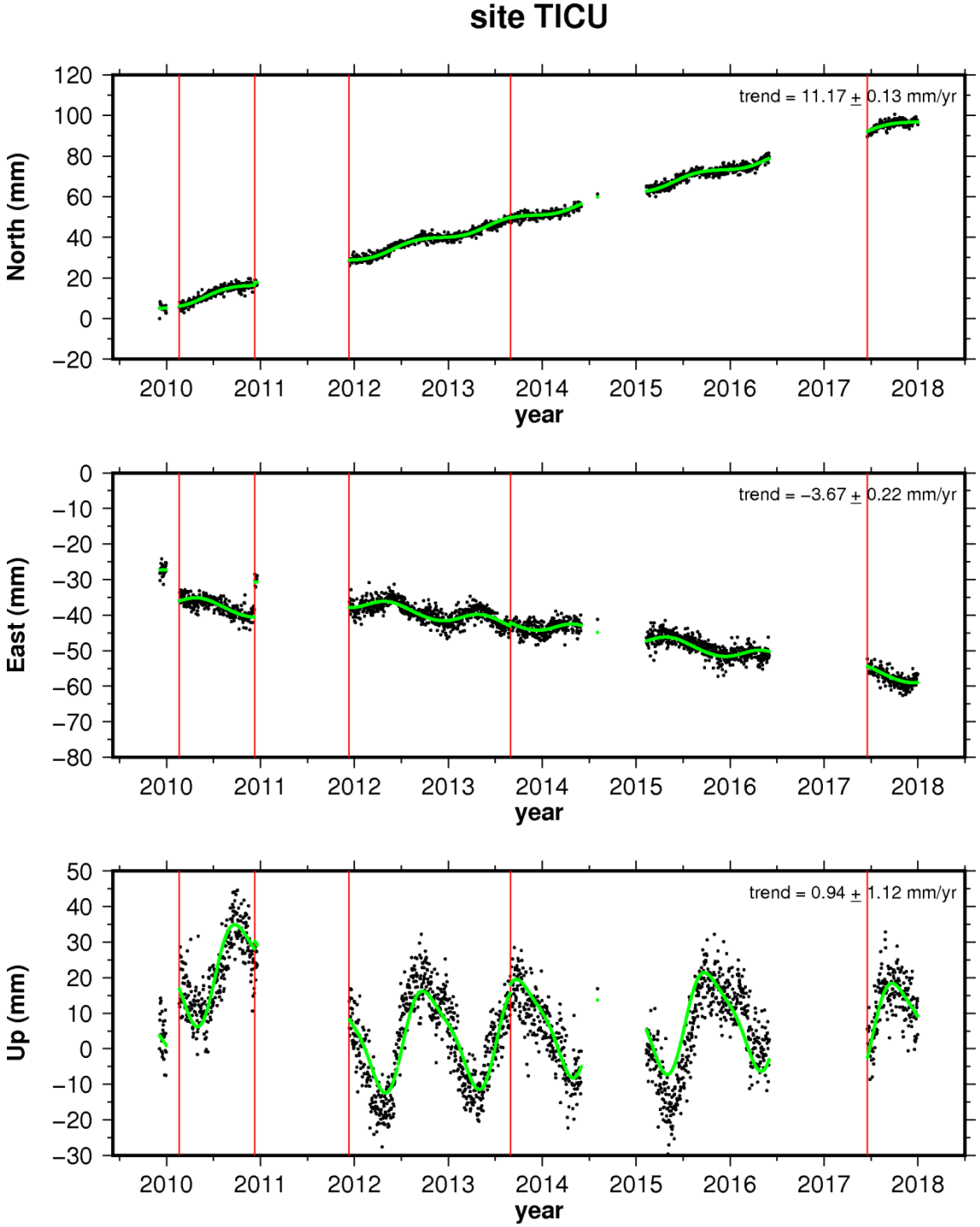
site TICU
trend = 11.17 ± 0.13 mm/yr
North (mm)
120
100
80
60
40
20
0
−20
2010
2011
2012
2013
2014
2015
2016
2017
2018
year
trend = −3.67 ± 0.22 mm/yr
East (mm)
0
−10
−20
−30
−40
−50
−60
−70
−80
year
trend = 0.94 ± 1.12 mm/yr
Up (mm)
50
40
30
20
10
0
−10
−20
−30
year

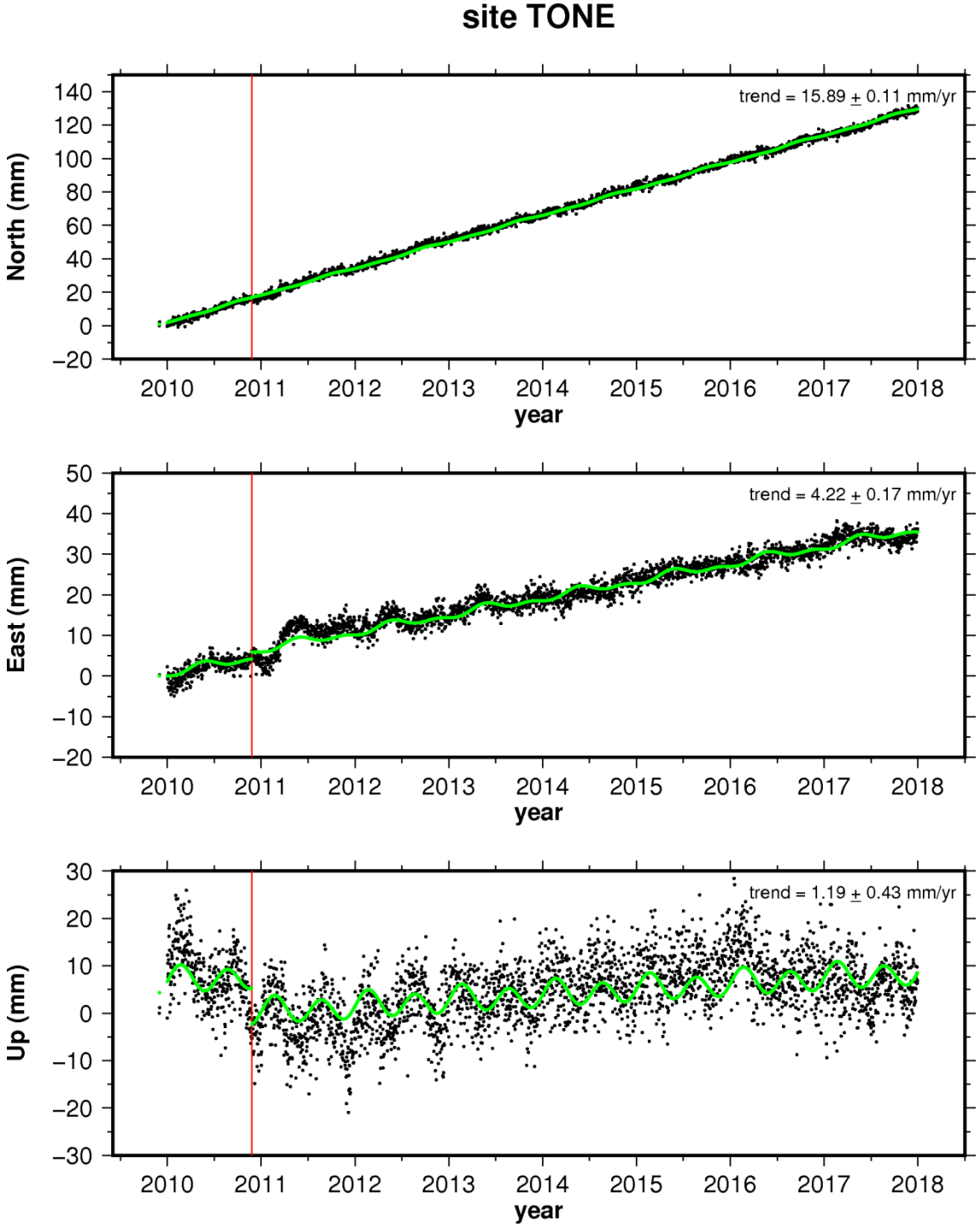
site TONE
trend = 15.89 ± 0.11 mm/yr
North (mm)
140
120
100
80
60
40
20
0
−20
2010
2011
2012
2013
2014
2015
2016
2017
2018
year
trend = 4.22 ± 0.17 mm/yr
East (mm)
50
40
30
20
10
0
−10
−20
year
trend = 1.19 ± 0.43 mm/yr
Up (mm)
30
20
10
0
−10
−20
−30
year

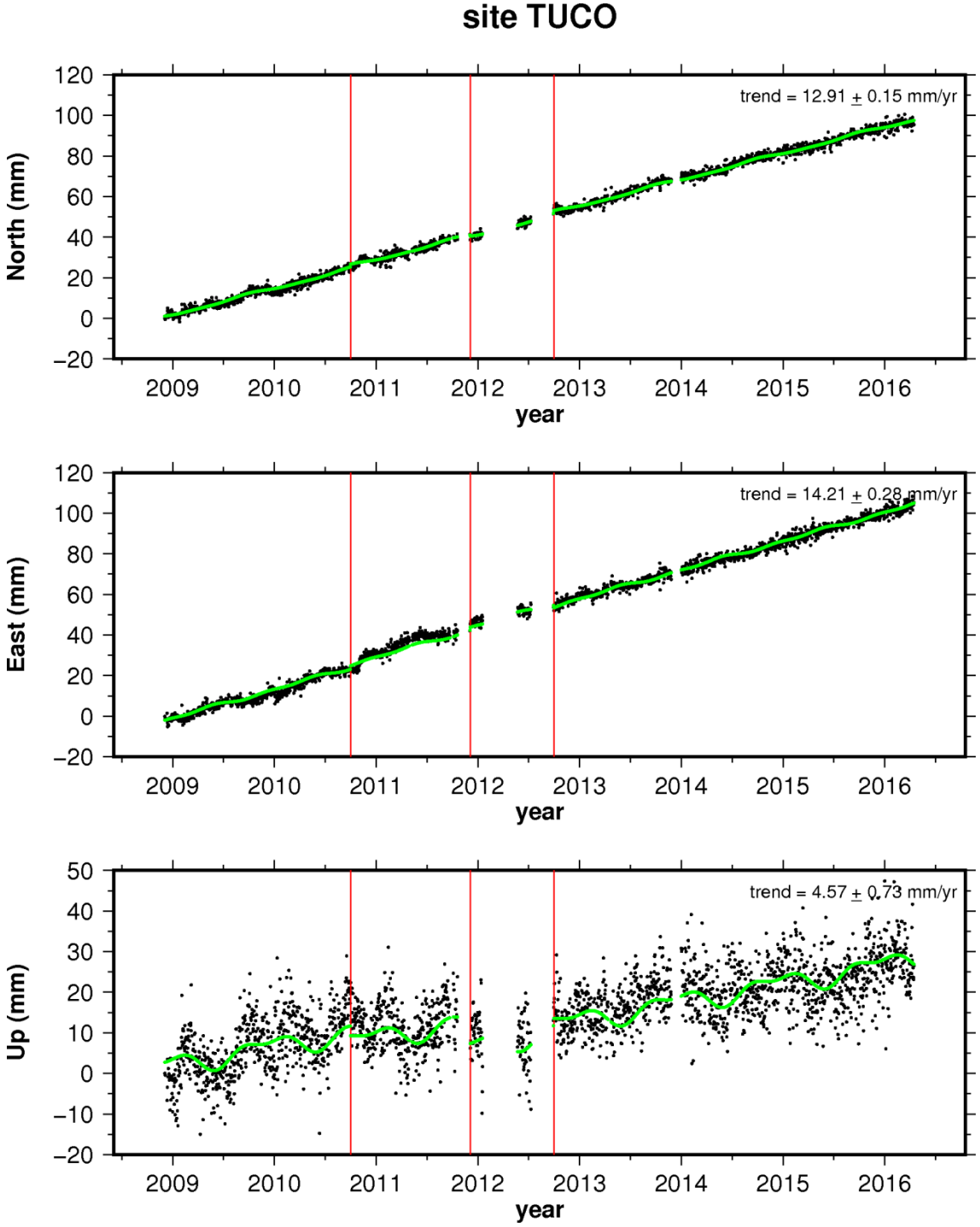
site TUCO
North (mm)
trend = 12.91 ± 0.15 mm/yr
East (mm)
trend = 14.21 ± 0.28 mm/yr
Up (mm)
trend = 4.57 ± 0.73 mm/yr
year
2009
2010
2011
2012
2013
2014
2015
2016

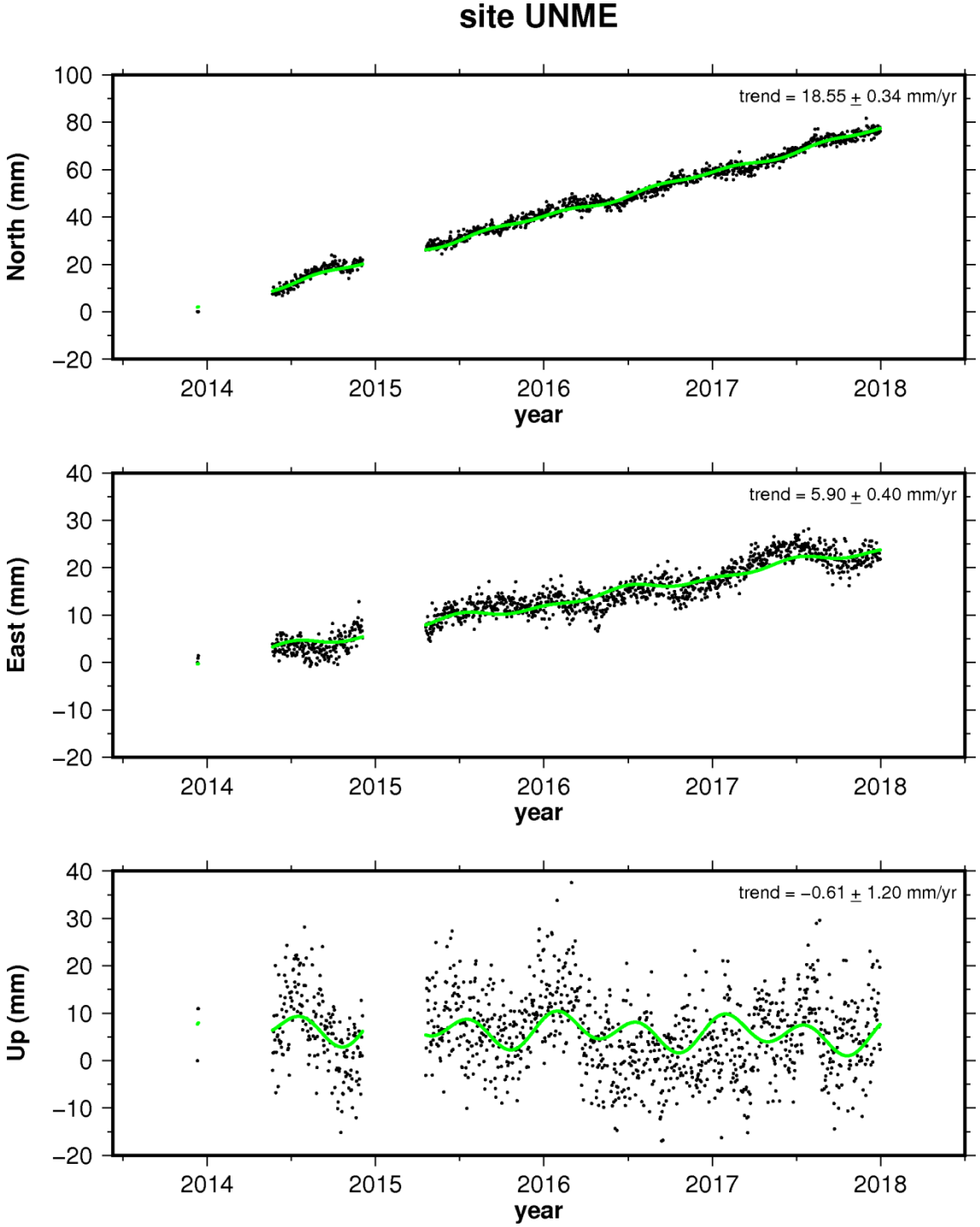
site UNME
trend = 18.55 ± 0.34 mm/yr
North (mm)
100
80
60
40
20
0
−20
2014
2015
2016
2017
2018
year
trend = 5.90 ± 0.40 mm/yr
East (mm)
40
30
20
10
0
−10
−20
2014
2015
2016
2017
2018
year
trend = −0.61 ± 1.20 mm/yr
Up (mm)
40
30
20
10
0
−10
−20
2014
2015
2016
2017
2018
year

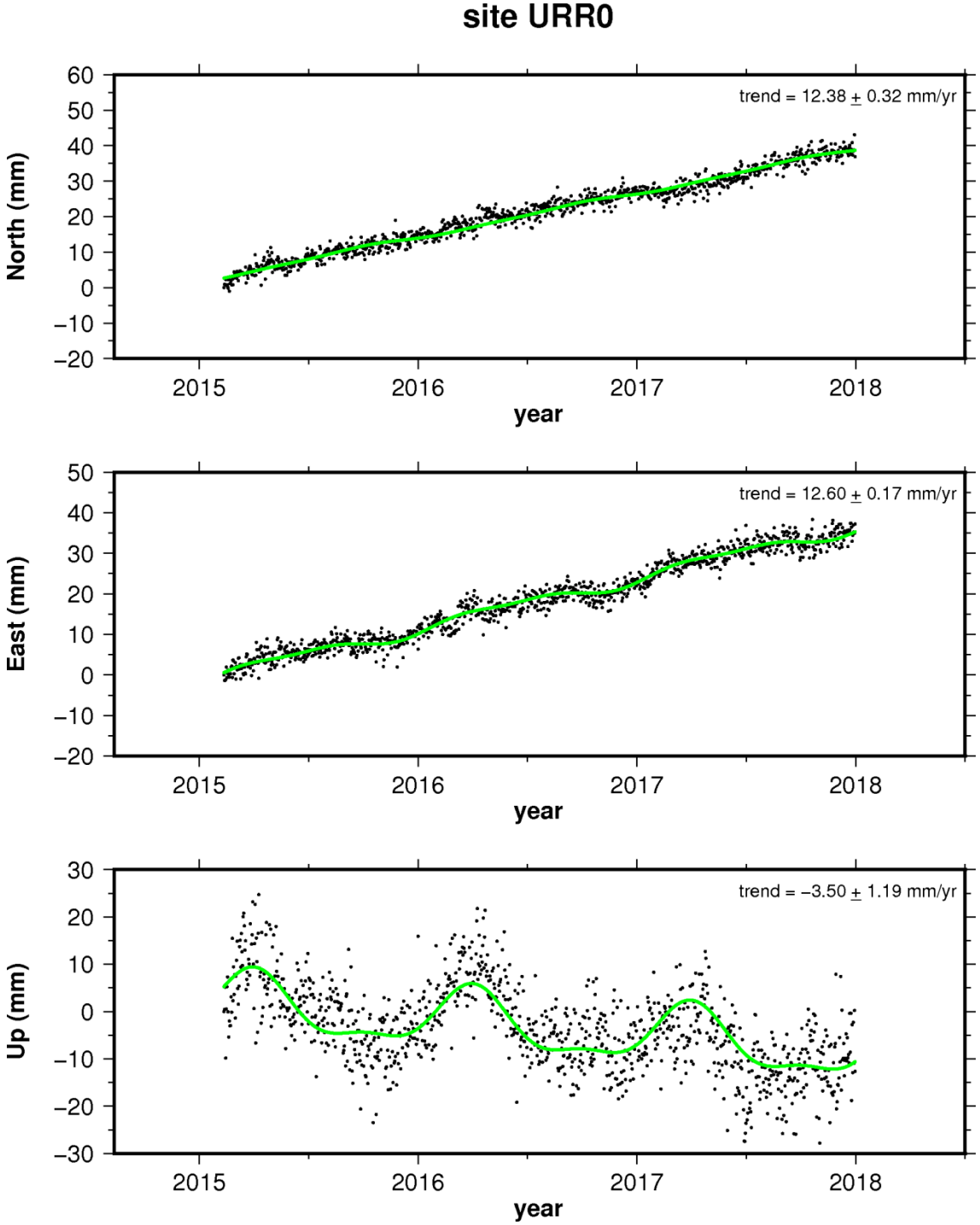
site URR0
trend = 12.38 ± 0.32 mm/yr
North (mm)
60
50
40
30
20
10
0
−10
−20
2015
2016
2017
2018
year
trend = 12.60 ± 0.17 mm/yr
East (mm)
50
40
30
20
10
0
−10
−20
2015
2016
2017
2018
year
trend = −3.50 ± 1.19 mm/yr
Up (mm)
30
20
10
0
−10
−20
−30
2015
2016
2017
2018
year

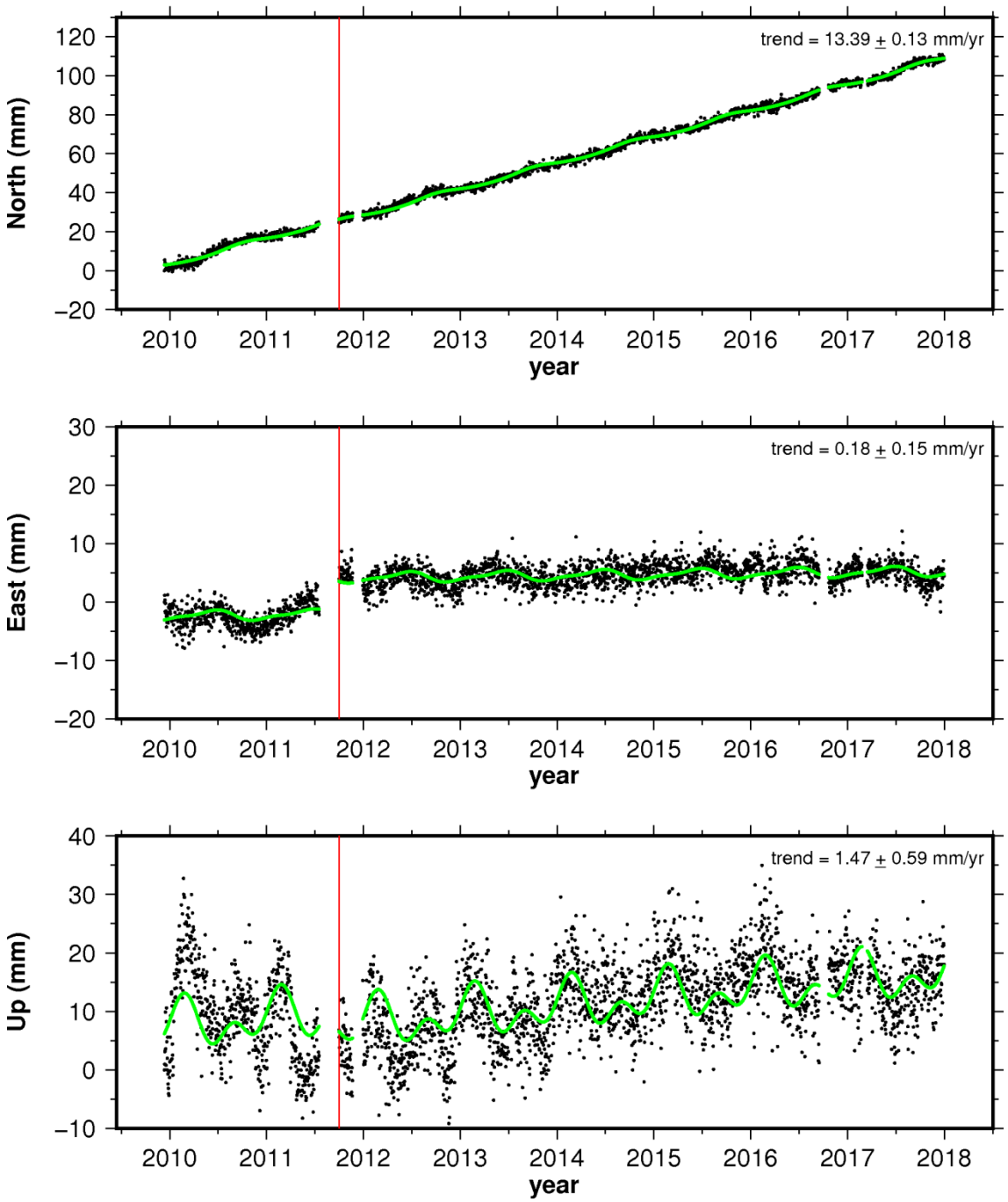
site UWAS
North (mm)
trend = 13.39 ± 0.13 mm/yr
East (mm)
trend = 0.18 ± 0.15 mm/yr
Up (mm)
trend = 1.47 ± 0.59 mm/yr
year
2010
2011
2012
2013
2014
2015
2016
2017
2018

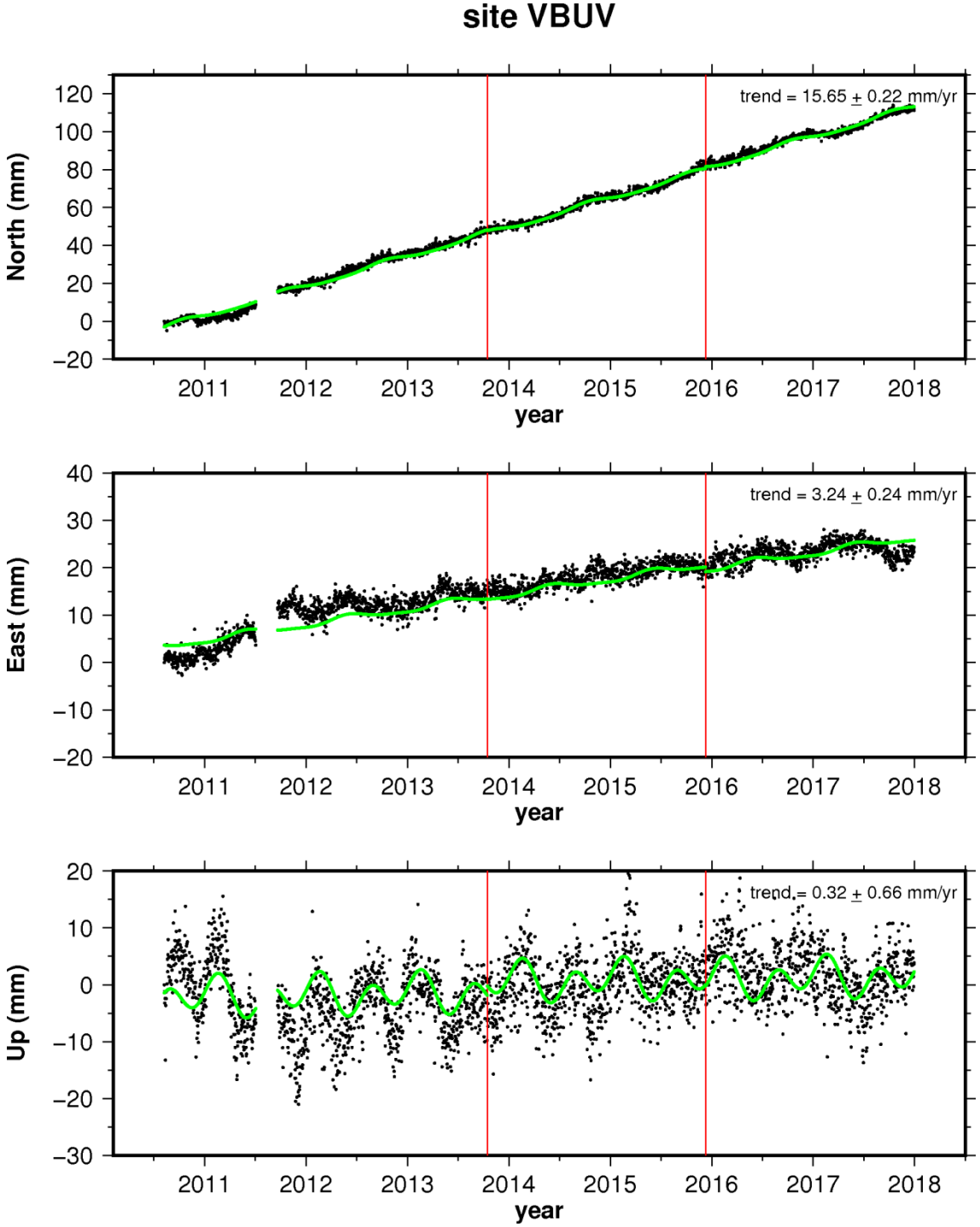
site VBUV
trend = 15.65 ± 0.22 mm/yr
North (mm)
120
100
80
60
40
20
0
−20
2011
2012
2013
2014
2015
2016
2017
2018
year
trend = 3.24 ± 0.24 mm/yr
East (mm)
40
30
20
10
0
−10
−20
year
trend = 0.32 ± 0.66 mm/yr
Up (mm)
20
10
0
−10
−20
−30
year

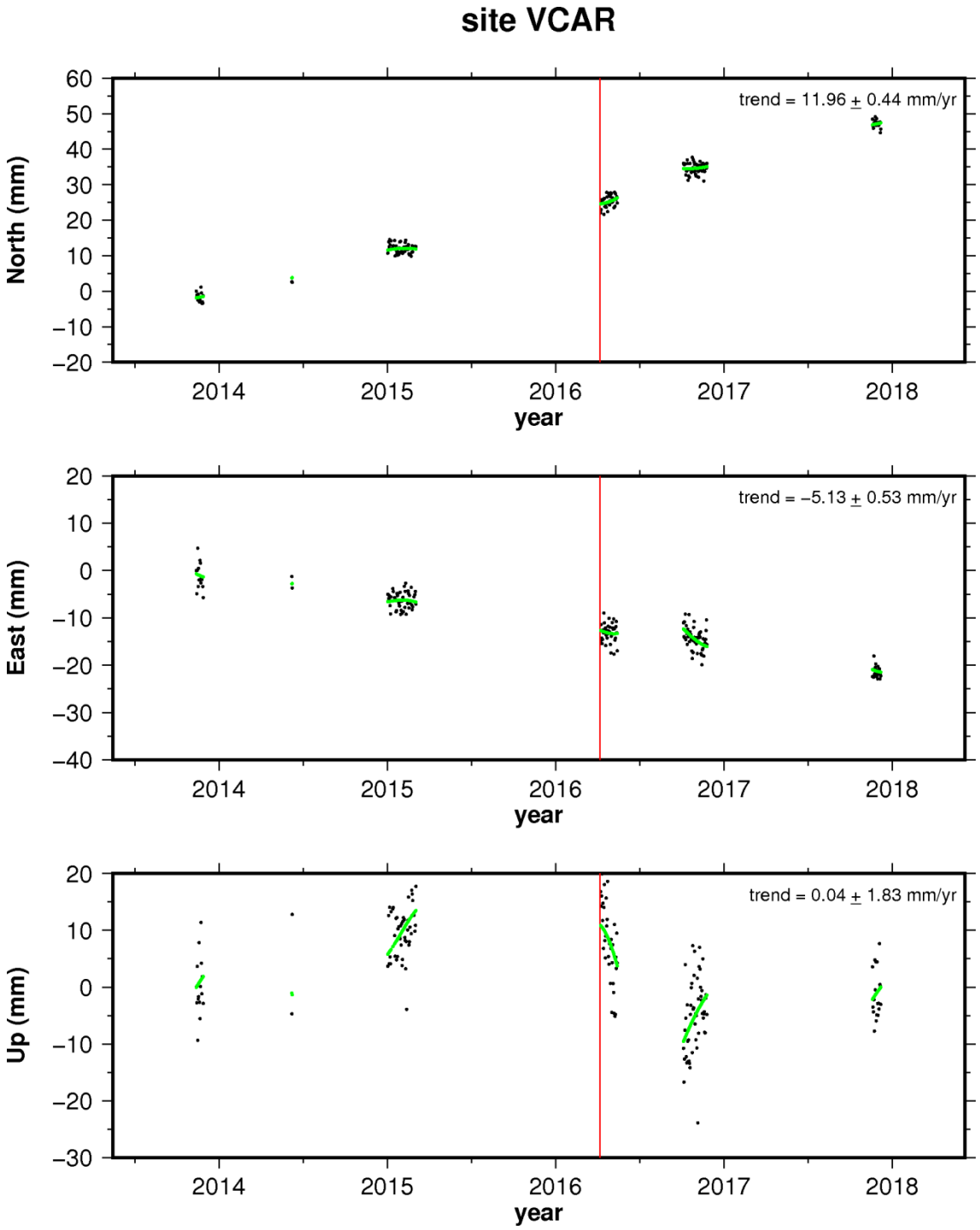
site VCAR
North (mm)
trend = 11.96 ± 0.44 mm/yr
East (mm)
trend = −5.13 ± 0.53 mm/yr
Up (mm)
trend = 0.04 ± 1.83 mm/yr
year
2014
2015
2016
2017
2018

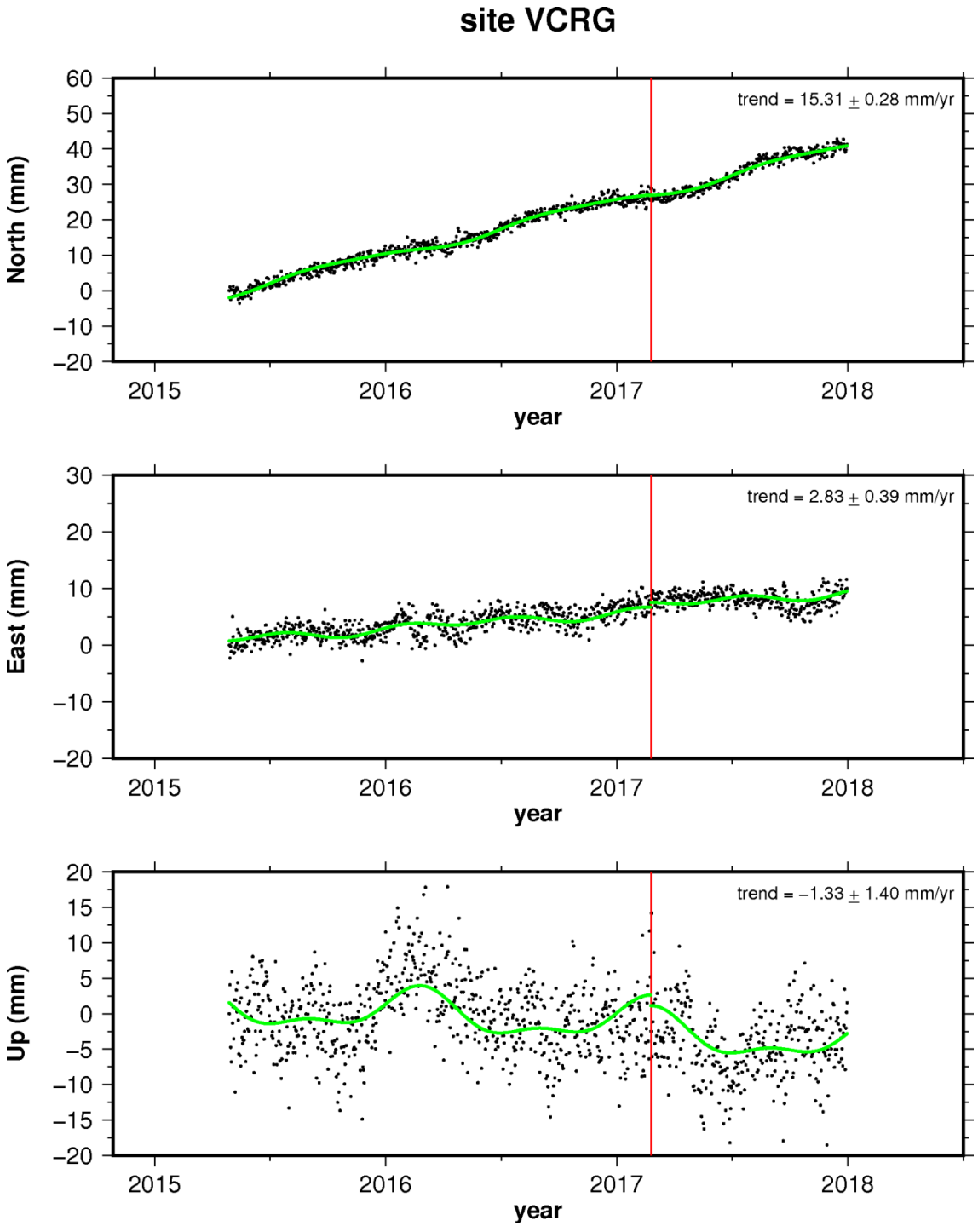
site VCRG
North (mm)
trend = 15.31 ± 0.28 mm/yr
year
East (mm)
trend = 2.83 ± 0.39 mm/yr
year
Up (mm)
trend = −1.33 ± 1.40 mm/yr
year
2015
2016
2017
2018

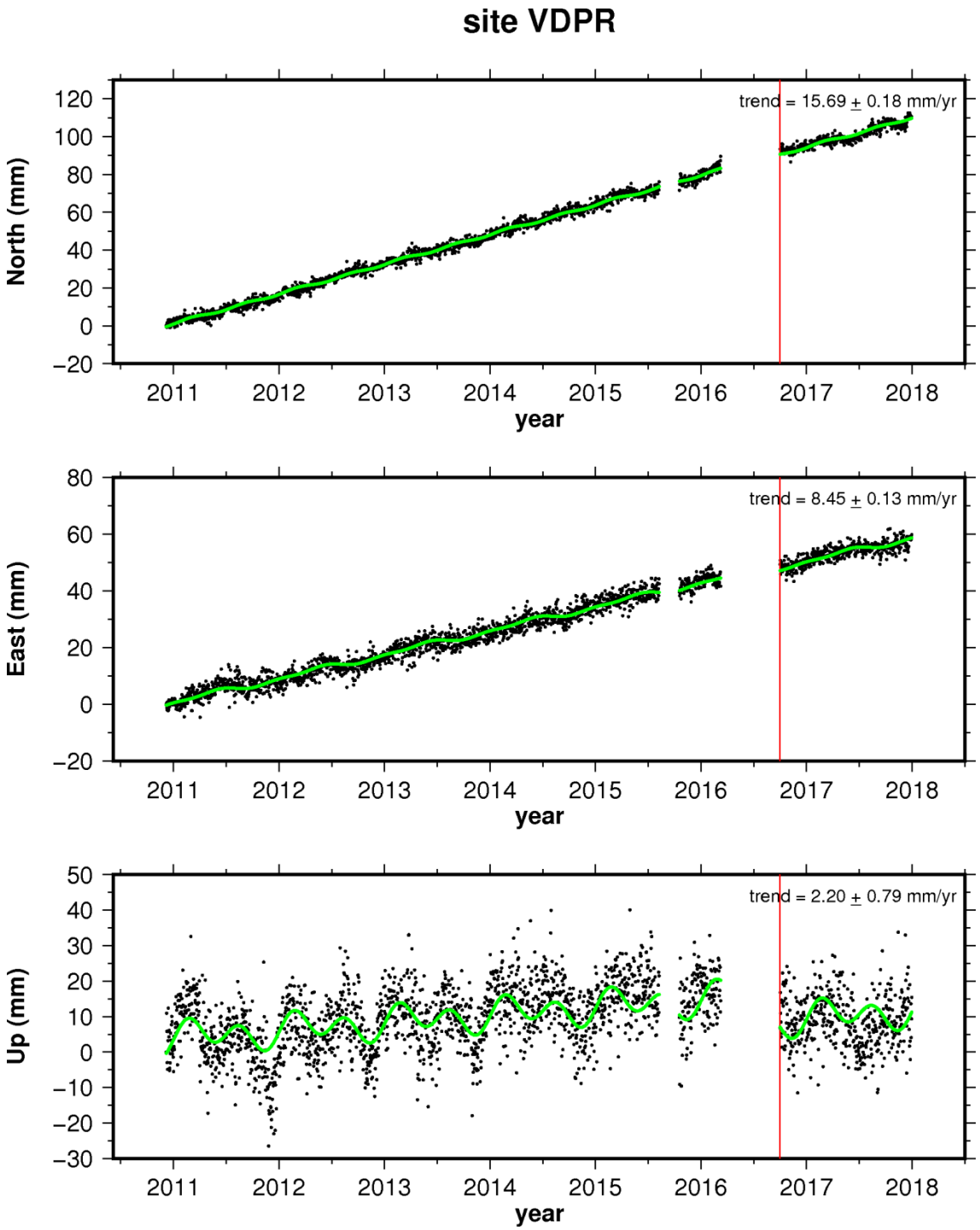
site VDPR
trend = 15.69 ± 0.18 mm/yr
North (mm)
120
100
80
60
40
20
0
−20
2011
2012
2013
2014
2015
2016
2017
2018
year
trend = 8.45 ± 0.13 mm/yr
East (mm)
80
60
40
20
0
−20
2011
2012
2013
2014
2015
2016
2017
2018
year
trend = 2.20 ± 0.79 mm/yr
Up (mm)
50
40
30
20
10
0
−10
−20
−30
2011
2012
2013
2014
2015
2016
2017
2018
year

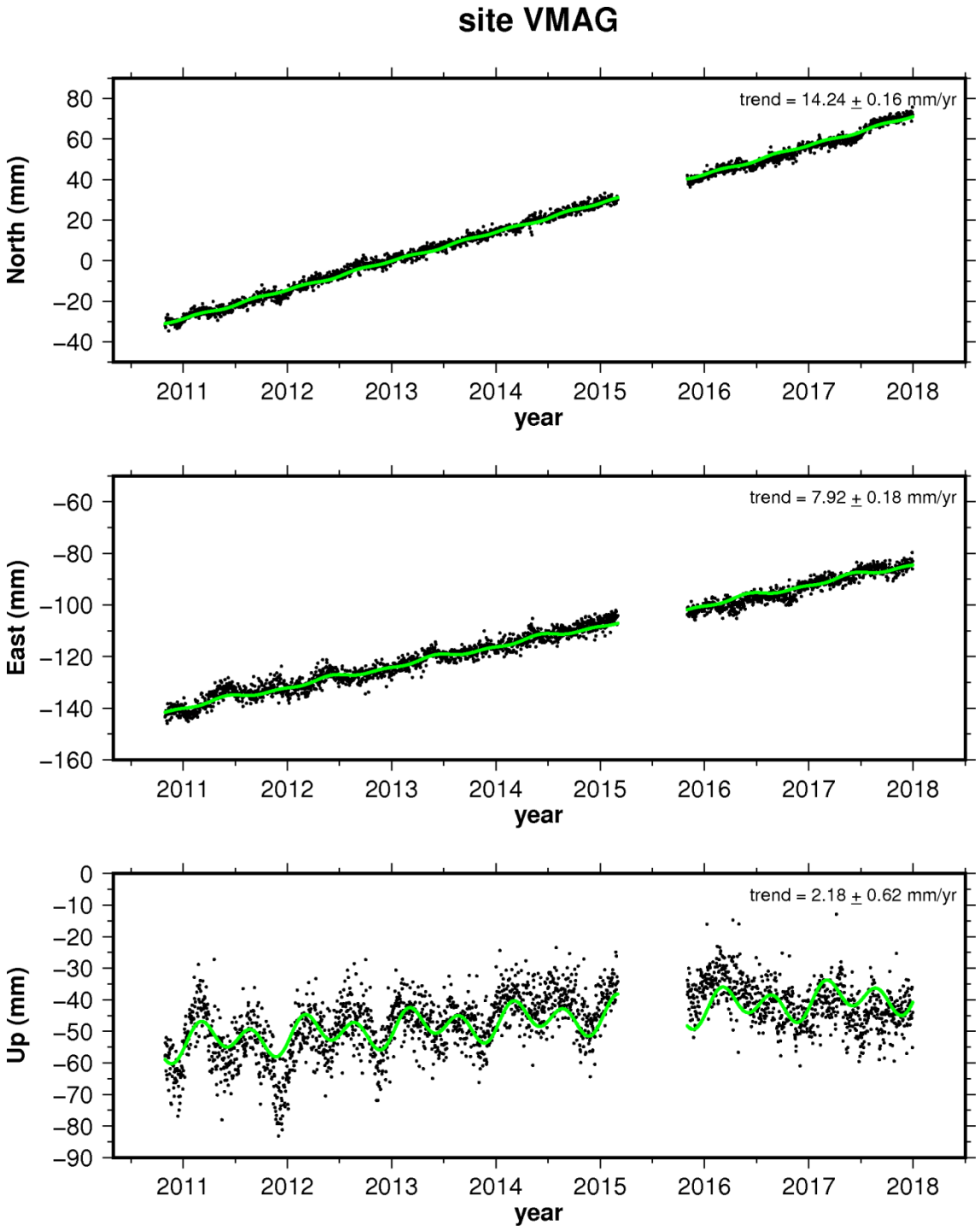
site VMAG
trend = 14.24 ± 0.16 mm/yr
North (mm)
80
60
40
20
0
−20
−40
2011
2012
2013
2014
2015
2016
2017
2018
year
trend = 7.92 ± 0.18 mm/yr
East (mm)
−60
−80
−100
−120
−140
−160
year
trend = 2.18 ± 0.62 mm/yr
Up (mm)
0
−10
−20
−30
−40
−50
−60
−70
−80
−90
year

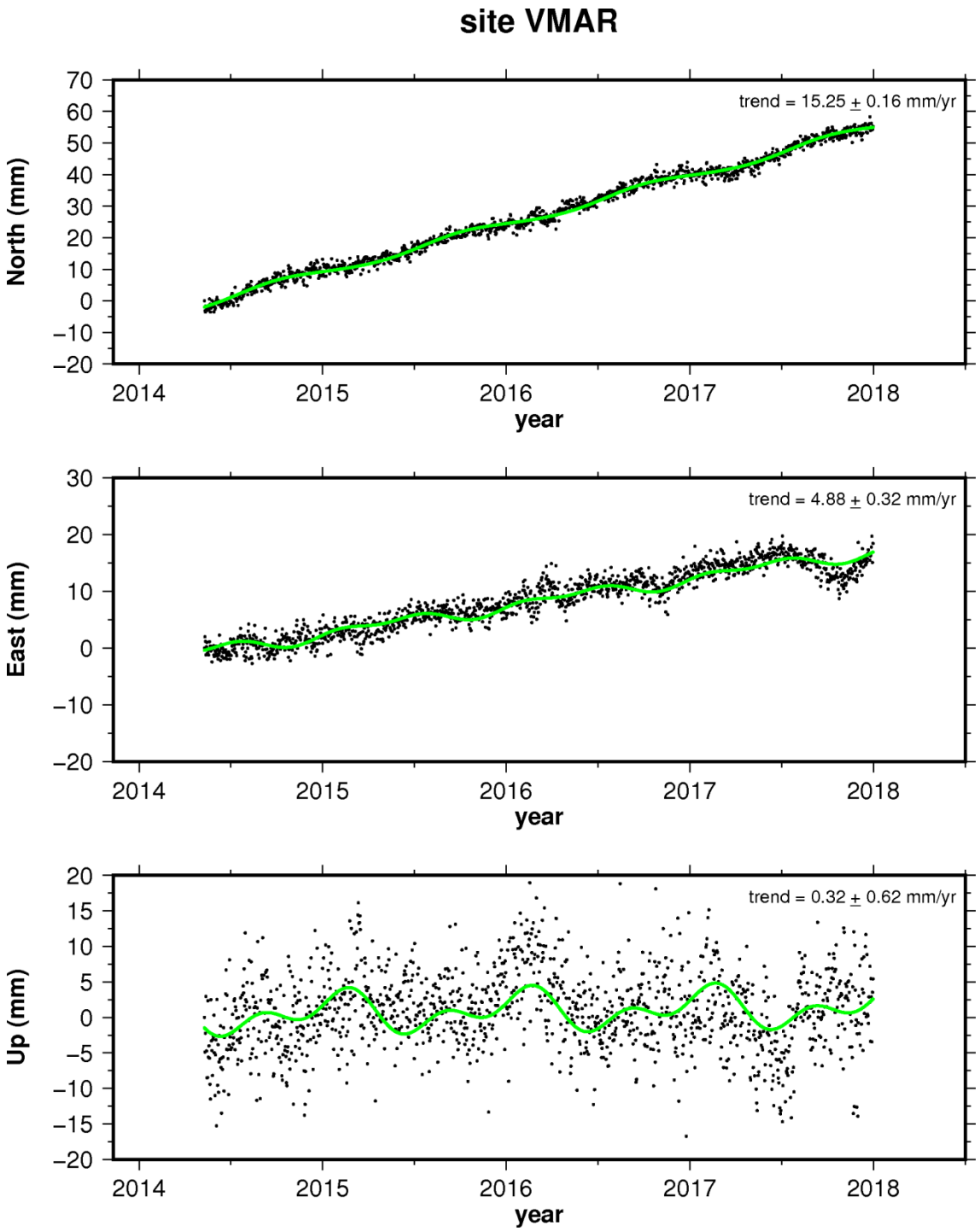
site VMAR
North (mm)
trend = 15.25 ± 0.16 mm/yr
East (mm)
trend = 4.88 ± 0.32 mm/yr
Up (mm)
trend = 0.32 ± 0.62 mm/yr
year
2014
2015
2016
2017
2018

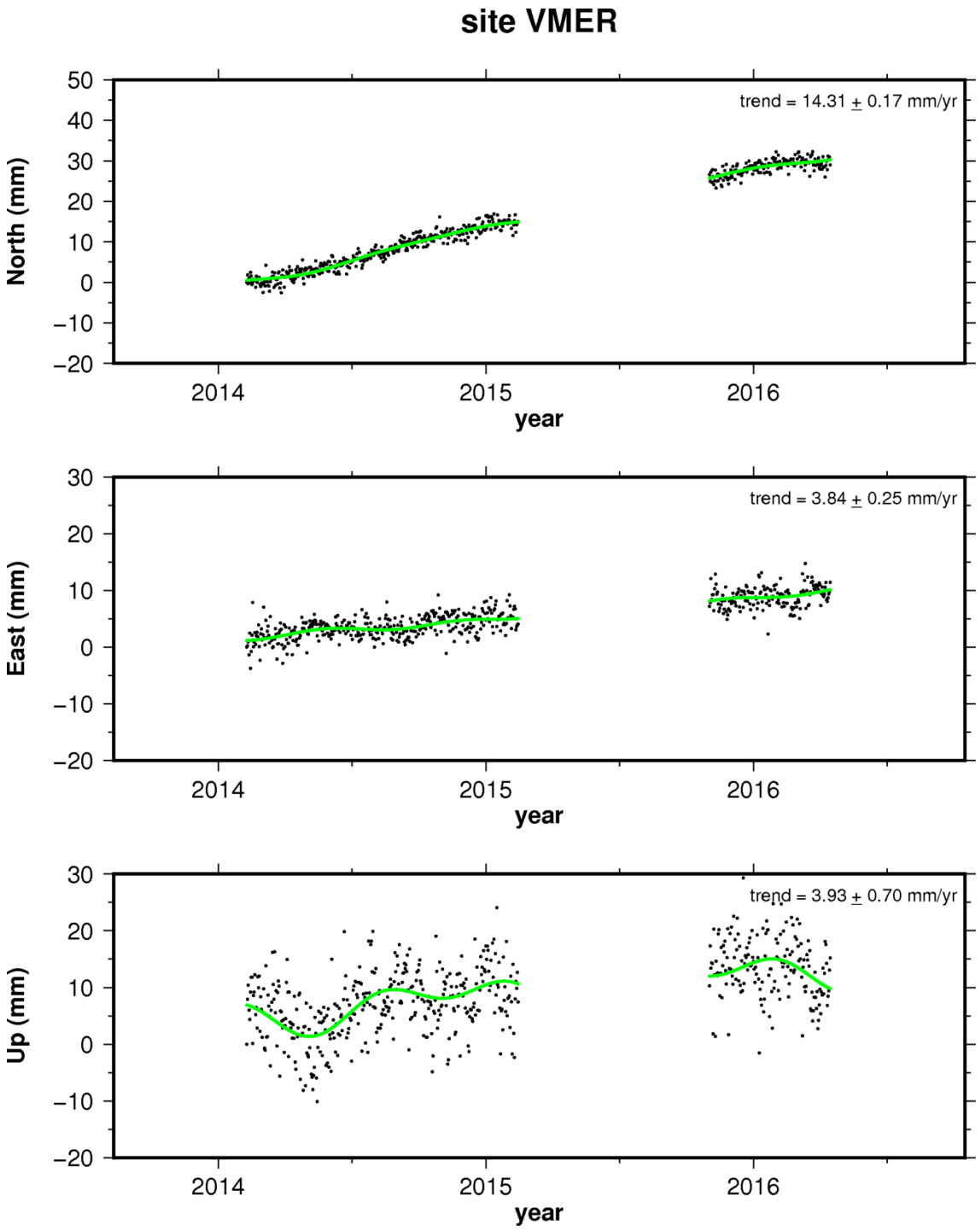
site VMER
North (mm)
trend = 14.31 ± 0.17 mm/yr
East (mm)
trend = 3.84 ± 0.25 mm/yr
Up (mm)
trend = 3.93 ± 0.70 mm/yr
year
2014
2015
2016

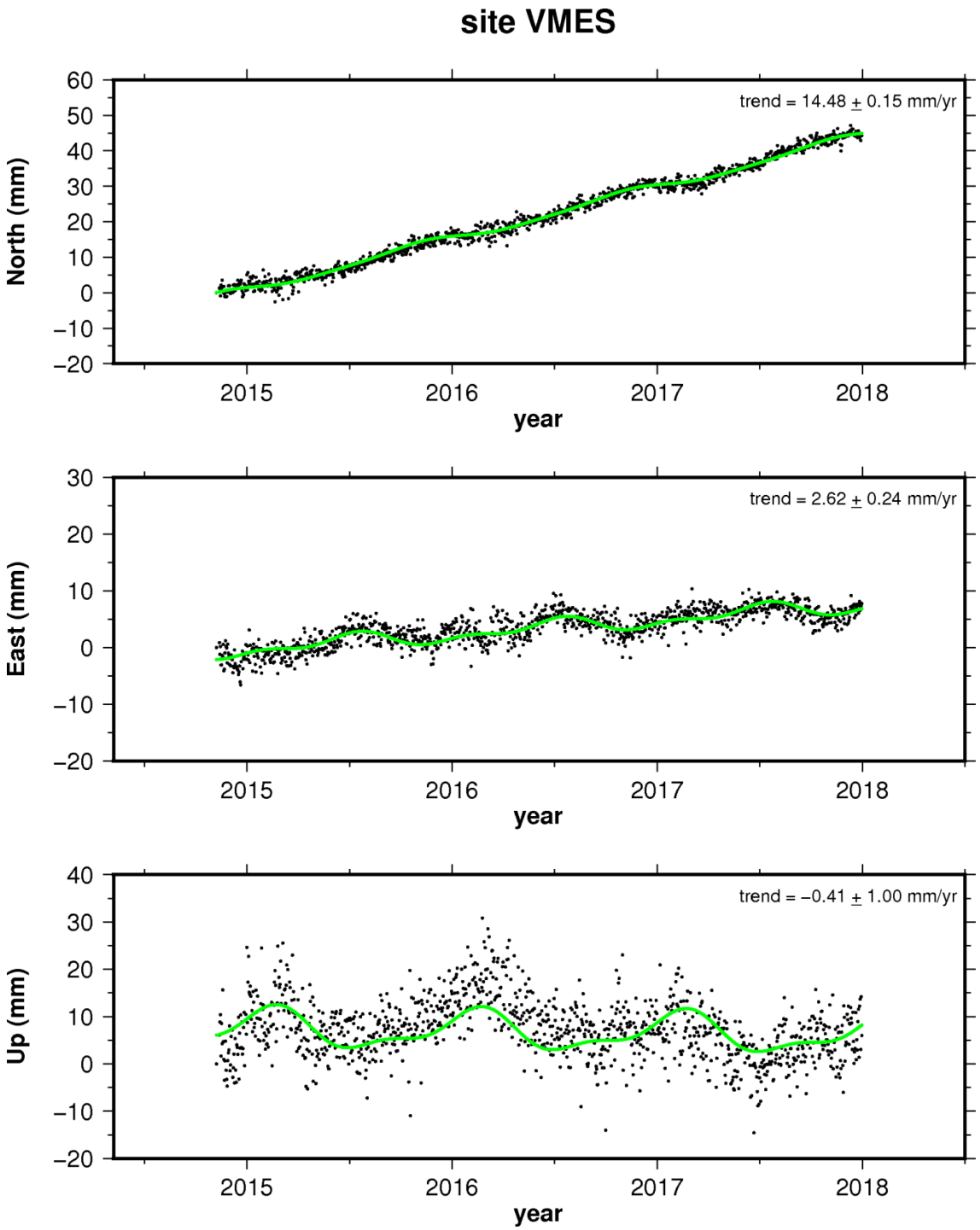
site VMES
North (mm)
trend = 14.48 ± 0.15 mm/yr
East (mm)
trend = 2.62 ± 0.24 mm/yr
Up (mm)
trend = −0.41 ± 1.00 mm/yr
year
2015
2016
2017
2018

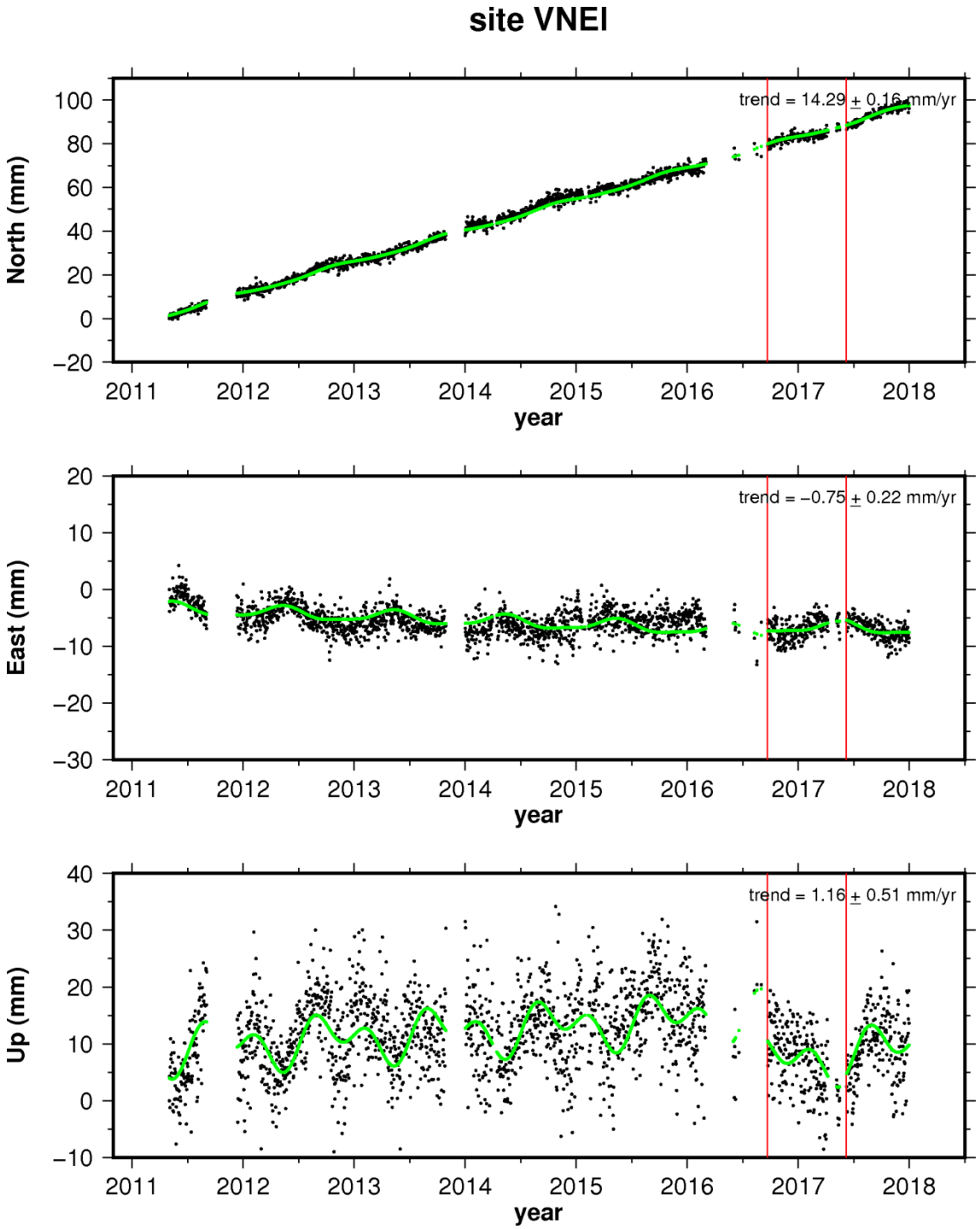
site VNEI
North (mm)
East (mm)
Up (mm)
year
trend = 14.29 ± 0.16 mm/yr
trend = −0.75 ± 0.22 mm/yr
trend = 1.16 ± 0.51 mm/yr
2011
2012
2013
2014
2015
2016
2017
2018

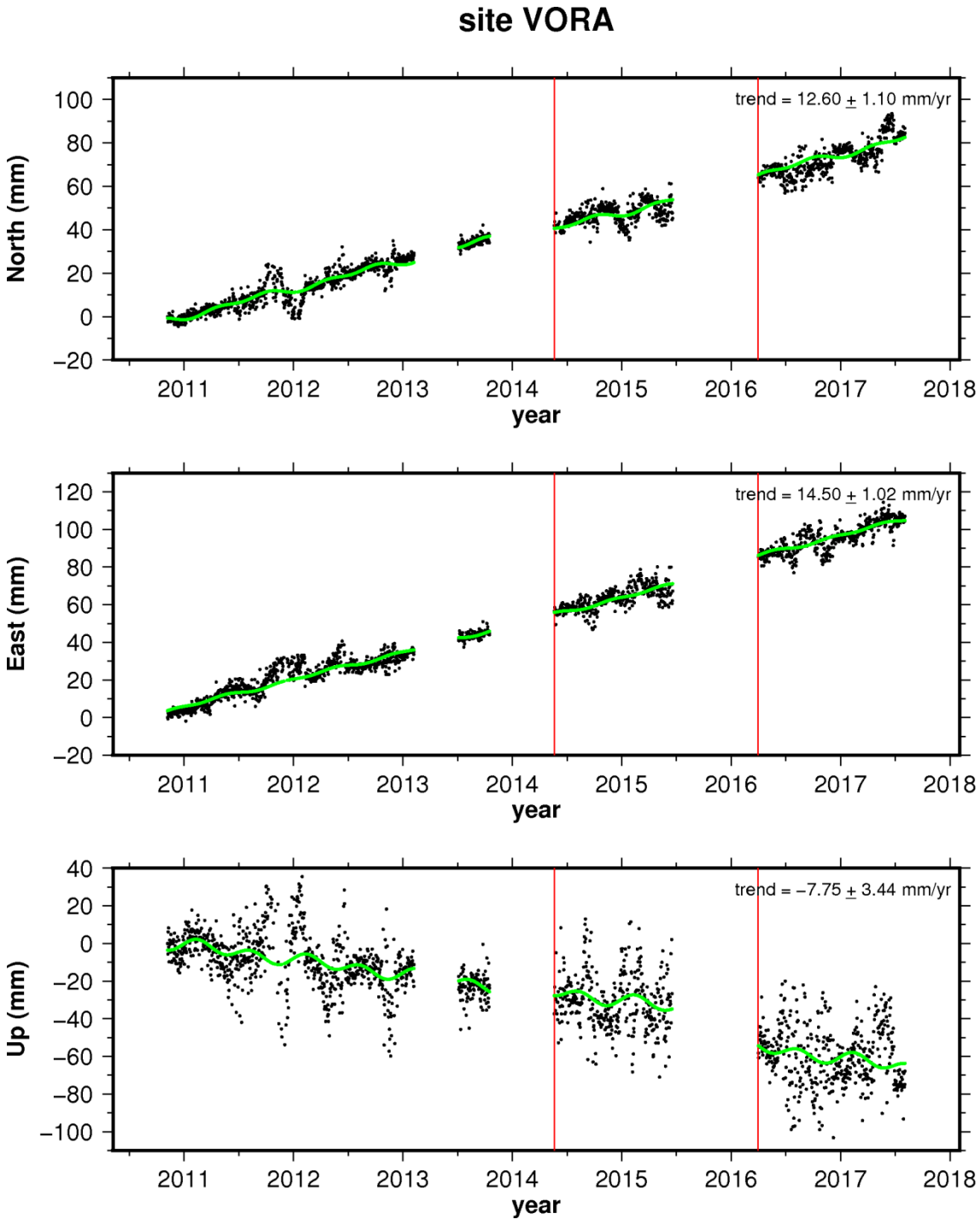
site VORA
North (mm)
trend = 12.60 ± 1.10 mm/yr
East (mm)
trend = 14.50 ± 1.02 mm/yr
Up (mm)
trend = −7.75 ± 3.44 mm/yr
year
2011
2012
2013
2014
2015
2016
2017
2018

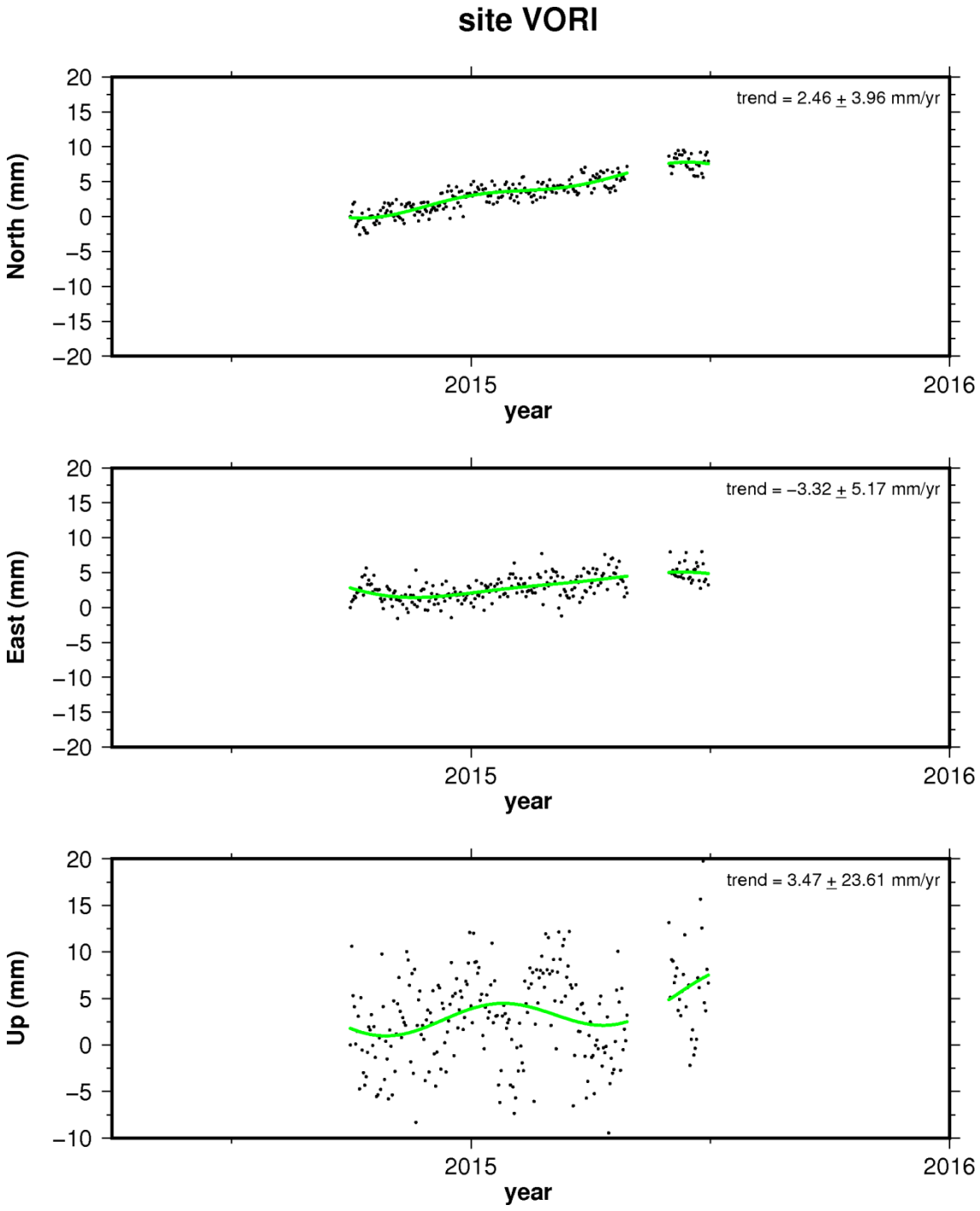
site VORI
North (mm)
East (mm)
Up (mm)
trend = 2.46 ± 3.96 mm/yr
trend = −3.32 ± 5.17 mm/yr
trend = 3.47 ± 23.61 mm/yr
20
15
10
5
0
−5
−10
−15
−20
2015
2016
year

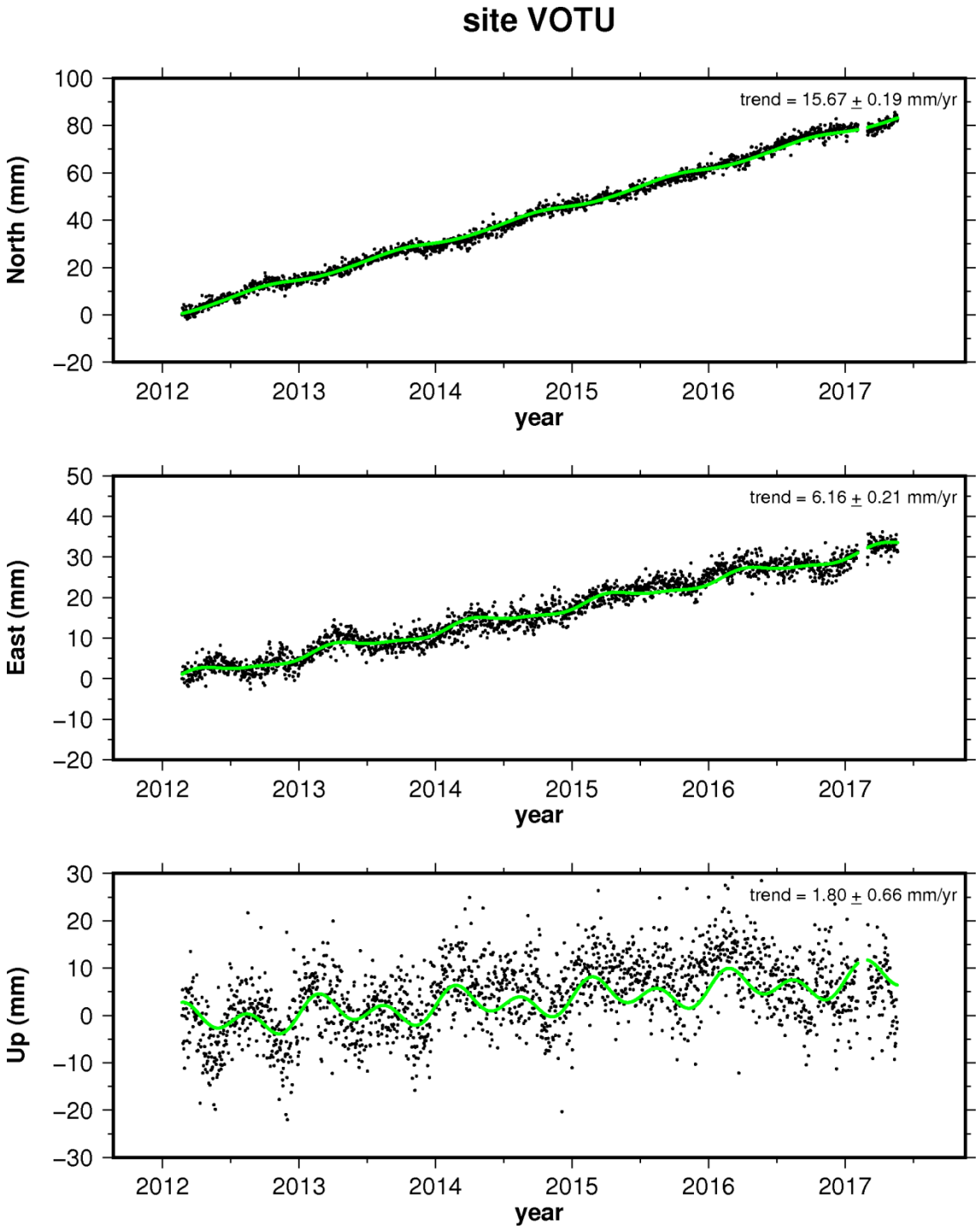
site VOTU
trend = 15.67 ± 0.19 mm/yr
North (mm)
100
80
60
40
20
0
−20
2012
2013
2014
2015
2016
2017
year
trend = 6.16 ± 0.21 mm/yr
East (mm)
50
40
30
20
10
0
−10
−20
2012
2013
2014
2015
2016
2017
year
trend = 1.80 ± 0.66 mm/yr
Up (mm)
30
20
10
0
−10
−20
−30
2012
2013
2014
2015
2016
2017
year

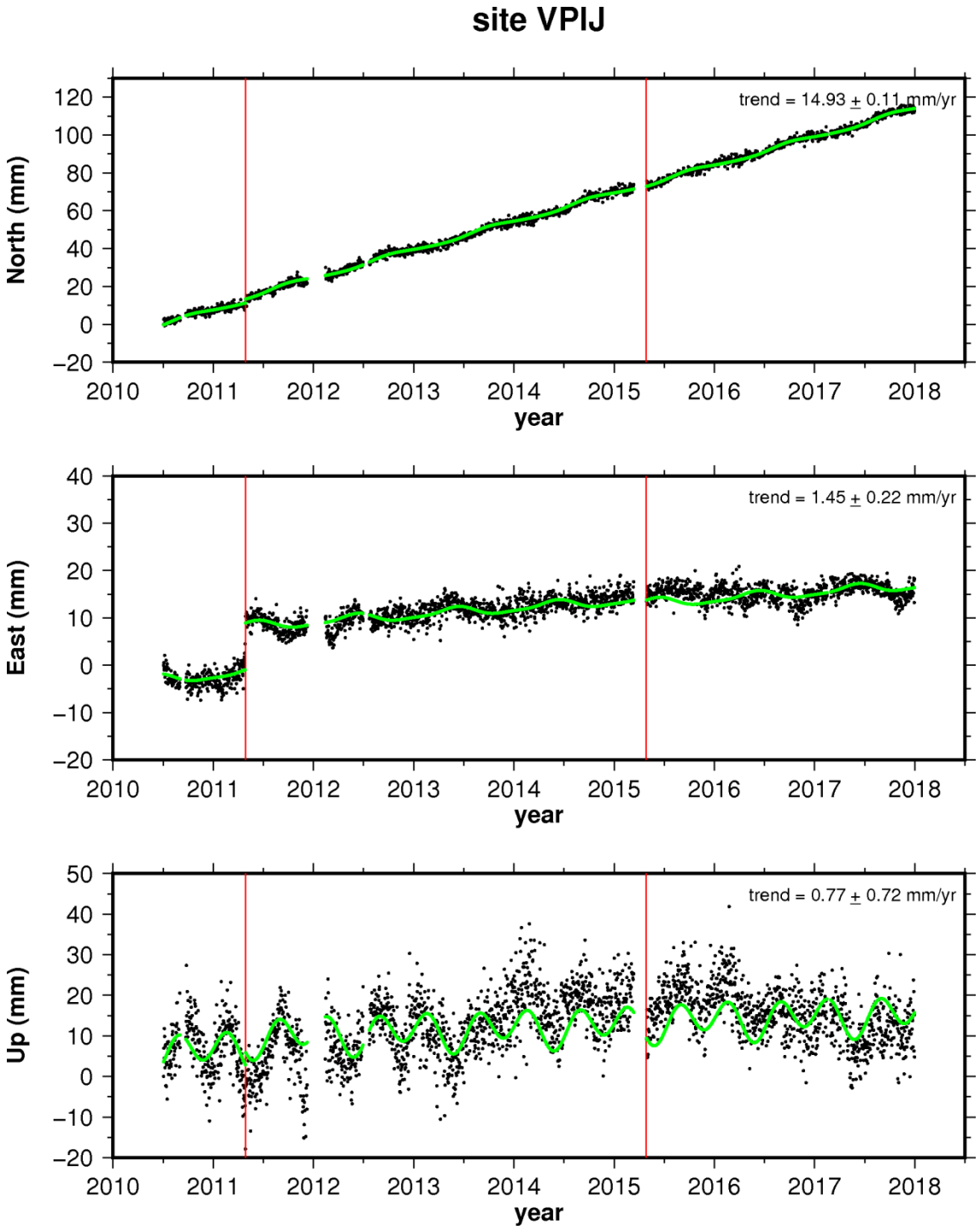
site VPIJ
North (mm)
trend = 14.93 ± 0.11 mm/yr
East (mm)
trend = 1.45 ± 0.22 mm/yr
Up (mm)
trend = 0.77 ± 0.72 mm/yr
year
2010
2011
2012
2013
2014
2015
2016
2017
2018

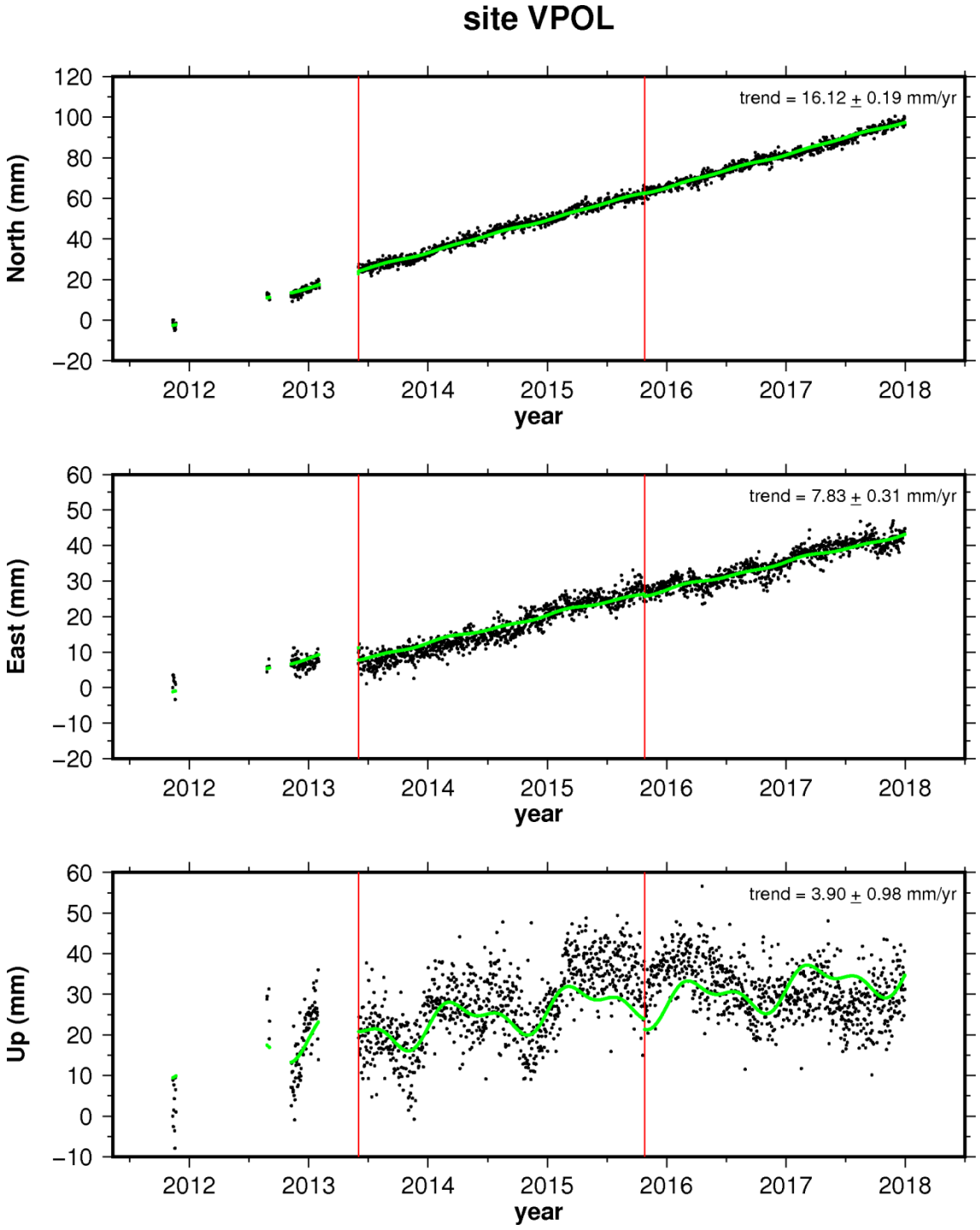
site VPOL
North (mm)
trend = 16.12 ± 0.19 mm/yr
East (mm)
trend = 7.83 ± 0.31 mm/yr
Up (mm)
trend = 3.90 ± 0.98 mm/yr
year
2012
2013
2014
2015
2016
2017
2018

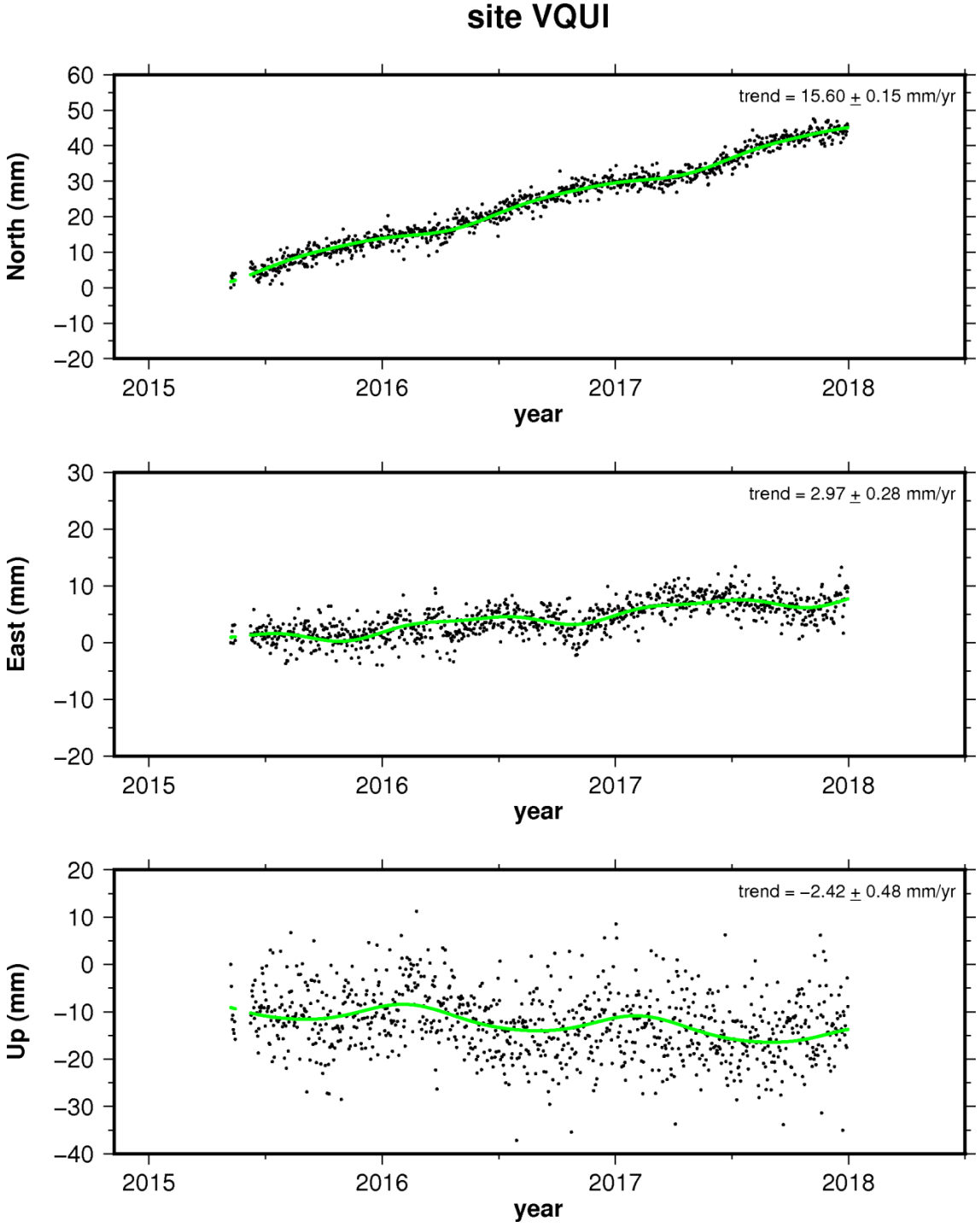
site VQUI
trend = 15.60 ± 0.15 mm/yr
North (mm)
60
50
40
30
20
10
0
−10
−20
2015
2016
2017
2018
year
trend = 2.97 ± 0.28 mm/yr
East (mm)
30
20
10
0
−10
−20
2015
2016
2017
2018
year
trend = −2.42 ± 0.48 mm/yr
Up (mm)
20
10
0
−10
−20
−30
−40
2015
2016
2017
2018
year

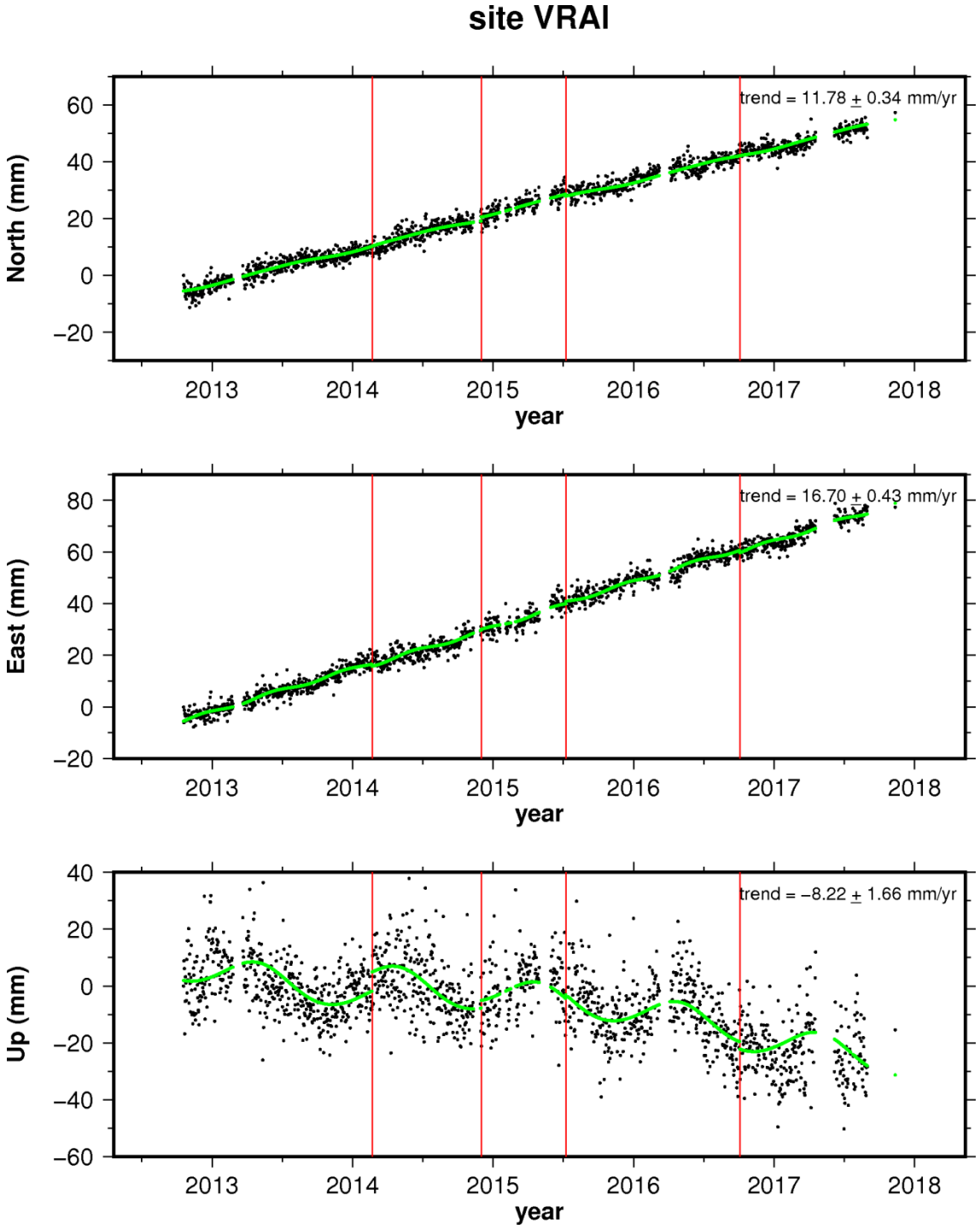
site VRAI
trend = 11.78 ± 0.34 mm/yr
North (mm)
60
40
20
0
−20
2013
2014
2015
2016
2017
2018
year
trend = 16.70 ± 0.43 mm/yr
East (mm)
80
60
40
20
0
−20
2013
2014
2015
2016
2017
2018
year
trend = −8.22 ± 1.66 mm/yr
Up (mm)
40
20
0
−20
−40
−60
2013
2014
2015
2016
2017
2018
year

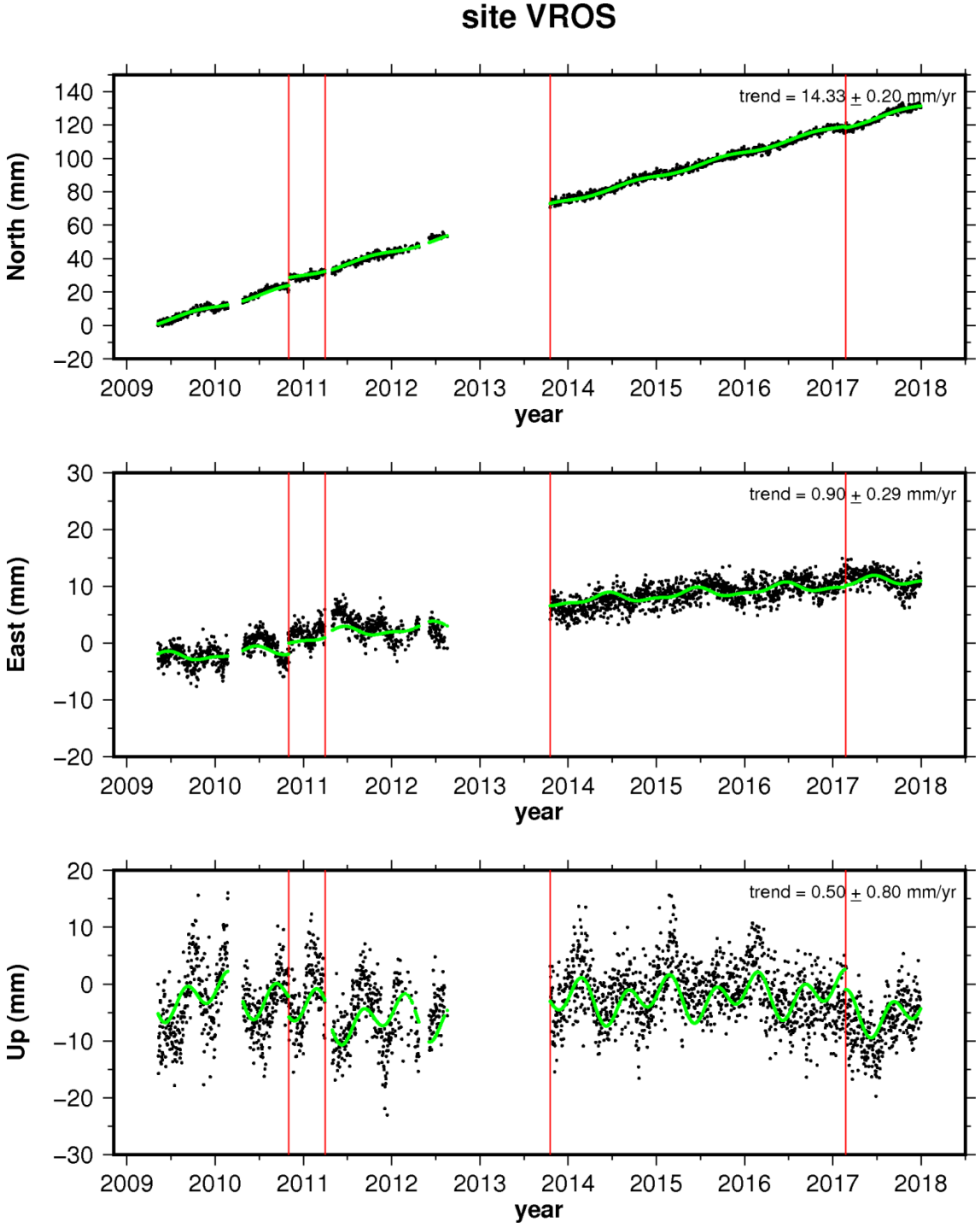
site VROS
trend = 14.33 ± 0.20 mm/yr
North (mm)
140
120
100
80
60
40
20
0
−20
2009
2010
2011
2012
2013
2014
2015
2016
2017
2018
year
trend = 0.90 ± 0.29 mm/yr
East (mm)
30
20
10
0
−10
−20
year
trend = 0.50 ± 0.80 mm/yr
Up (mm)
20
10
0
−10
−20
−30
year

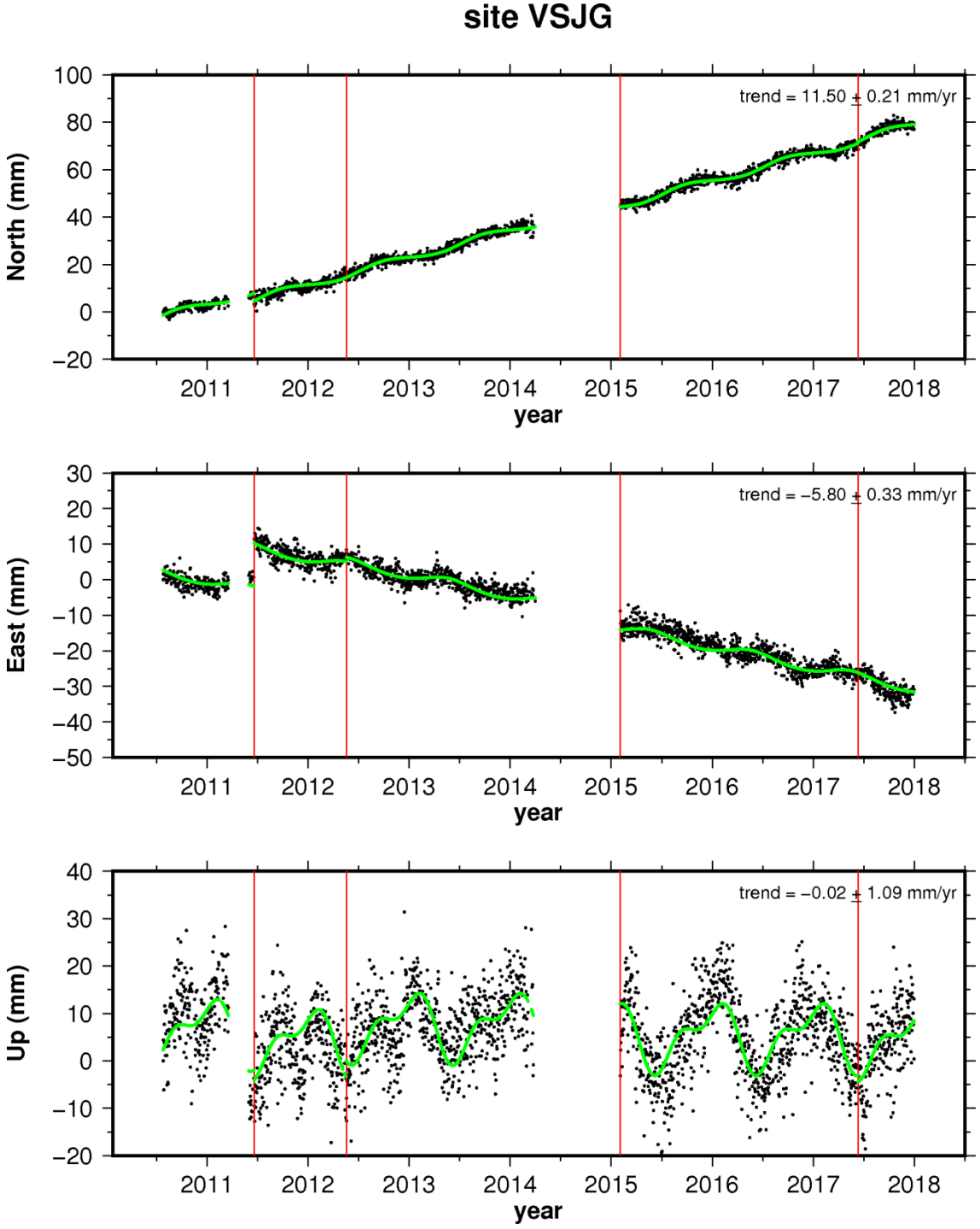
site VSJG
trend = 11.50 ± 0.21 mm/yr
North (mm)
100
80
60
40
20
0
−20
2011
2012
2013
2014
2015
2016
2017
2018
year
trend = −5.80 ± 0.33 mm/yr
East (mm)
30
20
10
0
−10
−20
−30
−40
−50
year
trend = −0.02 ± 1.09 mm/yr
Up (mm)
40
30
20
10
0
−10
−20
year

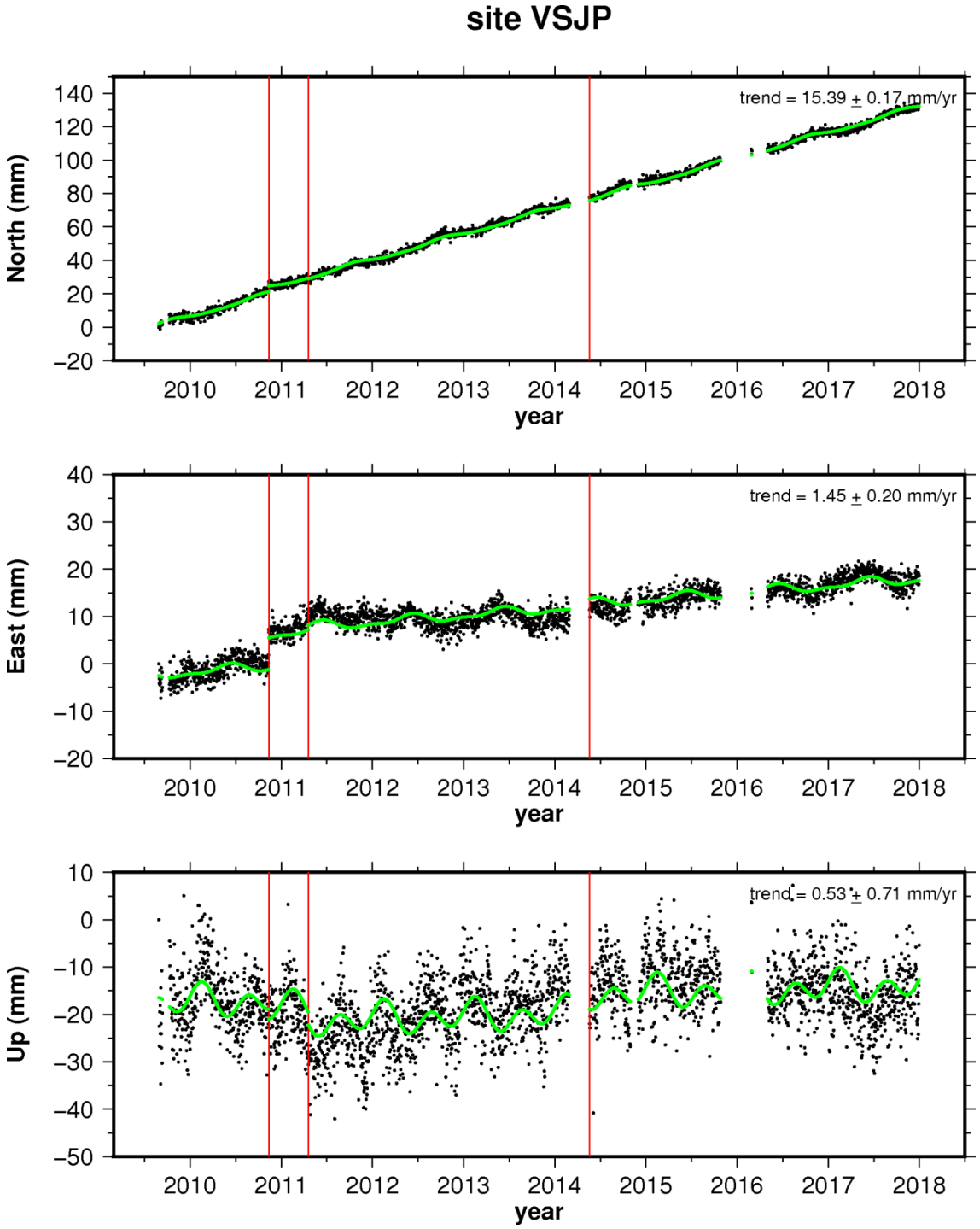
site VSJP
trend = 15.39 ± 0.17 mm/yr
North (mm)
140
120
100
80
60
40
20
0
−20
2010
2011
2012
2013
2014
2015
2016
2017
2018
year
trend = 1.45 ± 0.20 mm/yr
East (mm)
40
30
20
10
0
−10
−20
year
trend = 0.53 ± 0.71 mm/yr
Up (mm)
10
0
−10
−20
−30
−40
−50
year

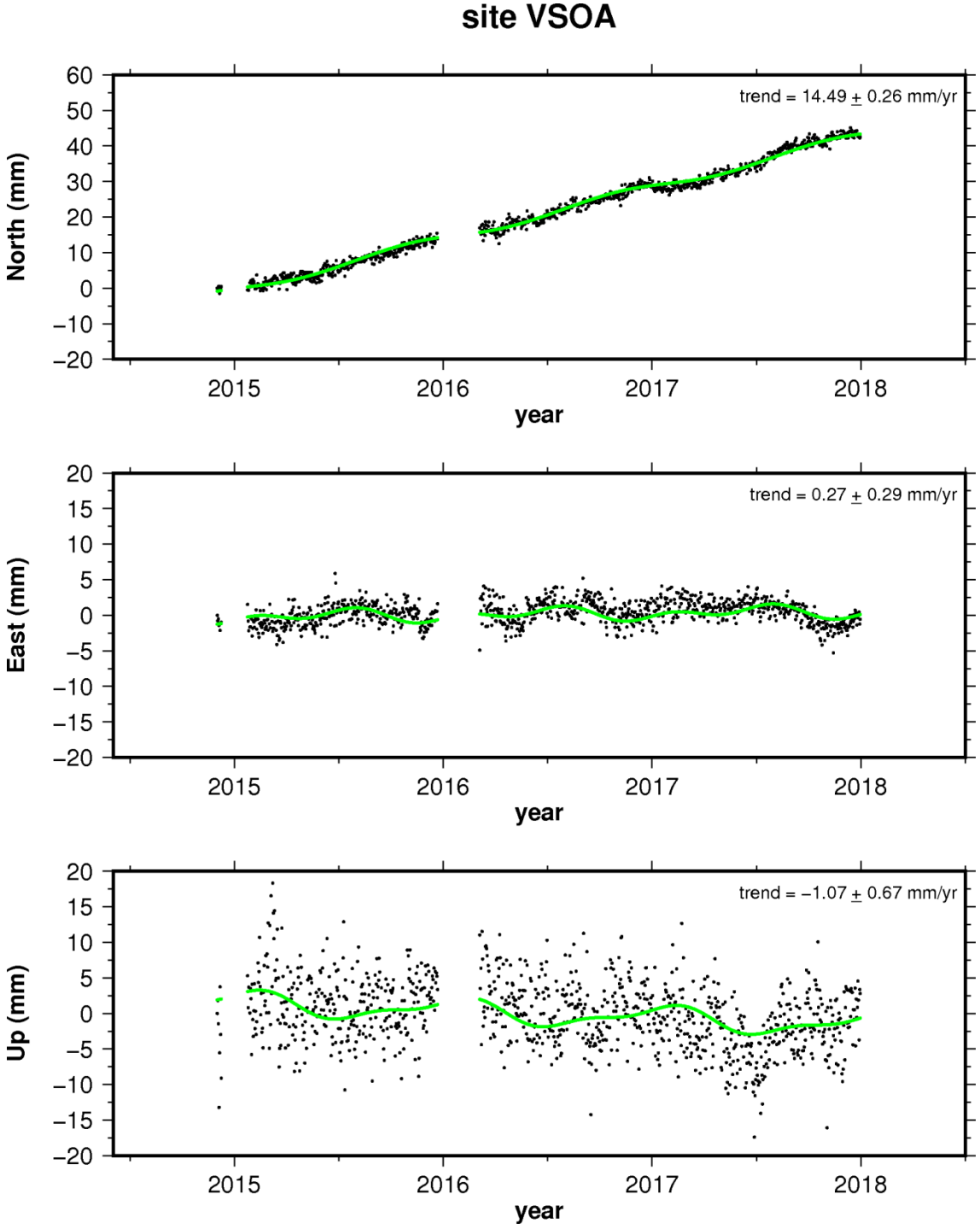
site VSOA
North (mm)
trend = 14.49 ± 0.26 mm/yr
year
East (mm)
trend = 0.27 ± 0.29 mm/yr
year
Up (mm)
trend = −1.07 ± 0.67 mm/yr
year
2015
2016
2017
2018

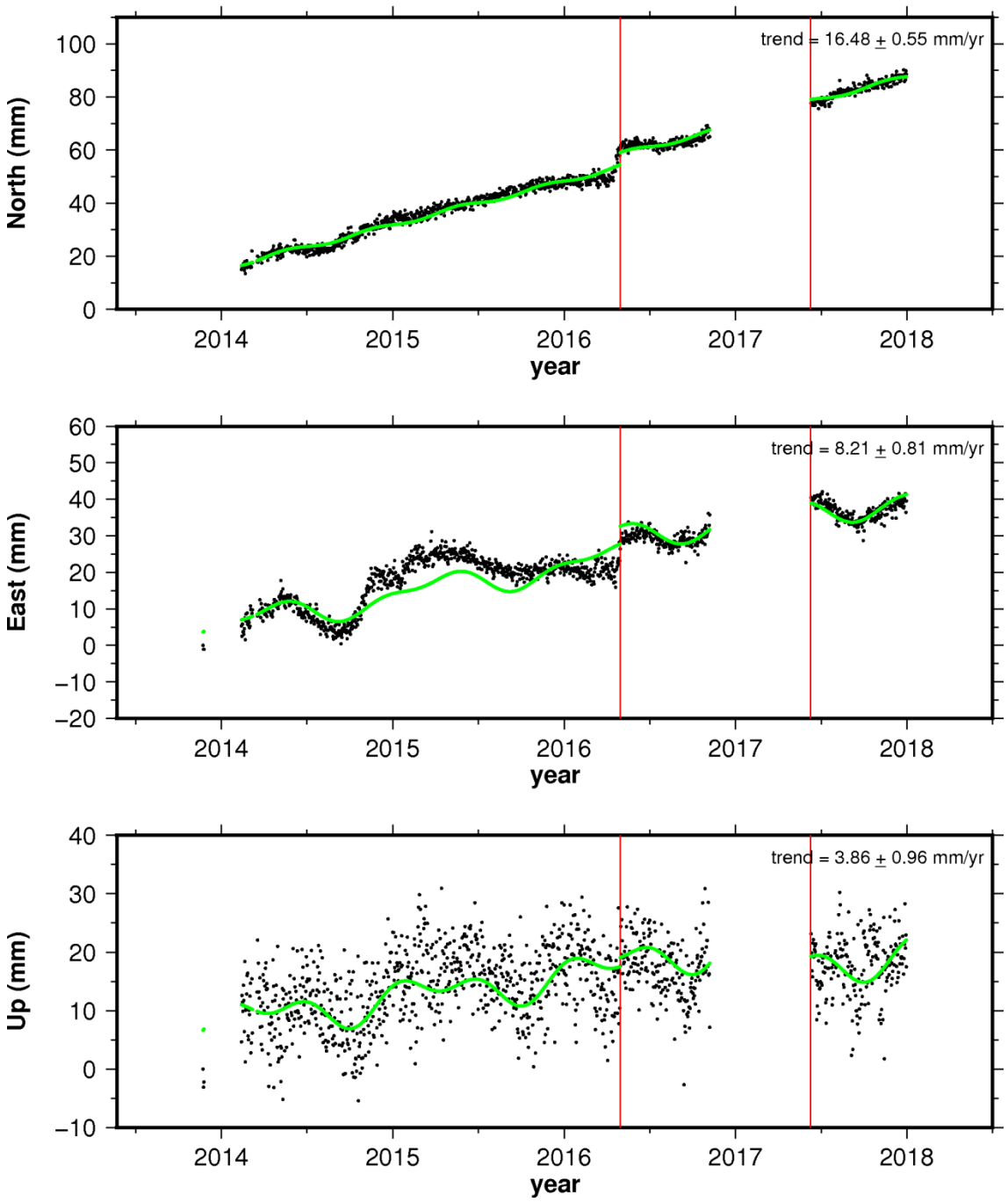
site VTUL
trend = 16.48 ± 0.55 mm/yr
North (mm)
100
80
60
40
20
0
2014
2015
2016
2017
2018
year
trend = 8.21 ± 0.81 mm/yr
East (mm)
60
50
40
30
20
10
0
−10
−20
2014
2015
2016
2017
2018
year
trend = 3.86 ± 0.96 mm/yr
Up (mm)
40
30
20
10
0
−10
2014
2015
2016
2017
2018
year

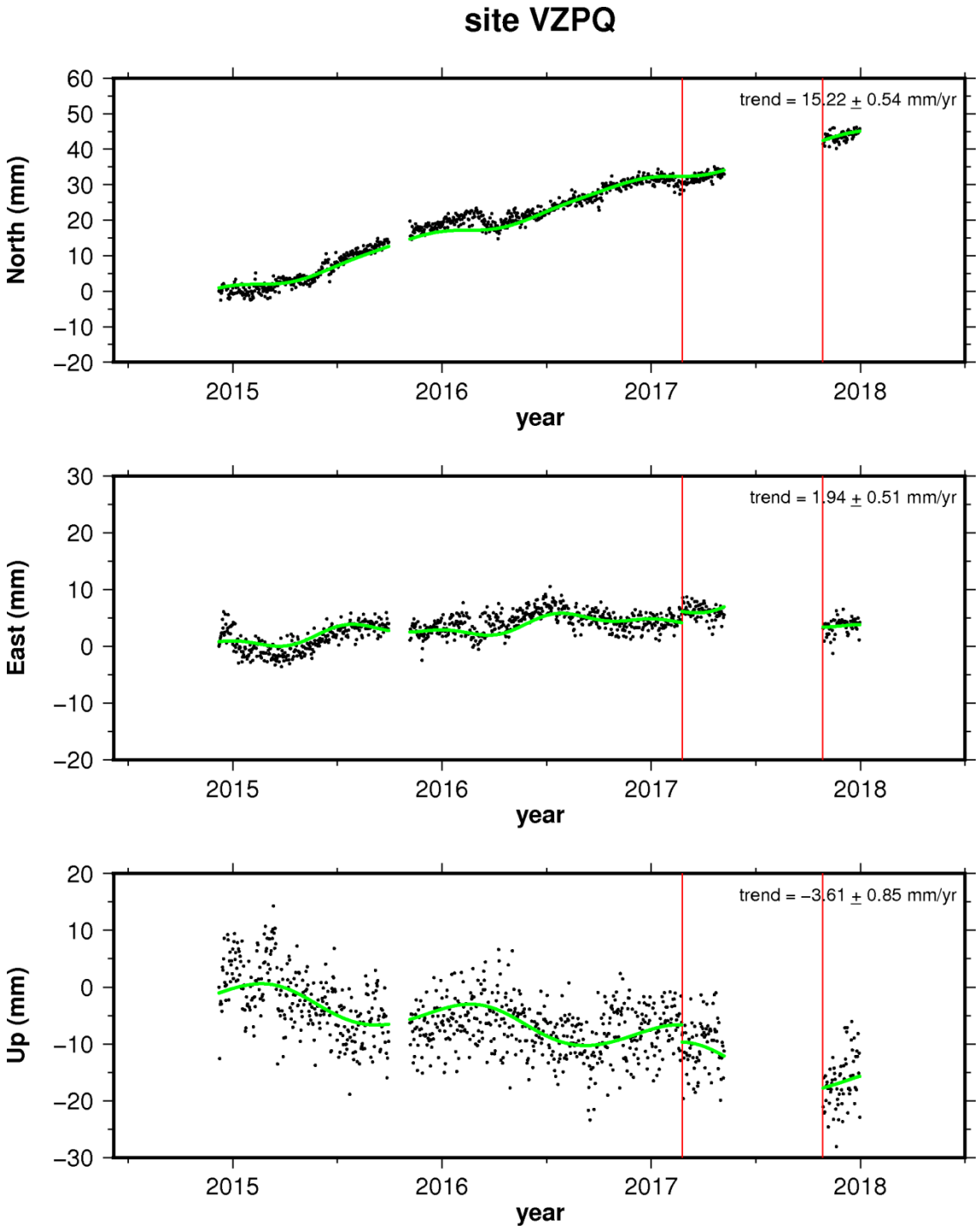
site VZPQ
North (mm)
trend = 15.22 ± 0.54 mm/yr
East (mm)
trend = 1.94 ± 0.51 mm/yr
Up (mm)
trend = −3.61 ± 0.85 mm/yr
year
2015
2016
2017
2018

APPENDIX B: NOISE PARAMETERS FOR GPS VELOCITY ESTIMATIONS IN 3-DIMENSIONAL COMPONENTS

STD: Standard deviation, WN: White Noise and PL: Power Law Noise

Noise parameters (East)					
No.	**ID station**	**STD driving noise**	**Spectral index**	**WN fraction**	**PL fraction**
1	ACP1	1.966	0.454	0.819	0.181
2	ACP6	1.782	0.459	0.684	0.316
3	AJCM	1.756	0.415	0.677	0.323
4	ALPA	1.691	0.494	0.691	0.309
5	ANCH	1.964	0.123	0.000	1.000
6	BAAP	1.600	0.400	0.588	0.412
7	BAME	1.548	0.483	0.631	0.369
8	BAPA	1.754	0.424	0.744	0.256
9	BARU	1.668	0.467	0.787	0.213
10	BASO	2.153	0.485	0.787	0.213
11	BOBG	2.147	0.473	0.829	0.171
12	BOGT	1.633	0.374	0.452	0.548
13	BUGT	1.916	0.454	0.827	0.173
14	CAPI	1.629	0.439	0.682	0.319
15	CAYS	1.608	0.451	0.731	0.269
16	CCAN	1.622	0.291	0.021	0.979
17	CIA1	1.604	0.498	0.257	0.743
18	CIOH	1.653	0.258	0.330	0.670
19	CN19	1.558	0.387	0.577	0.423
20	CN20	2.222	0.294	0.596	0.404
21	CN28	1.774	0.269	0.307	0.693
22	CN33	2.209	0.483	0.515	0.485
23	CN34	6.977	0.493	0.619	0.381

(continued on next page)

(continued)

Noise parameters (East)					
No.	**ID station**	**STD driving noise**	**Spectral index**	**WN fraction**	**PL fraction**
24	CN35	1.877	0.432	0.717	0.283
25	CN36	1.695	0.491	0.517	0.483
26	CN38	1.556	0.413	0.630	0.370
27	CN39	1.644	0.433	0.538	0.462
28	CN40	1.735	0.339	0.577	0.423
29	CN41	1.583	0.321	0.537	0.463
30	CN42	1.375	0.170	0.000	1.0000
31	CORO	1.662	0.474	0.786	0.214
32	COVE	1.627	0.452	0.652	0.348
33	CUC1	2.222	0.499	0.590	0.410
34	DIMA	1.839	0.381	0.661	0.339
35	GALE	1.591	0.460	0.694	0.306
36	GLPS	1.259	0.466	0.550	0.450
37	GUAP	1.820	0.476	0.838	0.162
38	IND1	2.141	0.493	0.683	0.317
39	INRI	1.522	0.473	0.729	0.271
40	INTO	1.406	0.477	0.647	0.353
41	ISCO	2.368	0.364	0.593	0.407
42	MALO	2.055	0.359	0.700	0.300
43	MECE	1.932	0.492	0.757	0.243
44	MITU	1.732	0.448	0.804	0.196
45	MZAL	1.588	0.498	0.658	0.342
46	OAMU	1.622	0.492	0.487	0.513
47	OCEL	1.493	0.483	0.766	0.234
48	PAL2	1.512	0.423	0.762	0.238

(continued on next page)

(continued)

Noise parameters (East)					
No.	**ID station**	**STD driving noise**	**Spectral index**	**WN fraction**	**PL fraction**
49	PASI	1.600	0.261	0.448	0.552
50	POVA	1.497	0.465	0.737	0.263
51	PUIN	1.736	0.429	0.803	0.197
52	QSEC	1.961	0.497	0.541	0.459
53	QUIL	1.676	0.491	0.722	0.278
54	RIOP	1.298	0.497	0.531	0.469
55	SAN0	1.735	0.493	0.720	0.280
56	SEL1	1.397	0.472	0.641	0.359
57	SUAM	1.589	0.487	0.669	0.331
58	TASA	1.605	0.410	0.594	0.406
59	TGPM	2.283	0.473	0.780	0.220
60	TICU	1.560	0.405	0.700	0.300
61	TONE	1.445	0.494	0.658	0.342
62	TUCO	1.577	0.487	0.695	0.305
63	UNME	1.656	0.481	0.594	0.406
64	URR0	1.764	0.170	0.004	0.996
65	UWAS	1.453	0.438	0.614	0.386
66	VBUV	1.290	0.497	0.519	0.481
67	VCAR	1.930	-0.034	0.000	1.000
68	VCRG	1.360	0.397	0.655	0.345
69	VDPR	2.020	0.332	0.632	0.368
70	VMAG	1.820	0.491	0.767	0.233
71	VMAR	1.348	0.466	0.577	0.423
72	VMER	1.693	0.171	0.000	1.000
73	VMES	1.442	0.405	0.699	0.301

(continued on next page)

(continued)

Noise parameters (East)					
No.	**ID station**	**STD driving noise**	**Spectral index**	**WN fraction**	**PL fraction**
74	VNEI	1.621	0.473	0.724	0.276
75	VORA	3.029	0.491	0.400	0.600
76	VORI	1.400	0.121	0.000	1.000
77	VOTU	1.684	0.479	0.788	0.212
78	VPIJ	1.429	0.489	0.700	0.300
79	VPOL	1.759	0.485	0.762	0.238
80	VQUI	1.944	0.307	0.603	0.397
81	VRAI	2.133	0.352	0.605	0.395
82	VROS	1.282	0.479	0.488	0.512
83	VSJG	1.700	0.484	0.765	0.235
84	VSJP	1.411	0.491	0.746	0.254
85	VSOA	1.202	0.442	0.622	0.378
86	VTUL	1.611	0.497	0.270	0.730
87	VZPQ	1.272	0.475	0.584	0.416

Noise parameters (North)					
No.	**ID station**	**STD driving noise**	**Spectral index**	**WN fraction**	**PL fraction**
1	ACP1	1.777	0.424	0.694	0.306
2	ACP6	2.006	0.338	0.206	0.794
3	AJCM	1.555	0.253	0.298	0.702
4	ALPA	1.421	0.497	0.624	0.376
5	ANCH	1.510	0.273	0.559	0.441
6	BAAP	1.179	0.382	0.615	0.385
7	BAME	1.140	0.472	0.668	0.332
8	BAPA	1.381	0.378	0.622	0.378
9	BARU	1.311	0.365	0.570	0.430
10	BASO	1.697	0.465	0.762	0.238
11	BOBG	1.486	0.426	0.737	0.263
12	BOGT	1.230	0.397	0.378	0.622
13	BUGT	1.702	0.480	0.819	0.181
14	CAPI	1.252	0.489	0.660	0.340
15	CAYS	1.368	0.432	0.626	0.374
16	CCAN	1.281	0.328	0.388	0.612
17	CIA1	1.262	0.497	0.423	0.577
18	CIOH	1.327	0.358	0.520	0.480
19	CN19	1.277	0.370	0.456	0.544
20	CN20	1.747	0.412	0.770	0.230
21	CN28	1.365	0.275	0.453	0.547
22	CN33	2.722	0.465	0.100	0.900
23	CN34	3.907	0.496	0.225	0.775
24	CN35	1.497	0.294	0.174	0.826
25	CN36	1.470	0.498	0.212	0.788
26	CN38	1.269	0.333	0.493	0.507

(continued on next page)

(continued)

Noise parameters (North)					
No.	**ID station**	**STD driving noise**	**Spectral index**	**WN fraction**	**PL fraction**
27	CN39	1.314	0.468	0.543	0.457
28	CN40	1.599	0.274	0.327	0.673
29	CN41	1.275	0.349	0.504	0.496
30	CN42	1.199	0.113	0.000	1.000
31	CORO	1.382	0.405	0.622	0.378
32	COVE	1.607	0.489	0.526	0.474
33	CUC1	1.702	0.494	0.697	0.303
34	DIMA	1.624	0.367	0.580	0.420
35	GALE	1.430	0.495	0.432	0.568
36	GLPS	1.003	0.409	0.164	0.836
37	GUAP	1.651	0.285	0.679	0.321
38	IND1	1.923	0.475	0.637	0.363
39	INEG	1.393	0.498	0.759	0.241
40	INRI	1.186	0.468	0.527	0.473
41	INTO	2.148	0.341	0.781	0.219
42	ISCO	1.697	0.486	0.550	0.450
43	MALO	1.568	0.292	0.725	0.275
44	MECE	1.453	0.490	0.560	0.440
45	MITU	1.479	0.270	0.577	0.423
46	MZAL	1.317	0.499	0.658	0.343
47	OAMU	1.342	0.488	0.537	0.463
48	OCEL	1.399	0.348	0.653	0.347
49	PAL2	1.183	0.423	0.000	1.000
50	PASI	1.278	0.134	0.743	0.257
51	POVA	1.418	0.490	0.737	0.263

(continued on next page)

(continued)

Noise parameters (North)					
No.	**ID station**	**STD driving noise**	**Spectral index**	**WN fraction**	**PL fraction**
52	PUIN	1.702	0.455	0.610	0.390
53	QSEC	1.367	0.494	0.669	0.331
54	QUIL	0.969	0.483	0.574	0.426
55	RIOP	1.457	0.494	0.716	0.284
56	SEL1	1.143	0.424	0.560	0.440
57	SUAM	1.278	0.470	0.485	0.515
58	TASA	1.541	0.258	0.230	0.770
59	TGPM	1.777	0.435	0.837	0.163
60	TICU	1.253	0.282	0.463	0.537
61	TONE	1.282	0.446	0.678	0.322
62	TUCO	1.339	0.418	0.773	0.227
63	UNME	1.493	0.475	0.616	0.384
64	URR0	1.523	0.414	0.655	0.345
65	UWAS	1.153	0.440	0.537	0.463
66	VBUV	1.105	0.489	0.430	0.570
67	VCAR	1.403	0.029	0.000	1.000
68	VCRG	1.101	0.367	0.648	0.352
69	VDPR	1.635	0.412	0.591	0.409
70	VMAG	1.430	0.490	0.724	0.276
71	VMAR	1.245	0.311	0.293	0.707
72	VMER	1.287	0.149	0.000	1.000
73	VMES	1.216	0.284	0.395	0.605
74	VNEI	1.281	0.448	0.669	0.331
75	VORA	2.891	0.487	0.201	0.799
76	VORI	1.065	0.125	0.000	1.000

(continued on next page)

(continued)

Noise parameters (North)					
No.	**ID station**	**STD driving noise**	**Spectral index**	**WN fraction**	**PL fraction**
77	VOTU	1.439	0.476	0.744	0.256
78	VPIJ	1.179	0.370	0.588	0.412
79	VPOL	1.449	0.418	0.752	0.248
80	VQUI	1.771	0.130	0.000	1.000
81	VRAI	1.898	0.295	0.536	0.464
82	VROS	1.084	0.438	0.483	0.517
83	VSJG	1.302	0.398	0.635	0.365
84	VSJP	1.273	0.480	0.757	0.243
85	VSOA	0.949	0.447	0.527	0.473
86	VTUL	1.295	0.490	0.538	0.462
87	VZPQ	1.165	0.491	0.523	0.477

Noise parameters (Vertical)					
No.	**ID station**	**STD driving noise**	**Spectral index**	**WN fraction**	**PL fraction**
1	ACP1	6.550	0.428	0.819	0.181
2	ACP6	6.180	0.335	0.520	0.480
3	AJCM	5.796	0.324	0.474	0.526
4	ALPA	5.196	0.493	0.674	0.326
5	ANCH	6.485	0.059	0.000	1.000
6	BAAP	4.889	0.442	0.752	0.248
7	BAME	4.495	0.332	0.232	0.768
8	BAPA	5.529	0.459	0.739	0.261
9	BARU	5.038	0.478	0.745	0.255
10	BASO	6.635	0.469	0.827	0.173
11	BOBG	5.977	0.466	0.784	0.216
12	BOGT	5.357	0.493	0.415	0.585
13	BUGT	6.648	0.470	0.797	0.203
14	CAPI	4.592	0.471	0.610	0.390
15	CAYS	5.782	0.440	0.673	0.327
16	CCAN	4.870	0.400	0.357	0.643
17	CIA1	5.172	0.499	0.396	0.604
18	CIOH	5.250	0.371	0.729	0.271
19	CN19	4.760	0.200	0.000	1.000
20	CN20	8.308	0.328	0.758	0.242
21	CN28	5.440	0.219	0.413	0.587
22	CN33	7.488	0.430	0.305	0.695
23	CN34	20.571	0.470	0.532	0.468
24	CN35	5.979	0.285	0.522	0.478
25	CN36	4.992	0.493	0.656	0.344
26	CN38	4.827	0.287	0.450	0.550

(continued on next page)

(continued)

Noise parameters (Vertical)					
No.	**ID station**	**STD driving noise**	**Spectral index**	**WN fraction**	**PL fraction**
27	CN39	4.980	0.444	0.825	0.175
28	CN40	5.186	0.433	0.647	0.353
29	CN41	4.691	0.439	0.677	0.323
30	CN42	4.725	0.175	0.000	1.000
31	CORO	5.548	0.490	0.697	0.303
32	COVE	5.446	0.474	0.722	0.278
33	CUC1	6.746	0.463	0.788	0.212
34	DIMA	6.896	0.307	0.716	0.284
35	GALE	5.135	0.467	0.668	0.332
36	GLPS	3.669	0.404	0.155	0.845
37	GUAP	6.387	0.407	0.680	0.320
38	IND1	7.187	0.459	0.832	0.168
39	INRI	5.770	0.342	0.667	0.333
40	INTO	4.712	0.255	0.334	0.666
41	ISCO	8.924	0.148	0.000	1.000
42	MALO	6.120	0.339	0.506	0.494
43	MECE	6.381	0.495	0.719	0.281
44	MITU	5.840	0.443	0.784	0.217
45	MZAL	5.464	0.494	0.597	0.403
46	OAMU	5.401	0.326	0.182	0.818
47	OCEL	5.264	0.299	0.436	0.564
48	PAL2	5.034	0.377	0.672	0.328
49	PASI	5.189	0.181	0.052	0.948
50	POVA	4.754	0.483	0.651	0.349

(continued on next page)

(continued)

Noise parameters (Vertical)					
No.	**ID station**	**STD driving noise**	**Spectral index**	**WN fraction**	**PL fraction**
51	PUIN	5.856	0.493	0.725	0.275
52	QSEC	6.642	0.285	0.398	0.602
53	QUIL	5.477	0.408	0.385	0.615
54	RIOP	3.704	0.459	0.397	0.603
55	SAN0	5.578	0.432	0.772	0.228
56	SEL1	4.410	0.485	0.591	0.409
57	SUAM	5.145	0.345	0.752	0.248
58	TASA	5.278	0.298	0.405	0.595
59	TGPM	7.705	0.463	0.845	0.155
60	TICU	5.173	0.492	0.686	0.314
61	TONE	4.695	0.441	0.603	0.397
62	TUCO	5.189	0.442	0.706	0.294
63	UNME	6.528	0.395	0.378	0.622
64	URR0	5.639	0.442	0.746	0.254
65	UWAS	4.329	0.470	0.514	0.486
66	VBUV	3.891	0.491	0.598	0.402
67	VCAR	5.220	0.083	0.000	1.000
68	VCRG	4.160	0.438	0.667	0.333
69	VDPR	6.404	0.446	0.656	0.344
70	VMAG	5.639	0.493	0.733	0.267
71	VMAR	4.643	0.355	0.528	0.472
72	VMER	4.894	0.162	0.000	1.000
73	VMES	4.656	0.477	0.778	0.222
74	VNEI	5.339	0.387	0.618	0.382

(continued on next page)

(continued)

Noise parameters (Vertical)					
No.	**ID station**	**STD driving noise**	**Spectral index**	**WN fraction**	**PL fraction**
75	VORA	11.075	0.478	0.421	0.579
76	VORI	4.121	0.319	0.000	1.000
77	VOTU	5.350	0.479	0.789	0.211
78	VPIJ	4.839	0.493	0.727	0.273
79	VPOL	5.533	0.494	0.792	0.208
80	VQUI	6.397	0.184	0.668	0.332
81	VRAI	8.837	0.368	0.727	0.273
82	VROS	3.676	0.482	0.550	0.450
83	VSJG	5.549	0.487	0.768	0.232
84	VSJP	5.189	0.440	0.575	0.425
85	VSOA	3.978	0.325	0.325	0.675
86	VTUL	4.844	0.346	0.566	0.434
87	VZPQ	4.204	0.260	0.000	1.000